Takeshi Hasegawa

Quantitative Infrared Spectroscopy for Understanding of a Condensed Matter

Springer

Quantitative Infrared Spectroscopy for Understanding of a Condensed Matter

Takeshi Hasegawa

Quantitative Infrared Spectroscopy for Understanding of a Condensed Matter

Springer

Takeshi Hasegawa
ICR
Kyoto University
Uji, Kyoto
Japan

ISBN 978-4-431-56491-1 ISBN 978-4-431-56493-5 (eBook)
DOI 10.1007/978-4-431-56493-5

Library of Congress Control Number: 2017935560

Printed on acid-free paper

This Springer imprint is published by Springer Nature
The registered company is Springer Japan KK
The registered company address is: Chiyoda First Bldg. East, 3-8-1 Nishi-Kanda, Chiyoda-ku, Tokyo 101-0065, Japan

Preface

Infrared (IR) spectroscopy strongly attracted the attention of theoretical physicists from the 1930s until the 1970s, and most of the important fundamentals were comprehensively organized in terms of molecular vibrations and rotations along with the rapid progress of quantum mechanics and chemistry. For experimental chemists, commercial IR spectrometers played a great role in the latter half of the twentieth century, and theoretical fundamentals were confirmed quantitatively by using a spectrometer. For example, the theoretical prediction of the Fermi resonance was experimentally recognized for many organic compounds.

At this early stage of IR spectroscopy, theoretical and experimental chemists made great efforts to establish fundamentals for analyzing IR spectra for chemistry. Some textbooks were devoted to summarizing IR bands characteristic of chemical groups in many organic and inorganic compounds in various chemical environments involving solvents and temperature. Correlations of some IR bands to hydrogen bonding, molecular conformation, and crystallinity were also studied, and IR spectroscopy was thus recognized as one of the most powerful analytical tools for discussing chemical compounds.

The accurate measurements of IR spectra were boosted by introducing the Fourier transform infrared (FT-IR) spectrometer, which guarantees both accuracy and precision in principle for both ordinate and abscissa axes thanks to the laser-based interferometer and stable digital electric circuits. Since FT-IR has great sensitivity, which can be used even for a monolayer analysis, many optical configurations were proposed, represented by the transmission, reflection–absorption (RA), attenuated total reflection (ATR), external reflection, and specular reflection techniques, so that the molecular orientation in an ultrathin film would be discussed by comparing it to the spectrum of a bulky sample. The great sensitivity of this "surface spectroscopy" is still outstanding in our current age. The power of molecular orientation analysis is also outstanding since it can be performed no matter how the crystallinity is in the film.

During the progress of FT-IR applications, another important theoretical framework was established in electrodynamics for surface spectroscopy. Since most of the analytical targets of FT-IR are condensed matter, electrodynamics

considering electric permittivity plays many crucial roles for revealing the surface selection rules of surface spectroscopies. The theoretical expressions of the surface spectrometry are particularly important for a strong absorbing matter represented by the carbonyl, nitrile, and perfluoroalkyl groups.

Unfortunately, education of electrodynamics in school is very far from popular in chemistry, and the aspect of "science of measurements" is not widespread even among vibrational spectroscopists. As a result, the overall picture of IR spectroscopy has long been oriented to quantum chemistry only, and surface spectroscopy has been forgotten except for some simple surface selection rules.

In recent years, nonlinear spectroscopic technique represented by the sum-frequency generation has rapidly been recognized even by a non-spectroscopist to be a powerful technique for discussing a detail of an interface. The problem is that such a user blindly relying on nonlinear spectroscopy *alone* is not aware of the intrinsic power of linear spectroscopy. The lack of an overall picture of IR spectroscopy is one of the reasons for the problem.

The goal of this book is, therefore, to summarize the overall picture of IR spectroscopy with respect to quantitative understanding of condensed matter. In particular, surface spectroscopy based on electrodynamics is described in detail in Chap. 3, so that a physical logic would not be omitted. In addition, the concept of convolution and the Kramers–Kronig relations are also described from a fundamental concept in Chap. 4. These concepts should not be introduced as formulae, since they comprise the essence of linear spectroscopy.

For a quantitative study using IR spectroscopy, in recent years multivariate analysis, i.e., chemometrics, is quite often employed. Therefore, the theoretical framework of chemometrics is presented in Chap. 5.

In Chap. 6, application studies of IR spectroscopy are presented. In particular, chemometrics and surface spectroscopy are merged to yield a new spectroscopic technique of p-polarized multiple-angle incidence resolution spectrometry (pMAIRS). This technique enables us to discuss the molecular orientation of each chemical group as well as the polymorph in a very thin film even with a surface roughness. As a good example to get beyond the analytical limit constrained by Maxwell equations, pMAIRS is introduced to provide an overall picture of IR spectroscopy.

In addition, quantitative discussion of IR spectra of perfluoroalkyl (Rf) compounds is added. An Rf compound has long been regarded as a compound similar to a normal hydrocarbon, and the particularity of an Rf compound in vibrational spectroscopy has been missed. As presented in detail in Chap. 6, the overall picture of IR spectroscopy works very powerfully to discuss an Rf compound. Moreover, the knowledge from factor group analysis based on quantum chemistry to surface spectroscopy in electrodynamics is necessary for fully discussing Rf compounds.

This book is a summary of my IR study with my colleagues, whom I thank greatly and appreciate deeply. In particular, the core part of Chap. 3 is the result of an invaluable contribution of a former student, Dr. Yuki Itoh.

I would be most happy if many scientists and engineers in the coming generations re-recognize the great intrinsic power of IR spectroscopy. Since FT-IR is widespread in laboratories, its power will help very much in studying material chemistry. What we need is only the overall picture of IR spectroscopy.

Kyoto, Japan Takeshi Hasegawa

Contents

1 Infrared Spectroscopy as a Vibrational Spectroscopy 1
1.1 Molecular Vibrations 1
1.2 Normal Coordinate and Normal Modes 2
1.3 Light Absorption by a Molecule: 1. Understanding by a Quantum Mechanical Approach 12
1.4 Selection Rule of IR Spectroscopy 16
1.5 Another Selection Rule on the Group Theory 20
1.6 Light Absorption by a Molecule: 2. Understanding on Electrodynamics for a Bulk Matter Toward Beer's Law 30
References 36

2 Fundamentals of FT-IR 37
2.1 Principle of Spectral Measurements 37
2.2 Introducing an Interferometer: FT-IR 39
2.3 Laser and FT Spectrometer 42
2.4 Apodization Function 45
Reference 46

3 Surface Spectroscopy Using FT-IR 47
3.1 Fundamentals of Ordinate Scale of FT-IR Spectra 47
3.2 Absorbance Spectra of a Weakly Absorbing Matter 50
3.3 Boundary Conditions in Electrodynamics 51
3.4 A Model-Based Approach to Generate the TO Energy Loss Function 56
3.5 Fresnel Equation and Optical Anisotropy 60
3.6 Transfer Matrix Method 65
3.7 Calculation of Single-Beam Spectra of the Background and the Sample Measurements 68

3.8 TO and LO Energy Loss Functions: Introduction of the Thin-Film Approximation . . . 71
3.9 Analytical Expression of a Transmission Spectrum . . . 77
3.10 Preparation for the Analytical Expression of a Reflection Spectrum . . . 82
3.11 Analytical Expression of an RA Spectrum . . . 85
3.12 Analytical Expression of an ER Spectrum . . . 89
3.13 Analytical Expression of an Attenuated Total Reflection (ATR) Spectrum . . . 92
3.14 Specular Reflection Spectrum . . . 96
3.15 Surface Selection Rules of IR Surface Spectroscopy . . . 96
3.16 Sampling Techniques . . . 110
References . . . 113

4 IR Absorption of a Dielectric Matter: Phase Retardation of the Polarization Density . . . 115
4.1 Dielectric Matter and Electric Permittivity . . . 115
4.2 Electric Susceptibility and Linear Convolution . . . 116
4.3 Electric Susceptibility and Green's Function . . . 120
4.4 Complex Electric Permittivity . . . 122
References . . . 126

5 Chemometrics for FTIR . . . 127
5.1 Beer's Law and a Single-Constituent System . . . 127
5.2 Extended Beer's Law for a Multi-Constituent System: CLS Regression . . . 130
5.3 Least Squares Solution of a Regression Equation . . . 133
5.4 Intrinsic Limitation of CLS Regression . . . 136
5.5 Inverse Beer's Law: ILS Regression (or MLR) . . . 139
5.6 Principal Component Analysis (PCA) . . . 142
5.7 Merge of ILS and PCA: PCR . . . 153
5.8 Independent Residual Terms: PLS . . . 154
5.9 Efficient Removal of Spectral Noise Using PCA . . . 157
5.10 Alternative Least Squares (ALS) for Spectral Decomposition . . . 159
5.11 Factor Analytical Resolution of Minute Signals (FARMS) . . . 161
References . . . 163

6 Applications: Various Techniques to Make the Best Use of IR Spectroscopy . . . 165
6.1 Specular Reflection and KK Analysis . . . 165
6.2 IR pMAIRS Technique: Quantitative Molecular Orientation Analysis in a Thin Film . . . 170
6.3 Fluorocarbon-Specific IR Spectroscopy . . . 184
References . . . 193

7 Appendix 195
7.1 Fundamental Parameters in Electrodynamics 195
7.2 Continuity of Electric and Magnetic Fields at an Interface. 197
7.3 Factor Group Analysis of PTFE Having the 13_6 Helix Conformation 199
References 200

Chapter 1
Infrared Spectroscopy as a Vibrational Spectroscopy

1.1 Molecular Vibrations

Atoms are connected by chemical bonds to generate a molecule. Let us consider covalently bonded atoms like an organic molecule. If the molecule were hit by a hammer to be vibrated, the molecular vibration would be highly complicated in shape because a polyatomic molecule (having more than two atoms) mostly has *multiple numbers of natural vibrations*. IR spectroscopy measures the natural vibrations as "normal modes" by exciting the molecular vibrations via the interaction between a dipole moment and an oscillating electric field of light instead of hitting the molecule.

To explain the concept of normal modes, let us take a look at an IR spectrum of polyethylene (PE) in Fig. 1.1. PE has a primary chemical structure of a series of the methylene groups ($-CH_2-$) terminated with the methyl groups at both ends. Since the number of the methylene groups is much larger than that of the methyl groups, the end groups can be ignored. In other words, PE can roughly be approximated to comprise methylene groups only. Although only one kind of a chemical group is measured, the spectrum has at least four peaks apparently. Why does the single group yield the many absorption bands?

Since a molecule comprises a number of atoms connected with each other via a covalent bond, the molecule can be recognized to be a "coupled oscillator." When a molecule is vibrated at various frequencies, multiple numbers of natural vibrations appear as the resonance vibrations.

When an alkyl chain is externally vibrated at a certain resonance frequency, each methylene group is excited to be vibrated with a symmetric shape simultaneously while the terminal methyl groups are not vibrated significantly. If the vibration frequency is made higher, the resonance vibration would soon be stopped. Of course, the entire molecule is moved at the externally added vibrational motion, but the motion is in phase with the external motion, which does not absorb vibrational energy and no resonance happens (as discussed in Sect. 4.4). If another faster

T. Hasegawa, *Quantitative Infrared Spectroscopy for Understanding of a Condensed Matter*, DOI 10.1007/978-4-431-56493-5_1

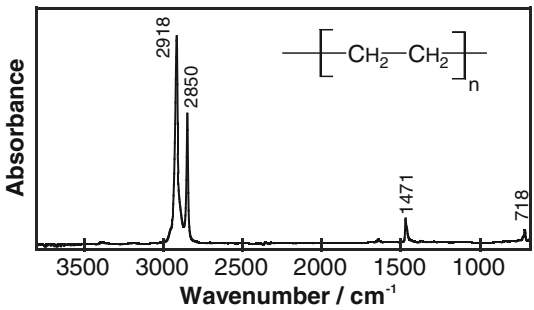

Fig. 1.1 IR absorption spectrum of low-density polyethylene

vibrational motion matches the next resonance frequency of the molecule, each methylene group would exhibit the anti-symmetric shaped vibration. As mentioned in Sect. 4.4, at the moment, the phase of the resonance vibration is delayed from the external vibration, which is a physical situation that a portion of the external energy is absorbed by the molecular vibration.

In this manner, a coupled oscillator has multiple numbers of resonance vibrations having different vibrational shapes, which yield many absorption bands in an IR spectrum. Therefore, if a chemical group has different shapes of vibrations, they are good candidates for appearance of absorption bands.

When the molecular vibrations are excited by irradiating an IR ray, each normal mode is excited on a rule of the "selection rule (see Sect. 1.4)," which determines which mode could appear in the spectrum. In practice, a compound is measured by a broadband IR ray, which excites all the possible normal modes at a time. To understand the reason of why the normal modes separately appear in the spectrum, the concept of "normal coordinate" should be known.

1.2 Normal Coordinate and Normal Modes

To discuss the concept of normal mode on a normal coordinate, a polyatomic molecule having three or more atoms should be taken into account, since a diatomic molecule has only one resonance vibration, which is not suitable for describing a coupled oscillator.

To simply understand the theory, a linear oscillator (Fig. 1.2) having weights (closed circles) with an identical mass, m, connected by springs with an identical spring constant, k, is modeled.

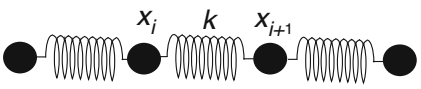

Fig. 1.2 A physical model of a linear oscillator

When the position of each weight with an index of j is denoted as x_j, the Lagrange equation of motion can be written using the kinetic energy, T, and the potential energy, V, which are described as:

$$T = \frac{1}{2}\left(\dot{q}_1{}^2 + \dot{q}_2{}^2 + \dot{q}_3{}^2 + \cdots\right) \tag{1.1}$$

$$V = \frac{k}{2m}\left[(q_2 - q_1)^2 + (q_3 - q_2)^2 + \cdots\right]. \tag{1.2}$$

A dot on a parameter denotes the time derivative operation. Here, another definition of $q_j \equiv \sqrt{m}x_j$ is introduced for making the equations simplified.

Equation (1.1) has a very simple form, in which each position is separated and no interference with another weight is found. On the other hand, Eq. (1.2) is complicated by cross terms, e.g., $q_j q_{j+1}$. The cross term indicates that the motions of the neighboring weights are interfered with each other, and discussion of an individual weight is difficult, which is a largely different situation from that in the kinetic energy. In this manner, the coupled oscillator may have a highly complicated motion for vibrational analysis at each weight *due to the potential term*, V.

To tell the truth, this equation is a poor expression *based on an inappropriate coordinate*, and the intrinsic physical phenomena are much simpler as shown soon later. For making the equations simpler and more general, the equations are rewritten using a vector as follows.

A vector, $\boldsymbol{q}$, is defined as

$$\boldsymbol{q} \equiv \begin{pmatrix} q_1 \\ q_2 \\ q_3 \\ \vdots \end{pmatrix}.$$

By introducing this vector, Eqs. (1.1) and (1.2) are simply rewritten as:

$$T = \frac{1}{2}\dot{\boldsymbol{q}}^{\mathrm{T}}\dot{\boldsymbol{q}} \tag{1.3}$$

$$V = \frac{1}{2}\boldsymbol{q}^{\mathrm{T}}\boldsymbol{B}\boldsymbol{q} \tag{1.4}$$

Here, the superscript, T, indicates the transpose of the vector. This expression has a great benefit that the equation is impervious to the number of weights. The newly introduced matrix, $\boldsymbol{B}$, is necessary to express the cross terms via the off-diagonal elements, and it involves all the parameters except q_j. In other words, if the equation could be cross-term free, $\boldsymbol{B}$ should become a diagonal matrix, which can be removed out from the equation as found in Eq. (1.3). This further means that it would be great to remove $\boldsymbol{B}$ from Eq. (1.4) by making $\boldsymbol{B}$ a diagonal matrix.

To do the diagonalization, the unitary transformation is employed. The unitary transformation is a general technique used for a complex vector. In the present case, only the direction of a vector of real numbers is rotated in space without changing the norm, the unitary transformation can thus be simplified to be an *orthogonal matrix*. An orthogonal matrix, $\boldsymbol{U}$, consists mutually orthogonal vectors, which satisfies the following simple relationship [Eq. (1.5)], since it is equivalent to $\boldsymbol{U}\boldsymbol{U}^{\mathrm{T}} = \boldsymbol{U}^{\mathrm{T}}\boldsymbol{U} = \boldsymbol{1}$ ($\boldsymbol{1}$ is the identity matrix).

$$\boldsymbol{U}^{-1} = \boldsymbol{U}^{\mathrm{T}} \tag{1.5}$$

Here, -1 denotes the inverse matrix.

With the simplified unitary transformation, a new coordinate, $\boldsymbol{Q}$, is defined as:

$$\boldsymbol{q} \equiv \boldsymbol{U}\boldsymbol{Q}. \tag{1.6}$$

By putting this transformation into Eqs. (1.3) and (1.4), the following equations are obtained by considering Eq. (1.5).

$$T = \frac{1}{2}\left(\boldsymbol{U}\dot{\boldsymbol{Q}}\right)^{\mathrm{T}}\left(\boldsymbol{U}\dot{\boldsymbol{Q}}\right) = \frac{1}{2}\boldsymbol{Q}^{\mathrm{T}}\boldsymbol{U}^{\mathrm{T}}\boldsymbol{U}\dot{\boldsymbol{Q}} = \frac{1}{2}\dot{\boldsymbol{Q}}^{\mathrm{T}}\dot{\boldsymbol{Q}} \tag{1.7}$$

$$V = \frac{1}{2}(\boldsymbol{U}\boldsymbol{Q})^{\mathrm{T}}\boldsymbol{B}(\boldsymbol{U}\boldsymbol{Q}) = \frac{1}{2}\boldsymbol{Q}^{\mathrm{T}}\boldsymbol{U}^{\mathrm{T}}\boldsymbol{B}\boldsymbol{U}\boldsymbol{Q} \tag{1.8}$$

We find that Eq. (1.7) has the same form as Eq. (1.3) even after the coordinate transformation. If Eq. (1.8) could readily be transformed to the same form of cross-term free, the motion of each weight could then be separated. In other words, *the coupled oscillator would be treated as a combination of separated oscillation localized on each weight*.

To reach this aim, $\boldsymbol{U}^{\mathrm{T}}\boldsymbol{B}\boldsymbol{U}$ involved in Eq. (1.8) must be a diagonal matrix, $\boldsymbol{\Lambda}$:

$$\boldsymbol{U}^{\mathrm{T}}\boldsymbol{B}\boldsymbol{U} = \boldsymbol{\Lambda}.$$

The sequence of $\boldsymbol{U}$ and $\boldsymbol{\Lambda}$ is exchangeable when only the diagonal component is considered, which results in Eq. (1.9).

$$\boldsymbol{B}\boldsymbol{U} = \boldsymbol{\Lambda}\boldsymbol{U} \tag{1.9}$$

This equation is an eigenvalue problem, which can be solved for any $\boldsymbol{B}$. Since $\boldsymbol{U}$ is obtained as eigenvectors of $\boldsymbol{B}$, the new coordinate, $\boldsymbol{Q}$, is simultaneously determined. In this manner, the coupled oscillation can be decomposed into each constituent vibration.

The new coordinate is called "*normal coordinate*," and each localized vibration is called "*normal mode*." To a practical molecule, this concept is applied using a molecular coordinate, which is generally put on the valence bonds and the valence angles. This analytical technique is accomplished by Wilson et al. [1], and the

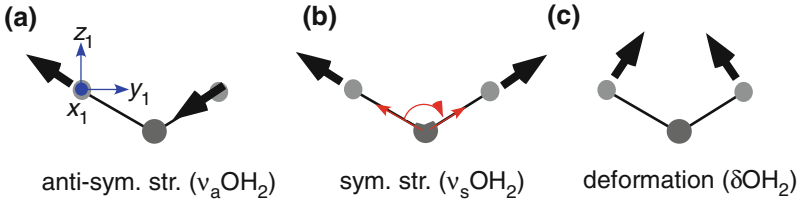

Fig. 1.3 Normal modes of a water molecule. sym. and str. stand for symmetric and stretching, respectively

method is called the Wilson GF-matrix method. Recently, quantum chemical calculation has replaced this technique in many chemistry fields, and the GF-matrix method is employed by vibrational spectroscopists only. Regardless, the physical concept of the normal mode is apparently involved in the method, which cannot be ignored for understanding the principle of vibrational spectroscopy.

On a practical molecule, a normal coordinate is placed along the chemical bonds. Cartesian coordinate (blue arrows in Fig. 1.3a) having the three degrees of freedom is recombined to have two axes on the two O–H bonds and an angle between the two bonds (red arrows in Fig. 1.3b), which is called *molecular coordinate*. This coordinate set is quite convenient for depicting molecular stretching and deformation vibrations, in fact.

The total number of normal modes of a small molecule (not a polymer of repeat units) is easily counted by considering the degree of freedom of each atom. To modify a normal mode, the original molecular shape is changed by displacing the atoms. The movement can be achieved by moving each atom with the use of an '*x*, *y*, *z*-switches' fixed on the atom. This three-direction switch is a schematic image of the degree of freedom of an atomic movement, i.e., an atom has three degrees. Therefore, a molecule having N atoms has $3N$ degrees of freedom in total.

Regardless, if all the atoms are displaced in the *x*-direction, for example, the molecule moves in the direction without vibration (translational motion). In addition, the molecule can be rotated about the *x*-axis without vibration. These translational and rotational motions about the *x*, *y* and *z* axes must be removed to leave "vibrational" motions only. As a result, the number of the normal modes can easily be counted as

$$3N - 6. \text{ (for a nonlinear molecule)}$$

When the molecule has a linear shape, the rotational motion about the linear axis should be excluded from the molecular rotations, the number should be corrected to be

$$3N - 5. \text{ (for a linear molecule)}$$

For example, a diatomic ($N = 2$) molecule such as N_2 and HCl is a linear molecule, which results in only one normal mode. This means that the number of absorption bands in an IR spectrum is only one "at most". As shown later (Sect. 1.4), N_2 does not yield an absorption band at all, and the number of bands can be different from that of the normal modes. The number of bands appeared in a spectrum obeys the "*selection rule* of IR spectroscopy," which is deduced from quantum mechanics (Sect. 1.4).

Precisely speaking, a normal mode is a molecular vibration *over the molecule*. In practice, however, the mode can roughly be regarded as a vibration *localized at a chemical group* such as CH_2, N–H and C=O, and the localized vibration is called the "*group vibration*," which is chemically quite useful (Table 1.1).

In many chemical discussions, the group vibration is conveniently used in place of the normal mode. As found in Table 1.1, the *stretching* and *deformation vibrations* are represented by the symbols of ν and δ, respectively. The asymmetric (degenerate) and anti-symmetric (non-degenerate) vibrations are both represented by the same subscript, a; whereas the symmetric one is denoted by s. An aromatic ring like benzene and thiophene has the *out-of-plane deformation* vibration of the C–H group, which is denoted as γC–H as well as the in-plane one (δC–H). γC–H is quite useful to discuss the molecular orientation of the ring thanks to the very strong IR absorption [2].

For example, polyethylene yields the methylene group-related bands in Fig. 1.1: the ν_aCH_2 (at 2918 cm^{-1}), ν_sCH_2 (at 2850 cm^{-1}), δCH_2 (at 1471 and 1463 cm^{-1}) and rCH_2 (at 718 cm^{-1}) bands appear. *When the* δCH_2 *mode appears as doublet peaks, the molecular packing is known to have the orthorhombic subcell packing* [3]. If the packing is monoclinic and hexagonal, the band becomes a singlet peak at ca. 1467 cm^{-1}.

In this manner, the band position sensitively responds to the molecular conformation, the neighboring chemical group and inter-molecular interactions. In

Table 1.1 Representative group vibrations corresponding to the normal modes represented by the symbols

Group vibration	Symbol	Band position (cm^{-1})
O–H stretching (str.) vib.	νOH	3150–3700 (broad)
N–H str. vib.	νNH	about 3200
CH_3 asymmetric str. vib.	ν_aCH_3	2955
CH_3 symmetric str. vib.	ν_sCH_3	2875
CH_2 anti-symmetric str. vib.	ν_aCH_2	2915–2927
CH_2 symmetric str. vib.	ν_sCH_2	2848–2856
C=O str. vib.	νC=O	1620–1750
CH_2 def. (scissoring) vib.	δCH_2	1462–1472
C–H in-plane def. vib. of benzene	δC–H	1000–1200
C–H out-of-plane def. vib. of benzene	γC–H	760–810
CH_2 rocking vib.	rCH_2	720

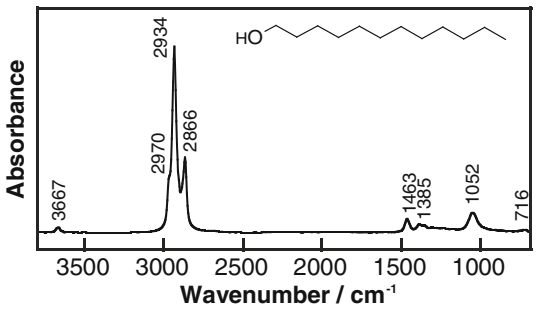

Fig. 1.4 IR spectrum of dodecanol in a gas phase

other words, *a fine analysis of chemical details can be performed through the band shift*.

As another example, an IR absorption spectrum of dodecanol in a gas phase [4] is presented in Fig. 1.4. Dodecanol consists of the methyl group and hydroxyl group as well as the methylene groups. As found in Fig. 1.1, the CH_2 stretching vibration bands appear in the same range of 2800–3000 cm^{-1}. The band positions are, however, apparently higher than those in Fig. 1.1. The position of the CH_2 stretching vibration bands sensitively responds to the *molecular conformation* as found in Table 1.2.

The extraordinarily high wavenumber position of the CH_2 stretching vibration bands in Fig. 1.4 indicate that the dodecanol molecule in the *gas phase* is highly flexible, which has disordered (gauche) conformation. In a similar manner, the gauche conformation is found for a melted sample even in a condensed matter. A gas molecule is not involved in a crystal, of course, and therefore the δCH_2 band appears as a singlet band at 1463 cm^{-1}.

Since dodecanol has the CH_3 group, the methyl-related bands are found at 2970 ($\nu_a CH_3$) and 1385 ($\delta_s CH_3$) cm^{-1}. The $\nu_s CH_3$ is unfortunately hidden by the two tall νCH_2 bands. In addition, the νO–H band is sharply found at 3667 cm^{-1}, which is very specific to the gas phase. In a condensed matter, the band appears as a broad band as a result of complicated molecular interactions mostly due to various hydrogen bondings. In other words, *the νO–H band is quite useful to discuss the hydrogen bonding*.

Another useful band is found at 1052 cm^{-1}, which is assigned to the C–O stretching vibration. If the molecular orientation of an alcohol is discussed, this band plays an important role, since the transition moment is along the bond.

Table 1.2 Band position depending on molecular conformation in a condensed matter (except hexane or shorter alkanes)

Normal mode	All-trans	Gauche
$\nu_s CH_2$	ca. 2850 cm^{-1}	2855 cm^{-1} or higher
$\nu_a CH_2$	ca. 2917 cm^{-1}	2924 cm^{-1} or higher

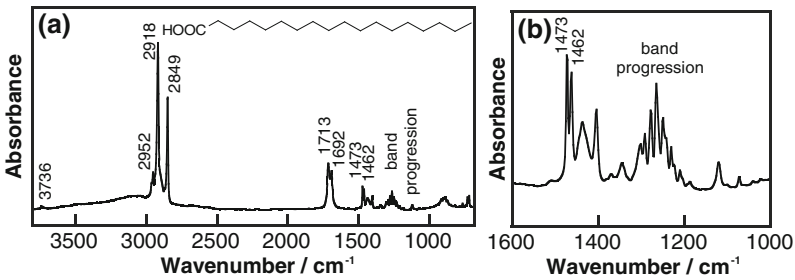

Fig. 1.5 IR spectrum of stearic acid in solid. A part of the spectrum (**a**) is magnified as presented in (**b**)

Figure 1.5 presents an IR spectrum of stearic acid in solid. At an ambient temperature, stearic acid is generally in a crystallite having the orthorhombic subcell packing.

In fact, the δCH_2 band appears as "doublet peaks" at 1473 and 1462 cm^{-1} (Fig. 1.5b) as mentioned above near Table 1.1. Another key point is that the alkyl chains of solid stearic acid are highly packed with the all-trans zigzag conformation, which yields the $\nu_a CH_2$ and $\nu_s CH_2$ bands at a low wavenumber position as expected from Table 1.2.

On closer inspection, the νC–H band region of Fig. 1.5 is complicated [3], which needs magnification as presented in Fig. 1.6. The $\nu_s CH_3$ band is found at 2870 cm^{-1}. Since only one methyl group is at the end of the alkyl chain of the 16 methylene groups, this band is relatively weak. The $\nu_a CH_3$ band is, on the other hand, split into two bands at 2962 and 2952 cm^{-1}, which are respectively known as the "in-skeleton (is)" and "out-of-skeleton (os)" asymmetric stretching vibration bands [3]. The "skeleton" means the molecular plane of the all-trans zigzag skeleton (Fig. 1.7).The band at 2938 cm^{-1} is known to be a *Fermi-resonance* band, which is a combination band of the overtone of the $\delta_a CH_3$ mode and the $\nu_s CH_3$ band [3, 5, 6] (see Sect. 1.5). This band often overlaps the adjacent $\nu_a CH_2$ band deeply, which makes the band position inaccurate.

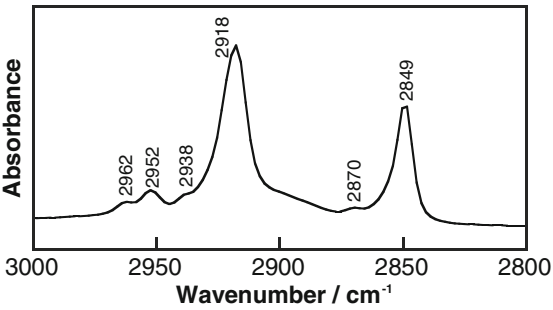

Fig. 1.6 A magnified spectrum of Fig. 1.5

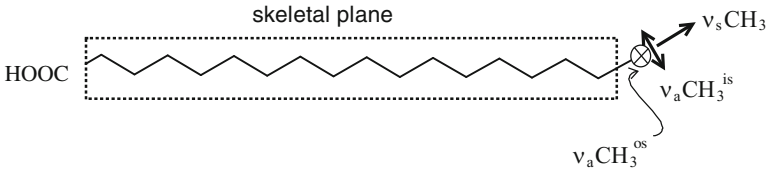

Fig. 1.7 The three CH_3 stretching vibration modes with respect to the molecular skeleton

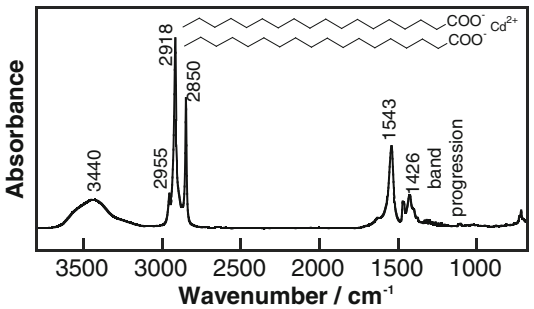

Fig. 1.8 IR spectrum of cadmium stearate measured by the KBr pellet technique

The carboxylic group yields the νC=O and νOH bands. The νOH band is largely broadened at about 3100 cm^{-1} because of complicated molecular interactions.

When stearic acid is reacted with dicationic metal ions, such as calcium, magnesium, and cadmium ions in an aqueous solution, the carboxylic group is changed to be the $-COO^-$ group by releasing a proton in the solution, which thus requires basic environment at about pH 8. For example, stearic acid readily reacts with cadmium ion (Cd^{2+}) at about pH 7.5 to generate a salt of cadmium stearate, which yields an IR spectrum as presented in Fig. 1.8.

Since this spectrum is measured using the KB-pellet technique (Sect. 3.16), the adsorbed water band is apparently found (at about 3440 cm^{-1}). A notable difference from Fig. 1.5 is that the νC=O at ca. 1700 cm^{-1} is completely lost, which indicates that the C=O bond is readily changed to another chemical bond at the pH. In fact, instead, a new set of two bands at 1543 and 1426 cm^{-1} are observed. These two bands are assigned to the $\nu_a COO^-$ and $\nu_s COO^-$ bands, respectively. The spectrum shows that the symmetric vibration of this group *in an isotropic sample (randomly oriented)* has a weaker intensity than the anti-symmetric one, which corresponds to the α-spectrum. In other words, the α-spectrum corresponds to the *intrinsic absorption spectrum* of the compound, which can be a standard to discuss molecular orientation when employing surface spectroscopy (Chap. 3).

In both Figs. 1.5 and 1.8, a series of bands having nearly equal intervals are found in the region of 1150–1350 cm^{-1}, which is called "*band progression*," which is visually recognized in a magnified spectrum in Fig. 1.9. This series of bands are a result of *vibrational coupling of the CH_2 wagging vibrations on an alkyl chain*

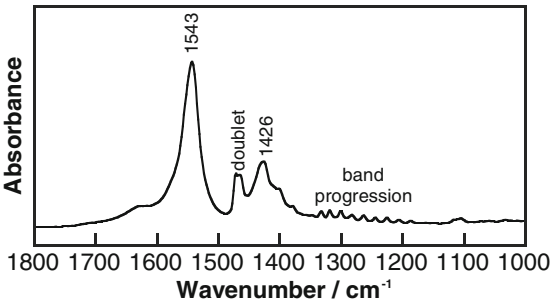

Fig. 1.9 A magnified spectrum of Fig. 1.8

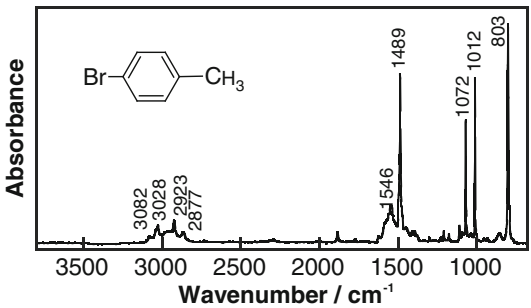

Fig. 1.10 IR spectrum of *p*-bromotoluene

(having a finite length) with the same vibrational phase. This in-phase vibration occurs *only when the alkyl chain has the all-trans conformation*. In other words, the band progression is a very useful marker to conclude the orderliness of the alkyl chain.

When an aromatic ring is involved, the spectral pattern becomes highly complicated. An example spectrum of *p*-bromotoluene is presented in Fig. 1.10. The methyl group yields the $\nu_a CH_3$ and $\nu_s CH_3$ bands at 2923 and 2877 cm^{-1}, respectively. On the other hand, the νC–H band of the benzene ring appears at a higher position than 3000 cm^{-1}, which is a marker of a C–H bond on an unsaturated carbon represented by an aromatic ring. The C–H bond yields another useful band in the range of 1000–1200 cm^{-1}, which are attributed to the C–H *in-plane deformation* vibration (δC–H) mode. The same group has an additional band near 800 cm^{-1}, which is known as the C–H *out-of-plane deformation* vibration (γC–H) mode. This band is quite useful to discuss the molecular orientation of the aromatic ring thanks to the strong IR absorption [2].

The strong peaks near 1500 cm^{-1} are due to the skeletal vibrations of the benzene ring, which is also an important marker of aromatic compounds.

Another important compound for IR spectroscopy is "amino acid." Figure 1.11 presents an IR spectrum of leucine ($(CH_3)_2CH(CH_2)CH(NH_2)COOH$) in solid. The CH_2 stretching vibration bands appear at higher positions than those of stearic acid *because the length of the alkyl part is very short*.

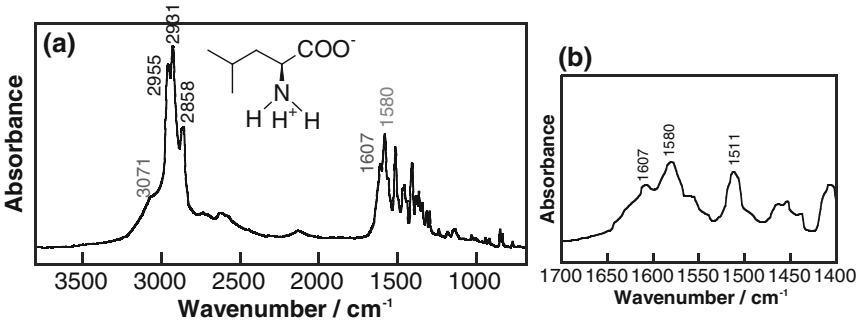

Fig. 1.11 **a** IR spectrum of leucine, and **b** a magnified spectrum

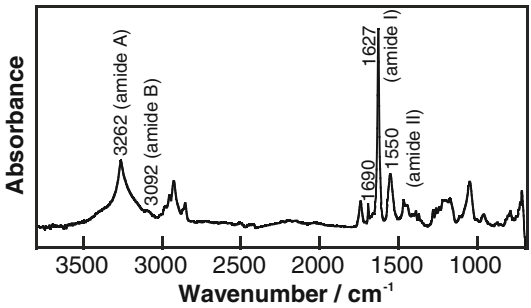

Fig. 1.12 IR spectrum of a compound involving a $(Leu)_6$ unit

The NH_2 group exhibits the $\nu_a NH_2$ and $\nu_s NH_2$ bands at ca. 3365 and 3285 cm^{-1}, which are missing in Fig. 1.11a. This suggests that the amine group is cationized to be NH_3^+ by adding a proton dissociated from the carboxylic group (Fig. 1.11b). In fact, the $\nu_s NH_3^+$ band appears at 2955 cm^{-1}, and no νC=O band (ca. 1700 cm^{-1}) is found in the spectrum, and instead the $\delta_a NH_3^+$ band is available at 1607 and 1580 cm^{-1} as well as the $\delta_s NH_3^+$ band at 1511 cm^{-1} (Fig. 1.11b).

When amino acids are polymerized to be a peptide, the amide bond-related bands appear instead. Figure 1.12 presents an IR spectrum of a compound having a peptide unit of $(Leu)_6$. Since the Leu residues are covalently connected to generate the amide bonds, the N–H and C=O related bands appear in the spectrum. For example, the νN–H mode appears at 3262 cm^{-1}, which is called "*amide A*" band. This band responds to the hydrogen bonding, and it appears at about 3450 cm^{-1}, if the N–H group is hydrogen bonding free. Therefore, the band at 3262 cm^{-1} strongly suggests that the N–H group is involved in hydrogen bonding.

The band at 1627 cm^{-1} is a quite useful band known as "*amide I*" band. This band mainly corresponds to the C=O stretching vibration and it is quite sensitive to the hydrogen bonding. Especially for a peptide, this band is conveniently used for determination of the secondary structure of an oligomer, polymer and in molecular aggregate as summarized in Table 1.3.

Table 1.3 Amide bands and the secondary structures of a peptide

Secondary structure	Amide I (cm^{-1})	Amide II (cm^{-1})
α-helix	1652	1548
β-sheet (parallel)	1634	1547
β-sheet (anti-parallel)	1628 and 1686	1537
3_1-helix [7]	Doublet at ca. 1650	1550

The spectrum in Fig. 1.12 has the amide I band at 1627 cm^{-1} accompanying a small characteristic band at 1690 cm^{-1}, which strongly tells us that the secondary structure should be anti-parallel β-sheet.

Accompanying this band, '*amide II*' band is also referred. This band is mainly due to the δN–H vibration mixed with a minor νC–N vibration. The transition moment of 'amide II' has roughly perpendicular to that of "amide I."

1.3 Light Absorption by a Molecule: 1. Understanding by a Quantum Mechanical Approach

Molecular vibrations are excited via light absorption. Light absorption by a molecule is physically modeled by an interaction of the electric field of light with a dipole moment of the molecule. Light comprises two mutually orthogonal oscillations of the electric and magnetic fields, both of which are orthogonal to the traveling direction of the light, i.e., the wavenumber vector. Except a spin-excitation spectroscopy, represented by NMR, the interaction of the magnetic field with a molecule is ignorable, and only the influence of the electric field is considered for the light absorption.

The interaction between the electric field oscillation and the vibrating dipole moment is theorized in two ways: quantum mechanics and electrodynamics. To discuss the selection rule of spectroscopy, quantum mechanics is the only way. The treatment by electrodynamics is described in Sect. 1.6.

In the framework of quantum mechanics, the electric field oscillation is treated as a perturbation of the wave function of the steady state. Therefore, the steady state, which means that the molecule is not excited by light, is described first by using the time-independent (steady) Schrödinger equation.

$$\hat{H}_0\psi = E_0\psi$$

Here, $\hat{H}_0$ is a Hamiltonian operator corresponding to the total molecular vibrations, E_0 is the total energy of the vibrations, and ψ is a wave function of the molecular vibration comprising all the normal modes.

Since the Hamiltonian operator is a Hermitian, all the eigenfunctions are mutually orthogonal, that is

$$\int \phi_i^* \phi_j \mathrm{d}\tau \equiv \langle i|j\rangle = \delta_{ij}. \tag{1.10}$$

Here, $\langle i|j\rangle$ is a bracket representation of the integral with respect to space, τ, and δ_{ij} is Kronecker's delta. In a similar manner, in terms of energy, the following relation holds.

$$E_0 = E_1 + E_2 + E_3 + \cdots$$

As a result, each component of a normal mode can be individually formulated as

$$\widehat{H}_0|j\rangle = E_j|j\rangle. \tag{1.11}$$

On a steady state, the molecular vibration, ψ, is the product of the normal modes, $\psi = \phi_1\phi_2\phi_3\phi_4\cdots$, since this satisfy the Schrödinger equation on the total energy.

$$\begin{aligned}\widehat{H}_0\psi &= \left\{\left(\widehat{H}\phi_1\right)\phi_2\phi_3\phi_4\cdots\right\} + \left\{\phi_1\left(\widehat{H}\phi_2\right)\phi_3\phi_4\cdots\right\} + \cdots \\ &= \{(E_1\phi_1)\phi_2\phi_3\phi_4\cdots\} + \{\phi_1(E_2\phi_2)\phi_3\phi_4\cdots\} + \cdots \\ &= (E_1 + E_2 + E_3 + \cdots)\psi \\ &= E_0\psi\end{aligned} \tag{1.12}$$

In this manner, the energy conservation holds. Since this solution is for a steady state, the solution can be written as a product of two independent terms in terms of r and t.

$$|j(r,t)\rangle = |j(r)\rangle \exp\left(-\mathrm{i}\frac{E_j}{\hbar}t\right) \tag{1.13}$$

When an IR ray is irradiated on the molecule, the steady state is perturbed in the following manner:

$$\mathrm{i}\hbar\frac{\mathrm{d}}{\mathrm{d}t}|\Psi\rangle = \left(\widehat{H}_0 + \widehat{H}'\right)|\Psi\rangle \tag{1.14}$$

Here, the first-order perturbation operator is represented by $\widehat{H}'$, and the time evolution is expressed by the time-dependent Schrödinger equation.

The framework of the mutually orthogonal functions (complete system) has already been generated by Eq. (1.13). On the perturbation, a new state is generated on the complete system as an expansion with the weight factors, a_j:

$$|\Psi\rangle = \sum_{j=1}^{\infty} a_j|j\rangle \exp\left(-\mathrm{i}\frac{E_j}{\hbar}t\right). \tag{1.15}$$

Therefore, a new aim of using this theory is now revealing the composition pattern, $|a_j|^2$, which can experimentally done by absorption spectroscopy.

Since the wave function of Eq. (1.15) is a solution of Eq. (1.14), they can be merged to have:

$$\begin{aligned} &\mathrm{i}\hbar\frac{\partial}{\partial t}\left|\sum_j a_j(t)\phi_j(\boldsymbol{r})\ \exp\left(-\mathrm{i}\frac{E_j}{\hbar}t\right)\right\rangle \\ &=\left(\widehat{H}_0+\widehat{H}'\right)\left|\sum_j a_j(t)\phi_j(\boldsymbol{r})\ \exp\left(-\mathrm{i}\frac{E_j}{\hbar}t\right)\right\rangle. \end{aligned} \tag{1.16}$$

The left-hand side of this equation is deformed as:

$$\begin{aligned} &\mathrm{i}\hbar\left(\left|\sum_j\frac{\partial a_j(t)}{\partial t}\phi_j(\boldsymbol{r})\ \exp\left(-\mathrm{i}\frac{E_j}{\hbar}t\right)\right\rangle-\mathrm{i}\frac{E_j}{\hbar}\psi\right) \\ &=\mathrm{i}\hbar\left|\sum_j\frac{\partial a_j(t)}{\partial t}\phi_j(\boldsymbol{r},t)\ \exp\left(-\mathrm{i}\frac{E_j}{\hbar}t\right)\right\rangle+E_j\psi. \end{aligned}$$

When this is compared to the right-hand side of Eq. (1.16) considering Eq. (1.11), the next equation is obtained.

$$\left|\sum_j\frac{\partial a_j(t)}{\partial t}\phi_j(\boldsymbol{r},t)\ \exp\left(-\mathrm{i}\frac{E_j}{\hbar}t\right)\right\rangle\quad=-\frac{\mathrm{i}}{\hbar}\widehat{H}'\left|\sum_j a_j(t)\phi_j(\boldsymbol{r},t)\ \exp\left(-\mathrm{i}\frac{E_j}{\hbar}t\right)\right\rangle$$

When $\langle\phi_k(\boldsymbol{r},t)|$ is operated from the left side, the next equation is obtained.

$$\begin{aligned} \frac{\mathrm{d}a_k(t)}{\mathrm{d}t}&=-\frac{\mathrm{i}}{\hbar}\sum_j\langle\phi_k(\boldsymbol{r},t)|\widehat{H}'|a_j(t)\phi_j(\boldsymbol{r},t)\rangle\ \exp\left(\mathrm{i}\omega_{kj}t\right) \\ &\equiv-\frac{\mathrm{i}}{\hbar}\sum_j a_j(t)H'_{kj}\ \exp\left(\mathrm{i}\omega_{kj}t\right) \end{aligned}$$

Here, $H'_{kj}=\langle\phi_k(\boldsymbol{r},t)|\widehat{H}'|a_j(t)\phi_j(\boldsymbol{r},t)\rangle$ is an matrix element, and ω_{kj} is also newly introduced as $\omega_{kj}\equiv\left(E_k-E_j\right)/\hbar$.

If the initial state has the energy state of E_0 and only the first excited state is considered, the sigma operator is removed to have

$$\frac{\mathrm{d}a_k(t)}{\mathrm{d}t}=-\frac{\mathrm{i}}{\hbar}a_k(t)H'_0\ \exp(\mathrm{i}\omega_{k0}t). \tag{1.17}$$

Let us consider that the perturbation can be represented by a simple cosine function:

$$H'(\boldsymbol{r},t) = H'_0(\boldsymbol{r})\left(\mathrm{e}^{\mathrm{i}\omega t} + \mathrm{e}^{-\mathrm{i}\omega t}\right) \tag{1.18}$$

Here, $1/2$ is incorporated in H'_0. After Eq. (1.18) is put in Eq. (1.17), the equation is integrated with regard to time to have:

$$a_k(t) = \frac{\langle k|H'_0|0\rangle}{\hbar}\left[\frac{1-\mathrm{e}^{\mathrm{i}(\omega_{k0}+\omega)t}}{\omega_{k0}+\omega} + \frac{1-\mathrm{e}^{\mathrm{i}(\omega_{k0}-\omega)t}}{\omega_{k0}-\omega}\right].$$

At the light-absorbing frequency ($\omega \approx \omega_{k0}$), the first term in the parenthesis can be ignored. Therefore, the following approximation is allowed:

$$|a_k(t)|^2 = \frac{4\left|\langle k|H'_0|0\rangle\right|^2}{\hbar^2}\frac{\sin^2\frac{\omega_{k0}-\omega}{2}t}{(\omega_{k0}-\omega)^2}.$$

If the sinc function [cf. Eq. (2.8)] is replaced by Dirac's delta function (Chap. 4), we have finally reached *Fermi's golden rule* [Eq. (1.19)].

$$\boxed{\frac{\mathrm{d}|a_k(t)|^2}{\mathrm{d}t} = \frac{2\pi}{\hbar}\left|\langle k|\widehat{H}'|j\rangle\right|^2\delta\left(E_k - E_j - \hbar\omega\right)} \tag{1.19}$$

The left-hand side is proportional to the absorbance or the band area; whereas the right-hand side consists of the squared transition integral and Dirac's delta function. The delta function means that the light energy of $\hbar\omega$ is absorbed only when it perfectly matches the difference of the energy levels of the states k and j (energy conservation). As a result, the absorbance is proportional to squared transfer integral, $\left|\langle k|\widehat{H}'|j\rangle\right|^2$.

The transfer integral should be discussed by considering the second quantization strictly speaking, but IR spectroscopy can more intuitively be modeled by considering the physical interaction between the dipole moment, $\boldsymbol{p} = q\boldsymbol{r}$, and the oscillating electric field, $\boldsymbol{E}$, of the IR light:

$$\widehat{H}' = \boldsymbol{p}\cdot\boldsymbol{E}.$$

Through this interaction, the molecule is excited to have normal modes. Since the wavelength of IR light ($\sim\mu$m) is much larger than the size of the dipole, $\boldsymbol{E}$ can be regarded as a constant in the integral range. Therefore, the transfer integral is rewritten as:

$$\langle k|\widehat{H}'|j\rangle = q\langle k|\boldsymbol{r}|j\rangle\cdot\boldsymbol{E}. \tag{1.20}$$

As a result, the dot product of the *transition moment*, $\langle k|\boldsymbol{r}|j\rangle$, and the electric field, $\boldsymbol{E}$, is found to govern the absorbance. This is the principle to discuss the

molecular orientation, since the direction of the transition moment is the same as that of the normal mode as described later (Sect. 1.5).

Here, we have to note that the electric field is not of the IR source, but of the "IR light at the molecule." When a molecule is at (or near) an interface, in practice, the molecule is often oriented, and the orientation is the key for understanding the material properties at the interface. For the analysis, the electric field vector "at the interface" must be calculated (Chap. 3). In this manner, the principle of the molecular orientation analysis is given by Fermi's golden rule as a result of the quantum dynamics approach, but the practical analysis requires *another analysis of the electric field on electrodynamics*, since the optical interface can be treated by the electrodynamics approach only.

1.4 Selection Rule of IR Spectroscopy

Fermi's golden rule is the most important milestone of the quantum mechanical discussion of absorption spectroscopy. In fact, the rule is the starting point to understand the principles of various spectroscopic techniques.

At the beginning of Sect. 1.1, we imagined the molecular vibration caused by hitting the molecule using a hammer. In this case, all the normal modes are excited at once. On spectroscopy, however, the molecular vibration is caused via the interaction between the dipole moment of the transition moment and the electric field. Therefore, a theoretical treatment of the interaction can be started from Fermi's golden rule, which generally provides a spectroscopic rule: only limited normal modes are excited by the light absorption. This rule is called *selection rule*. In other words, the maximum number of IR bands is given by the $3N - 6$ rule (Sect. 1.2).

The vibration of a molecule comprising the normal modes looks a highly complicated motion. As presented by Eq. (1.12), however, each normal mode can separately be discussed. Therefore, only a normal mode is good enough as a physical model for deducing the selection rule. Since the selection rule is for a dipole moment, the simplest case is employed to deduce the rule, i.e., a diatomic molecule.

When two atoms aligned along the x-axis giving a reduced mass of μ are connected by a spring with a spring constant of k, the Hamiltonian of the steady state of the molecule is represented as:

$$\widehat{H}_0 = \frac{\hat{p}_x^2}{2\mu} + \widehat{V}(x) = -\frac{\hbar^2}{2\mu}\frac{\mathrm{d}^2}{\mathrm{d}x^2} + \frac{1}{2}kx^2 \tag{1.21}$$

Here, the potential term is written on the harmonic oscillator approximation. The solving process of the Schrödinger equation with the Hamiltonian is found in many textbooks of physical chemistry, and the eigenfunctions, ϕ_v, and eigenvalues, E_v, are obtained as:

$$\phi_v = N_v H_v\left(\alpha^{1/2}x\right)\mathrm{e}^{-\alpha x^2/2} \quad \text{where } \alpha = \frac{\mu\omega}{\hbar}$$
$$E_v = \hbar\omega\left(v + \frac{1}{2}\right) \quad (v = 0, 1, 2, \cdots).$$

Here, v is the vibrational quantum number.

The selection rule of a spectroscopy is deduced from Fermi's golden rule, which can be calculated by putting the wave functions into Eq. (1.20). At the moment, however, no explicit function is available for the dipole moment, $\boldsymbol{p}$. Since the molecular vibration considered for IR spectroscopy is fairly small in comparison to the bond length, the dipole moment is represented by Taylor's expansion near $x = 0$ leaving the first two terms.

$$p(x) = p_0 + \left(\frac{\mathrm{d}p}{\mathrm{d}x}\right)_0 x + O\left(x^2\right)$$

Here, a one-dimensional coordinate along x-axis is taken into account for making the discussion simpler, and therefore a scalar parameter is used in the equation. With these equations, the transition moment is calculated after a variable transformation ($u \equiv \alpha^{1/2}x$).

$$\langle k|\boldsymbol{p}|j\rangle = \alpha^{-1/2}\int_{-\infty}^{\infty} N_k H_k(u)\mathrm{e}^{-u^2/2}\left[p_0 + \left(\frac{\mathrm{d}p}{\mathrm{d}u}\right)_0 u\right]N_j H_j(u)\mathrm{e}^{-u^2/2}\mathrm{d}u \tag{1.22}$$

When the orthogonality of the Hermite functions [Eq. (1.23)] is taken into account,

$$\int_{-\infty}^{\infty} H_k(x)H_j(x)\mathrm{e}^{-x^2}\mathrm{d}x = \delta_{k,j}2^k\sqrt{\pi}k!, \tag{1.23}$$

Equation (1.22) is then deformed to be:

$$\langle k|\boldsymbol{p}|j\rangle = \alpha^{-1/2}N_k N_j\left(\frac{\mathrm{d}p}{\mathrm{d}u}\right)_0\int_{-\infty}^{\infty} H_k(u)uH_j(u)\mathrm{e}^{-u^2}\mathrm{d}u. \tag{1.24}$$

Since the Hermite polynomials satisfy the recurrence relation [Eq. (1.25)]:

$$xH_n(x) = \frac{1}{2}H_{n+1}(x) + nH_{n-1}(x), \tag{1.25}$$

Equation (1.24) can be reduced to (u is got back to x):

$$\begin{aligned}\langle k|\boldsymbol{p}|j\rangle &= \alpha^{-1/2}N_kN_j\left(\frac{\mathrm{d}p}{\mathrm{d}x}\right)_0\int_{-\infty}^{\infty}H_k(x)xH_j(x)\mathrm{e}^{-x^2}\mathrm{d}x\\ &= \alpha^{-1/2}N_kN_j\left(\frac{\mathrm{d}p}{\mathrm{d}x}\right)_0\int_{-\infty}^{\infty}H_k(x)\left[\frac{1}{2}H_{j+1}(x)+jH_{j-1}(x)\right]\mathrm{e}^{-x^2}\mathrm{d}x\\ &= C\left(\frac{\mathrm{d}p}{\mathrm{d}x}\right)_0\left[\frac{1}{2}\int_{-\infty}^{\infty}H_k(x)H_{j+1}(x)\mathrm{e}^{-x^2}\mathrm{d}x+j\int_{-\infty}^{\infty}H_k(x)H_{j-1}(x)\mathrm{e}^{-x^2}\mathrm{d}x\right]\\ &= \left(\frac{\mathrm{d}p}{\mathrm{d}x}\right)_0\left(C_1\delta_{k,j+1}+C_2\delta_{k,j-1}\right)\end{aligned}$$

Constants are involved in C_1 and C_2 to make the equation visually clearer.

To make this transition moment nonzero (*IR active*), as a conclusion, the next conditions must *both* be satisfied.

$$\left(\frac{\mathrm{d}p}{\mathrm{d}x}\right)_0 \neq 0 \tag{1.26}$$

$$k = j+1 \text{ or } j-1 \tag{1.27}$$

Another notice is that the transition moment itself can be zero, if the symmetry of the wave function product is "odd." To analyze the symmetry of the function product, the group theory is often conveniently employed. These three conditions are called the *selection rules of IR spectroscopy*.

Equation (1.26) implies that IR absorption does not occur, if the dipole moment is not changed on a vibration ($\mathrm{d}x \neq 0$). For example, a homo-nuclear diatomic molecule has no permanent dipole moment, and no dipole is induced by the stretching vibration, which results in no IR absorption. In fact, nitrogen and oxygen that occupies a great part of ambient air do not provide IR bands at all. In other words, these two gas components do not interfere IR measurements.

On the other hand, water vapor is a strong interference to IR spectroscopy, since a water molecule has a large permanent dipole over the molecule. Unfortunately, water molecules yield many fine peaks due to a coupled motion of vibration and rotation (vibrotational) in the range of 1200–1700 cm^{-1}. This region is called "fingerprint region," since many IR key bands appear in the region, which characterize the molecule. Therefore, the air-purge in the spectrometer using dry air is crucial for IR spectroscopy.

Equation (1.27) is another important fundamental rule implying that the vibrational energy transition is strictly limited by the change of vibrational quantum

number of "one" for both upward and downward transitions. A schematic diagram of energy transition is presented in Fig. 1.13. The electronic and vibrational quantum states are denoted by the quantum numbers of n and v, respectively. Therefore, Eq. (1.27) can be denoted as $\Delta v = \pm 1$, which corresponds to the schematic transitions of (a)–(c).

IR "absorption" occurs as the upward transition with $\Delta v = +1$; whereas IR "emission" is a downward transition denoted as $\Delta v = -1$. Most of the IR absorption is governed by the transition of Fig. 1.13a, which is called "*fundamental*" transition. Although the excited fundamental mode emits IR light with the same energy absorbed (Fig. 1.13b), the *spontaneous emission* is generated from the excited dipole vibration, and the radiation occurs for a large solid angle. As a result, an ignorable portion of the emitted light attains the detector, which makes it possible to measure the absorption process only, fortunately.

Another IR absorption band due to an upward transition from an excited state (Fig. 1.13c) is called "hot band." Since the scheme in the figure is within a harmonic approximation, the vibrational states have equal space. A practical molecule has an anharmonic vibrational potential, however, and a hot band occurs within a narrower space, which results in a lower wavenumber shift than the fundamental mode. Regardless, the intensity of the hot band is very small, since the probability of the initial state is much less than the ground state due to the Boltzmann distribution. Therefore, this process is generally ignored in mid-IR spectroscopy.

The harmonic oscillator approximation strictly prohibits a transition other than $\Delta v = \pm 1$, and therefore the transition of Fig. 1.13d can also be ignored within the approximation. In practice, however, the harmonicity breaks a little bit, which makes the transition possible, although the absorption is extremely small. The energy nearly double of the fundamental energy corresponds to the "near IR" (NIR) region. This explains that many organic materials exhibit high transparency to NIR light, and absorbance is very small.

As a result, *the processes of (b)–(d) can be ignored* within a very good approximation leaving the process of (a) only. This is the reason IR absorption spectroscopy is performed using a relatively simple measurement apparatus. In addition, thanks to this simplicity, the discussion based on the group theory also becomes very simple as found in the next section.

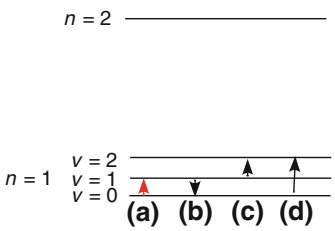

Fig. 1.13 Schematic diagram within a harmonic approximation of energy transitions for vibrational (v) and electronic (n) quantum states: **a** IR absorption, **b** IR emission, **c** hot transition, and **d** prohibited transition or NIR absorption

1.5 Another Selection Rule on the Group Theory

Even if the interaction of IR light with a molecule satisfies Eqs. (1.26) and (1.27), the transition moment, $\langle k|\boldsymbol{r}|j\rangle$, still can be zero depending on the symmetry of the molecular skeleton: the parity of the integrand of the transition moment is another key to discuss the selection rule. Since the integral is calculated in the range from $-\infty$ to $+\infty$, the integral is nonzero if the integrand has an even function; whereas it becomes zero for an odd function.

To determine the parity of the integrand of a three-dimensional function, the group theory in mathematics works powerfully. On group theory, "symmetry operations" of a chemical group or a molecule can be represented by matrix operators, and the operators are involved in a "group," on which independent symmetry species are built. "Independent" means that the symmetry species as a function of the operators are mutually orthogonal. In other words, a normal mode is classified into a symmetry species using the matrix operator, and the expression is obtained by "expanding" the reducible representation using mutually orthogonal irreducible species.

The analysis of molecular vibration on the group theory is a sophisticated technique, and the expansion using the matrix operator is carried out in a very simple manner. The matrix operators are "reduced" into a scalar when the symmetry species is not degenerated by considering the characteristic of the "trace" of the representation matrix.

A water molecule is employed as an example to roughly explain the concept. Cartesian coordinates are attached to each atom as in Fig. 1.14. Each atom "position" is indexed by a number with underline as $\underline{n}$. When the molecule is rotated by 180° about the z_2-axis, the vector of "y_1" on the atom of "$\underline{1}$" is displaced to "$-y_1$" on "$\underline{3}$", which is marked as "$\boldsymbol{y}_1$" and "$-\boldsymbol{y}_1$" in Eq. (1.28). In the same manner, all the vectors are operated by the C_2 rotation. As a result, the operator of C_2 can be represented by a 9×9 matrix as follows:

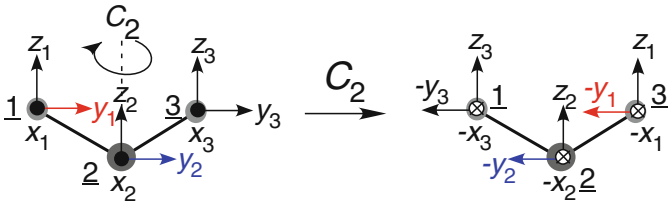

Fig. 1.14 Cartesian coordinates fixed at each atom of water. C_2 represents a rotation operation by 180° about the z_2 axis. The operation-independent absolute positions are indexed by $\underline{1}$, $\underline{2}$ and $\underline{3}$

$$\begin{pmatrix} -x_3 \\ -y_3 \\ z_3 \\ -x_2 \\ -\boldsymbol{y_2} \\ z_2 \\ -x_1 \\ -\boldsymbol{y_1} \\ z_1 \end{pmatrix} = \begin{pmatrix} & & & & & & -1 & 0 & 0 \\ & \boldsymbol{0} & & & \boldsymbol{0} & & 0 & -1 & 0 \\ & & & & & & 0 & 0 & 1 \\ & & & -1 & 0 & 0 & & & \\ & \boldsymbol{0} & & 0 & \boldsymbol{-1} & 0 & & \boldsymbol{0} & \\ & & & 0 & 0 & 1 & & & \\ -1 & 0 & 0 & & & & & & \\ 0 & \boldsymbol{-1} & 0 & & \boldsymbol{0} & & & \boldsymbol{0} & \\ 0 & 0 & 1 & & & & & & \end{pmatrix} \begin{pmatrix} x_1 \\ \boldsymbol{y_1} \\ z_1 \\ x_2 \\ \boldsymbol{y_2} \\ z_2 \\ x_3 \\ y_3 \\ z_3 \end{pmatrix}, \quad (1.28)$$

where $\boldsymbol{0}$ represents a 3 × 3 matrix of zero. Here, an issue comes up that the matrix representation depends on a coordinate system. Matrix algebra has, fortunately, a useful character that the summation of diagonal of the matrix, which is called "*trace*," is *impervious to the unitary transformation of the coordinate*. Therefore, it would be great, if the trace would conveniently be used in place of the matrix. In group theory, the trace is denoted as χ.

In the present case, the trace is calculated to be $\chi = -1$, which characterizes the C_2-operation matrix for water. As apparently found in Eq. (1.28), the trace is calculated using a small matrix due to the "unmoved atom" after the symmetric operation. If all the atoms are moved by the operation, the trace becomes zero, since no nonzero matrix remains on the diagonal. This implies that the trace should be calculated by *summing up traces of small matrices of unmoved atoms*. This calculation can readily be performed by using a *character table* that belongs to the point group, which represents the symmetry of the molecular skeleton. For example, water belongs to the point group of C_{2v}, and its character table is referred as Table 1.4.

The character table first definitely says that the point group of C_{2v} has *only four independent symmetry species* (A_1, A_2, B_1 and B_2) as long as the molecule belongs to C_{2v}. This is a very apparent conclusion made on the group theory, which means that any normal mode can be classified into only the four patterns. For each pattern, the symmetry operation is represented by the trace. For example, let us consider the unit vector, $\boldsymbol{y_2}$, in Cartesian coordinate on an unmoved atom, 2, (Fig. 1.14), which is marked by "$\boldsymbol{y}$" in the "linear" column in Table 1.4. When this unit vector is operated by C_2, for example, the direction is overturned from right to left, which is represented by "$-\mathbf{1}$," as presented in the C_2 column. This corresponds to the change from "y_2" to "$-y_2$" in Fig. 1.14, which is represented as "$\boldsymbol{y_2}$" and "$-\boldsymbol{y_2}$" in Eq. (1.28). In a similar manner, E, σ_v and $\sigma_{v'}$ are applied to the same unit vector of

Table 1.4 The character table of the point group of C_{2v}

C_{2v}	E	C_2	σ_v	$\sigma_{v'}$	Linear	Quadratic
A_1	1	**1**	1	1	$\boldsymbol{z}$	x^2, y^2, z^2
A_2	1	1	−1	−1	R_z	xy
B_1	1	**−1**	1	−1	R_y, $\mathbf{x}$	xz
B_2	1	**−1**	−1	1	R_x, $\boldsymbol{y}$	yz

Table 1.5 Normal-mode analysis of H_2O on C_{2v} (g = 4)

		R					
	C_{2v}	E	C_2	σ_v	$\sigma_{v'}$	linear	quadratic
χ_i	A_1	1	1	1	1	z	x^2, y^2, z^2
	A_2	1	1	-1	-1	R_z	xy
	B_1	1	-1	1	-1	R_y, x	xz
	B_2	1	-1	-1	1	R_x, y	yz
	N_R	**3**	*1*	1	3		
	χ_R	**3**	*-1*	1	1		
	χ	**9**	*-1*	1	3		

y, and the results are presented by 1, −1, and 1, respectively. In this fashion, the unit vector, y, is thus assigned to the symmetry species of B_2. In the same manner, x, z and rotational axes, R_x, R_y and R_z are all assigned as presented in Table 1.4.

These characteristic numbers are regarded as the elements of a small matrix of an unmoved atom. Therefore, the trace can be calculated by summation of the numbers without using a huge matrix. In fact, in the C_2 column, x, y, and z correspond to −1, −1, and 1, respectively, which perfectly reproduce the matrix elements of the small matrix on the diagonal line in Eq. (1.28). In short, the trace of the small matrix can simply be calculated by summation of the numbers at the rows of x, y and z in the character table, which is denoted as χ_R. If the number of unmoved atoms is denoted as N_R, the trace of the huge matrix can very simply be calculated as $N_R\chi_R \equiv \chi$. The calculation process is emphasized by the italic figures in Table 1.5. In the case of C_2 operation, the trace of the huge matrix, −1, is thus simply calculated as presented by the thick characters in the table.

One of the most important characteristics of "character table" is that the rows and columns are both in a mutually orthogonal system. For example, the dot product of the symmetry species of A_1 and A_2 is zero

$$(1 \quad 1 \quad 1 \quad 1) \cdot (1 \quad 1 \quad -1 \quad -1) = 0.$$

In a similar manner, E and C_2 are also mutually orthogonal as the next calculation.

$$\begin{pmatrix} 1 \\ 1 \\ 1 \\ 1 \end{pmatrix} \cdot \begin{pmatrix} 1 \\ 1 \\ -1 \\ -1 \end{pmatrix} = 0$$

These characters are mathematically proved, which is called the *wonderful (or great/grand) orthogonal theorem*. This characteristic is quite useful to *expand* any molecular vibration *using independent symmetry species*. We have to note, however, that the orthogonality is not normalized. In the case of C_{2v}, the norm of the row-wise vector is 4 (denoted as $g = 4$), which corresponds to the number of operators.

When the original huge size matrix in Eq. (1.28) is considered, for example, a symmetry operator of E is represented by a unit matrix with a size of 9×9, which yields the trace of 9, since all the three atoms are unmoved. This can easily be calculated by using the character table as found by the bold-and-italic characters in Table 1.5. The operators are denoted by a parameter, R, and the unmoved atoms are counted to be N_R for each R. In the case of a water molecule, *by referring the molecular skeleton* (Fig. 1.3), the counted number of the unmoved atoms is filled in the row of N_R. For the operator of E, N_R is 3 as filled in the table. The trace of each small matrix can be calculated by adding the numbers "in the rows of x, y, and z (in the 'linear' column)," which is filled in the row of χ_R, i.e., $\chi_R = 1 + 1 + 1 = 3$. As a result, the trace of the huge matrix, χ, can readily be calculated by simply multiplying N_R and χ_R, which is also filled in the row of χ ($\chi = 9$). After calculating the χ components for all the operators, the "vector" of χ is obtained as $(9 \quad -1 \quad 1 \quad 3)$ for a molecular water.

Now, we are ready to expand the huge matrix with the mutually orthogonal symmetry species using the wonderful orthogonality theorem. When the row vector of the symmetry species, i (for example B_2), is denoted as χ_i (i.e., $(1 \quad -1 \quad -1 \quad 1)$) the number of normal modes belonging to i, a_i, is calculated using the orthogonal character

$$a_i = \frac{1}{g}\sum_R \chi_i(R)\chi(R) = \frac{1}{g}\chi_i \cdot \chi.$$

The dot represents the inner product of the two vectors. For example, the number of the totally symmetric A_1 mode, a_{A_1}, is calculated as

$$a_{A_1} = \frac{1}{4}(1 \quad 1 \quad 1 \quad 1) \cdot (9 \quad -1 \quad 1 \quad 3) = 3.$$

In a similar manner, other components are calculated, and the total modes, Γ, are expressed as:

$$\Gamma = 3A_1 + A_2 + 2B_1 + 3B_2.$$

This means that the total 9 (= 3 + 1 + 2 + 3) modes are categorized into the four symmetry species. Nevertheless, some of the molecular "motions" do not contribute to molecular "vibrations." The translational and rotational motions must be removed to leave the vibrations only. To do that, the linear motions (x, y, z, R_x, R_y, and R_z) in the character table are referred, and the corresponding symmetry species

are removed out. As a result, the total vibrational modes, Γ^{vib}, are expressed by the next equation.

$$\Gamma^{\text{vib}} = 2A_1 + 0A_2 + 0B_1 + 1B_2 = 2A_1 + B_2$$

This result straightforwardly implies that the water molecule has three (2 + 1) normal modes as molecular vibrations, and two of them are assigned to the A_1 mode, and the rest one goes to B_2.

For the analysis of the anti-symmetric OH_2 stretching vibration ($\nu_a(OH_2)$; Fig. 1.3a), for example, the "arrows" in the figure are necessary. When the C_2 operation is applied to the figure, the arrows are turned over, which yields -1 in the character table. Therefore, only B_1 and B_2 remain as the candidates. Next, the σ_v operation is applied. Since the "mirror" overturns the arrows, the operation yields -1. As a result, B_2 is chosen as the symmetry species for the mode. Just in case, the rest $\sigma_{v'}$ operation is also applied to the arrows, which results in no change yielding 1. In this manner, the vibration fully satisfies the B_2 symmetry. In a similar manner, other two modes satisfy A_1.

All the normal modes are thus fully assigned to the symmetry species, which is called *spectral analysis on group theory*. The total number of "three" exactly agrees with the number predicted by the $3N - 6$ rule, which can be used as a check of the results of the group theory analysis.

Next, the parity of the product of wave functions is readily revealed by the direct product of the irreducible representation of the symmetry species. In the case of the transition moment, the three wave functions involved in the integral ($|j\rangle$, $|r\rangle$ and $|k\rangle$) are to be considered.

As discussed in Sect. 1.4 (near Fig. 1.13), only the transition from the ground state ($v = 0$) to the first excited state ($v = 1$) is enough to consider the IR absorption in a good approximation, which means that $|j\rangle$ corresponds to $v = 0$. At $v = 0$, no arrow representing vibration is available on the molecule, which is the "totally symmetric." Therefore, in the case of C_{2v}, $|j\rangle$ takes the symmetry species of A_1. To look for the symmetry species of r, the column of "linear" is referred to find x, y, and z. As an example of the excited state corresponding to $|k\rangle$, the $\nu_a(OH_2)$ mode is considered. As mentioned above, the B_2 species is referred, which is at the same row of y. Therefore, the reduced representations of $|k\rangle$ and $|r\rangle$ are found to be both B_2. Therefore, the parity of the product in the transition moment is obtained as:

$$\boldsymbol{B}_2 \otimes \boldsymbol{B}_2 \otimes \boldsymbol{A}_1 = \boldsymbol{A}_1, \tag{1.29}$$

since the *direct product* (denoted by $\otimes$) of the same symmetry species always becomes A_1, so that the product of the three functions in the transition moment has a totally symmetric species. This confirms that the $\nu_a(OH_2)$ mode is IR active.

Through this process, we find that *the excited state and* $\boldsymbol{r}$ *must have the same symmetric species for being IR active* when the ground state belongs to A_1. This means that the direction of a transition moment is the same as that of the vibrational

motion illustrated on the molecule. This simplicity is a great benefit of IR spectroscopy, with which the molecular orientation analysis can easily be performed.

Factor group analysis

For a molecule that has a *repeat structure of a simple unit* represented by a polymer molecule or a molecule in a crystal [8, 9], *factor group analysis* is necessary; otherwise an unreasonably great number of normal modes are generated. If the $3N - 6$ rule is simply employed for considering a polymer, the number of normal modes becomes huge, which makes the IR analysis impossible. As a matter of fact, however, this problem never occurs as found in Fig. 1.1, which implies that another theoretical concept should be added for treating a repeating structure.

Polyethylene (Fig. 1.1) has an alkyl chain of $(CH_2)_n$ that is a repeated part consisting of a $(CH_2)_2$ unit. In this case, the symmetry of the alkyl part is entirely considered instead of considering a methylene group unit only. Figure 1.15 presents schematic images of the $\nu_s CH_2$ mode on different coupled oscillations, which is denoted as d^+: d and + corresponds to the methylene group and the symmetric vibration, respectively.

As illustrated schematically in the figure, the entire chain has various *vibrational shapes as a coupled oscillator*. The top and bottom schemes are characterized by different phases, δ, between the adjacent methylene groups in a dashed parallelogram, i.e., $\delta = 0$ and π, respectively [10]. Therefore, the two schemes are denoted as $d^+(0)$ and $d^+(\pi)$ [11–13]. If a repeat unit is the ethylene group $[(CH_2)_2]$, the adjacent red and blue parallelogram units exhibit no wavy curve ($\lambda = \infty$), which is

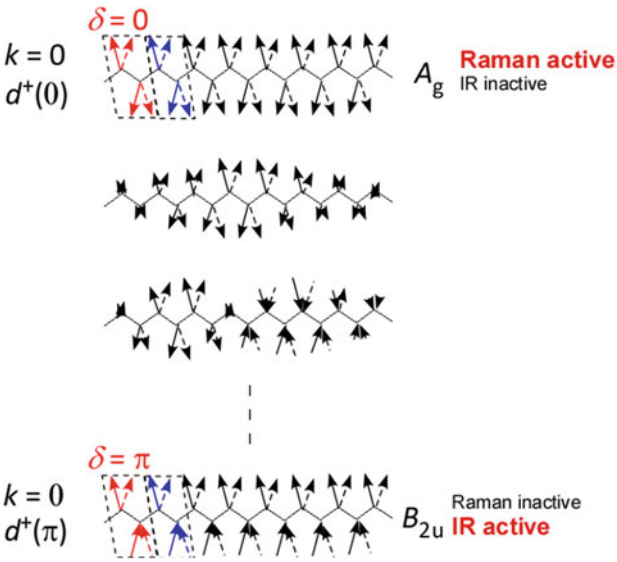

Fig. 1.15 A coupled oscillator of a $(CH_2)_{15}$ chain with different wavenumber vectors (k) describing the $\nu_s CH_2$ mode (d^+). If k is defined using a unit of $(CH_2)_2$, both $\delta = 0$ and π patterns correspond to $k = 0$, which is IR active

Table 1.6 Factor group analysis using D_{2h} for polyethylene (g = 8)

D_{2h}	E	$C_2(y)$	$C_2(z)$	$C_2^S(x)$	i	$\sigma(xy)$	$\sigma(yz)$	$\sigma_g(xz)$	Linear
A_g	1	1	1	1	1	1	1	1	
A_u	1	1	1	1	−1	−1	−1	−1	
B_{1g}	1	−1	1	−1	1	1	−1	−1	R_z
B_{1u}	1	−1	1	−1	−1	−1	1	1	z
B_{2g}	1	1	−1	−1	1	−1	−1	1	R_y
B_{2u}	1	1	−1	−1	−1	1	1	−1	y
B_{3g}	1	−1	−1	1	1	−1	1	−1	R_x
B_{3u}	1	−1	−1	1	−1	1	−1	1	x
N_R	6	**2**	0	0	0	2	**6**	0	
χ_R	3	−1	−1	−1	−3	1	1	1	
χ	18	−2	0	0	0	2	6	0	

represented by $k = 0$ (Brillouin-zone center) for both $d^+(0)$ and $d^+(\pi)$. Since the wavelength of IR and visible light is much longer than the unit length, only the vibrational modes of $k = 0$ are selectively observed by IR and Raman spectroscopy within a good approximation. As a result, only the $d^+(0)$ and $d^+(\pi)$ patterns can be the candidates for IR and Raman spectroscopy.

Both $d^+(0)$ and $d^+(\pi)$ patterns belong to the point group, D_{2h}. The normal-mode analysis of a compound consisting of a repeat unit is called "*factor group analysis*." The character table of D_{2h} is available in Table 1.6. In a factor group analysis, the repeat unit is referred for filling the matrix. The Cartesian coordinate and a repeat unit of two methylene groups [5] are presented in Fig. 1.16. Factor group analysis needs some additional symmetry operations: the *glide plane* and the *screw axis*, which are denoted as σ_g and C^S, respectively. The glide plane is an operation of mirror imaging followed by translation along the chain by a half unit length. The screw axis is another operation of rotation as C followed by the translation.

Note that, in the factor group analysis, C_n and σ operations are *performed twice at each dashed vertical line* in the figure. Therefore, as marked by bold in Table 1.6, *the number of unmoved atoms is doubled*. As a result, the irreducible representation is readily calculated to be

$$\Gamma = 3A_g + A_u + 2B_{1g} + 3B_{1u} + B_{2g} + 3B_{2u} + 3B_{3g} + 2B_{3u}.$$

In factor group analysis, we have to take another care that the *rotation about the y and z axes cannot be removed* for leaving the vibrational modes only (R_y and R_z are deleted in Table 1.6). In short, the number of the normal modes is ruled by $3N - 4$ for a nonlinear molecule. Therefore, the irreducible representation of vibrational modes is [14]:

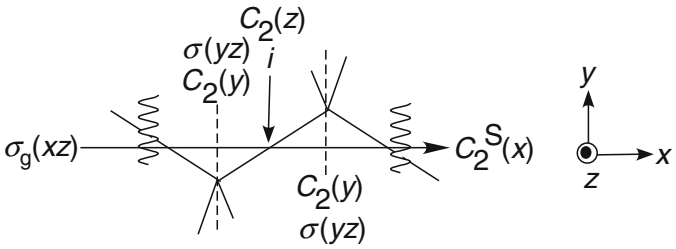

Fig. 1.16 The Cartesian coordinate and a repeat unit of $(CH_2)_2$ between the two wavy *vertical lines* [5]

$$\Gamma^{\text{vib}} = 3A_g + A_u + 2B_{1g} + 2B_{1u} + B_{2g} + 2B_{2u} + 2B_{3g} + B_{3u}.$$

The total number of the normal modes, 14 (=3+1+2+2+1+2+2+1), agrees with $3 \times 6 - 4 = 14$.

Of note is that *two different $\nu_s CH_2$ modes are available* in the molecules having the repeat units as marked in Fig. 1.15 corresponding to A_g and B_{2u}. By referring Eq. (1.29), the IR active modes are obtained as:

$$\Gamma^{\text{IR}} = 2B_{1u} + 2B_{2u} + B_{3u}.$$

The IR active $\nu_s CH_2$ mode is thus assigned only to B_{2u}. In fact, in the discarded coupled oscillator of A_g, the summation of all the dipole moments becomes nearly zero, which makes IR inactive; whereas it is Raman active [14]. Note that this is the reason why the $\nu_s CH_2$ mode appears at different positions in IR and Raman spectra at 2851 and 2848 cm^{-1}, respectively.

Since all the symmetry species are not degenerated, the number of IR bands is five. In Fig. 1.1, only four modes are found, since the rest CH_2 wagging mode (at ca. 1170 cm^{-1} [12, 13]) is split into many *band progression*, which is too many and too weak to find [15].

Fermi resonance

An overtone band is generally very weakly appeared because of the selection rule represented by Fig. 1.13. Nevertheless, when the energy of the overtone is coincidently close to another normal mode, they are talked to each other, and the overtone band receive energy to develop significantly. The coupling of the accidentally degenerated modes was first recognized by Fermi [16].

An example is presented in Fig. 1.17, which is an IR spectrum of benzoyl chloride. The most intense band of the carbonyl group at 1772 cm^{-1} accompanies a satellite band at 1732 cm^{-1}, which is attributed to the Fermi resonance. The resonance occurs between the νC=O and 2νPh–O (2×869 cm^{-1}) [17]. The overtone, 2νPh–O, couples with the strong fundamental νC=O mode, since the energies are coincidentally close to each other. As a result, the overtone band, which is

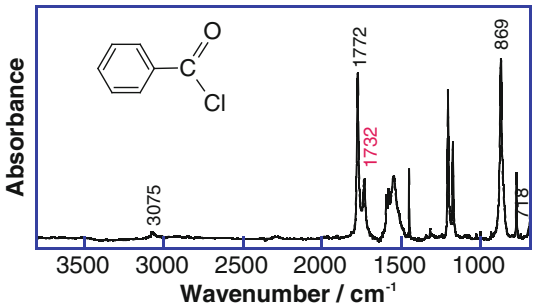

Fig. 1.17 IR spectrum of benzoyl chloride [1]

intrinsically very weak, receives energy from the strong νC=O band, which results in an apparently found satellite peak.

The cross talk between two different modes is theorized via an off-diagonal element in the eigenvalue matrix [18, 19]. If two modes, $\psi(Q_n)$ and $\psi(Q_m)$, are in resonance, Schrödinger equation of the steady state,

$$\widehat{H}\psi_{\text{vib}} = E\psi_{\text{vib}},$$

is described in an explicit manner

$$\widehat{H}\begin{bmatrix}\psi(Q_1)\\ \psi(Q_2)\\ \vdots\\ \psi(Q_n)\\ \psi(Q_m)\\ \vdots\\ \psi(Q_k)\end{bmatrix} = \begin{bmatrix}E(Q_1) & 0 & 0 & 0 & 0 & 0 & 0\\ 0 & E(Q_2) & 0 & 0 & 0 & 0 & 0\\ \vdots & \vdots & \vdots & \ddots & \vdots & \vdots & \vdots\\ 0 & 0 & 0 & E_n & E_{nm} & 0 & 0\\ 0 & 0 & 0 & E_{nm} & E_m & 0 & 0\\ \vdots & \vdots & \vdots & \vdots & \vdots & \ddots & \vdots\\ 0 & 0 & 0 & 0 & 0 & 0 & E(Q_k)\end{bmatrix}\begin{bmatrix}\psi(Q_1)\\ \psi(Q_2)\\ \vdots\\ \psi(Q_n)\\ \psi(Q_m)\\ \vdots\\ \psi(Q_k)\end{bmatrix}.$$

The off-diagonal element, E_{nm} , is generated as a result of an interaction of the two modes, i.e.,

$$E_{nm} = \langle\psi(Q_n)|\widehat{H}'|\psi(Q_m)\rangle.$$

If the small matrix is taken from the large matrix, the following equation holds.

$$\begin{vmatrix}E_{nm} - E & E_{nm}\\ E_{nm} & E_{nm} - E\end{vmatrix} = 0$$

As a result, the energy in resonance is found to be split into two states.

Table 1.7 Character table of C_{3v} for analyzing the methyl group ($g = 6$)

C_{3v}	E	$2C_3(z)$	$3\sigma_v$	Linear	Quadratic
A_1	1	1	1	z	$x^2 + y^2$, z^2
A_2	1	1	−1	R_z	
E	2	−1	0	(x, y) (R_x, R_y)	$(x^2 - y^2, xy)$ (xz, yz)

$$E = \frac{1}{2}(E_n + E_m) \pm \sqrt{4|E_{nm}|^2 + \delta^2} \quad (\delta \equiv E_n - E_m)$$

Here, δ is the energy difference of the un-perturbed levels. Of course the two mixed states, ψ^+ and ψ^-, are described as

$$\psi^+ = \frac{1}{N}[a\psi_m + b\psi_n] \quad \text{and} \quad \psi^- = \frac{1}{N}[a\psi_m - b\psi_n].$$

In this manner, Fermi resonance yields doubly split two bands. In many cases, one of them is overlaid on another band to be invisible.

In a spectrum of a paraffin (alkyl group), a Fermi-resonance band is often found at ca. 2935 cm^{-1}. For example, stearic acid yields the band at 2938 cm^{-1} as presented in Fig. 1.6. This is a result of a coupling of $2\delta_aCH_3$ with $\nu_s(CH_3)$ [20]. Since the fundamental band of the δ_aCH_3 mode is at 1453 cm^{-1}, the overtone (<2906 cm^{-1}) is coincidentally close to the position of the $\nu_s(CH_3)$ band at 2870 cm^{-1}. The rest of the two Fermi-resonance bands should appear at ca. 2880 cm^{-1}, but it is hidden in other crowded bands.

Note here that not only the energy agreement, but the symmetry matching is also necessary for generating Fermi resonance. Since the methyl group has the symmetry of C_{3v}, the character table of C_{3v} is referred (Table 1.7).

The asymmetric deformation vibration of the methyl group (δ_aCH_3) is degenerated, and the fundamental mode thus belongs to the symmetric species of E. Then, the overtone has the symmetric species of

$$E \otimes E = (4 \quad 1 \quad 0).$$

Therefore, the overtone can be decomposed by considering the great orthogonal theorem to have

$$E \otimes E = A_1 + A_2 + E.$$

In this manner, in the case of C_{3v}, the overtone of the E mode can be interacted with all the IR active modes to have a Fermi resonance band, if the energies are close to each other.

1.6 Light Absorption by a Molecule: 2. Understanding on Electrodynamics for a Bulk Matter Toward Beer's Law

Quantum mechanics yields many important rules for understanding absorption spectroscopy, but another framework of spectroscopic theory is necessary, which is electrodynamics. In particular for taking an *optical interface* account, electrodynamics is definitely necessary. One of the beautiful benefits of making discussion on electrodynamics is that the predicted results reproduce the experimental ones quantitatively. Another great benefit is that light absorption by a "bulk matter" that is a collection of many dipoles can easily be theorized, which is quite suitable to theorize IR spectroscopy.

In a limited case that an optical interface can be ignored, the system can easily be modeled. Such a system *with no interface* is defined as "bulk" in this book, which means that thin films and small particles are excluded at the moment. Let us imagine a dispersed sample in a KBr pellet, which is a good analytical target as a bulk matter, since the thickness of the pellet is much longer than the wavelength of IR light to readily ignore an interface. In this situation, only the interaction between a matter and light can be theorized without considering the optical configuration.

Since the IR light can be approximated as a plane wave, the light can be represented by *Maxwell equations*.

$$\nabla \cdot \boldsymbol{D} = 0 \tag{1.30}$$

$$\begin{aligned} &\nabla \cdot \boldsymbol{B} = 0 \\ &\nabla \times \boldsymbol{E} + \dot{\boldsymbol{B}} = 0 \end{aligned} \tag{1.31}$$

$$\nabla \times \boldsymbol{H} - \dot{\boldsymbol{D}} = 0 \tag{1.32}$$

The dot indicates the derivative in terms of time. These equations accompany the two *constituent equations*:

$$\boldsymbol{B} = \mu_0 \boldsymbol{H} \quad (\mu_r \approx 1) \tag{1.33}$$

and

$$\boldsymbol{D} = \varepsilon \boldsymbol{E}. \quad (\varepsilon = \varepsilon_0 \varepsilon_r) \tag{1.34}$$

Since these two equations are on linear approximations, these are not involved in Maxwell equations, and they are put aside. By putting Eq. (1.33) into Eq. (1.32), the next relationship is obtained.

$$\nabla \times \boldsymbol{B} = \mu_0 \dot{\boldsymbol{D}} \tag{1.35}$$

On the other hand, another rotation operator is applied to Eq. (1.31),

$$\nabla \times \nabla \times \boldsymbol{E} = -\nabla \times \dot{\boldsymbol{B}}$$

is obtained, which can be combined with Eq. (1.35) to have:

$$\nabla \times \nabla \times \boldsymbol{E} = -\mu_0 \ddot{\boldsymbol{D}}. \tag{1.36}$$

When a formula of

$$\nabla \times \nabla \times \boldsymbol{A} = \nabla(\nabla \cdot \boldsymbol{A}) - \nabla^2 \boldsymbol{A}$$

is applied to Eq. (1.36) considering Eq. (1.30), then we have:

$$\nabla^2 \boldsymbol{E} = \mu_0 \ddot{\boldsymbol{D}} = \mu_0 \varepsilon \ddot{\boldsymbol{E}}. \tag{1.37}$$

Since this derivative equation has a particular solution of:

$$\boldsymbol{E} = \boldsymbol{E}_0 \exp\ \mathrm{i}(\boldsymbol{k} \cdot \boldsymbol{r} - \omega t). \tag{1.38}$$

the following *dispersion relation* is obtained.

$$k^2 = \mu_0 \varepsilon \omega^2 = \mu_0 \varepsilon_0 \varepsilon_\mathrm{r} \omega^2 = \varepsilon_\mathrm{r} \omega^2 / c^2 \tag{1.39}$$

Here, c is the phase velocity of light. When the refractive index, n, is introduced by considering the phase velocity, $V = \omega/k = c/\sqrt{\varepsilon_\mathrm{r}}$:

$$n = \frac{c}{V} = \sqrt{\varepsilon_\mathrm{r}}. \tag{1.40}$$

The dispersion relation [Eq. (1.39)] can be modified to be

$$k^2 = \frac{n^2}{c^2}\omega^2 \Leftrightarrow k = \frac{n\omega}{c}. \quad (\because \omega \geq 0)$$

Since the refractive index is a complex (Chap. 4), $n \equiv n' + \mathrm{i}n''$ is incorporated into Eq. (1.38) with the modified dispersion relation to have:

$$\begin{aligned} \boldsymbol{E} &= \boldsymbol{E}_0\ \exp(\mathrm{i}kz - \mathrm{i}\omega t) = \boldsymbol{E}_0\ \exp\left(\mathrm{i}\frac{\omega n z}{c} - \mathrm{i}\omega t\right) \\ &= \boldsymbol{E}_0 \exp\left(-\frac{\omega n'' z}{c}\right) \exp\left(\mathrm{i}\frac{\omega n' z}{c} - \mathrm{i}\omega t\right). \end{aligned} \tag{1.41}$$

Here, the equation is changed to be a one-dimensional one (along z) for simplicity. Since the light intensity is proportional to $|\boldsymbol{E}|^2 = \boldsymbol{E}^*\boldsymbol{E}$, we have:

$$I = I_0 \exp\left(-\frac{2\omega n'' z}{c}\right). \tag{1.42}$$

If the definition of absorbance, A, is introduced [see Eq. (3.1)], A can be written as:

$$\begin{aligned} A &\equiv -\log_{10}\left(\frac{I}{I_0}\right) \\ &= -\frac{1}{\ln 10}\ln\left(\frac{I}{I_0}\right) = \frac{1}{\ln 10}\frac{2\omega n''}{c} z = \boxed{\frac{1}{\ln 10}\frac{4\pi n''}{\lambda} z \equiv \frac{1}{\ln 10}\alpha z}. \end{aligned} \tag{1.43}$$

In this manner, an absorbance spectrum has a shape of α (absorptivity), which depends on n'' and λ. Equation (1.43) presents the detail of *Beer's law*. Note again that this holds only when *no interface* is involved in the system, since no interface is taken into account in the deduction process.

The KBr pellet technique is quite important to obtain the α spectrum dominated by n''. This is because the influence of the interface can be ignored due to the large thickness of the pellet to the wavelength. To obtain the physical parameter specific to a material, n'', the KBr technique is thus the first choice. Due to a similar reason, the Nujol technique, and transparent measurement through an IR transparent solvent such as chloroform are also very important.

Because of Eq. (1.40), the physical insights of electric permittivity should be described, so that the light absorption mechanism via the interaction between dipoles and the electric field of light would readily be understood via the complex refractive index.

In electrodynamics, the coupling of light and a matter is theorized by a simple classical equation of an electron motion oscillated by electric field, $E(t)$, in which the electron with the charge of e is under constraint by the electromagnetic potential of an atomic core. Therefore, the electron motion is modeled by an electron constrained by a spring connected to the core, and the oscillation is damped with time, which can be written by a simple Newton equation.

$$m^*\ddot{r}(t) + m^*\gamma\dot{r}(t) + m^*\omega_0^2 r(t) = -eE(t) \tag{1.44}$$

Here, the effective mass of electron is denoted by m^*, and γ is the damping factor. The constraint is modeled by a spring with a spring constant, κ, which is involved in the *resonance* angular frequency, $\omega_0 = \sqrt{\kappa/m^*}$.

Equation (1.44) is Fourier transformed ($\frac{\mathrm{d}^n}{\mathrm{d}t^n} g(t) \rightarrow (-\mathrm{i}\omega)^n G(\omega)$) to have the frequency domain equation [Eq. (1.45)].

$$\begin{aligned} r(\omega)\left(-\omega^2 - \mathrm{i}\gamma\omega + \omega_0^2\right) &= \frac{-e}{m^*}E(\omega) \\ \Leftrightarrow r(\omega) &= \frac{-eE(\omega)}{m^*\left(\omega_0^2 - \omega^2 - \mathrm{i}\gamma\omega\right)} \end{aligned} \tag{1.45}$$

Here, the polarization, P, is introduced to involve N induced dipole moments, $p \equiv -er$, in an averaged manner where r is the distance of the two poles of the dipole. (For the details of P, refer to Sect. 7.1.)

$$P(\omega) \approx Np = -Ner(\omega) = \frac{e^2 NE(\omega)}{m^*\left(\omega_0^2 - \omega^2 - \mathrm{i}\gamma\omega\right)} \tag{1.46}$$

In this manner, the one-electron theory has been bridged to a bulk matter. In addition, the definition of the electric flux density, $D(= \varepsilon E)$ (see Sect. 7.1), and Eq. (1.34) are considered to have Eq. (1.47).

$$D \equiv \varepsilon_0 E + P \Leftrightarrow \varepsilon E = \varepsilon_0 E + P \Leftrightarrow \varepsilon_0 \varepsilon_\mathrm{r} = \varepsilon_0 + \frac{P}{E} \tag{1.47}$$

Here, ε_r is the relative electric permittivity. When Eqs. (1.45)–(1.47) are merged, the next equation is obtained.

$$\varepsilon_0 \varepsilon_\mathrm{r}(\omega) = \varepsilon_0 + \frac{e^2 N}{m^*\left(\omega_0^2 - \omega^2 - \mathrm{i}\gamma\omega\right)} = \varepsilon_0 + \frac{\varepsilon_0 \omega_\mathrm{p}^2}{\omega_0^2 - \omega^2 - \mathrm{i}\gamma\omega} \tag{1.48}$$

This equation has a problem that ε_r equals to unity for a high frequency ($\omega \to \infty$). The problem occurs since the physical model is too simple to quantitatively discuss the permittivity. Therefore, the first term is conveniently replaced by an empirical value, $\varepsilon_0 \varepsilon_{\mathrm{r},\infty}$, yielding the refractive index, n, of the material ($\varepsilon_{\mathrm{r},\infty} = n^2$).

In addition, the *plasma frequency*, ω_p, defined as Eq. (1.49) is newly introduced to make the equation simpler.

$$\omega_\mathrm{p}^2 \equiv \frac{e^2 N}{\varepsilon_0 m^*} \tag{1.49}$$

For a spectrum having a multiple number of absorption bands, Eq. (1.48) is expanded such as:

$$\boxed{\varepsilon_\mathrm{r}(\omega) = \varepsilon_{\mathrm{r},\infty} + \omega_\mathrm{p}^2 \sum_j \frac{f_j}{\omega_j^2 - \omega^2 - \mathrm{i}\gamma_j \omega}} \tag{1.50}$$

The oscillator strength, f_j, denotes the number of electrons characterized by ω_j and γ_j, which are delivered from the total Z electrons in the matter [Eq. (1.51)].

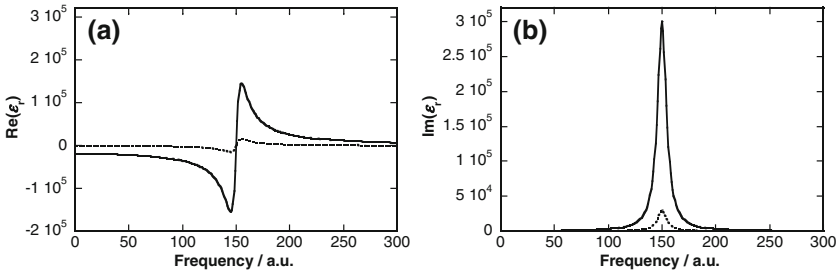

Fig. 1.18 Simulated complex electric permittivity having a single oscillator: $\varepsilon_{r,\infty} = 2.25$, $\omega_0 = 150$, $\gamma = 10$, $\omega_p^2 f = 500$ (*dashed line*) and $\omega_p^2 f = 5000$ (*solid line*). The real and imaginary parts are presented in (**a**) and (**b**), respectively

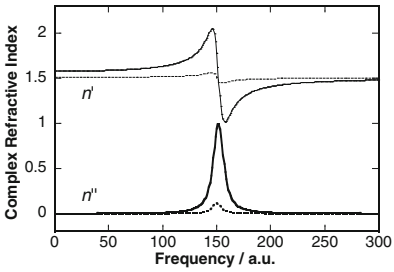

Fig. 1.19 Complex refractive index calculated from the permittivity in Fig. 1.18. The *thick* and *thin lines* represent the imaginary and real parts, respectively. The *dashed* and *solid lines* correspond to those in Fig. 1.18

$$\sum_j f_j = Z \tag{1.51}$$

Equation (1.50) is conveniently used as a physical expression of the electric permittivity as a function of the angular frequency, on which numerical simulations can be performed as presented in Fig. 1.18.

Through Eq. (1.40), the permittivity provides the corresponding complex refractive index, which is presented in Fig. 1.19.

The shape of permittivity is fairly similar to that of refractive index for each real and imaginary part. The imaginary part of both permittivity and refractive index looks an absorption band; whereas the real part has a derivative shape. Since the derivative shape has an opposite increase trend to the entire dispersion, the derivative-shaped region is sometimes called "anomalous dispersion." When the

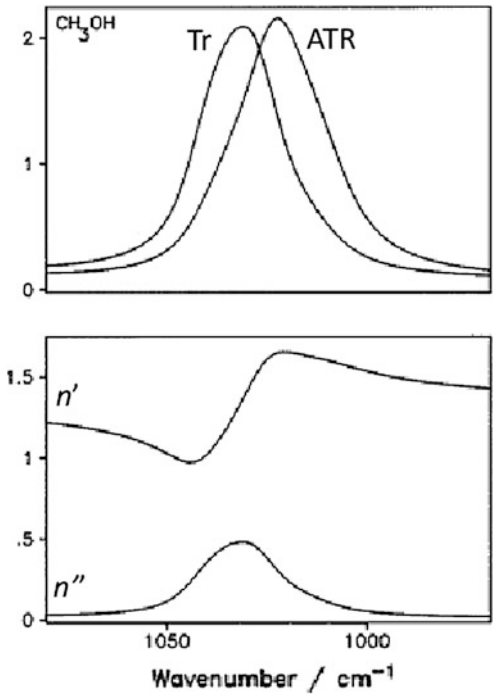

Fig. 1.20 IR "thick" transmission and ATR spectra of methanol in the C–O stretching vibration region (*upper panel*). The complex refractive index spectra (*lower panel*) accounts for both measured spectra [21]

imaginary part peak is large, the anomalous dispersion is fairly enhanced, which can make the absorption band distorted when an optical interface plays an important role in measurement (Chap. 3). *This is a very important key to quantitatively discuss the band positions and relative band intensity; otherwise the shift and intensity change may be attributed to a chemical reason in a wrong manner.*

The upper panel of Fig. 1.20 presents IR spectra of methanol measured by the transmission (Tr) and ATR techniques (Chap. 3), which exhibits a large band shift [21]. Of note is that the complex refractive index spectra (lower panel) are common to the two spectra.

Since the peak position of the imaginary part (n'') of the refractive index is very close to that of the Tr one, the ATR spectrum is largely influenced by the anomalous dispersion of the real part (n').

As described in detail in Chap. 3, the KBr pellet spectra have the same trend as the "thick" Tr spectrum, since it is free from an optical interface, and it reflects only n'' as presented in Eq. (1.43). *When a spectrum of a thin film is analyzed, on the other hand, we have to pay an attention on the matter*, since the spectrum is influenced not only by n'', but also by n'.

References

1. E.B. Wilson Jr., J.C. Decius, P.C. Cross, Molecular vibrations: the theory of infrared and Raman vibrational spectra (New York, Dover, 1980)
2. N. Shioya, T. Shimoaka, K. Eda, T. Hasegawa, Phys. Chem. Chem. Phys. **17**, 13472–13479 (2015).
3. D.L. Allara, R.G. Nuzzo. Langmuir **1**, 52–66 (1985).
4. IR spectra database of NIST Chemistry WebBook at http://webbook.nist.gov/chemistry/
5. S. Krimm, C.Y. Liang, G.B.B.M. Sutherland, J. Chem. Phys. **25**, 549–562 (1956)
6. I.R. Hill, I.W. Levin, J. Chem. Phys. **70**, 842–851 (1979)
7. T. Noda, S. Kondo, N. Yamada, T. Hasegawa, Kobunshi Ronbunshu **73**, 69–75 (2016)
8. M. Tasumi, T. Shimanouchi, J. Chem. Phys. **43**, 1245–1258 (1965)
9. R. Zbinden, Infrared Spectroscopy of high polymers (London, Academic Press, 1964)
10. M. Motoyama, Bull. NARO Inst. Livest. Grassl. Sci. **12**, 19–68 (2012)
11. R.G. Snyder, S.L. Hsu, S. Krimm, Spectrochim. Acta **34A**, 395–406 (1978)
12. J.H. Snyder, R.G. Schachtschneider, Spectrochim. Acta **19**, 85–116 (1963)
13. J.H. Schachtschneider, R.G. Snyder, Spectrochim. Acta **19**, 117–168 (1963)
14. T. Shimanouchi. Tables of molecular vibrational frequencies consolidated volume I. NSRDS-NBS-39 (Washington D.C., 1972) p. 156
15. P.C. Painter, M.M. Coleman, J.L. Koenig, The theory of vibrational spectroscopy and its application to polymeric materials (New York, Wiley, 1982) pp. 196–226
16. E. Fermi, Z. Physik **71**, 250–259 (1931)
17. C.N.R. Rao, R. Venkataraghaven. Spectrochim. Acta **18**, 273–278 (1962)
18. G. Herzberg. Molecular spectra and molecular structure II. Infrared and Raman spectra of polyatomic molecules. (Tronto, Canada, D. van Norstrand Company, 1945) pp. 215–227
19. M. Diem, Introduction to modern vibrational spectroscopy (New York, Wiley, 1993) pp. 58–103
20. A.N. Parikh, D.L. Allara, J. Chem. Phys. **96**, 927–945 (1985)
21. J.E. Bertie, K.H. Michaelian, J. Chem. Phys. **109**, 6764–6771 (1998)

Chapter 2
Fundamentals of FT-IR

2.1 Principle of Spectral Measurements

A schematic of IR spectroscopy is illustrated in Fig. 2.1, which presents the physical fundamental of spectroscopy. The IR source emits IR ray, and a portion of the ray through the slit is made a parallel light by mirrors (omitted in the figure), $I(t)$, going to the prism.

At the moment, the light has an image of the plane wave of electric and magnetic fields as a function of time, t, and the intensity, I, is proportional to the squared electric field (Eq. 3.17). The prism is an optical element working as the heart of the spectrometer: the refraction angle depends on the wavelength of the light. In this manner, the straight parallel light becomes a "dispersed" light. If the light is visible light, a rainbow pattern appears on the screen. Since the IR light is invisible, an IR detector must be used to have a spectrum instead of the visible pattern.

The spectrum appears as a graph developed by two axes of wavelength, λ, and intensity, S. Since the wavelength is directly interrelated with a more useful parameter, angular frequency (ω), the spectrum is denoted as $S(\omega)$ in the figure. In this manner, the optical element works to transform the time-domain function, $I(t)$, to the frequency-domain one, $S(\omega)$, which corresponds to Fourier transform in mathematics. In other words, the role of the optical element is Fourier transform the light to a spectrum very quickly with the light velocity. Regardless, this type of spectrometer using an optical dispersive element is *not* called a Fourier transform spectrometer, but a dispersion-type spectrometer.

Fourier transform is represented by a pair of equations.

$$S(\omega) = \int_{-\infty}^{\infty} I(t)\mathrm{e}^{-\mathrm{i}\omega t}\,\mathrm{d}t \tag{2.1}$$

T. Hasegawa, *Quantitative Infrared Spectroscopy for Understanding of a Condensed Matter*, DOI 10.1007/978-4-431-56493-5_2

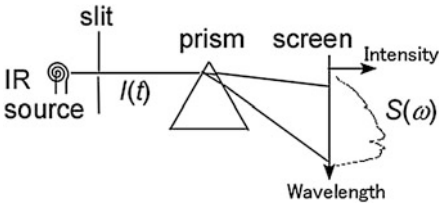

Fig. 2.1 Schematic of a dispersion-type spectrometry

$$I(t) = \frac{1}{2\pi} \int_{-\infty}^{\infty} S(\omega) e^{i\omega t} \, d\omega \tag{2.2}$$

Equation (2.2) is especially easy to understand intuitively. Since $e^{i\omega t}$ represents an oscillation like a cosine wave, the summation of the waves with the weighting function of $S(\omega)$ for all frequencies yields the time-domain representation of the broadband wave, $I(t)$. This equation is called "inverse Fourier transform." The role of the prism in Fig. 2.1 is represented by the Fourier transform: $I(t)$ is transformed to $S(\omega)$. If $I(t)$ is readily measured, the spectrum is thus obtained by calculation using Eq. (2.1) *without using an optical element like a prism*, which is called *Fourier transform spectrometry*.

A dispersion-type spectrometer has experimental limitations as follows.

(1) If the refraction (or diffraction) angle-variance is highly limited by using a narrow slit, the wavenumber resolution becomes high. This spatially limited light is, however, very dark, which results in a poor quality spectrum.
(2) To obtain a spectrum, a mechanical scanning of wavelength is necessary. A perfect reproducibility of mechanical scanning cannot be expected, and the calibration of the abscissa axis is necessary for each measurement. Therefore, reliable accumulation of spectra for improving spectral quality is generally difficult.
(3) The spectral quality depends on the speed of the mechanical scanning. To have a high-quality spectrum, a slow scanning is required, which takes much time. In other words, only a stable sample can be measured.

These intrinsic matters specific to a dispersive-type spectrometer can totally be overcome by introducing the Fourier transform (FT) technology in theory.

Nevertheless, a direct measurement of $I(t)$ requires a very high technique, since ultrafast measurements are necessary. Mid-IR light is generally recognized as the wavenumber range of 4000–400 cm^{-1}, which corresponds to the wavelength region of ca. $\lambda = 10\,\mu m$, which further corresponds to $\nu = 30$ THz = 3×10^{13} Hz ($c = \nu\lambda$). To measure the IR light in the time-domain, therefore, an ultrafast spectrometer having a time resolution of ca. 3×10^{-14} s (femtosecond region) is necessary. In other words, a femtosecond pulse laser must be employed for obtaining an IR spectrum to straightforwardly employ the FT principle, which needs much cost and a very high measurement skill.

To get over the technical difficulty, an alternative great idea is employed using an interferometer.

2.2 Introducing an Interferometer: FT-IR

For IR measurements, a unique optics is introduced to realize the FT spectrometry preventing the ultrafast measurements. The optics is an *interferometer* represented by Michelson's one as illustrated in Fig. 2.2.

The interferometer consists of a beam splitter and two plane mirrors. The beam splitter allows a half of the light pass through it, and the rest half is reflected on the surface. One of the mirrors is placed at a fixed position with a distance of x_1 to the splitting point, whereas the other mirror is on a rail to change the distance, x_2, which is called the "moving mirror." The moving mirror is moved very smoothly with an electronically controlled highly constant velocity, v_m.

When the moving mirror is displaced from the initial position of $x_2 = x_1$ with the constant velocity of v_m, the position of the moving mirror, $x_2(t)$ is represented as

$$x_2(t) = x_1 + v_m t.$$

A parallel IR ray is led to the interferometer, a half of the light goes to the fixed mirror, and the reflected light is half reflected on the splitter to go as output. In a similar manner, the rest half is reflected to go to the moving mirror, and the reflected light goes through the splitter to go as output. As a result, the two lines of light are overlaid in the output path, which generates interference.

The superposition of the two electric field oscillation waves, $E(t)$, can simply be expressed by considering three facts. (1) the amplitudes, A, of the two waves are the same as each other, since the beam splitter splits the light for the transmission and the reflection half-and-half, (2) the angular frequency, ω, is common to the two waves, and (3) a round trip between the beam splitter and a mirror influences the phase change. The superposition is thus simply expressed by Eq. (2.3).

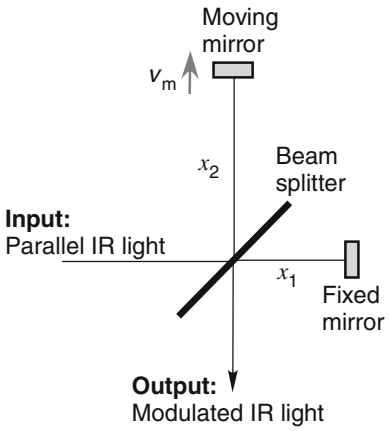

Fig. 2.2 A top-view schematic image of Michelson's interferometer

$$\begin{aligned} E(t) &= A\ \exp \mathrm{i}(2kx_1 - \omega t) + A\ \exp \mathrm{i}(2kx_2 - \omega t) \\ &= A[\exp \mathrm{i}(2kx_1 - \omega t) + \exp \mathrm{i}\{2k(x_1 + v_\mathrm{m} t) - \omega t\}] \\ &= A\{\exp \mathrm{i}(2kx_1 - \omega t)\}(1 + \exp \mathrm{i}2kv_\mathrm{m} t) \end{aligned} \tag{2.3}$$

The light "intensity" measured by the detector is the energy flow of the electromagnetic wave (Poynting vector in Sect. 3.3), which is proportional to the squared absolute value of the electric field. Therefore, the light intensity is calculated using Eq. (2.3) as:

$$\begin{aligned} |E|^2 &= E^* E = A^2(1 + \exp(-\mathrm{i}2kv_\mathrm{m} t))(1 + \exp \mathrm{i}2kv_\mathrm{m} t) \\ &= 2A^2(1 + \cos 2kv_\mathrm{m} t) \\ &= 2A^2(1 + \cos 2\pi f t) \end{aligned} \tag{2.4}$$

Here, the frequency, f, is obtained by considering $k = 2\pi/\lambda = 2\pi\tilde{\nu}$:

$$2\pi f = 2kv_\mathrm{m} \Leftrightarrow \boxed{f = 2\tilde{\nu} v_\mathrm{m}}. \tag{2.5}$$

This frequency is called "*modulation frequency*."

Here, $\tilde{\nu}$ is the wavenumber of the original IR light, which has a wide range from 400 to 4000 cm^{-1}. To consider the modulation frequency simpler, the wavenumber of He–Ne laser is conveniently used "as a constant" instead of using that of broadband IR. Since the wavelength of the laser is 632.816 nm in air, the wavenumber is calculated to be:

$$\tilde{\nu} = 1/\lambda = 15{,}802.4\,\mathrm{cm}^{-1}.$$

When the mirror velocity is $v_\mathrm{m} = 1.8984$ cm s^{-1}, for example, the modulation frequency is thus calculated to be $f = 60.0$ kHz. In other words, by introducing the wavenumber as a constant, *the mirror velocity can be interpreted to be the modulation frequency*. The scientific community of FT-IR has a tradition to write the modulation frequency instead of mirror velocity in a research paper.

When a wavenumber of IR light is put in Eq. (2.5), the modulation frequency becomes about 1 kHz, which is significantly smaller than the original IR frequency by about 1×10^{10} Hz. Therefore, the very fast oscillation of the electric field of IR light is invisible on the modulated IR light. Thanks to the low frequency of the modulated light, high-sensitive IR detectors are readily employed for FT-IR. Pyroelectric and semiconductor sensors are the representatives.

(1) Pyroelectric sensor

Deuterated triglycine sulfate (DTGS) has a character that the polarity on the surface changes on irradiation of IR light (or heat) via a molecular orientation change. Since the molecular orientation change happens in a millisecond range, a DTGS detector

responds to an electric oscillation at most a kHz order. The modulated IR light is quite suitable to employ the detector fortunately.

Since a thermal "variation" induces the surface charge, the background stable heat (ambient temperature) does not influence the output. Therefore, a DTGS detector works at an ambient temperature. This is a great benefit of using this detector. On the other hand, the sensitivity depends on the rate of molecular orientation change. In other words, the modulation frequency (or mirror velocity) is a dominant factor to influence the sensitivity. In general, a lower modulation frequency yields a high sensitivity, although the measurement time becomes longer. This technique is particularly useful to measure a very weakly absorbing sample. 5 kHz (i.e., $v_m = 0.15820$ cm s^{-1}) is a representative modulation frequency for high-sensitive measurements, although one scan needs a long time of about 4 s.

Since this detector is inferior to the MCT detector in sensitivity, DTGS is often selected for a bright (high throughput) measurement represented by reflection absorption (RA) and transmission spectrometries (Chap. 3).

(2) Semiconductor sensor

An alloy of mercury, cadmium, and telluride (MCT) works as a semiconductor sensor for IR light: an electron in the valence band is excited to be a free electron in the conduction band by absorbing the IR light. Since the ambient temperature contributes to the excitation, the detector must be cooled down to a working temperature using liquid nitrogen (LN_2). The container of LN_2 is covered by a Dewar bin, which must be vacuumed adequately; otherwise the duration time becomes very short.

An MCT detector has a wide frequency range, and the sensitivity does not respond to the modulation frequency significantly. The sensitivity is much higher than that of a DTGS one by one order of magnitude and it is thus suitable for detecting a low throughput measurement such as external reflection (ER) and attenuated total reflection (ATR) measurements (Chap. 3). Although MCT can also be used for RA and transmission measurements, a metal-mesh filter (light attenuator) must be placed in the light path to prevent the signal saturation of the detector.

Let us get back to Eq. (2.4). $A(\tilde{\nu})^2$ is the observed light intensity, and therefore it can be replaced by a spectral pattern, $S(\tilde{\nu})$. In addition, another replacement of $x \equiv 2v_m t$ is introduced, with which the time-domain measurements are converted to the measurements on the mirror position. Since the mirror position is precisely controlled electromecanically, the position is accurately read. In this manner, the following measurements at a wavenumber of $\tilde{\nu}$ are readily carried out.

$$A^2 \cos 2\pi 2\tilde{\nu} v_m t = S(\tilde{\nu}) \cos 2\pi \tilde{\nu} x$$

In practice, this measurement is performed for a broadband IR light, which results in $I(x)$ as:

$$I(x) \equiv \frac{2}{\pi} \int_0^\infty S(\tilde{\nu}) \cos 2\pi \tilde{\nu} x \, \mathrm{d}\tilde{\nu}. \tag{2.6}$$

An example of the observed *interferogram*, $I(x)$, is presented in Fig. 2.3. Note that the interferogram is the "raw experimental data" on FT-IR. Equation (2.6) has a formation of the even-function part of the Fourier transform, and thus $S(\tilde{\nu})$ is pulled out by performing the FT calculation as Eq. (2.7).

$$S(\tilde{\nu}) = 2 \int_0^\infty I(x) \cos 2\pi \tilde{\nu} x \, \mathrm{d}x \tag{2.7}$$

In this fashion, an ultrafast measurement in the time domain is readily avoided by introducing the interferometer. This technique is accomplished thanks to a good detector working in a low-frequency range, which fortunately corresponds to the modulation frequency.

This lucky holds for the mid- and near-IR regions. In other words, the FT technology employing the interferometer is not used for the UV-vis region. This is a reason why no FT-Vis is commercialized, which is another reason why no FT-Raman spectrometer with a visible excitation-laser is available.

2.3 Laser and FT Spectrometer

In an FT-IR spectrometer, a He–Ne laser optics is equipped as well as the IR optics: the laser-beam path is parallel to the IR path in the interferometer, and a laser detector is also available near the exit of the interferometer (Fig. 2.4). As described for the modulation frequency, a He–Ne laser is conveniently used to determine the frequency of the modulated IR light. To understand the necessity of the laser, the interrelationship between the time- and frequency-domain functions should be understood.

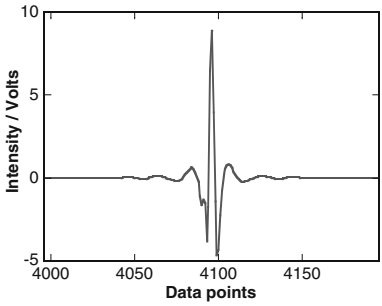

Fig. 2.3 An interferogram measured by FT-IR. This curve is subjected to the inverse FT calculation to obtain an IR spectrum

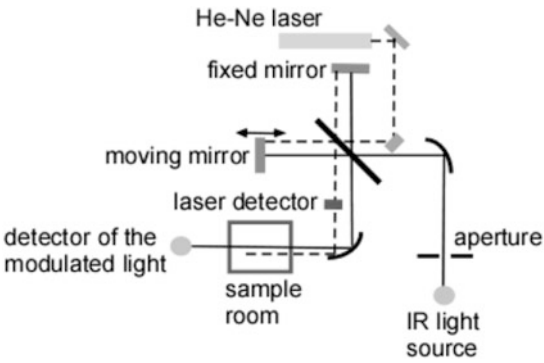

Fig. 2.4 A schematic view of the optics of IR (*solid line*) and laser (*dashed line*) light paths

(1) When $I(x)$ is the interferogram of IR broadband light:

The IR source emits broadband IR light that covers entire wavenumber range of mid-IR (4000–400 cm^{-1}). To make the discussion simpler, no intensity variation is assumed, and a simple boxcar function is considered.

The boxcar function, $S(\omega)$, illustrated in Fig. 2.5 is mathematically described as:

$$S(\omega) = \begin{cases} 1 & (0 \leq \omega \leq \omega_0) \\ 0 & (\omega < 0,\ \omega > \omega_0) \end{cases}$$

To apply this function to Eq. (2.6), the complex FT calculation is performed and the real part is extracted.

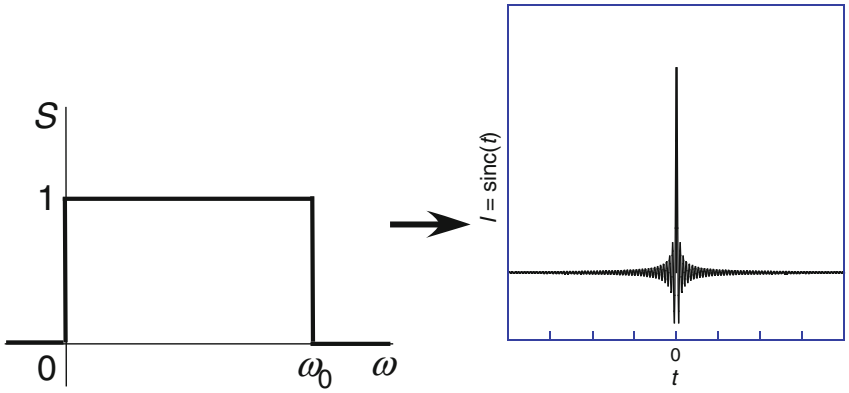

Fig. 2.5 Fourier transform of a box function to have an interferogram

$$\begin{aligned}\mathrm{Re}\left[\int_{-\infty}^{\infty} S(\omega)\mathrm{e}^{-\mathrm{i}\omega t}\mathrm{d}\omega\right] &= \mathrm{Re}\left[\int_{0}^{\omega_0} \mathrm{e}^{-\mathrm{i}\omega t}\mathrm{d}\omega\right] = \mathrm{Re}\left(\frac{\mathrm{i}}{t}\left[\mathrm{e}^{-\mathrm{i}\omega t}\right]_0^{\omega_0}\right) \\ &= \mathrm{Re}\left[\frac{\mathrm{i}}{t}\left(\mathrm{e}^{-\mathrm{i}\omega_0 t} - 1\right)\right] \\ &= \frac{\sin\omega_0 t}{t} = \omega_0 \,\mathrm{sinc}\ \omega_0 t\end{aligned} \tag{2.8}$$

This calculated result, which can be expressed using the "sinc" function (Eq. 2.8), is plotted in the right panel of Fig. 2.5. The sinc function provides a typical shape of a "wave packet," which has a center burst and decreasing envelopes for both sides. In this manner, the origin (center position) of the interferogram is accurately determined experimentally using the center burst after the measurements of the IR broadband light.

Note that even a simple calculation yields a fairly similar interferogram to the observed one presented in Fig. 2.3.

(2) When $I(x)$ is the interferogram of the He–Ne laser light:

On the contrary, what would happen, if the input light is given by a laser that has a single frequency? This case is expressed as: $S(\omega)$ has a needle-like peak at $\omega = \omega_0$ only. This situation is approximately theorized by using Dirac's delta function. On referring to a character of the Delta function (Eq. 4.9), the cosine function is obtained as the Fourier transform of Dirac's delta function (Eq. 2.9).

$$\mathrm{Re}\left[\int_{-\infty}^{\infty} \delta(\omega - \omega_0)\mathrm{e}^{-\mathrm{i}\omega t}\mathrm{d}\omega\right] = \mathrm{Re}\left(\mathrm{e}^{-\mathrm{i}\omega_0 t}\right) = \cos\omega_0 t \tag{2.9}$$

This means that the interferogram of a laser light becomes a cosine curve.

In short, when a laser light is input into the interferometer, a cosine-shaped wave is generated as the interferogram, as already shown by Eq. (2.4). This cosine shape can be used as graduation marks of the interferogram.

With the characteristics of (1) and (2), the origin and the graduation marks of the interferogram are both accurately determined by the simultaneous measurements of IR broadband light and a laser. Therefore, a laser light is a necessary item for FT-IR, and we need no calibration for the abscissa axis of the final output (cm^{-1}). This high accuracy of abscissa is a great benefit of using FT spectroscopy.

As shown in Fig. 2.4, the laser detector is placed near the exit of the interferometer "before" the sample room. In general, the laser detector allows a portion of the laser light pass through the laser detector, which attains the sample room. Since the IR light is invisible, this "leaked" red laser light is quite useful to consider the light path especially for optical alignment. Note that the laser light has already been detected, and the leaked red light can be interrupted by an opaque sample.

2.4 Apodization Function

The inverse FT calculation is, in theory, performed using Eq. (2.7). Here, we have to pay an attention to the integral range from 0 to $+\infty$. Since the integral is carried out in terms of x (mirror position), the integral range means that the moving mirror moves over an infinitely large distance. In practice, however, a long retardation (i.e., $x_2 - x_1$) is a technically difficult, and it is not necessary for a practical wavenumber resolution for a condensed matter. Although a single molecule in vacuum exhibits a very sharp absorption band, a condensed matter yields a relatively broad band due to the variety of molecular interactions. In practice, the resolution of 4 cm^{-1} is adequate, which needs a retardation of 0.25 cm (=1/4 cm^{-1}) in theory. In this manner, the moving mirror moves in a distance of ca. 5 mm, which is significantly smaller than the length theoretically expected. This discrepancy between the theory and the practical measurements is expressed using the truncation function, $D(x)$.

$$D(x) = \begin{cases} 1 & (0 \le x \le L) \\ 0 & (x > L) \end{cases} \quad \text{(a boxcar window)}$$

With this window function, the integral in a limited range up to L can be written as in the original form.

$$\begin{aligned} S_D(\tilde{\nu}) &= 2\int_0^L I(x)\cos 2\pi\tilde{\nu}x \, \mathrm{d}x \\ &= 2\int_0^\infty I(x)D(x)\cos 2\pi\tilde{\nu}x \, \mathrm{d}x \end{aligned} \tag{2.10}$$

In other words, the observed FT-IR spectrum, $S_D(\tilde{\nu})$, involving the truncation function is different from the ideal spectrum, $S(\tilde{\nu})$. Equation (2.10) has a form of *FT of a function product* of $I(x)$ and $D(x)$, which is a *convolution* (see Sect. 4.2) of $\mathscr{F}[I(x)]$ and $\mathscr{F}[D(x)]$ where '$\mathscr{F}$' is the Fourier transform operator.

$$\begin{aligned} \int_0^\infty I(x)D(x)\cos 2\pi\tilde{\nu}x \, \mathrm{d}x &\equiv \mathscr{F}[I(x)D(x)] \\ &= \mathscr{F}[I(x)] * \mathscr{F}[D(x)] \\ &= \frac{1}{2\pi}\int_{-\infty}^{\infty} \mathscr{F}[I(u)] \cdot \mathscr{F}[D(x-u)]\mathrm{d}u \end{aligned}$$

Here, * denotes the convolution.

As shown by Eq. (2.8) and Fig. 2.5, $\mathscr{F}[D(x)]$ (sometimes called "*instrumental line shape* (*ILS*) *function*") has a shape of the sinc function that has a many fringe-like tails on both sides of the main peak. Therefore, the fringes of the sinc function should influence the final spectrum, $S_D(\tilde{\nu})$.

To remove the fringes, the boxcar function, $D(x)$, is modified to have another window function, $A(x)$. By replacing $D(x)$ with $A(x)$, the fringe-like oscillations can largely be reduced, and this fringe-reduction effect is called "apodization," and therefore $A(x)$ is called an "apodization function." An apodization function has a side effect that the wavenumber resolution and intensity linearity are degraded [1]. The suppression of the oscillation and the degradation are trade-off with each other.

At any rate, the selection of an apodization function is necessary to use FT-IR. Many apodization functions have been proposed thus far. The representative functions are: triangular, trapezoidal, cosine and Happ–Genzel functions. For the detail, the reader is referred to the literature elsewhere [1]. Once an apodization function is selected, the user should not change the function for a series of measurements; otherwise the spectra lose consistency.

Reference

1. P.R. Griffiths, J.A. de Haseth, *Fourier Transform Infrared Spectroscopy*, 2nd edn. (Wiley, Hoboken, NJ, 2007)

Chapter 3
Surface Spectroscopy Using FT-IR

3.1 Fundamentals of Ordinate Scale of FT-IR Spectra

IR spectroscopy is one of the absorption spectroscopies, and the fundamentals of the quantitative ordinate scale are common to other absorption spectrometries such as UV–Vis. Since the measurements of IR spectra are mostly performed on FT-IR, we do not have to pay attention to a double beam spectrometry, and only the single-beam spectrometer is taken into account.

To obtain an absorption spectrum on FT-IR, two spectral measurements are needed: the sample and background measurements. As the simplest case, the sample is imagined as a thin film deposited on an IR-transparent substrate, and the background measurement needs the substrate only without a film. When a single-beam measurement is performed on FT-IR, a light *intensity* spectrum, $I(\tilde{\nu})$, as a function of wavenumber, $\tilde{\nu}$, is obtained, which is called "single-beam spectrum." The wavenumber is defined as $\tilde{\nu} \equiv 1/\lambda$ and it usually has a unit of cm^{-1}. Before treating a thin film sample, let us consider a bulk sample first to make the logic simpler as follows.

Figure 3.1 presents IR single-beam spectra of the sample ($I_{\mathrm{sample}}(\tilde{\nu})$) and background ($I_{\mathrm{BG}}(\tilde{\nu})$) measurements. The sample is a polystyrene film. The shape of $I_{\mathrm{BG}}(\tilde{\nu})$ is a results of the IR lamp function based on the black-body radiation, $\Phi(\tilde{\nu})$, and the apparatus function as a result of the optics after the IR light source as well as the detector function, $\Psi(\tilde{\nu})$.

$$I_{\mathrm{BG}}(\tilde{\nu}) = \Phi(\tilde{\nu})\Psi(\tilde{\nu})$$

In a similar manner, the shape of $I_{\mathrm{sample}}(\tilde{\nu})$ can be denoted as:

$$I_{\mathrm{sample}}(\tilde{\nu}) = \Phi(\tilde{\nu})\Psi(\tilde{\nu})T(\tilde{\nu}).$$

T. Hasegawa, *Quantitative Infrared Spectroscopy for Understanding of a Condensed Matter*, DOI 10.1007/978-4-431-56493-5_3

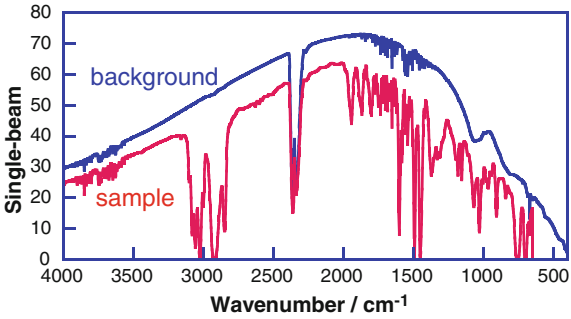

Fig. 3.1 Single-beam spectra of the air (*background*) and a polystyrene film (*sample*)

$T(\tilde{\nu})$ stands for the *transmittance* after the light absorption by the sample. This simple formulation is possible because the spectrometer is built on a single-beam optics, which requires no correction function as needed for a double beam spectrometer. Since the refractive index of polystyrene is different from that of air, the two single-beam spectra exhibit an apparent mismatch even for the no absorption regions. The transmittance is obtained by making the ratio of the two single-beam spectra:

$$T(\tilde{\nu}) = \frac{I_{\text{sample}}(\tilde{\nu})}{I_{\text{BG}}(\tilde{\nu})}.$$

$T(\tilde{\nu})$ is an exponential function of the light absorption (cf, Eq. 1.42), but it is defined by using a base of 10 due to a historical reason.

$$T(\tilde{\nu}) = 10^{-\varepsilon(\tilde{\nu})cd}$$

Here, c and d are the sample concentration and the optical path length, respectively, and $\varepsilon(\lambda)$ is the absorption spectrum at a virtual concentration of 1 mol dm^{-3}, which is understood as the molar extinction. In this manner, $T(\tilde{\nu})$ is not proportional to the concentration, which is inconvenient for a quantitative analysis.

To overcome this inconvenience, another definition of *absorbance*, $A(\tilde{\nu})$, is introduced.

$$A(\tilde{\nu}) \equiv -\log_{10} T(\tilde{\nu}) = \varepsilon(\tilde{\nu})cd \tag{3.1}$$

The equation is known as *Beer–Lambert's law*, which holds *only for* a *bulk sample*, as mentioned in Sect. 1.6. Equation (3.1) involves logarithm, and therefore absorbance has no unit (dimensionless), since a logarithm is defined as an integral of $\mathrm{d}x/x$ having no unit.

Figure 3.2 presents IR transmission and absorbance spectra of polystyrene calculated from the single-beam spectra in Fig. 3.1. These two spectra are two different representations of an identical spectrum. A straight line having no absorption

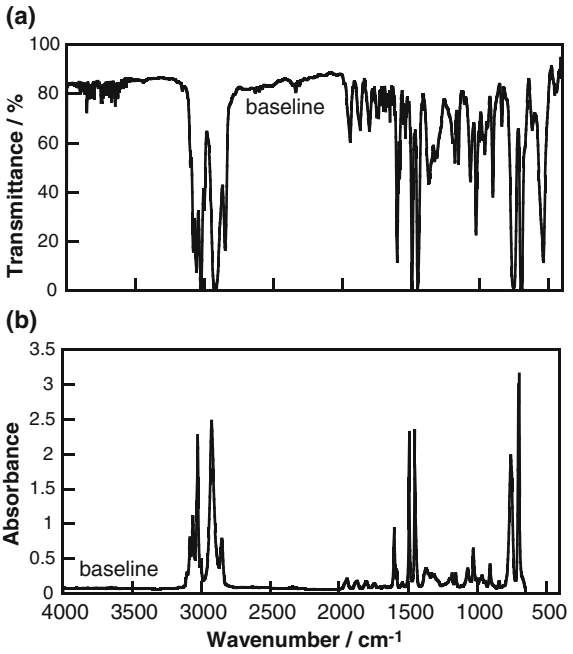

Fig. 3.2 IR spectrum of polystyrene in a representation of **a** transmittance and **b** absorbance, both of which are calculated from the single-beam spectra in Fig. 3.1

band is named the "baseline" of the spectrum. In principle, the baseline appears at the position of 1.0 (or 100%) for a transmission spectrum, and 0 for an absorbance spectrum. The actual shift of the baseline from the theoretical position is due the height mismatch of the single-beam spectra in Fig. 3.1.

Note that "band height" measured from the baseline has a chemical meaning only for an absorbance spectrum, since absorbance is obtained via logarithm. In other words, the band height of a transmittance spectrum from the baseline has no meaning directly, and it cannot be used for a quantitative discussion.

Since absorbance spectra are useful for a quantitative analysis, the reader may consider that transmittance spectra are no longer necessary. Absorbance spectra, however, have an intrinsic problem that they are not suitable for a strongly absorbing material that yields $T \approx 0$. This condition generates a quantitative problem because the logarithm of nil cannot be calculated in principle, which is found for some strong peaks in Fig. 3.2a.

One of the representative samples of a strongly absorbing material is an optical filter. Figure 3.3 presents UV–Vis spectra of an identical glass filter in the transmittance and absorbance representations. The transmittance spectrum apparently shows that this glass cut the wavelength region below 400 nm, which works as an optical filter. On the other hand, the absorbance spectrum gives an artifact due to the largely inaccurate calculation via $\log 0$.

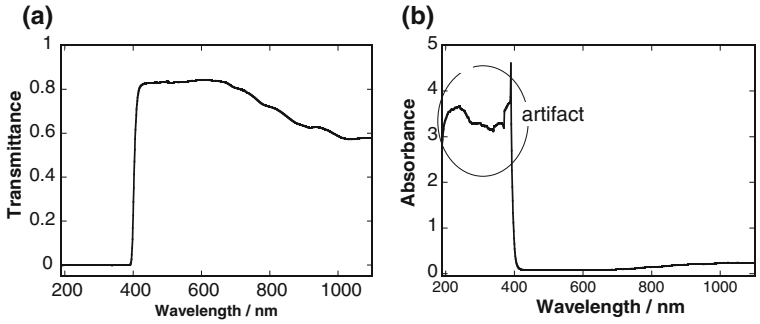

Fig. 3.3 **a** Transmittance and **b** absorbance UV–vis spectra of an identical glass filter

This is a reason why the transmittance representation is preferred by organic chemists, since a newly synthesized material may exhibit an unexpectedly strong absorption at an important peak.

Note that, however, the absorbance scale has, in general, a much better benefit that a relative band intensity ratio can be discussed. For a physicochemical or a quantitative analytical discussion, IR spectra should always be presented the in absorbance scale; otherwise the spectral shape would be influenced by the concentration. For obtaining a subtracted spectrum, the absorbance representation is also necessary.

3.2 Absorbance Spectra of a Weakly Absorbing Matter

The deduction process of Beer's law from Maxwell equations (Sect. 1.6) involves no optical interface. In fact, *Beer's law holds only for a bulk matter* thanks to a fact that the influence of the sample cell can be ignored within a good approximation. This *approximation is broken for thin film measurements on a substrate*, since an influence of the optical interface figures out significantly.

In this chapter, a "thin film" is defined as a film deposited on a substrate, and the film thickness, d, is adequately thinner than the wavelength of the IR light, i.e., $d\lambda/ \ll 1$ (*thin film approximation*). On this condition, the absorption of the thin film becomes very minor. For example, if the thin film is measured by using the transmission optical geometry, the single-beam intensity of the sample measurement, I_{sample}, is very close to that of the background one, I_{BG}:

$$I_{\text{sample}} = I_{\text{BG}} - \Delta I$$

where ΔI is a very minor difference. With the newly introduced parameter, the absorbance is calculated as:

$$A = -\log_{10}\frac{I_{\text{sample}}}{I_{\text{BG}}} = -\frac{1}{\ln 10}\ln\frac{I_{\text{BG}} - \Delta I}{I_{\text{BG}}} = -\frac{1}{\ln 10}\ln\left(1 - \frac{\Delta I}{I_{\text{BG}}}\right).$$

Since $\Delta I/I_{\text{BG}} \ll 1$ holds, the natural logarithm term can be expanded by using Taylor's expansion, so that ln is readily removed. As a result, a simple approximated equation of:

$$\boxed{A \approx \frac{1}{\ln 10}\frac{\Delta I}{I_{\text{BG}}}} = \frac{1}{\ln 10}\frac{I_{\text{BG}} - I_{\text{sample}}}{I_{\text{BG}}} = \frac{1}{\ln 10}\left(1 - \frac{I_{\text{sample}}}{I_{\text{BG}}}\right) \tag{3.2}$$

is obtained. In this manner, an *absorbance* spectrum of a thin film (or a weakly absorbing film) can readily be calculated by using $\Delta I/I_{\text{BG}}$ or making a simple ratio of $I_{\text{sample}}/I_{\text{BG}}$.

What we have to do next is the calculation of I_{sample} and I_{BG} on electrodynamics, in which an interface can explicitly be introduced. To incorporate an interface into a physical model, the continuous conditions of the electric and magnetic fields at an interface must be used, which are deduced from Maxwell equations.

3.3 Boundary Conditions in Electrodynamics

Figure 3.4 presents a schematic side view of an optical interface when the incidental light comes from the lower part of the x–z plane with an angle of incidence of θ_{i}. In optics, the angle of incidence is defined as the angle measured from the surface normal (z-axis). A, T, and R represent electric (or magnetic) field amplitudes of the incident, transmitted and reflected rays, respectively. p and s represent *p*- and *s-polarizations*, respectively. The definitions of p- and s-polarizations are that the amplitude vector is involved (**p**arallel) in the incidental plane and perpendicular (**s**enkrecht in German) to the plane, respectively.

As described in Appendix 7.2, an important conclusion is obtained at an interface from Maxwell equations:

$$\boldsymbol{n}_{12} \times (\boldsymbol{E}_2 - \boldsymbol{E}_1) = 0.$$

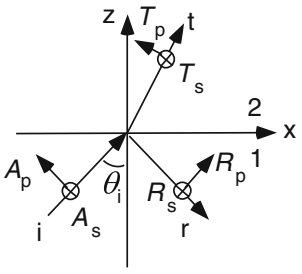

Fig. 3.4 A schematic optical interface

Here, $\boldsymbol{n}_{12}$ is the surface normal vector to the interface. Therefore, this means that the *tangential component of the electric field to the interface must be continuous* at a discontinuous boundary. Therefore, by referring to Fig. 3.4, the following equations hold.

$$E_x^{\mathrm{i}} + E_x^{\mathrm{r}} = E_x^{\mathrm{t}} \tag{3.3}$$

$$E_y^{\mathrm{i}} + E_y^{\mathrm{r}} = E_y^{\mathrm{t}} \tag{3.4}$$

$$H_x^{\mathrm{i}} + H_x^{\mathrm{r}} = H_x^{\mathrm{t}} \tag{3.5}$$

$$H_y^{\mathrm{i}} + H_y^{\mathrm{r}} = H_y^{\mathrm{t}} \tag{3.6}$$

Here, the subscripts, x and y, indicate the tangential components in the directions of x and y, respectively. In this manner, the superposition principle holds in an identical phase as well as the field continuity at the boundary.

Note that the tangential component of A_{p} is driven by the angle of $\pi/2 - \theta_{\mathrm{i}}$, i.e.,

$$A_{\mathrm{p}} \sin\left(\frac{\pi}{2} - \theta_{\mathrm{i}}\right) = A_{\mathrm{p}} \cos\theta_{\mathrm{i}}$$

Therefore, Eqs. (3.3) and (3.4) can be rewritten as:

$$\cos\theta_{\mathrm{i}}\left(A_{\mathrm{p}} - R_{\mathrm{p}}\right) = \cos\theta_{\mathrm{t}} T_{\mathrm{p}} \tag{3.7}$$

and

$$A_{\mathrm{s}} + R_{\mathrm{s}} = T_{\mathrm{s}}. \tag{3.8}$$

Besides, the wavenumber vector, $\boldsymbol{k}$, which has the traveling direction of light, is introduced.

$$\boldsymbol{k} = k\boldsymbol{a} = k\begin{pmatrix} \sin\theta_{\mathrm{i}} \\ 0 \\ \cos\theta_{\mathrm{i}} \end{pmatrix} \equiv k\begin{pmatrix} a_x \\ a_y \\ a_z \end{pmatrix}$$

Here, the scaler, k, is the amplitude of the wavenumber vector. With this definition, ∇ and $\partial/\partial t$ in Maxwell equations can be replaced by $\mathrm{i}k\boldsymbol{a}$ and $-\mathrm{i}\omega$, respectively, to have:

$$\begin{aligned} \boldsymbol{a} \times \boldsymbol{H} &= -\frac{\omega}{k}\boldsymbol{D} \Leftrightarrow \boldsymbol{H} \times \boldsymbol{a} = \frac{\omega}{k}\boldsymbol{D} \\ \boldsymbol{a} \times \boldsymbol{E} &= \frac{\omega}{k}\boldsymbol{B} \\ \boldsymbol{D} \cdot \boldsymbol{a} &= 0 \\ \boldsymbol{H} \cdot \boldsymbol{a} &= 0 \end{aligned} \tag{3.9}$$

Since the incidental plane is identical to the x–z plane, $a_y = 0$ holds irrespective of the polarization. By taking $\boldsymbol{B} = \mu_0 \mu_\mathrm{r} \boldsymbol{H}$ into account, Eq. (3.9) becomes:

$$\boldsymbol{a} \times \boldsymbol{E} = \frac{\omega}{k}\boldsymbol{B} = \frac{\omega}{k}\mu_0 \mu_\mathrm{r} \boldsymbol{H}.$$

This equation can further be rewritten by considering $k = n\omega/c$ (Eq. 1.34) and $c = 1/\sqrt{\varepsilon_0 \mu_0}$ as:

$$\boldsymbol{H} = \frac{\sqrt{\varepsilon_\mathrm{r}}}{Z_0}\boldsymbol{a} \times \boldsymbol{E}. \tag{3.10}$$

Here, $Z_0 \equiv \mu_0 / \varepsilon_0$. By taking this equation into account, Eqs. (3.5) and (3.6) can be rewritten as:

$$\sqrt{\varepsilon_{\mathrm{r},1}} \cos\theta_\mathrm{i}(A_\mathrm{s} - R_\mathrm{s}) = \sqrt{\varepsilon_{\mathrm{r},2}} \cos\theta_\mathrm{t} T_\mathrm{s} \tag{3.11}$$

and

$$\sqrt{\varepsilon_{\mathrm{r},1}}\left(A_\mathrm{p} + R_\mathrm{p}\right) = \sqrt{\varepsilon_{\mathrm{r},2}} T_\mathrm{p}. \tag{3.12}$$

Equations (3.7), (3.8), (3.11) and (3.12) yield the following four equations considering $n = \sqrt{\varepsilon_\mathrm{r}}$.

$$T_\mathrm{p} = \frac{2n_1 \cos\theta_\mathrm{i}}{n_2 \cos\theta_\mathrm{i} + n_1 \cos\theta_\mathrm{t}} A_\mathrm{p} \equiv t_\mathrm{p} A_\mathrm{p} \tag{3.13}$$

$$T_\mathrm{s} = \frac{2n_1 \cos\theta_\mathrm{i}}{n_1 \cos\theta_\mathrm{i} + n_2 \cos\theta_\mathrm{t}} A_\mathrm{s} \equiv t_\mathrm{s} A_\mathrm{s} \tag{3.14}$$

$$R_\mathrm{p} = \frac{n_2 \cos\theta_\mathrm{i} - n_1 \cos\theta_\mathrm{t}}{n_2 \cos\theta_\mathrm{i} + n_1 \cos\theta_\mathrm{t}} A_\mathrm{p} \equiv r_\mathrm{p} A_\mathrm{p} \tag{3.15}$$

$$R_\mathrm{s} = \frac{n_1 \cos\theta_\mathrm{i} - n_2 \cos\theta_\mathrm{t}}{n_1 \cos\theta_\mathrm{i} + n_2 \cos\theta_\mathrm{t}} A_\mathrm{s} \equiv r_\mathrm{s} A_\mathrm{s} \tag{3.16}$$

The coefficients of t and r are called *Fresnel's amplitude transmission* and *reflection coefficients*, respectively. In practice, the amplitude is not measured, but instead the energy flow of the light is measured by the detector of the spectrometer.

The energy flow is represented by Poynting's vector, $\boldsymbol{S}$, which is calculated by using Eq. (3.10) to be *proportional to squared electric field* as follows:

$$\begin{aligned}\boldsymbol{S} &= \boldsymbol{E} \times \boldsymbol{H} \\ &= \frac{\sqrt{\varepsilon_{\mathrm{r}}}}{Z_0}\boldsymbol{E} \times (\boldsymbol{a} \times \boldsymbol{E}) \\ &= \frac{\sqrt{\varepsilon_{\mathrm{r}}}}{Z_0}[(\boldsymbol{E} \cdot \boldsymbol{E})\boldsymbol{a} - (\boldsymbol{E} \cdot \boldsymbol{a})\boldsymbol{E}] \\ &= \frac{\sqrt{\varepsilon_{\mathrm{r}}}}{Z_0}E^2\boldsymbol{a}\end{aligned} \tag{3.17}$$

where the next mathematical formula is referred.

$$\boldsymbol{a} \times (\boldsymbol{b} \times \boldsymbol{c}) = (\boldsymbol{a} \cdot \boldsymbol{c})\boldsymbol{b} - (\boldsymbol{a} \cdot \boldsymbol{b})\boldsymbol{c}$$

If the time factor is involved in the equation to make the discussion more practical, $\boldsymbol{S}$ can be calculated as follows:

$$\begin{aligned}\boldsymbol{S} &= \boldsymbol{E} \times \boldsymbol{H} \\ &= \mathrm{Re}\left(\boldsymbol{E}\mathrm{e}^{\mathrm{i}\omega t}\right) \times \mathrm{Re}\left(\boldsymbol{H}\mathrm{e}^{\mathrm{i}\omega t}\right) \\ &= \frac{1}{2}\left(\boldsymbol{E}\mathrm{e}^{\mathrm{i}\omega t} + \boldsymbol{E}^*\mathrm{e}^{-\mathrm{i}\omega t}\right) \times \frac{1}{2}\left(\boldsymbol{H}\mathrm{e}^{\mathrm{i}\omega t} + \boldsymbol{H}^*\mathrm{e}^{-\mathrm{i}\omega t}\right) \\ &= \frac{1}{4}\left(\boldsymbol{E} \times \boldsymbol{H}^* + \boldsymbol{E}^* \times \boldsymbol{H} + \boldsymbol{E} \times \boldsymbol{H}\mathrm{e}^{\mathrm{i}2\omega t} + \boldsymbol{E}^* \times \boldsymbol{H}^*\mathrm{e}^{-\mathrm{i}2\omega t}\right) \\ &= \frac{1}{4}\left(\boldsymbol{E} \times \boldsymbol{H}^* + (\boldsymbol{E} \times \boldsymbol{H}^*)^* + \boldsymbol{E} \times \boldsymbol{H}\mathrm{e}^{\mathrm{i}2\omega t} + \left(\boldsymbol{E} \times \boldsymbol{H}\mathrm{e}^{\mathrm{i}2\omega t}\right)^*\right) \\ &= \frac{1}{2}\mathrm{Re}(\boldsymbol{E} \times \boldsymbol{H}^*) + \frac{1}{2}\mathrm{Re}\left(\boldsymbol{E} \times \boldsymbol{H}\mathrm{e}^{\mathrm{i}2\omega t}\right)\end{aligned} \tag{3.18}$$

Since the time average is known to be:

$$\langle \boldsymbol{S} \rangle = \frac{1}{T}\int_0^T \boldsymbol{S}(t)\mathrm{d}t,$$

the second term in the last line of Eq. (3.18) becomes nil on the time average. As a result, the next equation is obtained.

$$\langle \boldsymbol{S} \rangle = \frac{1}{2}\mathrm{Re}(\boldsymbol{E} \times \boldsymbol{H}^*) \tag{3.19}$$

This means that the time average of Poynting's vector is easily obtained by simply multiplying a factor of $1/2$.

If a unit area is imaginably set on the boundary through which the energy of J flows, the perpendicular component of $\boldsymbol{S}$ to the unit area is represented as:

Incidence flow: $J_j^{\mathrm{i}} = \left|\boldsymbol{S}_j^{\mathrm{i}}\right| \cos\theta_{\mathrm{i}}$ (j = p or s)

Reflected flow: $J_j^{\mathrm{r}} = \left|\boldsymbol{S}_j^{\mathrm{r}}\right| \cos\theta_{\mathrm{i}}$

Transmitted flow: $J_j^{\mathrm{t}} = \left|\boldsymbol{S}_j^{\mathrm{t}}\right| \cos\theta_{\mathrm{t}}$

With these equations, the *reflectivity*, $\mathcal{R}$, can easily be obtained:

$$\mathcal{R}_j \equiv \frac{J_j^{\mathrm{r}}}{J_j^{\mathrm{i}}} = \frac{\left|R_j\right|^2}{\left|A_j\right|^2} = \left|r_j\right|^2, \tag{3.20}$$

since $\sqrt{\varepsilon_{\mathrm{i}}} = \sqrt{\varepsilon_{\mathrm{r}}}$ and $\theta_{\mathrm{i}} = \theta_{\mathrm{r}}$ hold. In this manner, $\mathcal{R}$ can simply be obtained by calculating the absolute square of r. This works powerfully when a specular reflection spectrum is converted to a transmission spectrum (Sect. 6.1).

As an example, when the normal incidence ($\theta_{\mathrm{i}} = \theta_{\mathrm{r}} = \theta_{\mathrm{t}} = 0$) is considered, the following equation is deduced, which is common to both polarizations.

$$\mathcal{R} = |r|^2 = \left|\frac{n_2 - n_1}{n_2 + n_1}\right|^2 \tag{3.21}$$

If the incidence phase is air ($n_1 = 1.0$), the equation becomes further simpler.

$$\mathcal{R} = \left|\frac{n_2 - 1}{n_2 + 1}\right|^2 \tag{3.22}$$

This indicates that the reflectance becomes down to nil when the refractive index of the material (n_2) is close to 1.0. On the contrary, a high refractive index material exhibits a high reflectance. For example, an IR light is incident on a germanium (Ge; $n_2 = 4.0$) substrate normally, the reflectance increased up to 0.36. In other words, the transmittance through a Ge substrate is decreased down to 0.64 although Ge is transparent (nonabsorbing) to IR light.

On the other hand, the transmittance, $\mathcal{T}$, is obtained to be complicated, since the light goes in the two different phases across the boundary.

$$\mathcal{T}_j \equiv \frac{J_j^{\mathrm{t}}}{J_j^{\mathrm{i}}} = \frac{n_2}{n_1}\frac{\cos\theta_{\mathrm{t}}}{\cos\theta_{\mathrm{i}}}\frac{\left|T_j\right|^2}{\left|A_j\right|^2} = \frac{n_2}{n_1}\frac{\cos\theta_{\mathrm{t}}}{\cos\theta_{\mathrm{i}}}\left|t_j\right|^2 \tag{3.23}$$

3.4 A Model-Based Approach to Generate the TO Energy Loss Function

As an example study using the amplitude transmission/reflection coefficients, let us calculate an s-polarization reflection spectrum on a three-phase sample: air/thin film/dielectric substrate, which is most easy to deduce a mathematical expression of an absorbance spectrum. Let us put indices of 1, 2 and 3 for the air, film and substrate phases, respectively (Fig. 3.5). Here, the thickness of the first and third phases are both infinity, and that of the second phase is a thin thickness of d ($d/\lambda \ll 1$).

As found in many references, the multiple reflection model is conveniently employed in the thin film (Fig. 3.5a). Since the wavelength is much larger than the thickness, the reader may be concerned whether the multiple reflections occur in a very thin layer or not. Fortunately, however, this intuitively understandable model works properly limitedly when the light can be recognized to be a 'plane wave' [1, 2]. This can be proved by using a model-free theory, i.e., Abeles' transfer matrix method (Sect. 3.12).

When a light comes from the first phase of the three-phase system, the amplitude of the reflected light, r_{123}, is theorized by the summation of the reflected rays of the multiple reflections (Fig. 3.5a) using the amplitude transmittance and reflection coefficients at each interface considering the traveling direction of the light (Fig. 3.5b).

$$\begin{aligned} r_{123} &= r_{12} + t_{12}t_{21}r_{23}\exp(2\mathrm{i}\beta) + t_{12}t_{21}r_{23}r_{21}r_{23}\exp(4\mathrm{i}\beta) + \cdots \\ &= r_{12} + \frac{t_{12}t_{21}r_{23}\exp(2\mathrm{i}\beta)}{1 - r_{21}r_{23}\exp(2\mathrm{i}\beta)} \end{aligned} \tag{3.24}$$

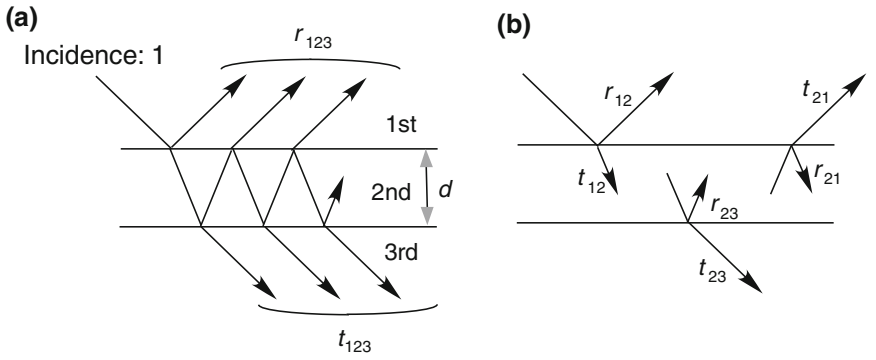

Fig. 3.5 Schematics of the three-phase system with a multiple reflection model (**a**). Each amplitude transmittance and reflection coefficient is defined in (**b**)

Here, β is the phase difference due to the path length in the second layer, which is expressed as:

$$\beta = \frac{2\pi d n_2 \cos\theta_2}{\lambda}.$$

$n_2 \equiv n_2' + \mathrm{i}n_2''$ is the complex refractive index of the second layer. θ_2 is the light direction measured from the interface normal.

When referring to Eqs. (3.13)–(3.16), in addition, the following relations are obtained.

$$\begin{aligned} r_{21} &= -r_{12} \\ t_{12} &= 1 + r_{12} \\ t_{21} &= 1 + r_{21} = 1 - r_{12} \end{aligned}$$

With these relations, Eq. (3.24) can be simplified as:

$$\begin{aligned} r_{123} &= \frac{r_{12} + \cancel{r_{12}^2 r_{23} \exp(2\mathrm{i}\beta)} + r_{23}\exp(2\mathrm{i}\beta) \cancel{- r_{12}^2 r_{23}\exp(2\mathrm{i}\beta)}}{1 + r_{12}r_{23}\exp(2\mathrm{i}\beta)} \\ &= \frac{r_{12} + r_{23}\exp(2\mathrm{i}\beta)}{1 + r_{12}r_{23}\exp(2\mathrm{i}\beta)} \end{aligned} \tag{3.25}$$

Here, the thin film approximation ($\beta \ll 1$) is employed to perform the Taylor expansion of the exponential function. As a result, the exponential part is removed to have a simple form:

$$r_{123} \approx \frac{r_{12} + r_{23}(1 + 2\mathrm{i}\beta)}{1 + r_{12}r_{23}(1 + 2\mathrm{i}\beta)}. \tag{3.26}$$

This coefficient enables us to calculate the "single-beam spectrum" of a single-sided film sample on a substrate. What we have to do next is, therefore, the calculation of the two-phase system without the film, r_{12}, which corresponds to the background single-beam spectrum. r_{12} can simply be obtained by putting $d = 0$ (i.e., $\beta = 0$) in Eq. (3.25).

$$r_{12} = \frac{r_{12} + r_{23}}{1 + r_{12}r_{23}} \equiv \frac{b}{1 + a} \quad \text{where } a \equiv r_{12}r_{23} \text{ and } b \equiv r_{12} + r_{23}$$

By using these new parameters, Eq. (3.26) is rewritten as:

$$r_{123} \approx \frac{b + 2\mathrm{i}r_{23}\beta}{(a+1) + 2\mathrm{i}a\beta} \cdot \frac{(a+1) - 2\mathrm{i}a\beta}{(a+1) - 2\mathrm{i}a\beta}$$
$$= \frac{b}{a+1}\left[1 + 2\mathrm{i}\beta\left(\frac{r_{23}}{b} - \frac{a}{a+1}\right)\right].$$

Therefore, the ratio of r_{123} to r_{12} is calculated to be:

$$\frac{r_{123}}{r_{12}} = 1 + 2\mathrm{i}\beta\left[\frac{r_{23}\left(r_{12}^2 - 1\right)}{(r_{12} + r_{23})(1 + r_{12}r_{23})}\right].$$

Thanks to the simple and useful relationship of Eq. (3.20), the observable is easily obtained as:

$$\frac{R_{\text{sample}}}{R_{\text{BG}}} = \left|\frac{r_{123}}{r_{12}}\right|^2. \tag{3.27}$$

Here, the very convenient weakly absorbing approximation (Eq. 3.2) is referred to have the next equation.

$$A = \frac{1}{\ln 10}\left(1 - \frac{R_{\text{sample}}}{R_{\text{BG}}}\right) \tag{3.28}$$

When Eq. (3.27) is put into Eq. (3.28), Eq. (3.16) is referred to take the polarization into account. Since the refractive index of the first layer (air) is real ($n'' = 0$; no absorption), the next equation is deduced.

$$\frac{r_{123}^{\text{s}}}{r_{13}^{\text{s}}} = 1 + \frac{4\pi\mathrm{i}dn_1\cos\theta_1}{\lambda}\left(\frac{n_2^2\cos^2\theta_2 - n_3^2\cos^2\theta_3}{n_1'^2\cos^2\theta_1 - n_3^2\cos^2\theta_3}\right)$$

Therefore, Eq. (3.27) is calculated by ignoring the β^2 terms:

$$\frac{R_{\text{sample}}^{\text{s}}}{R_{\text{BG}}^{\text{s}}} = \left|\frac{r_{123}^{\text{s}}}{r_{13}^{\text{s}}}\right|^2 = \left(\frac{r_{123}^{\text{s}}}{r_{13}^{\text{s}}}\right)^* \frac{r_{123}^{\text{s}}}{r_{13}^{\text{s}}}$$
$$\approx 1 - \frac{8\pi dn_1\cos\theta_1}{\lambda}\,\mathrm{Im}\left(\frac{n_2^2\cos^2\theta_2 - n_3^2\cos^2\theta_3}{\cos^2\theta_1 - n_3^2\cos^2\theta_3}\right). \tag{3.29}$$

Here, $n_1' = 1$ (air phase) is used. In addition, Snell's law [appearing later at Eq. (3.42)] is taken into account under an assumption of isotropic media, and the numerator of the fraction part can be simplified as:

$$
\begin{aligned}
&n_2^2\cos^2\theta_2 - n_3^2\cos^2\theta_3 \\
&= n_2^2\left(1-\sin^2\theta_2\right) - n_3^2\left(1-\sin^2\theta_3\right) \\
&= n_2^2 - n_3^2 \\
&= \varepsilon_2 - \varepsilon_3.
\end{aligned}
$$

In a similar manner, the denominator is also simplified. As a result, Eq. (3.29) can largely be simplified to be:

$$
\frac{R^{\mathrm{s}}_{\mathrm{sample}}}{R^{\mathrm{s}}_{\mathrm{BG}}} = 1 - \frac{8\pi d n_1 \cos\theta_1}{\lambda}\,\mathrm{Im}\left(\frac{\varepsilon_2-\varepsilon_3}{1-\varepsilon_3}\right). \tag{3.30}
$$

If the substrate does not absorb an IR ray ($\varepsilon_3 = \varepsilon_3' > 1$), the imaginary part of Eq. (3.30) can further be simplified as:

$$
\mathrm{Im}\left(\frac{\varepsilon_2-\varepsilon_3'}{1-\varepsilon_3'}\right) = \mathrm{Im}\left(\frac{\varepsilon_2'-\varepsilon_3'}{1-\varepsilon_3'} + \mathrm{i}\frac{\varepsilon_2''}{1-\varepsilon_3'}\right) = -\frac{1}{\varepsilon_3'-1}\,\mathrm{Im}(\varepsilon_2).
$$

As a result, we finally obtain the absorbance spectrum of the thin film sample by using Eqs. (3.2) and (3.28),

$$
\begin{aligned}
A^{\mathrm{s}}_{\mathrm{reflection}} &= \frac{1}{\ln 10}\left(1 - \frac{R^{\mathrm{s}}_{\mathrm{sample}}}{R^{\mathrm{s}}_{\mathrm{BG}}}\right) \\
&\boxed{= -\frac{1}{\ln 10}\,\frac{8\pi d n_1 \cos\theta_1}{\lambda\left(\varepsilon_3'-1\right)}\,\mathrm{Im}(\varepsilon_2)}
\end{aligned} \tag{3.31}
$$

This equation apparently implies that the s-polarized external reflection spectrum (Sect. 3.12) always exhibits 'negative absorbance' irrespective of the angle of incidence. Of another note is that the spectrum is governed by a function of $\mathrm{Im}(\varepsilon_2)$ that is specific to the thin film layer only. This imaginary part is called "TO energy loss function [3–6]." Although TO reminds us of the TO phonon, but the definition of the energy loss function is totally different from the TO phonon in the solid-state physics. In fact, "TO function" is used for a spectrum of an amorphous film. Details are found later below Eq. (3.68).

One of the great benefits of building an absorbance spectrum "on electrodynamics" is that the *spectrum shape is explicitly obtained*, and the *band intensity is quantitatively predicted*. Note that the theoretically predicted absorbance always agrees with the observed one very accurately.

This example study is performed on an explicit layer model with a multiple-reflection assumption, which is intuitively understandable. For a broader versatility, however, a model-free theorization is more preferred. A great theorization framework for the purpose is Abeles' transfer matrix method in Sect. 3.6.

3.5 Fresnel Equation and Optical Anisotropy

In the previous section, the electric permittivity is recognized to be a scalar (isotropic) to make the logic simpler. As shown later, however, the isotropic system has a big problem that the p-polarization light cannot be taken into account. To expand the concept of permittivity to both s- and p-polarizations, in this section, the permittivity is treated as a tensor.

Here, the light is conveniently considered to be a plane wave, which is a very good approximation, when the light source is very far from the interface. Since the particular solution involves a term of exp i($\boldsymbol{k} \cdot \boldsymbol{r} - \omega t$), the derivative operators in Maxwell equations are simplified as:

$$\begin{aligned} \boldsymbol{k} \cdot \boldsymbol{D} &= 0 \\ \boldsymbol{k} \cdot \boldsymbol{B} &= 0 \\ \boldsymbol{k} \times \boldsymbol{H} &= -\omega \boldsymbol{D} \\ \boldsymbol{k} \times \boldsymbol{E} &= \omega \boldsymbol{B} \end{aligned} \tag{3.32}$$

To take an optical anisotropy into account, the constituent (or material) equations are separately prepared as always.

$$\begin{aligned} \boldsymbol{D} &= \boldsymbol{\varepsilon} \boldsymbol{E} \\ \boldsymbol{B} &= \mu_0 \boldsymbol{H} \end{aligned}$$

Here, the electric permittivity ($\boldsymbol{\varepsilon} = \varepsilon_0 \boldsymbol{\varepsilon}_\mathrm{r}$) consists of a constant, ε_0, and the relative permittivity, $\boldsymbol{\varepsilon}_\mathrm{r}$, and a practically good approximation of $\mu_\mathrm{r} = 1$ is used. In this manner, the material response to the light is introduced. Of note is that the electric permittivity is not a molecular character, but a characteristic of a bulk matter. Electrodynamics thus enables us to consider the *light absorption by a bulk matter*.

If the coordinates are common to both laboratory and permittivity systems, i.e., the light comes parallel to the material axis, the permittivity tensor can largely be simplified as:

$$\boldsymbol{\varepsilon} = \begin{pmatrix} \varepsilon_x & 0 & 0 \\ 0 & \varepsilon_y & 0 \\ 0 & 0 & \varepsilon_z \end{pmatrix} = \varepsilon_0 \begin{pmatrix} \varepsilon_{\mathrm{r},x} & 0 & 0 \\ 0 & \varepsilon_{\mathrm{r},y} & 0 \\ 0 & 0 & \varepsilon_{\mathrm{r},z} \end{pmatrix} \equiv \varepsilon_0 \boldsymbol{\varepsilon}_\mathrm{r}.$$

If $\varepsilon_{\mathrm{r},x} = \varepsilon_{\mathrm{r},y} = \varepsilon_{\mathrm{r},z}$ holds, the system is called "isotropic," which corresponds to a system of randomly oriented molecules. If $\varepsilon_{\mathrm{r},x} = \varepsilon_{\mathrm{r},y} \neq \varepsilon_{\mathrm{r},z}$ or $\varepsilon_{\mathrm{r},x} \neq \varepsilon_{\mathrm{r},y} \neq \varepsilon_{\mathrm{r},z}$ holds, the system is called "anisotropic," and the former and latter correspond to the *uniaxial* and *biaxial* systems, respectively.

Here, let us simplify the theory using the uniaxial system with $\varepsilon_{\mathrm{r},x} = \varepsilon_{\mathrm{r},y}$. Uniaxial means that the orientation distribution is governed by only an angle about one axis (mostly z axis). When the axis of z is perpendicular to the interface, the axis corresponds to the optical axis (described at Fig. 3.6).

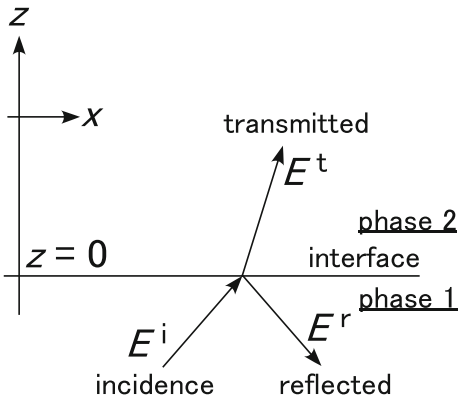

Fig. 3.6 Light reflection in the incidental plane (x–z) at an interface (x–y) whose optical axis is in the z direction

On the plane wave approximation, the electric and magnetic waves ($\boldsymbol{E}$ and $\boldsymbol{H}$, respectively) are expressed as follows.

$$\boldsymbol{E} = \boldsymbol{E}_0 \exp \mathrm{i}(\boldsymbol{k} \cdot \boldsymbol{r} - \omega t)$$
$$\boldsymbol{H} = \boldsymbol{H}_0 \exp \mathrm{i}(\boldsymbol{k} \cdot \boldsymbol{r} - \omega t)$$

Here, let us consider the **p-polarization**. Since the *incidental plane* of the p-polarization involves only x and z axes, the wavenumber vector, $\boldsymbol{k}$, is written as:

$$\boldsymbol{k} = \begin{pmatrix} k_x \\ 0 \\ k_z \end{pmatrix} = k \begin{pmatrix} a_x \\ 0 \\ a_z \end{pmatrix}, \tag{3.33}$$

where $a_x \equiv \sin\theta$ and $a_z \equiv \cos\theta$. Here, the scalar, k, is the length of $\boldsymbol{k}$.

Now, let us introduce a new index set of o and e, so that the calculation can comprehensively be visualized.

$$\boldsymbol{E} = \begin{pmatrix} E_x^{\mathrm{e}} \\ E_y^{\mathrm{o}} \\ E_z^{\mathrm{e}} \end{pmatrix} \quad \text{and} \quad \boldsymbol{H} = \begin{pmatrix} H_x^{\mathrm{o}} \\ H_y^{\mathrm{e}} \\ H_z^{\mathrm{o}} \end{pmatrix} \tag{3.34}$$

When Eq. (3.34) put into the fourth equation of Eq. (3.32), which is:

$$\boldsymbol{k} \times \boldsymbol{E} = \omega \boldsymbol{B} = \omega \mu_0 \boldsymbol{H}. \tag{3.35}$$

Then, the following relationship is obtained.

$$\begin{pmatrix} -k_z E_y^{\mathrm{o}} \\ k_z E_x^{\mathrm{e}} - k_x E_z^{\mathrm{e}} \\ k_x E_y^{\mathrm{o}} \end{pmatrix} = \omega \mu_0 \begin{pmatrix} H_x^{\mathrm{o}} \\ H_y^{\mathrm{e}} \\ H_z^{\mathrm{o}} \end{pmatrix} \tag{3.36}$$

This equation should be noted that each row is categorized into o or e. In a similar manner, Eq. (3.34) is put in the next equation:

$$\boldsymbol{k} \times \boldsymbol{H} = -\omega \boldsymbol{D} = -\omega \varepsilon_0 \boldsymbol{\varepsilon}_\mathrm{r} \boldsymbol{E},$$

then, Eq. (3.37) is obtained.

$$\begin{pmatrix} -k_z H_y^\mathrm{e} \\ k_z H_x^\mathrm{o} - k_x H_z^\mathrm{o} \\ k_x H_y^\mathrm{e} \end{pmatrix} = -\omega \varepsilon_0 \boldsymbol{\varepsilon}_\mathrm{r} \begin{pmatrix} E_x^\mathrm{e} \\ E_y^\mathrm{o} \\ E_z^\mathrm{e} \end{pmatrix} = -\omega \varepsilon_0 \begin{pmatrix} \varepsilon_{\mathrm{r},x} E_x^\mathrm{e} \\ \varepsilon_{\mathrm{r},y} E_y^\mathrm{o} \\ \varepsilon_{\mathrm{r},z} E_z^\mathrm{e} \end{pmatrix} \tag{3.37}$$

This equation also has a character that each row is driven by either o or e. In other words, o and e are separated readily. With this character, Eqs. (3.36) and (3.37) can be merged in terms of "o," by putting the first and third equations of Eq. (3.36) in the second equation of Eq. (3.37) by referring Eq. (3.33).

$$\begin{aligned} &-\frac{k_z^2}{\omega \mu_0} E_y^\mathrm{o} - \frac{k_x^2}{\omega \mu_0} E_y^\mathrm{o} = -\omega \varepsilon_0 \varepsilon_{\mathrm{r},x} E_y^\mathrm{o} \\ &\Leftrightarrow k_z^2 + k_x^2 = \omega^2 \mu_0 \varepsilon_0 \varepsilon_{\mathrm{r},x} \\ &\Leftrightarrow k^2 = \frac{\omega^2}{c^2} \varepsilon_{\mathrm{r},x} \end{aligned}$$

This straightforwardly indicates that the light indexed with "o" depends only on the permittivity of $\varepsilon_{\mathrm{r},x}$, which is *independent of the traveling direction*. This light is called "*ordinary light*," which is applicable for isotropic materials.

When Eqs. (3.36) and (3.37) are merged in terms of "e," in a similar manner, on the other hand, two equations are generated as follows.

$$\begin{pmatrix} -k_z^2 E_x^\mathrm{e} + k_x k_z E_z^\mathrm{e} \\ k_x k_z E_x^\mathrm{e} - k_x^2 E_z^\mathrm{e} \end{pmatrix} = -\frac{\omega^2}{c^2} \begin{pmatrix} \varepsilon_{\mathrm{r},x} E_x^\mathrm{e} \\ \varepsilon_{\mathrm{r},z} E_z^\mathrm{e} \end{pmatrix} \tag{3.38}$$

Here, a new parameter, $\bar{\varepsilon}$, is introduced.

$$\boxed{\bar{\varepsilon} \equiv \frac{c^2 k^2}{\omega^2}} \quad \text{or} \quad \bar{n} \equiv \frac{ck}{\omega} \tag{3.39}$$

Then, Eq. (3.38) can be organized to be:

$$\begin{pmatrix} -\bar{\varepsilon} a_z^2 + \varepsilon_x^\mathrm{r} & a_x a_z \bar{\varepsilon} \\ a_x a_z \bar{\varepsilon} & -\bar{\varepsilon} a_x^2 + \varepsilon_z^\mathrm{r} \end{pmatrix} \begin{pmatrix} \varepsilon_{\mathrm{r},x} E_x^\mathrm{e} \\ \varepsilon_{\mathrm{r},z} E_z^\mathrm{e} \end{pmatrix} = 0,$$

when considering $k_x / k = a_x$ and $k_z / k_z = a_z$ ($\because k^2 = k_z^2 + k_x^2$). To make this equation have a nontrivial solution for E_x^e and E_z^e, the next relationship must be held.

$$-\bar{\varepsilon}\left(\varepsilon_{\mathrm{r},z}a_z^2+\varepsilon_{\mathrm{r},x}a_x^2\right)+\varepsilon_{\mathrm{r},x}\varepsilon_z^{\mathrm{r}}=0$$
$$\boxed{\Leftrightarrow \frac{1}{\bar{\varepsilon}}=\frac{a_x^2}{\varepsilon_{\mathrm{r},z}}+\frac{a_z^2}{\varepsilon_{\mathrm{r},x}}} \tag{3.40}$$

Equation (3.40) is called *Fresnel's equation* [4, 7]. For the s-polarization case, a very similar result is obtained, but the result is for an isotropic one. Equation (3.40) apparently implies that the material constant (permittivity; $\bar{\varepsilon}$) *depends on the traveling direction* (a_x and a_z). This light indexed by "e" is called "*extraordinary light*." If $\varepsilon_{\mathrm{r},x}=\varepsilon_{\mathrm{r},z}$ is put in Eq. (3.40), $\bar{\varepsilon}=\varepsilon_{\mathrm{r},x}=\varepsilon_{\mathrm{r},z}$ is obtained, which means that Eq. (3.40) is a general equation that can involve the ordinary light. This further means that the ordinary light corresponds to the s-polarization.

In other words, if light is incident into an anisotropic medium, the light is split into two paths, i.e., the ordinary and extraordinary light paths. Regardless, there is a specific angle exhibiting no light splitting. The direction along this specific angle is called "*optical axis*." For a thin film with the uniaxial molecular orientation, the optical axis is mostly parallel to the z axis, which makes the theory very simple.

Now, let us consider a light reflection within the incidental plane at an interface having the optical axis parallel to the z axis (Fig. 3.6).

As found in Sect. 3.3, the tangential component of the electric field to the boundary is continuous at an optical interface. Since ωt is a common part in the phase part of the plane wave functions, the rest part must be continuous at the interface [1].

$$\left(\boldsymbol{k}^{\mathrm{i}}\cdot\boldsymbol{r}\right)_{z=0}=\left(\boldsymbol{k}^{\mathrm{r}}\cdot\boldsymbol{r}\right)_{z=0}=\left(\boldsymbol{k}^{\mathrm{t}}\cdot\boldsymbol{r}\right)_{z=0}$$

When Eq. (3.33) and $\boldsymbol{r}=(x,0,z)_{z=0}$ are taken into account, another form is available:

$$\begin{aligned} k_x^{\mathrm{i}}&=k_x^{\mathrm{r}}=k_x^{\mathrm{t}}\\ k_z^{\mathrm{i}}&=-k_z^{\mathrm{r}}. \end{aligned} \tag{3.41}$$

When Eq. (3.39) is taken into account, the next equation is obtained:

$$\begin{aligned} k_x^{\mathrm{i}}&=k_x^{\mathrm{r}}\\ &\Leftrightarrow \frac{\bar{n}_1\omega}{c}a_x^{\mathrm{i}}=\frac{\bar{n}_1\omega}{c}a_x^{\mathrm{r}}\\ &\Leftrightarrow \sin\theta^{\mathrm{i}}=\sin\theta^{\mathrm{r}}\\ &\Leftrightarrow \theta^{\mathrm{i}}=\theta^{\mathrm{r}}, \end{aligned}$$

which means that the *reflection angle* is equal to the angle of incidence no matter what material is chosen for the interface. In a similar manner,

$$\begin{aligned} & k_x^{\mathrm{i}} = k_x^{\mathrm{t}} \\ \Leftrightarrow & \frac{\bar{n}_1 \omega}{c} a_x^{\mathrm{i}} = \frac{\bar{n}_2 \omega}{c} a_x^{\mathrm{t}} \\ \Leftrightarrow & \boxed{\bar{n}_1 \sin\theta^{\mathrm{i}} = \bar{n}_2 \sin\theta^{\mathrm{t}}} \end{aligned} \tag{3.42}$$

is obtained in terms of *refraction*. The last line is called *Snell's law*. Snell's equation is often used for an isotropic system, but Eq. (3.42) is the general formula using $\bar{n}_j$. If an absorbing material is chosen, the refractive index becomes a complex and the refraction angle would also become a complex, which is different from the observed refraction angle. Therefore, the representation of $k_x^{\mathrm{i}} = k_x^{\mathrm{t}}$ is better than Snell's law to generally express the refraction phenomenon.

Now, let us consider the **p-polarization**, whose electric field is within the x–z plane (incidental plane), i.e, the magnetic field is exactly parallel to the y-axis. To consider the field continuity, therefore the magnetic field, $\boldsymbol{H}$, is more convenient to be theorized in this case.

As found in Eq. (3.35), $\boldsymbol{H} \times \boldsymbol{k} = \omega \boldsymbol{D}$ is employed to have [8]:

$$\begin{aligned} & \begin{pmatrix} 0 \\ H_y \\ 0 \end{pmatrix} \times k \begin{pmatrix} a_x \\ 0 \\ a_z \end{pmatrix} = \omega \begin{pmatrix} \varepsilon_x E_x \\ \varepsilon_y E_y \\ \varepsilon_z E_z \end{pmatrix} \\ \Leftrightarrow & H_y \frac{k}{\omega} \begin{pmatrix} a_z \\ 0 \\ -a_x \end{pmatrix} = \begin{pmatrix} \varepsilon_x E_x \\ \varepsilon_y E_y \\ \varepsilon_z E_z. \end{pmatrix}. \end{aligned}$$

This can be rewritten in terms of the electric field as:

$$\boldsymbol{E} = H_y \frac{k}{\omega} \begin{pmatrix} \varepsilon_x^{-1} a_z \\ 0 \\ -\varepsilon_z^{-1} a_x \end{pmatrix}. \tag{3.43}$$

Since Eq. (3.39) can be rewritten as:

$$\frac{k}{\omega} = \frac{\sqrt{\bar{\varepsilon}}}{c} = \frac{\bar{n}}{c},$$

then Eq. (3.43) can be another form as:

$$\boldsymbol{E} = H_y \frac{\bar{n}}{c} \begin{pmatrix} \varepsilon_x^{-1} a_z \\ 0 \\ -\varepsilon_z^{-1} a_x \end{pmatrix}.$$

Then, the tangential component of the electric field, E_x, of the p-polarization is correlated with H_y as:

$$\boxed{E_x = \frac{\bar{n} a_z}{c\varepsilon_x} H_y.} \tag{3.44}$$

In the same manner, the tangential component of the magnetic field, H_x, for the s-polarization is correlated with E_y, since the electric field of the **s-polarization** is perpendicular to that of the p-polarization, and it obeys the isotropic system, i.e., $\bar{n} = n_x$. (In other words, the s-polarization is *not* interacted with n_z.)

$$\boxed{H_x = -\frac{n_x a_z}{c\mu_0} E_y} \tag{3.45}$$

3.6 Transfer Matrix Method

The multiple-reflection model used in Sect. 3.4 is intuitively quite understandable. Nevertheless, no one knows whether multiple reflections occur or not in a very thin film for a long-wavelength light such as IR light, whose wavelength is much larger than the film thickness. To calculate the transmittance and reflectance at an interface *without using an intuitive model*, Abeles' transfer matrix method works powerfully [4, 5, 7, 8]. This general method is free from an intuitive model, and instead only the continuities of the electric and magnetic fields are sophisticatedly theorized. Here, a generalized theoretical framework of electrodynamics for calculating transmittance and reflectance at an interface is described.

Abeles' method is significant that no physical model is needed, and instead, only the electric field parameters at each interface are prepared as presented in Fig. 3.7, which can be employed for any stratified layers.

Light goes across obliquely at the interface indexed with j, which accompanies the electric field of E_j^{i}. Some of the incident light is reflected and the rest transmits the interface accompanying E_j^{r} and E_j^{t}, respectively. Of note is that the E_j^{t} is influenced by another reflected light coming from the interface indexed with $j + 1$ via E_j^{rb}. In this manner, in this theoretical framework, only the electric field components of E_j^{i}, $E_j^{\mathrm{r}}, E_j^{\mathrm{t}}$ and E_j^{rb} at an interface are simply correlated with each other by

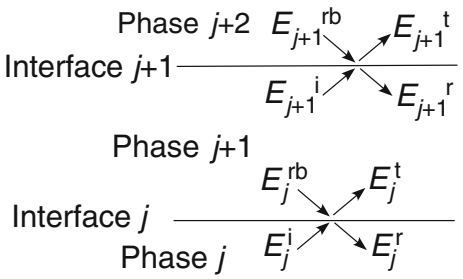

Fig. 3.7 Definitions of electric field parameters at an interface in stratified layers. The *arrow* indicates the light propagation direction. The light goes upward across the interfaces

using the continuous condition. In other words, *we don't have to be care of a multiple-reflection in the film* [8].

$$\begin{aligned} E_j^{\mathrm{i}} + E_j^{\mathrm{r}} &= E_j^{\mathrm{t}} + E_j^{\mathrm{rb}} \\ H_j^{\mathrm{i}} + H_j^{\mathrm{r}} &= H_j^{\mathrm{t}} + H_j^{\mathrm{rb}} \end{aligned} \tag{3.46}$$

Here, the phase number index of j is added to $\bar{n}a_z/c\varepsilon_x$ found in Eq. (3.44) (**p-polarization**), which is defined in m_j:

$$\boxed{m_j \equiv \frac{\bar{n}_j a_{z,j}}{c\varepsilon_{x,j}}} \tag{3.47}$$

When the second equation of Eq. (3.41) (reflection law) is taken into account, the four electric field components are written with the use of this new parameter as:

$$\begin{aligned} E_j^{\mathrm{i}} &= m_j H_j^{\mathrm{i}} \\ E_j^{\mathrm{r}} &= -m_j H_j^{\mathrm{r}} \\ E_j^{\mathrm{t}} &= m_{j+1} H_j^{\mathrm{t}} \\ E_j^{\mathrm{rb}} &= -m_{j+1} H_j^{\mathrm{rb}} \end{aligned}$$

Note that the t and rb components are influenced by the $j + 1^{\mathrm{th}}$ phase. When these components are put in Eq. (3.46), the following equation holds.

$$\boldsymbol{Q}_j \boldsymbol{N}_j = \boldsymbol{Q}_{j+1} \boldsymbol{F}_j$$

where

$$\boldsymbol{Q}_j \equiv \begin{pmatrix} m_j & -m_j \\ 1 & 1 \end{pmatrix}, \quad \boldsymbol{N}_j \equiv \begin{pmatrix} H_j^{\mathrm{i}} \\ H_j^{\mathrm{r}} \end{pmatrix} \quad \text{and} \quad \boldsymbol{F}_j \equiv \begin{pmatrix} H_j^{\mathrm{t}} \\ H_j^{\mathrm{rb}} \end{pmatrix}. \tag{3.48}$$

At the moment, nothing is taken care for the phase retardation when the components go across a phase *with a thickness*. When a component travels from the j^{th} interface to the $j + 1^{\mathrm{th}}$ interface, the retardation of $\delta_j \equiv k_{z,j} d_j$ must be taken into account such as:

$$\begin{aligned} H_j^{\mathrm{t}} \exp\left(\mathrm{i}\delta_{j+1}\right) &= H_{j+1}^{\mathrm{i}} \\ H_{j+1}^{\mathrm{r}} \exp\left(\mathrm{i}\delta_{j+1}\right) &= H_j^{\mathrm{rb}}. \end{aligned} \tag{3.49}$$

Since only the surface tangential component is considered for the continuity at the interface, only the surface-perpendicular (z) component of the wavenumber vector, $k_{z,j}$, is necessary.

Equation (3.49) can simply be represented by using a matrix of:

$$\boldsymbol{P}_j \equiv \begin{pmatrix} \exp(\mathrm{i}\delta_j) & 0 \\ 0 & \exp(-\mathrm{i}\delta_j) \end{pmatrix} \tag{3.50}$$

to be:

$$\boldsymbol{N}_{j+1} = \boldsymbol{P}_{j+1}\boldsymbol{F}_j$$

With this equation, all the representation of the field continuity and the phase retardation are summarized as:

$$\boxed{\begin{matrix} \boldsymbol{Q}_j\boldsymbol{N}_j = \boldsymbol{Q}_{j+1}\boldsymbol{F}_j \\ \boldsymbol{N}_{j+1} = \boldsymbol{P}_{j+1}\boldsymbol{F}_j \end{matrix}}. \tag{3.51}$$

This equation set is the fundamental of the thin-film optics, which is called "*transfer matrix method*." With this set, the magnetic fields at the first and last interfaces are directly interrelated with each other.

For example, when $j = 1$ is put in the equation set, we have:

$$\begin{aligned} \boldsymbol{Q}_1\boldsymbol{N}_1 = \boldsymbol{Q}_2\boldsymbol{F}_1 &\Leftrightarrow \boldsymbol{N}_1 = \boldsymbol{Q}_1^{-1}\boldsymbol{Q}_2\boldsymbol{F}_1 \\ \boldsymbol{N}_2 = \boldsymbol{P}_2\boldsymbol{F}_1 &\Leftrightarrow \boldsymbol{F}_1 = \boldsymbol{P}_2^{-1}\boldsymbol{N}_2 \end{aligned}$$

The two equations are merged to hide $\boldsymbol{F}_1$ resulting in:

$$\boldsymbol{N}_1 = \boldsymbol{Q}_1^{-1}\boldsymbol{Q}_2\boldsymbol{P}_2^{-1}\boldsymbol{N}_2 \tag{3.52}$$

When $j = 2$ is put in the first equation of Eq. (3.51), we have:

$$\boldsymbol{Q}_2\boldsymbol{N}_2 = \boldsymbol{Q}_3\boldsymbol{F}_2 \Leftrightarrow \boldsymbol{N}_2 = \boldsymbol{Q}_2^{-1}\boldsymbol{Q}_3\boldsymbol{F}_2,$$

which can further be put into Eq. (3.52) to hide $\boldsymbol{N}_2$ resulting in:

$$\boldsymbol{N}_1 = \boldsymbol{Q}_1^{-1}\boldsymbol{Q}_2\boldsymbol{P}_2^{-1}\boldsymbol{Q}_2^{-1}\boldsymbol{Q}_3\boldsymbol{F}_2. \tag{3.53}$$

Here, note that $H_2^{\mathrm{rb}} = 0$, since the interface of $j = 2$ is the last boundary to receive no back reflection. Therefore, we have the vector set as:

$$\boldsymbol{N}_1 = \begin{pmatrix} H_1^{\mathrm{i}} \\ H_1^{\mathrm{r}} \end{pmatrix} \quad \text{and} \quad \boldsymbol{F}_2 = \begin{pmatrix} H_2^{\mathrm{t}} \\ 0 \end{pmatrix}.$$

In this manner, the magnetic fields at the first and second interfaces are directly connected.

If we consider a double-sided thin film sample such as a Langmuir–Blodgett (LB) film in a five-phase system of air/film/substrate/film/air, in a similar manner, the next equation is built.

$$\boldsymbol{N}_1 = \boldsymbol{Q}_1^{-1}\boldsymbol{Q}_2\boldsymbol{P}_2^{-1}\boldsymbol{Q}_2^{-1}\boldsymbol{Q}_3\boldsymbol{P}_3^{-1}\boldsymbol{Q}_3^{-1}\boldsymbol{Q}_2\boldsymbol{P}_2^{-1}\boldsymbol{Q}_2^{-1}\boldsymbol{Q}_1\boldsymbol{F}_4 \tag{3.54}$$

This equation accompanies the two vectors:

$$\boldsymbol{N}_1 = \begin{pmatrix} H_1^{\mathrm{i}} \\ H_1^{\mathrm{r}} \end{pmatrix} \quad \text{and} \quad \boldsymbol{F}_4 = \begin{pmatrix} H_4^{\mathrm{t}} \\ 0 \end{pmatrix}. \tag{3.55}$$

Here, $H_1^{\mathrm{i}}, H_1^{\mathrm{r}}$ and H_4^{t} are magnetic fields of incident, reflected and transmitted light, respectively. Since Eq. (3.17) can be rewritten by using the magnetic field, the light intensity is calculated by using the magnetic fields. For our purposes, the absolute intensity is not needed, and thus the light intensity is calculated via a normalization by H_1^{i}, as shown later at Eq. (3.61).

3.7 Calculation of Single-Beam Spectra of the Background and the Sample Measurements

In the previous section, the fundamental for calculating the magnetic field intensities is presented. In the present section, the same procedure is employed for calculating the background and sample single-beam spectra.

Let us calculate the "sample" spectrum first, since the result would soon be applied to the calculation of the background spectrum. If the double-sided thin film sample consists of the optical phases of air/thin film/substrate/thin film/air, the 5-phase system must be taken into account.

Since $\boldsymbol{Q}_i^{-1}\boldsymbol{Q}_j$ repeatedly appears in Eq. (3.54), this term is calculated first by using Eq. (3.48).

$$\begin{aligned} \boldsymbol{Q}_i^{-1}\boldsymbol{Q}_j &= \frac{1}{2m_i}\begin{pmatrix} 1 & m_i \\ -1 & m_i \end{pmatrix}\begin{pmatrix} m_j & -m_j \\ 1 & 1 \end{pmatrix} \\ &= \frac{1}{2m_i}\begin{pmatrix} m_i + m_j & m_i - m_j \\ m_i - m_j & m_i + m_j \end{pmatrix} \\ &= t_{ij}^{-1}\begin{pmatrix} 1 & r_{ij} \\ r_{ij} & 1 \end{pmatrix} \end{aligned} \tag{3.56}$$

Here, the phases indexed by i and j are adjacent to each other, and the next new definitions are used.

$$\begin{aligned} t_{ij} &\equiv \frac{2m_i}{m_i + m_j} \\ r_{ij} &\equiv \frac{m_i - m_j}{m_i + m_j} \end{aligned} \tag{3.57}$$

In a similar manner, the inversed matrix of $\boldsymbol{P}_j$ is also calculated in advance.

$$\boldsymbol{P}_j^{-1} = \begin{pmatrix} \exp(-\mathrm{i}\delta_j) & 0 \\ 0 & \exp(\mathrm{i}\delta_j) \end{pmatrix} \tag{3.58}$$

Although the 3-phase system is easily calculated, the 5-phase system needs a technical modification as follows:

$$\begin{aligned} \boldsymbol{N}_1 &= \boldsymbol{Q}_1^{-1}\boldsymbol{Q}_2\boldsymbol{P}_2^{-1}\boldsymbol{Q}_2^{-1}\boldsymbol{Q}_3\boldsymbol{P}_3^{-1}\boldsymbol{Q}_3^{-1}\boldsymbol{Q}_2\boldsymbol{P}_2^{-1}\boldsymbol{Q}_2^{-1}\boldsymbol{Q}_1\boldsymbol{F}_4 \\ &= \varphi_{\mathrm{A}}\boldsymbol{P}_3^{-1}\varphi_{\mathrm{B}}\boldsymbol{F}_4, \end{aligned} \tag{3.59}$$

where

$$\begin{aligned} \varphi_{\mathrm{A}} &= \boldsymbol{Q}_1^{-1}\boldsymbol{Q}_2\boldsymbol{P}_2^{-1}\boldsymbol{Q}_2^{-1}\boldsymbol{Q}_3 \\ \varphi_{\mathrm{B}} &= \boldsymbol{Q}_3^{-1}\boldsymbol{Q}_2\boldsymbol{P}_2^{-1}\boldsymbol{Q}_2^{-1}\boldsymbol{Q}_1 \end{aligned}$$

Each of which can easily be calculated to have:

$$\begin{aligned} \varphi_{\mathrm{A}} &= t_{13}^{-1}\begin{pmatrix} 1 & -r_{31} \\ r_{13} & R \end{pmatrix} \\ \varphi_{\mathrm{B}} &= t_{13}^{-1}\begin{pmatrix} 1 & -r_{13} \\ r_{31} & R \end{pmatrix} \end{aligned}$$

These newly introduced parameters have a character that several amplitude transmittance and reflection coefficients on 'un-neighboring phases' are involved. Each of which has an explicit form as follows:

$$\begin{aligned} t_{13} &\equiv \frac{t_{12}t_{23}}{r_{12}r_{23}\exp(\mathrm{i}\delta_2) + \exp(-\mathrm{i}\delta_2)} \\ t_{31} &\equiv \frac{t_{32}t_{21}}{r_{32}r_{21}\exp(\mathrm{i}\delta_2) + \exp(-\mathrm{i}\delta_2)} \\ r_{13} &\equiv \frac{r_{12}\exp(-\mathrm{i}\delta_2) + r_{23}\exp(\mathrm{i}\delta_2)}{r_{12}r_{23}\exp(\mathrm{i}\delta_2) + \exp(-\mathrm{i}\delta_2)} \\ r_{31} &\equiv \frac{r_{32}\exp(-\mathrm{i}\delta_2) + r_{21}\exp(\mathrm{i}\delta_2)}{r_{12}r_{23}\exp(\mathrm{i}\delta_2) + \exp(-\mathrm{i}\delta_2)} \\ R &= \frac{r_{12}r_{23}\exp(-\mathrm{i}\delta_2) + \exp(\mathrm{i}\delta_2)}{r_{12}r_{23}\exp(\mathrm{i}\delta_2) + \exp(-\mathrm{i}\delta_2)}. \end{aligned} \tag{3.60}$$

By putting Eq. (3.55) into Eq. (3.59), the next equation is readily obtained after an easy calculation.

$$\begin{pmatrix} H_1^{\mathrm{i}} \\ H_1^{\mathrm{r}} \end{pmatrix} = \frac{H_4^{\mathrm{t}}}{t_{13}t_{31}} \begin{pmatrix} \exp(-\mathrm{i}\delta_3) - r_{31}^2 \exp(\mathrm{i}\delta_3) \\ \exp(-\mathrm{i}\delta_3) + r_{31}R\exp(\mathrm{i}\delta_3) \end{pmatrix}$$

As a result, an important ratio that connects the both end phases can soon be obtained.

$$\begin{aligned} \frac{H_4^{\mathrm{t}}}{H_1^{\mathrm{i}}} &= \frac{t_{13}t_{31}}{\exp(-\mathrm{i}\delta_3) - r_{31}^2 \exp(\mathrm{i}\delta_3)} \\ &= \frac{t_{13}t_{31}\exp(\mathrm{i}\delta_3)}{1 - r_{31}^2 \exp(2\mathrm{i}\delta_3)}. \end{aligned}$$

Since the light intensity is the energy flow of the electromagnetic wave (Poynting vector), the transmitted light intensity spectrum, i.e., the single-beam spectrum of the sample is thus readily obtained as:

$$\left|\frac{H_4^{\mathrm{t}}}{H_1^{\mathrm{i}}}\right|^2 = \left|\frac{t_{13}t_{31}}{1 - r_{31}^2 \exp(2\mathrm{i}\delta_3)}\right|^2.$$

This equation involves a vibration as a function of the film thickness represented by $\exp(2\mathrm{i}\delta_3)$, which is called *optical fringe*. When the thickness of the substrate (d_3 of $\delta_3 = k_{z,3}d_3$) is large enough, the fringe interval becomes too large to find. As a result, *spectral averaging* occurs, which is obtained as [4]:

$$T_{\mathrm{sample}} \equiv \left\langle \left|\frac{H_4^{\mathrm{t}}}{H_1^{\mathrm{i}}}\right|^2 \right\rangle = \frac{|t_{13}t_{31}|^2}{1 - |r_{31}|^4}. \tag{3.61}$$

Here, T_{sample} is the transmitted light intensity of the 5-phase system (double-sided thin-film sample). In this manner, the single-beam spectrum of the sample is calculated.

In a similar manner, the single-beam spectrum of the background (3-layer system) is calculated by using Eqs. (3.53) and (3.60).

$$\frac{H_2^{\mathrm{t}}}{H_1^{\mathrm{i}}} = \frac{t_{12}t_{23}}{r_{12}r_{23}\exp(\mathrm{i}\delta_2) + \exp(-\mathrm{i}\delta_2)} = t_{13}$$

Therefore, the experimentally observed single beams spectrum of the background, T_{BG}, is formulated as:

$$T_{\mathrm{BG}} = \left\langle \left|\frac{H_2^{\mathrm{t}}}{H_1^{\mathrm{i}}}\right|^2 \right\rangle = \left\langle |t_{13}|^2 \right\rangle.$$

In the 3-layer system of air/substrate/air, $t_{23} = t_{21}$ and $r_{12} = -r_{23}$ hold. Therefore, T_{BG} can be simplified to be:

$$T_{\mathrm{BG}} = \frac{|t_{12}t_{21}|^2}{1 - |r_{12}|^4}. \tag{3.62}$$

In this manner, single-beam spectra of both sample and background have readily been calculated analytically. To obtained the final form of absorbance spectrum, an additional mathematical step is needed, i.e., the thin-film approximation.

3.8 TO and LO Energy Loss Functions: Introduction of the Thin-Film Approximation

In the deduction process of the absorbance spectrum by making the ratio of T_{sample} and T_{BG}, the parameters defined at Eq. (3.60) have exponential functions, which makes the calculation highly complicated. If the thickness of the thin-film layer is adequately thinner than the wavelength of the IR light, i.e., $d/\lambda \ll 1$, the exponential term can largely be simplified by using Taylor's expansion.

By considering Eqs. (3.33) and (3.39), the wavenumber in $\delta_j \equiv k_{z,j}d_j$ can be rewritten as:

$$k_{z,j} = ka_{z,j} = \frac{\omega}{c}\bar{n}_j a_{z,j}.$$

Therefore, the phase, δ_j, can be obtained as:

$$\delta_j = \frac{\omega}{c}\bar{n}_j a_{z,j} d_j = \frac{2\pi}{\lambda}\bar{n}_j a_{z,j} d_j.$$

Let us define the thickness of the second thin-film layer of the 5-layer system as β,

$$\beta \equiv \delta_2 = \frac{2\pi}{\lambda}\bar{n}_2 a_{z,2} d_2$$

Since β is small enough to unity, t_{13} can be simplified by Taylor's expansion. In addition, higher terms of β^2 or more are ignored, and replacements of $a \equiv t_{12}t_{23}$ and

$b \equiv r_{12}r_{23}$ are used.

$$\begin{aligned} t_{13} &\equiv \frac{t_{12}t_{23}}{r_{12}r_{23}\exp(\mathrm{i}\beta)+\exp(-\mathrm{i}\beta)} \\ &\approx \frac{a}{b(1+\mathrm{i}\beta)+(1-\mathrm{i}\beta)}+O(\beta^2) \\ &= \frac{a}{(1+b)+\mathrm{i}\beta(b-1)}\frac{(1+b)-\mathrm{i}\beta(b-1)}{(1+b)-\mathrm{i}\beta(b-1)} \\ &= \frac{a(1+b)+\mathrm{i}a\beta(1-b)}{(1+b)^2+\cancel{\beta^2(b-1)^2}} \\ &\approx \frac{a}{1+b}\left(1+\mathrm{i}\frac{1-b}{1+b}\beta\right)+O(\beta^2) \\ &= \frac{t_{12}t_{23}}{1+r_{12}r_{23}}\left(1+\mathrm{i}\frac{1-r_{12}r_{23}}{1+r_{12}r_{23}}\beta\right) \\ &\equiv t_{130}\left(1+\mathrm{i}\frac{1-r_{12}r_{23}}{1+r_{12}r_{23}}\beta\right) \end{aligned} \tag{3.63}$$

With the use of this result, t_{31} is easily obtained as:

$$\begin{aligned} t_{31} &= \frac{t_{32}t_{21}}{1+r_{32}r_{21}}\left(1+\mathrm{i}\frac{1-r_{32}r_{21}}{1+r_{32}r_{21}}\beta\right) \\ &\equiv t_{310}\left(1+\mathrm{i}\frac{1-r_{32}r_{21}}{1+r_{32}r_{21}}\beta\right). \end{aligned}$$

Here, the fraction part is represented by α_{ij} such as:

$$\alpha_{13} \equiv \frac{1-r_{12}r_{23}}{1+r_{12}r_{23}},$$

and Eq. (3.57) is referred to have:

$$\alpha_{13} = \frac{m_1m_3+m_2^2}{m_2(m_1+m_3)} = \alpha_{31} \equiv \alpha$$

With this replacement parameter, t_{13} and t_{31} can be written as:

$$t_{13} \approx t_{130}(1 + \mathrm{i}\alpha\beta)$$
$$t_{31} \approx t_{310}(1 + \mathrm{i}\alpha\beta).$$

Since both α and β are complex, the conjugate is multiplied to have the squared intensity.

$$\begin{aligned} |t_{13}t_{31}|^2 &= t_{130}^2 t_{310}^2 \left|(1 + \mathrm{i}\alpha\beta)^2\right|^2 \\ &\approx t_{130}^2 t_{310}^2 |1 + 2\mathrm{i}\alpha\beta|^2 + O(\beta^2) \\ &= t_{130}^2 t_{310}^2 (1 + 2\mathrm{i}\alpha\beta)(1 - 2\mathrm{i}\alpha^*\beta^*) \\ &\approx t_{130}^2 t_{310}^2 \{1 + 2\mathrm{i}(\alpha\beta - \alpha^*\beta^*)\} + O(\beta^2) \\ &= t_{130}^2 t_{310}^2 (1 - 4\mathrm{Im}(\alpha\beta)) \end{aligned} \tag{3.64}$$

Since, $t_{130}^2 t_{310}^2$ has nothing to do with the IR absorbing (second) phase, the spectral shape depends on only $\mathrm{Im}(\alpha\beta)$. Now, $\alpha\beta$ has thus to be calculated. This product is a function of m_j (see Eq. 3.47), and refractive index is needed. Remember that the *refractive index to the extraordinary light depends on the traveling direction* of the light (below Eq. 3.40). In this case, the expanded Snell law using complex refractive indices is conveniently used to be connected to the first phase. Thus, the expanded Snell law and the Fresnel equation are resolved as a matter of simultaneous equations.

$$n_1 a_{x,1} = \bar{n}_2 a_{x,2} \equiv X \quad \left(\text{Expanded Snell}'\text{s law}\right)$$
$$\frac{1}{\bar{\varepsilon}_2} = \frac{a_{x,2}^2}{\varepsilon_{z,2}} + \frac{a_{z,2}^2}{\varepsilon_{x,2}} \quad \left(\text{Fresnel equation}\right)$$

X is newly defined to make the calculation simpler. Note that X is a function of the angle of incidence in the phase 1, and thus a real parameter. When Eq. (3.42) is taken into account, the next equations are obtained (see also Eq. 3.33).

$$a_{x,2} = \frac{X}{\bar{n}_2} \text{ and } a_{z,2}^2 = 1 - \frac{X^2}{\bar{n}_2^2}$$

These are conveniently used to calculate the Fresnel equation as:

$$\begin{aligned}
\frac{1}{\bar{\varepsilon}_2} &= \frac{1}{\varepsilon_{z,2}}\frac{X^2}{\bar{n}_2^2} + \frac{1}{\varepsilon_{x,2}}\left(1 - \frac{X^2}{\bar{n}_2^2}\right) \\
&= \frac{1}{\varepsilon_{z,2}}\frac{X^2}{\bar{\varepsilon}_2} + \frac{1}{\varepsilon_{x,2}}\left(1 - \frac{X^2}{\bar{\varepsilon}_2}\right) \\
&\Leftrightarrow 1 = \frac{X^2}{\varepsilon_{z,2}} + \frac{1}{\varepsilon_{x,2}}\left(\bar{\varepsilon}_2 - X^2\right) \\
&\Leftrightarrow \varepsilon_{x,2}\varepsilon_{z,2} = \varepsilon_{x,2}X^2 + \varepsilon_{z,2}\left(\bar{\varepsilon}_2 - X^2\right) \\
&= X^2\left(\varepsilon_{x,2} - \varepsilon_{z,2}\right) + \varepsilon_{z,2}\bar{\varepsilon}_2 \\
&\Leftrightarrow \bar{\varepsilon}_2 = \frac{1}{\varepsilon_{z,2}}\left\{\varepsilon_{x,2}\varepsilon_{z,2} - X^2\left(\varepsilon_{x,2} - \varepsilon_{z,2}\right)\right\} \\
&= \varepsilon_{x,2} + \left(1 - \frac{\varepsilon_{x,2}}{\varepsilon_{z,2}}\right)X^2
\end{aligned} \tag{3.65}$$

In this manner, the complex electric permittivity of $\bar{\varepsilon}_2$ (corresponding to the IR absorbing phase) is now directly related to the angle of incidence. Next, β / m_2 in

$$\alpha\beta = \frac{m_1 m_3 + m_2^2}{m_2(m_1 + m_3)}\beta$$

is partially simplified by introducing a replacement of:

$$\beta = \frac{2\pi}{\lambda}\bar{n}_2 a_{z,2} d_2 = \eta \bar{n}_2 a_{z,2} \quad \left(\eta \equiv \frac{2\pi d_2}{\lambda}\right)$$

to have:

$$\frac{\beta}{m_2} = \frac{\eta \bar{n}_2 a_{z,2}}{\dfrac{\bar{n}_2 a_{z,2}}{\varepsilon_{x,2}}} = \eta\varepsilon_{x,2}.$$

Note that c in m_j (Eq. 3.47) is removed, since it does not influence r_{ij} and t_{ij}, either. Then, $\alpha\beta$ is a little simplified to be:

$$\alpha\beta = \frac{m_1 m_3 + m_2^2}{m_1 + m_3}\eta\varepsilon_{x,2}. \tag{3.66}$$

Since the first and third phases are unabsorbing layers, both m_1 and m_3 are real. η is also real. Only $\varepsilon_{x,2}$ is complex. Therefore, the next equation is obtained.

$$\begin{aligned}\mathrm{Im}(\alpha\beta) &= \mathrm{Im}\left[\frac{m_1 m_3 + m_2^2}{m_1 + m_3}\eta\varepsilon_{x,2}\right] \\ &= \frac{\eta}{m_1 + m_3}\mathrm{Im}\left[\left(m_1 m_3 + m_2^2\right)\varepsilon_{x,2}\right] \\ &= \frac{\eta}{m_1 + m_3}\left[m_1 m_3 \mathrm{Im}\left(\varepsilon_{x,2}\right) + \mathrm{Im}\left(m_2^2\varepsilon_{x,2}\right)\right]\end{aligned}$$

In this equation, $m_2^2\varepsilon_{x,2}$ is calculated in detail by considering Eq. (3.33) as follows.

$$\begin{aligned}m_2^2\varepsilon_{x,2} &= \left(\frac{\bar{n}_2 a_{z,2}}{\varepsilon_{x,2}}\right)^2 \varepsilon_{x,2} \\ &= \frac{\bar{\varepsilon}_2}{\varepsilon_{x,2}}\left(1 - a_{x,2}^2\right) \\ &= \frac{\bar{\varepsilon}_2 - X^2}{\varepsilon_{x,2}}\end{aligned}$$

Here, Fresnel's equation is modified by using X.

$$\begin{aligned}1 &= \frac{\bar{\varepsilon}_2 a_{x,2}^2}{\varepsilon_{z,2}} + \frac{\bar{\varepsilon}_2 a_{z,2}^2}{\varepsilon_{x,2}} \\ &= \frac{X^2}{\varepsilon_{z,2}} + \frac{\bar{\varepsilon}_2\left(1 - a_{x,1}^2\right)}{\varepsilon_{x,2}} \\ &\Leftrightarrow \varepsilon_{z,2} = X^2 + \frac{\varepsilon_{z,2}}{\varepsilon_{x,2}}\left(\bar{\varepsilon}_2 - X^2\right) \\ &\Leftrightarrow \frac{\bar{\varepsilon}_2 - X^2}{\varepsilon_{x,2}} = \frac{\varepsilon_{z,2} - X^2}{\varepsilon_{z,2}} = 1 - \frac{X^2}{\varepsilon_{z,2}}\end{aligned}$$

Therefore, the next equation is obtained by considering that X is real.

$$\mathrm{Im}\left(m_2^2\varepsilon_{x,2}\right) = \mathrm{Im}\left(1 - \frac{X^2}{\varepsilon_{z,2}}\right) = X^2\mathrm{Im}\left(-\frac{1}{\varepsilon_{z,2}}\right) \tag{3.67}$$

As a result, the next formulation is obtained.

$$\mathrm{Im}(\alpha\beta) = \frac{\eta}{m_1 + m_3}\left[m_1 m_3 \mathrm{Im}\left(\varepsilon_{x,2}\right) + X^2\mathrm{Im}\left(-\frac{1}{\varepsilon_{z,2}}\right)\right]$$

With this organized formulation, $|t_{13}t_{31}|^2$ (*cf.* Eqs. 3.61 and 3.64) is finally obtained as:

$$
\begin{aligned}
|t_{13}t_{31}|^2 &= t_{130}^2 t_{310}^2(1-4\mathrm{Im}(\alpha\beta)) \\
&= t_{130}^2 t_{310}^2\left(1-4\frac{\eta}{m_1+m_3}\left[m_1m_3\mathrm{Im}\left(\varepsilon_{x,2}\right)+X^2\mathrm{Im}\left(-\frac{1}{\varepsilon_{z,2}}\right)\right]\right) \\
&\equiv t_{130}^2 t_{310}^2\left(1-4\frac{\eta}{m_1+m_3}\left[m_1m_3\cdot\mathrm{TO}+n_1^2\sin^2\theta\cdot\mathrm{LO}\right]\right)
\end{aligned}
\tag{3.68}
$$

The impressive two functions of $\mathrm{Im}\left(\varepsilon_{x,2}\right)$ and $\mathrm{Im}\left(-1/\varepsilon_{z,2}\right)$ are the *TO* and *LO energy loss functions*, respectively [3–6]. The names of the functions are derived from a fact that the TO and LO spectra reveals the transverse optic (TO) and longitudinal optic (LO) phonon modes of a thin crystallite layer. In the thin film spectrometry, however, the "TO and LO functions" are conveniently used for describing the spectral shape regardless of whether the TO and LO modes are available or not. In fact, *TO and LO functions are also used for amorphous films* [9]. In short, *TO and LO functions are used for explaining the spectral shape depending on the optical configuration.* As found in the case of the s-polarization ER measurements (Eq. 3.31), the surface-parallel electric field observes the TO function spectrum only.

For example, as the simplest case, the *normal incidence transmission* measurements are easily formulated by putting $X = 0$, since the angle of incidence is zero. As a result, the spectrum is driven by the *TO energy loss function only*.

To calculate the single-beam spectrum of the sample, T_{sample} (Eq. 3.61), $|r_{31}|^4$ has to be calculated. As found in the thin-film approximation, r_{31} is calculated.

$$
\begin{aligned}
r_{31} &= \frac{r_{32}+r_{21}\exp\left(2\mathrm{i}\beta\right)}{r_{32}r_{21}\exp\left(2\mathrm{i}\beta\right)+1}. \\
&\approx \frac{r_{32}+r_{21}\left(1+2\mathrm{i}\beta\right)}{r_{32}r_{21}\left(1+2\mathrm{i}\beta\right)+1} \\
&= \frac{r_{32}+r_{21}+\mathrm{i}2r_{21}\beta}{r_{32}r_{21}+1+\mathrm{i}2r_{32}r_{21}\beta} \\
&\equiv \frac{b+\mathrm{i}2r_{21}\beta}{(a+1)+\mathrm{i}2a\beta}\frac{(a+1)-\mathrm{i}2a\beta}{(a+1)-\mathrm{i}2a\beta} \\
&= \frac{b(a+1)+\cancel{4ar_{21}\beta^2}+\mathrm{i}2\beta\left(r_{21}(a+1)-ab\right)}{(a+1)^2+\cancel{4a^2\beta^2}} \\
&\approx \frac{b}{a+1}\left[1+\mathrm{i}2\beta\left(\frac{r_{21}}{b}-\frac{a}{a+1}\right)\right] \\
&= \frac{r_{32}+r_{21}}{r_{32}r_{21}+1}\left[1+\mathrm{i}2\beta A\right] \\
&= r_{310}\left[1+\mathrm{i}2\beta A\right]
\end{aligned}
\tag{3.69}
$$

Here, some replacements are conveniently used such as:

$$a \equiv r_{32}r_{21}, b \equiv r_{32} + r_{21}, \text{ and } A \equiv \frac{r_{21}}{b} - \frac{a}{a+1}.$$

In this manner, the analytical expression of the transmission measurements is figured out. To explicitly calculate $|r_{31}|^4$, $|r_{31}|^2$ is first calculated as:

$$\begin{aligned} |r_{31}|^2 &= r_{310}^2(1 + \mathrm{i}2\beta A)(1 - \mathrm{i}2\beta^* A^*) \\ &= r_{310}^2\{1 + 4\mathrm{Im}(\beta A) + O(\beta^2)\} \end{aligned}$$

Therefore, $|r_{31}|^4$ is calculated in a good thin-film approximation as:

$$|r_{31}|^4 = r_{310}^4\{1 + 8\mathrm{Im}(\beta A) + O(\beta^2)\} \tag{3.70}$$

If the refractive index of the thin-film phase is assumed to be 1.5, and the angle of incidence is less than Brewster's angle for a transmission measurement, then $r_{310}^4 \ll 1$ holds. In this practical situation, the next equation holds.

$$T_{\text{sample}} = \frac{|t_{13}t_{31}|^2}{1 - |r_{31}|^4} \approx |t_{13}t_{31}|^2\left(1 + |r_{31}|^4\right)$$

The single-beam spectrum of the background, T_{BG}, is also calculated in a similar manner by using Eq. (3.62) to have:

$$T_{\text{BG}} = \frac{|t_{12}t_{21}|^2}{1 - |r_{12}|^4} \approx t_{130}^2 t_{310}^2\left(1 + r_{310}^4\right).$$

3.9 Analytical Expression of a Transmission Spectrum

A long story is coming to the end. Every part necessary is available to have the absorbance spectrum of transmission measurements. Although the absorbance is defined by using the natural logarithm as:

$$A \equiv -\log_{10}\frac{T_{\text{sample}}}{T_{\text{BG}}} = -\frac{1}{\ln 10}\ln\frac{T_{\text{sample}}}{T_{\text{BG}}}, \tag{3.71}$$

it is good enough to have $\ln\left(T_{\text{sample}}/T_{\text{BG}}\right)$. The ratio part is calculated by using the analytical expressions obtained in the previous section. To visualize Eq. (3.68) simpler, a new parameter of Φ is introduced.

$$|t_{13}t_{31}|^2 = t_{130}^2 t_{310}^2 \left(1 - 4\frac{\eta}{m_1 + m_3}\left[m_1 m_3 \mathrm{TO} + X^2 \mathrm{LO}\right]\right) \equiv t_{130}^2 t_{310}^2 (1 - \Phi)$$

Then, the ratio is calculated by using this new parameter and Eq. (3.70).

$$\begin{aligned}\frac{T_{\text{sample}}}{T_{\text{BG}}} &= \frac{|t_{13}t_{31}|^2\left(1 + |r_{31}|^4\right)}{t_{130}^2 t_{310}^2\left(1 + r_{310}^4\right)} \\ &= \frac{t_{130}^2 t_{310}^2(1 - \Phi)}{t_{130}^2 t_{310}^2} \cdot \frac{1 + r_{310}^4\{1 + 8\mathrm{Im}(\beta A)\}}{1 + r_{310}^4} \\ &= (1 - \Phi)\frac{1 + r_{310}^4\{1 + 8\mathrm{Im}(\beta A)\}}{1 + r_{310}^4}\end{aligned}$$

When the common logarithm is applied to this ratio, the next equation is obtained.

$$\begin{aligned}-\ln\frac{T_{\text{sample}}}{T_{\text{BG}}} &= -\ln(1 - \Phi) - \ln\left(\frac{1 + r_{310}^4\{1 + 8\mathrm{Im}(\beta A)\}}{1 + r_{310}^4}\right) \\ &\approx \Phi \\ &= 4\frac{\eta}{m_1 + m_3}\left[m_1 m_3 \mathrm{TO} + X^2 \mathrm{LO}\right]\end{aligned}$$

Here, two approximations of $\ln(1 - x) \approx -x$ and $r_{310}^4 \ll 1$ are used. As a result of the long deduction process, an explicit function of the **p-polarized** transmission measurements in the absorbance scale, A^{Tr}, is finally obtained.

$$\begin{aligned}A^{\mathrm{Tr,p}} &= \frac{1}{\ln 10} \cdot \frac{4\eta}{m_1 + m_3}\left[m_1 m_3 \mathrm{Im}\left(\varepsilon_{x,2}\right) + X^2 \mathrm{Im}\left(-\frac{1}{\varepsilon_{z,2}}\right)\right] \\ &= \boxed{\frac{1}{\ln 10 \cdot \lambda} \cdot \frac{8\pi d_2}{m_1 + m_3}\left[m_1 m_3 \mathrm{Im}\left(\varepsilon_{x,2}\right) + n_1^2 \sin^2\theta_1 \mathrm{Im}\left(-\frac{1}{\varepsilon_{z,2}}\right)\right]} \\ &\equiv \frac{8\pi d_2}{\ln 10 \cdot \lambda}\left(C_{\mathrm{pTO}} \cdot \mathrm{TO} + C_{\mathrm{pLO}} \cdot \mathrm{LO}\right)\end{aligned} \tag{3.72}$$

In the case of the p-polarization, Eq. (3.72) cannot be simplified further. For the *normal incidence* as a particular case,

$$\begin{aligned}A_{\theta_1=0}^{\mathrm{Tr}} &= \frac{1}{\ln 10 \cdot \lambda} \cdot \frac{8\pi d_2 m_1 m_3}{m_1 + m_3}\mathrm{Im}\left(\varepsilon_{x,2}\right) \\ &= \boxed{\frac{1}{\ln 10 \cdot \lambda} \cdot \frac{8\pi d_2}{n_1 + n_3}\mathrm{Im}\left(\varepsilon_{x,2}\right)}\end{aligned} \tag{3.73}$$

is obtained, which is apparently driven by the TO energy loss function only.

In other words, normal incidence transmission spectrometry is a good technique for retrieving the TO function only from a thin film sample. Since the TO function is a function of $\varepsilon_{2,x}$, only the surface-parallel molecular vibration is observed in the

Table 3.1 Absorbance at 2900 cm^{-1} of a thin film deposited on various substrates having different refractive index, n_3 [10]

Substrate	n_3	Absorbance/10^{-3}
CaF_2	1.42	3.43
ZnSe	2.46	2.40
Si	3.43	1.88
Ge	4.03	1.65

spectrum. This characteristic is called *surface selection rule of the transmission spectrometry* (Sect. 3.15) [5].

Another notable point is that $A^{\mathrm{Tr}}_{\theta_1=0}$ apparently depends on the refractive index of the substrate (n_3). This is an intuitively surprising result, since the absorbance spectrum is obtained via $T_{\mathrm{sample}}/T_{\mathrm{BG}}$ (Eq. 3.71), which makes us have an impression that the influence of the background has been canceled. As a matter of fact, the absorbance is indeed influenced apparently by choice of the substrate as found in Table 3.1 [10]. The reason occurring the discrepancy from the intuitive speculation is that both T_{sample} and T_{BG} are related to the electric field of IR ray "far from the sample surface." In practice, however, $A^{\mathrm{Tr}}_{\theta_1=0}$ is driven by the electric field "in the film on the substrate," which is *significantly influenced by the optical interface*, and *totally different from the far field*. In this manner, we understand that a normal incidence transmission spectrum cannot be understood by simply changing the sample thickness only. All the surface spectroscopies that are influenced by an optical interface are thus out of Beer's law considering no optical interface.

To check Eq. (3.72), p-polarized Tr spectra are simulated by using example optical parameters presented in Fig. 3.8, which is experimentally obtained from a 5-monolayer LB film of cadmium stearate after fitting analysis using the in-plane and out-of-plane dielectric functions to the external reflection spectra measured at two angles of incidence [11].

By using the refractive index ($n^2 = \varepsilon_{\mathrm{r}}$), Eq. (3.72) is calculated to have the blue curve in Fig. 3.9. Since the angle of incidence of 45° is employed, both $n''(x)$ and $n''(z)$ characters are found in the p-polarization spectrum.

The coefficients of C_{pTO} and C_{pLO} in Eq. (3.72) are calculated and plotted in Fig. 3.10 by the red and blue curves, respectively.

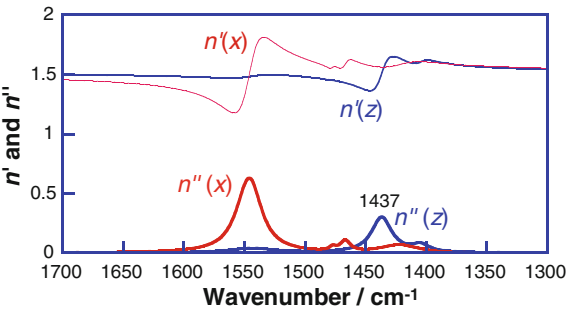

Fig. 3.8 Complex refractive indices of a 5-monolayer LB film of cadmium stearate in the in-plane (x) and out-of-plane (z) directions

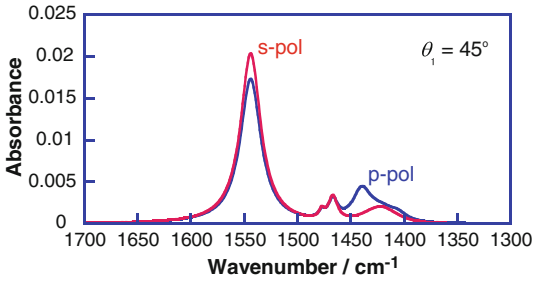

Fig. 3.9 Simulated Tr spectra calculated by Eqs. (3.72) and (3.74) using the complex refractive index in Fig. 3.8. The optical parameters of n_3 = 3.42 (Si), d_2 = 2.5 nm and θ_1 = 45° are used

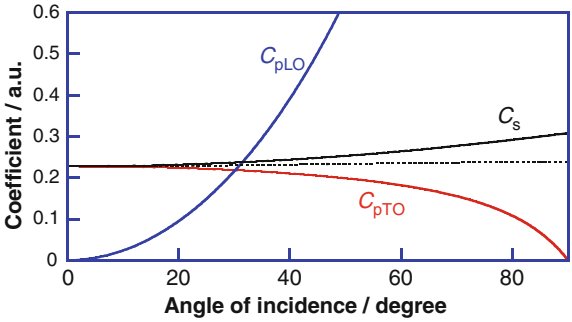

Fig. 3.10 Coefficients in Eqs. (3.72) and (3.74) as a function of the angle of incidence calculated for a Si substrate (n = 3.4). The dotted line is for the s-polarization only when the path length change in the thin film is taken into account

In the case of a silicon substrate, the two coefficients are almost the same as each other at the angle of incidence of 30°. When the angle is large, the TO component gradually decreased while the LO component becomes significantly large rapidly.

For **s-polarization**:

When Eq. (3.45) is referred for the s-polarization, Eq. (3.47) has to be changed to be:

$$m_j^{\mathrm{s}} \equiv \frac{n_{x,j} a_{z,j}}{c\mu_0}.$$

Note that $\varepsilon_{x,j}$ does not appear in the denominator. Since the constants of c and μ_0 are disappeared by making a ratio in t and r, *these parameters are removed out in the following deformation*, i.e.,

$$\boxed{m_j^{\mathrm{s}} \equiv n_{x,j} a_{z,j}}.$$

Then, Eq. (3.66) can be modified to be for the s-polarization:

$$(\alpha\beta)^{\mathrm{s}} = \frac{m_1^{\mathrm{s}} m_3^{\mathrm{s}} + m_2^{\mathrm{s}2}}{m_1^{\mathrm{s}} + m_3^{\mathrm{s}}} \eta$$

Then, the imaginary part becomes:

$$\mathrm{Im}[(\alpha\beta)^{\mathrm{s}}] = \frac{\eta}{m_1^{\mathrm{s}} + m_3^{\mathrm{s}}}\mathrm{Im}(m_1^{\mathrm{s}} m_3^{\mathrm{s}} + m_2^{\mathrm{s}2}) = \frac{\eta}{m_1^{\mathrm{s}} + m_3^{\mathrm{s}}}\mathrm{Im}\ (m_2^{\mathrm{s}2}).$$

Here,

$$\begin{aligned} m_2^{\mathrm{s}2} &= n_{x,2}^2 a_{z,2}^2 \\ &= \varepsilon_{x,2}\cos^2\theta_2 \\ &= \varepsilon_{x,2}\left(1 - \sin^2\theta_2\right) \\ &= \varepsilon_{x,2} - X^2 \end{aligned}$$

Since X is real,

$$\mathrm{Im}(\alpha\beta^{\mathrm{s}}) = \frac{\eta}{m_1^{\mathrm{s}} + m_3^{\mathrm{s}}}\mathrm{Im}\left(\varepsilon_{x,2}\right)$$

holds. Therefore, we reach the following result.

$$\begin{aligned} A^{\mathrm{Tr,s}} &= \frac{1}{\ln 10 \cdot \lambda} \cdot \frac{8\pi d_2}{m_1^{\mathrm{s}} + m_3^{\mathrm{s}}}\mathrm{Im}\left(\varepsilon_{x,2}\right) \\ &= \boxed{\frac{8\pi d_2}{\ln 10 \cdot \lambda} \cdot \frac{\xi_1 - \xi_3}{\varepsilon_1 - \varepsilon_3}\mathrm{Im}\left(\varepsilon_{x,2}\right)} \\ &\equiv \frac{8\pi d_2}{\ln 10 \cdot \lambda} C_{\mathrm{s}}\mathrm{Im}\left(\varepsilon_{x,2}\right) \end{aligned} \tag{3.74}$$

where $\xi_j \equiv \sqrt{\varepsilon_j - \varepsilon_1 \sin^2\theta_1}$ is used. In this manner, only the surface-parallel component of a transition moment is observed.

With the use of Eq. (3.74), the s-polarization spectrum is simulated by using the complex refractive indices presented in Fig. 3.8 in the same manner as the p-polarization, which is presented by the red curve in Fig. 3.9. Since the s-polarization spectra are influenced by the TO energy loss function only, an apparent difference from the p-polarization spectrum is found especially at about 1440 cm^{-1}. If the normal incidence ($\theta_1 = 0$) measurement is performed, the s- and p-polarization spectra are identical to each other, of course.

The coefficient, C_{s}, in Eq. (3.74) is plotted in Fig. 3.10 by the black curve, which is a moderate change to the angle of incidence. This is striking that the s-polarization absorbance does not simply reflect the path length (see the dotted line) in the thin-film phase. Therefore, *the molecular orientation analysis based on an intuitive model considering the path length only leads you to an incorrect conclusion especially when a larger angle than 40° is taken.*

3.10 Preparation for the Analytical Expression of a Reflection Spectrum

We have already shown a deduction process of the analytical form of an s-polarized ER spectrum (Eq. 3.31) using the intuitive multiple-reflection model in Sect. 3.4. Here, let us calculate the analytical form of a p-polarized reflection spectrum using a model-free technique, i.e., Abeles' transfer matrix method. Reflection spectra are largely influenced by the dielectric property of the substrate, and they are categorized into two representative spectrometries: reflection absorption (RA) on a metallic surface, and external reflection (ER) on a nonmetallic surface. Since both RA and ER techniques are performed on a 3-phase system, the first steps of calculations are commonly involved as follows.

On Abeles' transfer matrix method, the 3-phase system can be formulated as:

$$\boldsymbol{N}_1 = \boldsymbol{Q}_1^{-1}\boldsymbol{Q}_2\boldsymbol{P}_2^{-1}\boldsymbol{Q}_2^{-1}\boldsymbol{Q}_3\boldsymbol{F}_2$$

where the next two parameters are defined as shown before.

$$\boldsymbol{N}_1 \equiv \begin{pmatrix} H_1^{\mathrm{i}} \\ H_1^{\mathrm{r}} \end{pmatrix} \quad \text{and} \quad \boldsymbol{F}_2 \equiv \begin{pmatrix} H_2^{\mathrm{t}} \\ 0 \end{pmatrix}$$

In the case of a reflection spectrum analysis, the ratio of H_1^{r} to H_1^{i} is necessary. By introducing Eqs. (3.56)–(3.58), the following calculation can be done.

$$\begin{aligned}
\begin{pmatrix} H_1^{\mathrm{i}} \\ H_1^{\mathrm{r}} \end{pmatrix} &= t_{12}^{-1}t_{23}^{-1}\begin{pmatrix} 1 & r_{12} \\ r_{12} & 1 \end{pmatrix}\begin{pmatrix} \mathrm{e}^{-\mathrm{i}\delta_2} & 0 \\ 0 & \mathrm{e}^{\mathrm{i}\delta_2} \end{pmatrix}\begin{pmatrix} 1 & r_{23} \\ r_{23} & 1 \end{pmatrix}\begin{pmatrix} H_1^{\mathrm{t}} \\ 0 \end{pmatrix} \\
&= t_{12}^{-1}t_{23}^{-1}\begin{pmatrix} \mathrm{e}^{-\mathrm{i}\delta_2} + r_{12}r_{23}\mathrm{e}^{\mathrm{i}\delta_2} & r_{23}\mathrm{e}^{-\mathrm{i}\delta_2} + r_{12}\mathrm{e}^{\mathrm{i}\delta_2} \\ r_{12}\mathrm{e}^{-\mathrm{i}\delta_2} + r_{23}\mathrm{e}^{\mathrm{i}\delta_2} & r_{12}r_{23}\mathrm{e}^{-\mathrm{i}\delta_2} + \mathrm{e}^{\mathrm{i}\delta_2} \end{pmatrix}\begin{pmatrix} H_1^{\mathrm{t}} \\ 0 \end{pmatrix} \\
&\Leftrightarrow \\
H_1^{\mathrm{i}} &= t_{12}^{-1}t_{23}^{-1}\left(\mathrm{e}^{-\mathrm{i}\delta_2} + r_{12}r_{23}\mathrm{e}^{\mathrm{i}\delta_2}\right)H_1^{\mathrm{t}} \\
H_1^{\mathrm{r}} &= t_{12}^{-1}t_{23}^{-1}\left(r_{12}\mathrm{e}^{-\mathrm{i}\delta_2} + r_{23}\mathrm{e}^{\mathrm{i}\delta_2}\right)H_1^{\mathrm{t}} \\
&\Leftrightarrow \frac{H_1^{\mathrm{r}}}{H_1^{\mathrm{i}}} = \frac{r_{12}\mathrm{e}^{-\mathrm{i}\delta_2} + r_{23}\mathrm{e}^{\mathrm{i}\delta_2}}{\mathrm{e}^{-\mathrm{i}\delta_2} + r_{12}r_{23}\mathrm{e}^{\mathrm{i}\delta_2}} \\
&= \frac{r_{12} + r_{23}\mathrm{e}^{2\mathrm{i}\delta_2}}{1 + r_{12}r_{23}\mathrm{e}^{2\mathrm{i}\delta_2}} \equiv r_{13}
\end{aligned}$$

Of note is that this conclusion calculated on the model-free Abeles method is exactly the same as that obtained at Eq. (3.25) by using the intuitive multiple-reflection model. This perfect agreement paradoxically implies that *the*

multiple-reflection model works well in the stratified layers irrespective of the film thickness *in the plane wave approximation*. In this manner, we have experienced that Abeles' method works powerfully to theorize the light propagation about an optical interface.

The single-beam spectrum of the reflected light, R, is simply obtained by the squared ratio:

$$R_{\text{sample}} = \left|\frac{H_1^{\text{r}}}{H_1^{\text{i}}}\right|^2 = |r_{13}|^2. \tag{3.75}$$

r_{13} is calculated in a similar manner to the calculation of r_{31} (Eq. 3.69) by exchanging the indices of 1 and 3.

$$\begin{aligned} r_{13} &\approx r_{130}\left\{1 + 2\mathrm{i}\beta\frac{m_1\left(m_2^2 - m_3^2\right)}{m_2\left(m_1^2 - m_3^2\right)}\right\} + O\left(\beta^2\right) \\ &\equiv r_{130}\{1 + 2\mathrm{i}\beta B\} \end{aligned} \tag{3.76}$$

Here, r_{130} and B are defined as:

$$r_{130} = \frac{r_{12} + r_{23}}{r_{12}r_{23} + 1} = \frac{m_1 - m_3}{m_1 + m_3}$$

and

$$B \equiv \frac{m_1\left(m_2^2 - m_3^2\right)}{m_2\left(m_1^2 - m_3^2\right)}.$$

As a result, the single-beam spectrum of the sample measurements is obtained as:

$$\begin{aligned} R_{\text{sample}} &= |r_{13}|^2 \\ &\approx |r_{130}|^2|1 + 2\mathrm{i}\beta B|^2 \\ &\approx |r_{130}|^2\{1 + 4\mathrm{i}\mathrm{Im}(\beta B)\} + O\left(\beta^2\right). \end{aligned}$$

For the single-beam spectrum of the "background," r_{13} is immediately obtained by putting $d_2 = 0$ into $\beta = \frac{2\pi}{\lambda}\bar{n}_2 a_{z,2} d_2$ in Eq. (3.76) to be:

$$r_{13} = r_{130}\{1 + 2\mathrm{i}\beta B\} \rightarrow r_{130}$$

As a result, the single-beam spectrum of the background is:

$$R_{\text{BG}} = |r_{130}|^2$$

Then, the absorbance spectrum of the reflection measurements is calculated via:

$$A \equiv -\log_{10}\frac{R_{\text{sample}}}{R_{\text{BG}}} = -\frac{\ln(1-4\text{Im}(\beta B))}{\ln 10}. \tag{3.77}$$

Note that the 1st and 3rd phases can be considered to be optically isotropic in practice, i.e., $\bar{n}_j = n_j$ and $\varepsilon_{x,j} = \varepsilon_j$, although the 3rd phase can be IR absorbing phase (especially for RA spectrometry). By considering the isotropic character, m_j can be simplified as:

$$m_j = \frac{\bar{n}_j a_{z,j}}{\bar{\varepsilon}_{x,j}} \to \frac{a_{z,j}}{n_j}. \quad (j = 1 \text{ or } 3)$$

Therefore, a simpler form of

$$\beta = 2\pi\frac{d_2}{\lambda}n_2 a_{z,2} \equiv \eta n_2 a_{z,2}$$

is obtained. With a newly introduced parameter of $\eta \equiv 2\pi d_2 / \lambda$,

$$\frac{\beta}{m_2} = \eta\varepsilon_{x,2} \tag{3.78}$$

is obtained by using the permittivity in the x direction. Therefore, the following deformation can be done.

$$\begin{aligned}\text{Im}(\beta B) &= \text{Im}\left(\beta\frac{m_1\left(m_2^2 - m_3^2\right)}{m_2\left(m_1^2 - m_3^2\right)}\right) \\ &= \eta m_1 \text{Im}\left(\frac{m_2^2 - m_3^2}{m_1^2 - m_3^2}\varepsilon_{x,2}\right)\end{aligned} \tag{3.79}$$

As noted above, m_3 can be a complex, which should not be remained in the denominator in the fraction. To remove the light absorbing parameter from the denominator, the next deformation is carried out.

$$\begin{aligned}m_3^2 &= \frac{a_{z,3}^2}{n_3^2} \\ &= \frac{n_3^2\left(1 - a_{x,3}^2\right)}{n_3^4} \\ &= \frac{\varepsilon_3 - n_3^2 a_{x,3}^2}{\varepsilon_3^2} \\ &= \frac{\varepsilon_3 - n_1^2 a_{x,1}^2}{\varepsilon_3^2}.\end{aligned}$$

The last deformation is done by using Snell's law. By using this formulation, a little bit tricky deformation is also carried out.

$$\begin{aligned}\frac{m_1^2 - m_3^2}{m_1^2} &= 1 - \frac{m_3^2}{m_1^2} \\ &= 1 - \frac{\varepsilon_1\left(\varepsilon_3 - n_1^2 a_{x,1}^2\right)}{\varepsilon_3^2 a_{z,1}^2} \\ &= \frac{1}{\varepsilon_3^2}\left\{\varepsilon_3^2 - \frac{\varepsilon_1\varepsilon_3}{a_{z,1}^2} + \varepsilon_1^2 \tan^2\theta_1\right\} \\ &= \frac{1}{\varepsilon_3^2}\left\{\varepsilon_3^2 - \varepsilon_1\varepsilon_3\left(1 + \tan^2\theta_1\right) + \varepsilon_1^2 \tan^2\theta_1\right\} \\ &= \frac{1}{\varepsilon_3^2}\left(\varepsilon_3 - \varepsilon_1\right)\left(\varepsilon_3 - \varepsilon_1 \tan^2\theta_1\right)\end{aligned}$$

With this formulation, the next equation is obtained.

$$\begin{aligned}\mathrm{Im}(\beta B) &= \eta m_1 \mathrm{Im}\left(\frac{m_2^2 - m_3^2}{m_1^2 - m_3^2}\varepsilon_{x,2}\right) \\ &= \frac{\eta}{m_1}\mathrm{Im}\left(\frac{\varepsilon_{x,2}\varepsilon_3^2\left(m_2^2 - m_3^2\right)}{\left(\varepsilon_3 - \varepsilon_1\right)\left(\varepsilon_3 - \varepsilon_1 \tan^2\theta_1\right)}\right).\end{aligned} \tag{3.80}$$

Now, we are ready to consider both RA and ER cases. The RA case is discussed in the following section, since it is especially important to retrieve the LO energy loss function spectrum.

3.11 Analytical Expression of an RA Spectrum

When the substrate (3rd phase) is metallic, i.e., ε_3 is complex, the reflection measurements are called *reflection absorption* (*RA*) spectrometry. Metal has a significantly large electric permittivity for both real and imaginary parts in the IR range [12]. Therefore, in the case of the metallic surface, an approximation of $|\varepsilon_3| \gg \varepsilon_1$ is practically useful. If the angle of incidence is set at 85° or less, $|\varepsilon_3| \gg \varepsilon_1 \tan^2\theta_1$ also holds in a good approximation. Then, the next approximation can be done.

$$\begin{aligned}\mathrm{Im}(\beta B) &= \frac{\eta}{m_1}\mathrm{Im}\left(\frac{\varepsilon_{x,2}\varepsilon_3^2\left(m_2^2 - m_3^2\right)}{\left(\varepsilon_3 - \varepsilon_1\right)\left(\varepsilon_3 - \varepsilon_1 \tan^2\theta_1\right)}\right) \\ &\approx \frac{\eta}{m_1}\mathrm{Im}\left\{\varepsilon_{x,2}\left(m_2^2 - m_3^2\right)\right\}\end{aligned} \tag{3.81}$$

If we recall Eq. (3.67), then Eq. (3.81) can further be deformed.

$$\begin{aligned}\mathrm{Im}(\beta B) &\approx \frac{\eta}{m_1}\mathrm{Im}\left\{1-\frac{X^2}{\varepsilon_{z,2}}-\varepsilon_{x,2}m_3^2\right\}\\ &= \frac{\eta}{m_1}\mathrm{Im}\left\{1-\frac{X^2}{\varepsilon_{z,2}}-\varepsilon_{x,2}m_3^2\right\}\\ &= \frac{\eta}{m_1}\left\{X^2\mathrm{Im}\left(-\frac{1}{\varepsilon_{z,2}}\right)-\varepsilon_{x,2}m_3^2\right\}\end{aligned}$$

The last term in the parenthesis can be calculated by considering Snell's law as (c is omitted as stated above):

$$\begin{aligned}\varepsilon_{x,2}m_3^2 &= \varepsilon_{x,2}\frac{n_3^2a_{z,3}^2}{\varepsilon_3^2}\\ &= \varepsilon_{x,2}\frac{n_3^2\left(1-a_{x,3}^2\right)}{\varepsilon_3^2}\\ &= \varepsilon_{x,2}\frac{n_3^2-n_3^2a_{x,3}^2}{\varepsilon_3^2}\\ &= \varepsilon_{x,2}\frac{\varepsilon_3-n_1^2a_{x,1}^2}{\varepsilon_3^2}\\ &= \frac{\varepsilon_{x,2}}{\varepsilon_3}-\frac{\varepsilon_{x,2}n_1^2a_{x,1}^2}{\varepsilon_3^2}.\end{aligned}$$

When $|\varepsilon_3| \gg |\varepsilon_2|$ is also taken into account, this term can totally be ignored. As a result, the ratio can be calculated as:

$$\begin{aligned}\frac{R_{\mathrm{sample}}}{R_{\mathrm{BG}}} &= 1-4\mathrm{Im}(\beta B)\\ &= 1-4\frac{\eta}{m_1}X^2\mathrm{Im}\left(-\frac{1}{\varepsilon_{z,2}}\right)\\ &= 1-\frac{8\pi d_2}{m_1\lambda}n_1^2\sin^2\theta_1\mathrm{Im}\left(-\frac{1}{\varepsilon_{z,2}}\right)\\ &= 1-\frac{8\pi d_2}{\lambda}n_1^3\frac{\sin^2\theta_1}{\cos\theta_1}\mathrm{Im}\left(-\frac{1}{\varepsilon_{z,2}}\right).\end{aligned}$$

With this ratio, the analytical representation of an RA spectrum measured by using the p-polarization is calculated by referring Eq. (3.77) to be:

$$A^{\mathrm{RA}} = -\frac{\ln(1 - 4\mathrm{Im}(\beta B))}{\ln 10} = \boxed{\frac{8\pi d_2}{\ln 10 \cdot \lambda} n_1^3 \frac{\sin^2 \theta_1}{\cos \theta_1} \mathrm{Im}\left(-\frac{1}{\varepsilon_{z,2}}\right)} \tag{3.82}$$

Note that this representation is for p-polarization measurements on a metallic surface. The RA spectrum is thus found to be driven by the *LO energy loss function only*. In other words, the RA technique employing the p-polarization is an important technique to *retrieve the pure LO function* spectrum. Since the LO function involves $\varepsilon_{z,2}$ only, the surface-*perpendicular* component of a transition moment in the thin film is selectively observed. This rule is called the *surface selection rule* (*SSR*) of the RA measurements [5].

Another important note is that this representation involves *no parameter of the 3rd phase*, which straightforwardly implies that the RA spectra are impervious to the choice of the substrate as long as the substrate is metallic.

As done for the Tr spectra, a p-polarized RA spectrum is also simulated by using the same complex refractive indices in Fig. 3.8, which is presented by the blue curve in Fig. 3.11. As mentioned above, no optical parameter of the metallic substrate is necessary for the calculation, and of course, the spectrum shape agrees with the $n''(z)$ function.

In addition, we have to pay attention to the angle of incidence, too. When θ_1 is close to 90°, A^{RA} rapidly runs up monotonously because of $\sin^2 \theta_1 / \cos \theta_1$, which seems good for a high-sensitive measurement. Regardless, the assumption of $|\varepsilon_3| \gg \varepsilon_1 \tan^2 \theta_1$ is broken for a too large θ_1, with which pure LO function is *not* obtained. *Therefore ca.* $\theta_1 = 80°$ *is practically the best angle for the incidence to keep both the SSR and high sensitivity*.

Figure 3.12a presents a p-polarized IR RA spectrum of 5-monolayer Langmuir–Blodgett film of cadmium stearate deposited on a gold surface with an angle of incidence of 80°. The shape of the spectrum is *largely different from the KBr-pellet spectrum* in Fig. 1.7: both $\nu_a CH_2$ and $\nu_s CH_2$ bands are largely suppressed to be comparative to the $\nu_a CH_3$ and $\nu_s CH_3$ bands. In the multilayered film, the molecules stand almost perpendicularly to the surface. With the molecular stance, both $\nu_a CH_2$ and $\nu_s CH_2$ modes have a nearly parallel transition moment to the surface, which

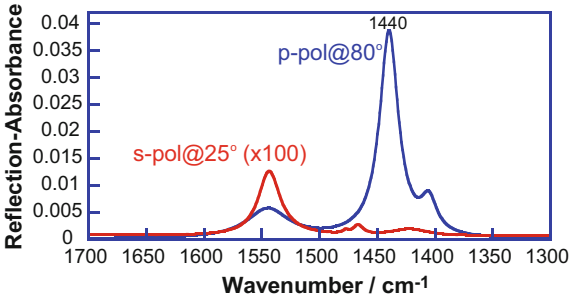

Fig. 3.11 Simulated RA spectra calculated by Eqs. (3.82) and (3.83) using the complex refractive index in Fig. 3.8. The optical parameters of d_2 = 2.5 nm and θ_1 = 80° are used. The s-polarized spectrum is 100 times magnified

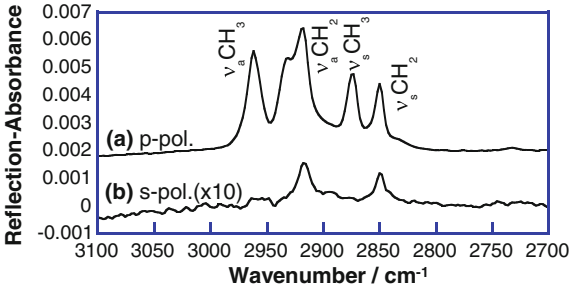

Fig. 3.12 IR RA spectra of a 5-monolayer Langmuir–Blodgett film of cadmium stearate on gold measured by using **a** the p-polarization at 80° and **b** s-polarization at 25°. The s-polarized spectrum is 10 times magnified

yield fairly weak absorbance peaks, since the LO function is driven by $\varepsilon_{z,2}$ only. In this manner, *the relative band intensity is directly influenced by the molecular orientation*. By the comparison of the RA and KBr spectra, in this manner, the orientation of each transition moment can be discussed. The intrinsic IR spectral pattern [α spectrum; Eq. (1.43)] is obtained by using an unoriented sample, which is obtained by the KBr-pellet technique (Sect. 3.16A).

In the case of RA spectrometry, the s-polarization measurements are not used practically. Here, just in case, the analytical expression for the unusual measurements is presented. As found in the transmission case, $m_j^{\mathrm{s}} \equiv n_{x,j} a_{z,j}$ is used. Then, Eq. (3.78) is simplified as:

$$\frac{\beta}{m_2^{\mathrm{s}}} = \frac{\eta n_{x,2} a_{z,2}}{n_{x,2} a_{z,2}} = \eta.$$

Therefore,

$$\begin{aligned}
\mathrm{Im}(\beta B)^{\mathrm{s}} &= \mathrm{Im}\left(\beta \frac{m_1^{\mathrm{s}}\left(m_2^{\mathrm{s}2} - m_3^{\mathrm{s}2}\right)}{\left(m_2^{\mathrm{s}2} - m_3^{\mathrm{s}2}\right)}\right) \\
&\approx \eta m_1^{\mathrm{s}} \mathrm{Im}\left(\frac{\varepsilon_2 - X^2 - \varepsilon_3 + X^2}{-\varepsilon_3}\right) \\
&\approx \eta m_1^{\mathrm{s}} \mathrm{Im}\left(\frac{\varepsilon_2 - X^2 - \varepsilon_3 + X^2}{-\varepsilon_3}\right) \\
&= \frac{2\pi d_2 n_1 \cos\theta_1}{\lambda} \mathrm{Im}\left(-\frac{\varepsilon_2}{\varepsilon_3}\right)
\end{aligned}$$

$$\therefore A^{\mathrm{RA,s}} \boxed{= \frac{8\pi d_2 \cos\theta_1}{\ln 10 \cdot \lambda} \mathrm{Im}\left(-\frac{\varepsilon_2}{\varepsilon_3}\right)}. \tag{3.83}$$

In the case of the s-polarization, $\varepsilon_2 = \varepsilon_{x,2}$ (isotropic) holds, which means that only the surface-parallel component of a transition moment is observed. Since $|\varepsilon_3| \gg |\varepsilon_2|$ holds on a metallic surface, the absorbance of the s-polarization on a metallic surface becomes very minor. Another concern is that the polarizer yields an impurity a little bit, and the leaked minor impurity polarization contributes to the high-sensitive p-polarization measurements, which hides the weak s-polarized spectrum. If you do need the surface-parallel information on a metallic surface, double polarizers should be put in series to remove the impurity as possible, or a small angle of incidence should be chosen to make the contribution of the leaked p-polarization as small as possible.

The simulated s-polarized RA spectrum at the angle of incidence of 25° is overlaid on the p-polarized spectrum in Fig. 3.11. Note that the ordinate scale is 100 times magnified for the better visibility. In this manner, the s-polarization largely loses the sensitivity making the signal-to-noise ration very poor, but instead the $n''(x)$ spectrum (TO function) can readily be obtained.

Figure 3.12b presents an actually measured s-polarized IR RA spectrum of the same sample as used for the p-polarized one. To earn the sensitivity, a low angle of incidence of 25° is chosen considering Eq. (3.83). As mentioned above about Fig. 3.12, a very much suppressed TO energy loss function appears, which has a common shape to a transmission spectrum.

3.12 Analytical Expression of an ER Spectrum

When the substrate is nonmetallic and unabsorbing, ε_3 is real. Reflection measurements on this condition are called *external reflection* (*ER*) spectrometry [5, 13, 14]. In this case, Eq. (3.80) for **the p-polarization** is a little bit deformed.

$$\begin{aligned}\mathrm{Im}(\beta B) &= \frac{\eta}{m_1}\mathrm{Im}\left(\frac{\varepsilon_{x,2}\varepsilon_3^2\left(m_2^2 - m_3^2\right)}{(\varepsilon_3 - \varepsilon_1)(\varepsilon_3 - \varepsilon_1\tan^2\theta_1)}\right) \\ &= \frac{\eta\varepsilon_3^2\mathrm{Im}\left(\varepsilon_{x,2}\left(m_2^2 - m_3^2\right)\right)}{m_1(\varepsilon_3 - \varepsilon_1)(\varepsilon_3 - \varepsilon_1\tan^2\theta_1)}\end{aligned}$$

Here, $\varepsilon_{x,2}m_2^2 = 1 - X^2/\varepsilon_{z,2}$ is taken into account, the ratio of $R_{\mathrm{Sample}}/R_{\mathrm{BG}}$ can be simplified by using the TO and LO functions.

$$\begin{aligned}\frac{R_{\text{sample}}}{R_{\text{BG}}} &= 1 - 4\text{Im}(\beta B) \\ &= 1 - \frac{4\eta\varepsilon_3^2 \text{Im}\left(\varepsilon_{x,2}\left(m_2^2 - m_3^2\right)\right)}{m_1(\varepsilon_3 - \varepsilon_1)(\varepsilon_3 - \varepsilon_1 \tan^2\theta_1)} \\ &= 1 - \frac{4\eta\varepsilon_3^2 \text{Im}\left((1 - X^2/\varepsilon_{z2}) - \varepsilon_{x,2} m_2^3\right)}{m_1(\varepsilon_3 - \varepsilon_1)(\varepsilon_3 - \varepsilon_1 \tan^2\theta_1)} \\ &= 1 + \frac{4\eta\varepsilon_3^2\left(m_3^2 \cdot \text{TO} - X^2 \cdot \text{LO}\right)}{m_1(\varepsilon_3 - \varepsilon_1)(\varepsilon_3 - \varepsilon_1 \tan^2\theta_1)}\end{aligned}$$

Therefore, the p-polarized ER spectrum in the absorbance scale is obtained as:

$$\begin{aligned}A^{\text{ER,p}} &= -\frac{\ln(1 - 4\text{Im}(\beta B))}{\ln 10} \\ &\approx -\frac{1}{\ln 10}\frac{4\eta\varepsilon_3^2\left(m_3^2\text{TO} - X^2\text{LO}\right)}{m_1(\varepsilon_3 - \varepsilon_1)(\varepsilon_3 - \varepsilon_1 \tan^2\theta_1)} \\ &= \boxed{\frac{8\pi d_2}{\ln 10 \cdot \lambda}\frac{\left(\sin^2\theta_1 - \varepsilon_3\right) \cdot \text{TO} + \varepsilon_3^2 \sin^2\theta_1 \cdot \text{LO}}{\cos\theta_1(\varepsilon_3 - 1)(\varepsilon_3 - \tan^2\theta_1)}} \\ &\equiv \frac{8\pi d_2}{\ln 10 \cdot \lambda}\left(C_{\text{pTO}} \cdot \text{TO} + C_{\text{pLO}} \cdot \text{LO}\right),\end{aligned} \tag{3.84}$$

where the incident light comes from the air phase ($\varepsilon_1 = 1$).

This conclusion implies that $A^{\text{ER,p}}$ measured on a nonmetallic surface is a linear combination of both TO and LO function spectra. In addition, the weighting coefficients strongly depend on the permittivity of the substrate yielding negative and positive absorbance *depending on the angle of incidence and the molecular orientation*, which is totally different from RA spectrometry. Since TO and LO function spectra respond to the surface-parallel and -perpendicular components of the permittivity, respectively, the *p-polarization ER spectra respond to the molecular orientation* very sensitively.

The coefficients of C_{pTO} and C_{pLO} are calculated and plotted in Fig. 3.13. Since the TO and LO function does not exhibit the same peak intensity for an identical

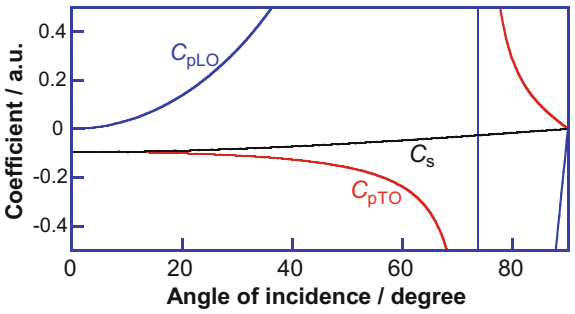

Fig. 3.13 Coefficients in Eqs. (3.84) and (3.86) as a function of the angle of incidence calculated for a Si substrate (n = 3.4)

permittivity, the coefficients exhibit schematic variations. For example, at $\theta_1 = 0$, C_{pLO} is nil; whereas C_{pTO} is negative. Therefore, if the angle of incidence is nearly zero, the p-polarized ER spectrum is driven by the TO function only, and the absorption peak should appear as a negative peak. In other words, the surface-parallel component of a normal mode is selectively observed by the negative bands.

When the angle of incidence is close to 60°, C_{pLO} and C_{pTO} have a large intensity with positive and negative signs, respectively. This means that the surface-perpendicular and –parallel components appear as positive and negative peaks, respectively, and the intensity is much higher than the normal incidence measurements. In this manner, the p-polarized ER measurements reveal the molecular orientation, and the sensitivity largely depends on the angle of incidence. For the detail, refer to Sect. 3.15C.

It is of interest that the band signs overturn when the angle of incidence goes across a specific angle. According to Eq. (3.84), in fact, the sign of the spectra depends on θ_1, since $\varepsilon_3 - \varepsilon_1 \tan^2 \theta_1$ can be zero when θ_1 satisfies:

$$\begin{aligned} &\varepsilon_3 - \varepsilon_1 \tan^2 \theta_1 = 0 \\ &\Leftrightarrow \tan^2 \theta_1 = \frac{n_3^2}{n_1^2}. \end{aligned} \tag{3.85}$$

This specific angle is called *Brewster's angle*. In short, the surface selection rule of the p-polarized ER spectrometry is a function of the molecular orientation and the angle of incidence, which will be mentioned later in Sect. 3.15C. As a matter of fact, this surface selection rule is quite useful to retrieve the molecular orientation in a thin film deposited on a nonmetallic substrate.

The discussion made above is readily recognized by looking at a simulated ER spectrum (blue curve in Fig. 3.14) using the complex refractive indices in Fig. 3.8.

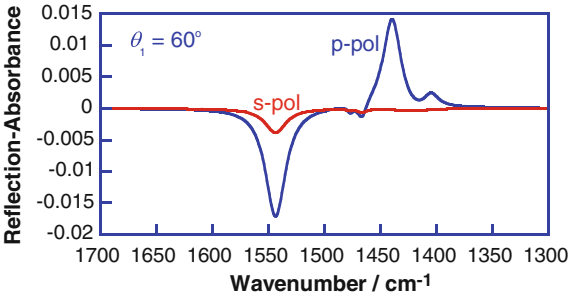

Fig. 3.14 Simulated ER spectra calculated by Eqs. (3.84) and (3.86) using the complex refractive index in Fig. 3.8. The optical parameters of n_3 = 3.42 (Si), d_2 = 2.5 nm and θ_1 = 60° are used

In the p-polarization ER spectrum, TO and LO functions appear as negative and positive peaks, respectively, as predicted by the discussion about Fig. 3.13. Details about the molecular orientation will be discussed in Sect. 3.15C.

In the case of the **s-polarized** ER spectrometry, the substrate has no absorption (ε_3 is real), Eq. (3.83) can be further simplified to have:

$$\begin{aligned}\mathrm{Im}(\beta B)^{\mathrm{s}} &= \eta m_1^{\mathrm{s}} \mathrm{Im}\left(\frac{m_2^{\mathrm{s}2} - m_3^{\mathrm{s}2}}{m_1^{\mathrm{s}2} - m_3^{\mathrm{s}2}}\right) \\ &= \eta m_1^{\mathrm{s}} \mathrm{Im}\left(\frac{\varepsilon_2 - \varepsilon_3'}{1 - \varepsilon_3'}\right) \\ &= -\frac{8\pi d_2 n_1 \cos\,\theta_1}{\lambda\left(\varepsilon_3' - 1\right)} \mathrm{Im}(\varepsilon_2).\end{aligned}$$

Therefore,

$$\begin{aligned}A^{\mathrm{ER,s}} &= -\frac{\ln(1 - 4\mathrm{Im}(\beta B)^{\mathrm{s}})}{\ln 10} \\ &\approx \boxed{-\frac{1}{\ln 10 \cdot \lambda} \frac{8\pi d_2 n_1 \cos\theta_1}{\varepsilon_3' - 1} \mathrm{Im}(\varepsilon_2)} \\ &\equiv \frac{8\pi d_2}{\ln 10 \cdot \lambda} C_{\mathrm{s}} \cdot \mathrm{TO}\end{aligned} \tag{3.86}$$

This result perfectly agrees with Eq. (3.31). In this manner, the analytical representation deduced by using Abeles' transfer matrix method readily reproduces the result obtained by using the intuitive multiple-reflection model. This agreement confirms in a paradoxical manner that *an ultrathin film has multiple reflections of the IR light* indeed, although the wavelength is much longer than the film thickness.

Equation (3.86) apparently implies that the absorption peak is always *negative irrespective of the angle of incidence*, since $\varepsilon_3' - 1 > 0$. In fact, as found in Fig. 3.13, C_{s} is negative. In contrast to the p-polarization, the absorption 'intensity' is getting larger when the angle of incidence is smaller.

3.13 Analytical Expression of an Attenuated Total Reflection (ATR) Spectrum

When the incident IR light goes in a high refractive index material to an interface with a lower refractive index material, the measurements are categorized into the *internal reflection* measurements. *The intrinsic difference from the ER measurements is only the order of the phases*. In the new optical configuration, ε_3 is unity for the ER measurement, since the IR light is incident to the sample from the air phase in many cases. In ATR measurements, however, another matter than air can

occupy the 3rd phase, ε_3 is thus remained as is in the equation. In short, the ER and ATR measurements are very similar to each other from the viewpoint of electrodynamics.

For the **p-polarization**,

$$\begin{aligned} A^{\mathrm{ATR,p}} &= -\frac{1}{\ln 10}\frac{4\eta\varepsilon_3{}^2\left(m_3{}^2\mathrm{TO}-X^2\mathrm{LO}\right)}{m_1\left(\varepsilon_3-\varepsilon_1\right)\left(\varepsilon_3-\varepsilon_1\tan^2\theta_1\right)} \\ &= \frac{1}{\ln 10}\frac{8\pi d_2\varepsilon_3{}^2\left(\dfrac{\cos^2\theta_3}{n_3{}^2}\cdot\mathrm{TO}-\varepsilon_1\sin^2\theta_1\cdot\mathrm{LO}\right)}{\lambda\dfrac{\cos\theta_1}{n_1}\left(\varepsilon_1-\varepsilon_3\right)\left(\varepsilon_3-\varepsilon_1\tan^2\theta_1\right)} \\ &= \boxed{\frac{8\pi d_2 n_1}{\ln 10\cdot\lambda}\frac{\left(n_1{}^2\sin^2\theta_1-n_3{}^2\right)\cdot\mathrm{TO}+\varepsilon_3{}^2\varepsilon_1\sin^2\theta_1\cdot\mathrm{LO}}{\cos\theta_1\left(\varepsilon_1-\varepsilon_3\right)\left(\varepsilon_1\tan^2\theta_1-\varepsilon_3\right)}} \\ &\equiv \frac{8\pi d_2}{\ln 10\cdot\lambda}\left(C_{\mathrm{pTO}}\cdot\mathrm{TO}+C_{\mathrm{pLO}}\cdot\mathrm{LO}\right) \end{aligned} \tag{3.87}$$

is obtained. Although ATR spectrometry yields a spectrum having a similar shape to that of a KBr pellet spectrum in practice, note that Eq. (3.87) is largely different from Eq. (1.43): the ATR spectrum is driven by both TO and LO energy loss functions; whereas the KBr pellet spectrum is influenced by only n''. Since the TO and LO functions are influenced not only by n'', but also n', the band position can be shifted from the KBr spectrum by the anomalous dispersion of n' (Fig. 1.7). As a conclusion, we have to carefully note that *an ATR spectrum cannot be a substitute of a KBr spectrum*.

To show this important comment explicitly, the calculated ATR spectra of an isotropic sample are compared to a calculated KBr-pellet spectrum by dotted curve in Fig. 3.15. Since an isotropic sample is considered, both s- and p-polarized ATR spectra have a similar spectral shape. On closer inspection, however, the peak positions of the strong absorption (the COO^- antisymmetric stretching vibration) band are found different from each other: p- and s-polarization exhibit the peak at

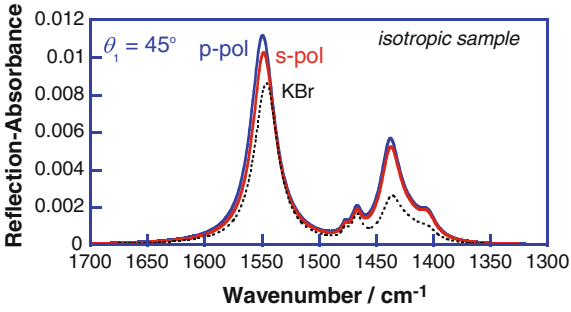

Fig. 3.15 Simulated ATR spectra of a thin film having isotropic structure. The *dotted* spectrum represents a KBr pellet spectrum

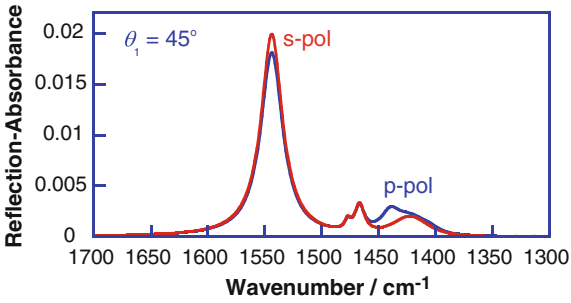

Fig. 3.16 Simulated ATR spectra calculated by Eqs. (3.87) and (3.88) using the complex refractive index in Fig. 3.8. The optical parameters of n_1 = 3.42 (Si), n_3 = 1.00 (air), d_2 = 2.5 nm and θ_1 = 45° are used

1549.4 and 1548.5 cm^{-1}, respectively. In addition, we have to note that the KBr-pellet spectrum yields the same band at 1546.1 cm^{-1}. This complicated situation has already been found at the example shown by Fig. 1.19. In this manner, a strongly absorbing band needs a special attention.

As done for other spectrometries, simulated p-polarized ATR spectrum of an oriented thin film is presented by the blue curve in Fig. 3.16. The angle of incidence is set to 45°, which is most commonly employed for ATR measurements. It should be noted that Eq. (3.87) that is intrinsically the same as Eq. (3.84) yields the ATR spectra by only exchanging the optical parameters between n_1 and n_3.

As shown later in Sect. 6.3, an ATR spectrum can be converted to an α spectrum (Eq. 1.43) that describes the KBr spectrum. If the ATR spectrum is discussed by comparing to a KBr spectrum, the ATR spectrum must be converted to an α spectrum.

When the angle of incidence is larger than the critical angle that is defined as $n_3 - n_1 \sin\theta_1 < 0$, both coefficients of the TO and LO functions (C_{pTO} *and* C_{pLO}) are negative. For a high refractive index substrate ($n_1^2 \gg 1$)and $n_3 = 1$, at the critical angle of the total reflection, $\tan\theta_c \approx \sin\theta_c$ holds because of:

$$\tan\theta_c = \frac{\sin\theta_c}{\cos\theta_c} = \frac{1/n_1}{\sqrt{1-(1/n_1)^2}} = \frac{1}{\sqrt{n_1^2-1}} \approx \frac{1}{n_1} = \sin\theta_c.$$

Therefore, the term of $\varepsilon_3 - \varepsilon_1 \tan^2\theta_1$ becomes negative for $\theta > \theta_c$ Since $\varepsilon_1 - \varepsilon_3 = n_1^2 - n_3^2 > 0$ holds, $A^{ATR,p}$ *is always positive when the 3rd phase is air*. Some representative simulation curves are available in Fig. 3.17. For the analysis of a thin film deposited on the ATR prism, refer to Fig. 3.17a. On the other hand, if a bulky sample is pressed onto the prism, refer to Fig. 3.17b.

As plotted in Fig. 3.17b, C_{pLO} and C_{pTO} are both positive irrespective of the angle of incidence as long as it is greater than the critical angle. In contrast to the intuitive speculation, however, the ratio of C_{pLO}/C_{pTO} is impervious to the angle of

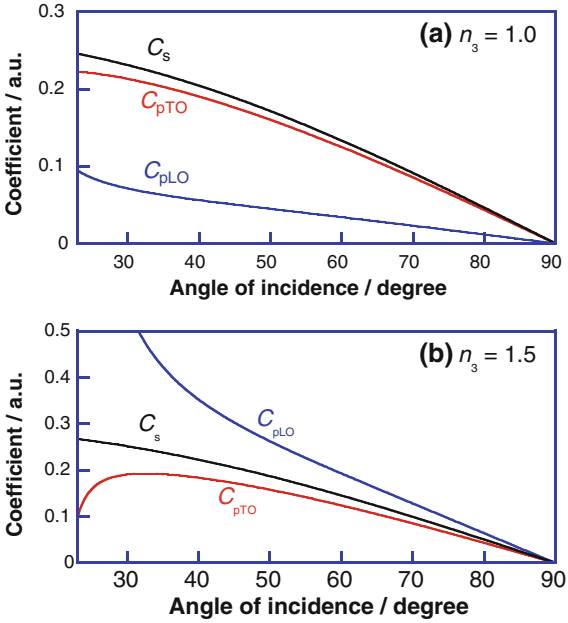

Fig. 3.17 Coefficients in Eqs. (3.87) and (3.88) as a function of the angle of incidence calculated for the interface of an ATR prism made of Ge (n_1 = 4.0) contacted with **a** air (n_3 = 1.0) and **b** a sample (n_3 = 1.5)

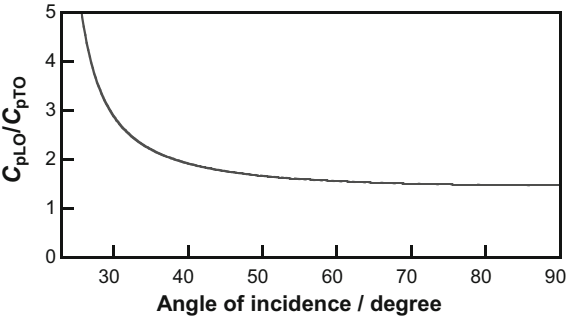

Fig. 3.18 Ratio of the coefficients of C_{pLO} to C_{pTO} against the angle of incidence

incidence as plotted in Fig. 3.18.When the angle of incidence is apart from the critical angle by 10° or larger, the variation of the ratio is very minor. This implies that an accurate molecular orientation analysis is difficult even with p-polarized spectra dependent on the angle of incidence.

If the ATR measurements are performed by using the **s-polarization**, a simpler spectrum is obtained, which can directly be compared to the normal incidence transmission spectrum, since the spectrum is governed by the TO energy loss function only.

$$A^{\mathrm{ATR,s}} = \boxed{-\frac{1}{\ln 10 \cdot \lambda} \frac{8\pi d_2 n_1 \cos\theta_1}{\varepsilon_3' - \varepsilon_1} \mathrm{Im}\left(\varepsilon_{x,2}\right)} \equiv \frac{8\pi d_2}{\ln 10 \cdot \lambda} C_\mathrm{s} \cdot \mathrm{TO} \tag{3.88}$$

As $\varepsilon_3' - \varepsilon_1 < 0$ holds, *the s-polarization ATR spectra have positive absorbance peaks only* as found in Fig. 3.17.

3.14 Specular Reflection Spectrum

When *no* film is on the surface of a *weakly absorbing* (*nonmetallic*) *bulk matter*, and IR light is directly incident on the surface, the reflection measurements are called *specular reflection spectrometry*. In this case, the concept of the background measurements is ambiguous, and only the reflectivity is considered.

If the incidental phase is assumed to be air, Eq. (3.22) can simply be used for the normal incidence measurements. In practice, small angle incidence (less than 15°) is used in place of the normal incidence within a good approximation.

$$\begin{aligned}\mathcal{R} &= \left|\frac{n_2 - 1}{n_2 + 1}\right|^2 = \left(\frac{n_2 - 1}{n_2 + 1}\right)\left(\frac{n_2^* - 1}{n_2^* + 1}\right) \\ &= \frac{1 + |n_2|^2 - 2\mathrm{Re}(n_2)}{1 + |n_2|^2 + 2\mathrm{Re}(n_2)} = \frac{1 + n_2'^2 + n_2''^2 - 2n_2'}{1 + n_2'^2 + n_2''^2 + 2n_2'} \\ &= \frac{\left(1 + n_2'\right) + n_2'' - 4n_2'}{\left(1 + n_2'\right)^2 + n_2''^2} \approx \frac{\left(1 + n_2'\right)^2 - 4n_2'}{\left(1 + n_2'\right)^2} \\ &= 1 - \frac{4\mathrm{Re}(n_2)}{A},\end{aligned}$$

where $A \equiv \left(1 + n_2'\right)^2$. Since the anomalous dispersion of n_2' is also weak (Fig. 1.7), and therefore A can roughly be approximated to be a constant. As a result, the spectrum is driven by the real part of the refractive index of the bulk material, which requires a spectral conversion technique to have an absorbance-like spectrum. The details will be mentioned later in Sect. 6.1.

3.15 Surface Selection Rules of IR Surface Spectroscopy

In the former sections, analytical procedures and expressions of practically useful IR surface spectroscopy are studied on electrodynamics using Abeles' transfer matrix method. Through the techniques, we have found that the surface

spectroscopy for a thin-film analysis is theorized by using the TO and LO energy loss functions only. Since TO and LO functions are a function of $\varepsilon_{x,2}$ and $\varepsilon_{z,2}$, respectively, they retrieve the surface-parallel and -perpendicular components of a transition moment, which is a quite useful rule to discuss the *average molecular orientation* in a thin film.

The analytical expressions can thus be summarized to be simple and practical rules for conveniently discussing the molecular orientation in a thin layer. The simplified rules are called the *surface selection rules* (*SSRs*) [5, 15, 16], which are summarized in Table 3.2.

The SSRs are highly useful for discussing the molecular orientation in a thin film. The practical aspects are described as follows:

Table 3.2 Surface selection rules depending on measurement techniques and polarizations

Measurement techniques	Pol.	Surface selection rules
(A) Transmission	s	Irrespective of angles of incidence, only the surface-parallel component of a transition moment appears in the spectrum. All the bands appear as positive peaks
	p	When IR light is normally incident on the surface, only the surface-parallel component of a transition moment is observed. When the angle of incidence is increased, the surface normal component appears and increased with the angle
(B) Reflection Absorption (RA)	s	Practically useless because of a poor SN ratio. If this spectrum is needed, a small angle of incidence should be chosen. In addition, the band intensities respond to choice of the substrate material
	p	A grazing angle of incidence (at near 80°) is chosen for high-sensitive measurements of a thin film on a metallic surface. Only the surface normal component of a transition moment is observed. This spectrum is impervious to choice of the substrate material as long as the substrate is metallic
(C) External Reflection (ER)	s	Irrespective of angles of incidence, only the surface-parallel component of a transition moment appears in the spectrum. All the bands appear as negative peaks, and the peak intensity decreases with an angle of incidence
	p	When the angle of incidence is less than Brewster's angle of the substrate, the surface-parallel component of a transition moment yields a negative absorbance peak; whereas the surface normal component yields a positive peak. When the angle of incidence is larger than Brewster's angle, the relationships are overturned
(D) Attenuated Total Reflection (ATR)	s	As long as the angle of incidence is greater than the critical angle, only the surface-parallel component of a transition moment appears in the spectrum. All the bands appear as positive peaks
	p	All the bands appear as positive peaks. Both surface normal and parallel components of a transition moment appear in the spectrum

(A) Transmission spectrometry

When an IR ray is irradiated on a thin film deposited on an IR-transparent substrate and the transmitted light is measured by the spectrometer (Fig. 3.19), this measurement technique is called *transmission spectrometry*. In most cases, the angle of incidence is set to be zero. In the case of the normal incidence, no discrimination is available for the s- and p-polarizations.

As found in the figure, for the normal incidence, the oscillating direction of the electric field is parallel to the film surface. As a result, only the surface-parallel component of a transition moment appears in a transmission spectrum. This intuitive understanding agrees with the Eq. (3.73) that the light absorption is governed by $\varepsilon_{x,2}$ that is the surface-parallel component of the permittivity of the thin film, which is the SSR of transmission spectrometry.

Note that the absorbance is a function of $\mathrm{Im}\left(\varepsilon_{x,2}\right) = 2n'_{x,2}n''_{x,2}$ (TO energy loss function), which is influenced not only by $n''_{x,2}$ but also by $n'_{x,2}$. Therefore, the direct comparison with a KBr pellet spectrum (Eq. 1.36) makes us go to a wrong direction on an inaccurate band position and relative band intensity especially for a strongly absorbing band (Fig. 1.20). If we need a direct comparison, the KBr pellet spectrum $\left(n''_{x,2}\right)$ should be converted by using the Kramers–Kronig relationship (Sect. 4.4) to have the corresponding $\mathrm{Im}\left(\varepsilon_{x,2}\right)$ spectrum. In this case, note that the concentration diluted by the KBr powder must be taken into account.

In Fig. 3.20, an IR transmission (Tr) spectrum of a 7-monolayer Langmuir–Blodgett (LB) film of cadmium stearate deposited on a calcium fluoride substrate is presented on the bottom.

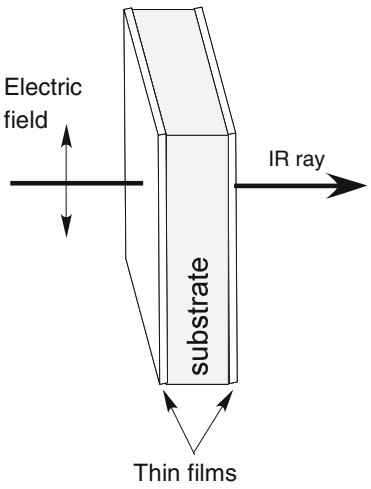

Fig. 3.19 Schematic of transmission spectrometry with a normal incidence

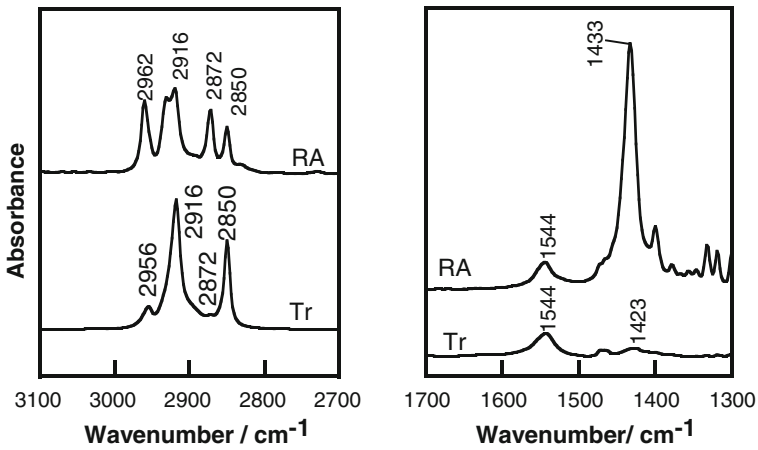

Fig. 3.20 IR Transmission (Tr) and RA spectra of a 7-monolayer Langmuir–Blodgett film of cadmium stearate deposited on a CaF_2 (Tr) and silver (RA) substrate, respectively

Both antisymmetric and symmetric CH_2 stretching vibration [$\nu_a(CH_2)$ and $\nu_s(CH_2)$] bands appear strongly at 2916 and 2850 cm^{-1} in the Tr spectrum, respectively. The strong appearance straightforwardly indicates that both modes are nearly parallel to the substrate surface judging from the SSR. These vibrational modes respond to the molecular conformation, and both positions are specific to the all-trans zigzag conformation within a planer skeleton (Fig. 3.21), which implies that the molecules are highly packed. With this ordered conformation, the two modes and the molecular axis are mutually orthogonal to each other. As a result, the strong appearance of the two bands implies a nearly perpendicular orientation of the molecular axis to the substrate surface (Fig. 3.20).

The terminal methyl (CH_3) group yields three normal modes of the asymmetric in-skeleton, asymmetric out-of-skeleton, and symmetric CH_3 stretching vibrations, which are denoted as $\nu_a(CH_3)^{is}$, $\nu_a(CH_3)^{os}$ and $\nu_s(CH_3)$, respectively (see Fig. 3.21), appeared at 2962, 2956 and 2872 cm^{-1}. Since the $\nu_a(CH_3)^{os}$ mode is highly parallel orientation to the surface, this band appears in the Tr spectrum only; whereas the rest two bands appear in both Tr and RA spectra. Note that the $\nu_s(CH_3)$ band is relatively much weaker than the $\nu_a(CH_2)$ and $\nu_s(CH_2)$ bands in the Tr spectrum.

If the molecular axis has a perpendicular stance, the ionized carboxylic group would also have a nearly perpendicular stance to the surface (Fig. 3.21). In fact, the antisymmetric COO^- stretching vibration [$\nu_a(COO^-)$] mode appears strongly at 1544 cm^{-1}, while the symmetric COO^- stretching vibration [$\nu_s(COO^-)$] mode appears weakly at 1423 cm^{-1}, which confirms the orientation model proposed by the analysis of the $\nu_a(CH_2)$ and $\nu_s(CH_2)$ bands.

In this manner, a small chemical group such as CH_2 and COO^- has multiple number of normal modes, which totally depict a molecular picture, which is one of the great benefits of using vibrational spectroscopy with an aid of SSR.

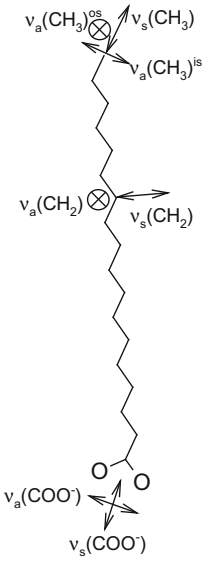

Fig. 3.21 Schematic of a cadmium stearate molecule in an LB film

(B) Reflection absorption (RA) spectrometry

When a thin film is deposited on a *metallic surface*, and the IR spectrum is measured by using the reflection geometry with a grazing angle of incidence, the technique is called reflection absorption (RA) spectrometry [17] (Fig. 3.22).

In RA spectrometry, only the p-polarization is employed as shown in Eq. (3.82). The RA spectra are defined as:

$$A^{\mathrm{RA,p}} \equiv -\log_{10}\frac{R^{\mathrm{p}}_{\mathrm{sample}}}{R^{\mathrm{p}}_{\mathrm{BG}}}. \tag{3.89}$$

This reflection-specific absorbance via reflectance is defined as "*reflection absorbance*." Nevertheless, the direct observable on FT-IR is not reflectance, but the single-beam spectra on the sample and background surfaces (I_{sample} and I_{BG}, respectively) are measured. The reflectance spectra are defined as:

$$R^{\mathrm{p}}_{\mathrm{sample}} = \frac{I_{\mathrm{sample}}}{I_0} \text{ and } R^{\mathrm{p}}_{\mathrm{BG}} = \frac{I_{\mathrm{BG}}}{I'_0}$$

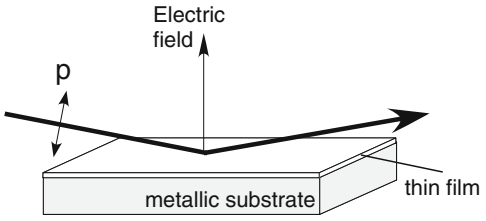

Fig. 3.22 Schematic of RA spectrometry with a grazing angle of incidence

where I_0 and I_0' are the IR single-beam spectra before irradiating on the surface. Since $I_0 \approx I_0'$ holds within an acceptable approximation,

$$A^{\mathrm{RA,p}} = -\log_{10}\frac{R^{\mathrm{p}}_{\mathrm{sample}}}{R^{\mathrm{p}}_{\mathrm{BG}}} = -\log_{10}\frac{I_{\mathrm{sample}}}{I_{\mathrm{BG}}}$$

is conveniently obtained. Therefore, *the reflection absorbance can be regarded as the normal absorbance*.

As illustrated in Fig. 3.22, the electric fields of the incident and reflected rays are interfered with each other to generate an RA specific electric field in the vicinity of the surface, whose direction is perpendicular to the substrate surface. Therefore, only the surface normal component of normal modes appears in the RA spectra, which is called the *SSR of RA spectrometry*.

The SSR is theorized by Eq. (3.82), in which only the surface normal component the electric permittivity of the thin film phase $(\varepsilon_{z,2})$ is measured via the LO energy loss function $(\mathrm{Im}(-1/\varepsilon_{z2}))$. To obtain the pure LO function of an ultrathin film, therefore, RA spectrometry is an important technique, which is complimentary with the transmission spectrometry.

When we compare an RA spectrum to a spectrum obtained by another technique, such as Tr and KBr techniques, we have to pay a special attention to the band shift and change of the relative band intensities. This is because a direct comparison between the LO function to the TO and α (Eq. 1.36) functions can mislead the scientific discussion to a wrong direction. For practical details, please refer to Sect. 6.3.

In Fig. 3.20, an RA spectrum of an identical thin film deposited on a silver surface is presented with a corresponding Tr spectrum. Although the stearic acid has only one methyl group, the $\nu_s(CH_3)$ band appears apparently thanks to the SSR with the perpendicular orientation. The $\nu_a(CH_2)$ and $\nu_s(CH_2)$ bands are largely suppressed when considering the number (sixteen) of methylene groups. The reason why even the suppressed bands have a comparable intensity with the Tr bands is that the RA spectrum is enhanced. Indeed, RA spectrometry is known as a *high-sensitive technique*, whose enhancement factor is ca. 10, which is quite powerful for studying a thin film or molecular adsorbates on a metallic surface.

If unpolarized light is used for the RA measurements, the contribution of the s-polarization component is ignorable, which does not matter significantly for a practical analysis. In this sense, the polarizer can be removed. In this *simplified* experiments, however, we have to note that *half absorbance is obtained* because of the following reason (see also Eq. 3.2).

$$A^{\mathrm{RA,un\text{-}polarized}} \approx \frac{1}{\ln 10}\frac{\Delta I^{p}_{\mathrm{sample}} + \cancel{\Delta I^{\mathrm{s}}_{\mathrm{sample}}}}{I^{\mathrm{p}}_{\mathrm{BG}} + I^{\mathrm{s}}_{\mathrm{BG}}} \approx \frac{1}{\ln 10}\frac{\Delta I^{p}_{\mathrm{sample}}}{2I^{\mathrm{p}}_{\mathrm{BG}}} = \frac{A^{\mathrm{RA,p}}}{2}$$

Here, $I^{\mathrm{p}}_{\mathrm{BG}} \approx I^{\mathrm{s}}_{\mathrm{BG}}$ holds on a highly reflective metallic surface, and the polarization dependence of FT-IR is ignored. Of course, the un-polarized light intensity is twice as large as the p-polarization, which makes the SN ratio better. As a result, in terms of the

spectral quality, ignorable difference is found between the un-polarized and p-polarized measurements. Regardless, the p-polarization measurements should be employed, since we don't have to take care about the polarization dependence of FT-IR with the single polarization. In short, if you want to discuss the RA spectra quantitatively based on an electromagnetic theory, p-polarization measurements is the only choice.

(C) External reflection (ER) spectrometry

When the analyte thin film is deposited on a *nonmetallic surface* (Fig. 3.23), the reflection measurements are categorized into external reflection (ER) spectrometry, which is strictly discriminated from RA spectrometry. The ordinate scale of an ER spectrum is reflection absorbance, whose definition is the same as that of RA spectrometry (Eq. 3.89).

The analytical expressions of the p- and s-polarized ER spectrometries are presented in Sect. 3.12. These equations are quite convenient to understand that a p-polarized ER spectrum comprises TO and LO energy loss functions; whereas an s-polarized ER spectrum is governed by the TO function only. Since the TO and LO functions involves $\varepsilon_{x,2}$ and $\varepsilon_{z,2}$, respectively, the ER spectra should respond to the molecular uniaxial orientation in the thin film via the anisotropic permittivity.

To understand the equations more intuitively, Hansen's approximated equations (Eqs. 3.90–3.91) are highly useful. He expanded the equations of reflectance (Eq. 3.75) in Taylor's manner in terms of the film thickness. With the use of the thin-film approximation (Eq. 3.2), the following equations are obtained.

$$A_{sy} = -\frac{4}{\ln 10}\left(\frac{\cos\theta_i}{n_3^2 - 1}\right) n_{2x}\alpha_{2x}d_2 \tag{3.90}$$

$$\begin{aligned} A_{sz} &= 0 \\ A_{px} &= \frac{4}{\ln 10}\left(\frac{\cos\theta_i}{\xi_3^2/n_3^4 - \cos^2\theta_i}\right)\frac{\xi_3^2}{n_3^4} n_{2x}\alpha_{2x}d_2 \\ A_{pz} &= \frac{4}{\ln 10}\left(\frac{\cos\theta_i}{\xi_3^2/n_3^4 - \cos^2\theta_i}\right)\frac{\sin^2\theta_i}{\left(n_{2z}^2 + k_{2z}^2\right)^2} n_{2z}\alpha_{2z}d_2 \end{aligned} \tag{3.91}$$

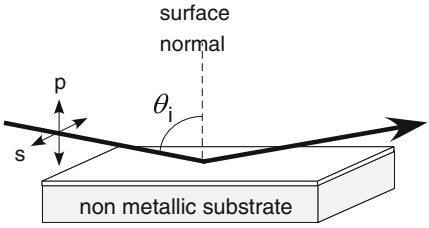

Fig. 3.23 Schematic of ER spectrometry for both s- and p-polarizations

Here, $\alpha_{2\sigma} \equiv 4\pi k_{2\sigma}\tilde{\nu}\,(\sigma = x, z)$, and $\xi_j \equiv n_j \cos\theta_j$. In his original paper, two equations of A_s and $A_{px} + A_{pz}$ are obtained by the expansion. Very fortunately, however, $A_{px} + A_{pz}$ can simply be separated for the surface-parallel and -perpendicular components. In a similar manner, A_s can be recognized as $A_{sy} + A_{sz}$ which is also separated. Hansen's equations are very much user friendly, which holds well when (1) the thickness of the film is adequately thin $(d/\lambda \ll 1)$. and (2) the substrate does not absorb IR light. Therefore, these equations cannot be used for RA spectrometry.

$k_{2x}\left(= k_{2y}\right)$ and k_{2z} reflects the orientation of a transition moment, which are related to the bulk (un-oriented) absorption coefficient, k_{bulk}, by [13]:

$$\frac{k_{2x} + k_{2y} + k_{2z}}{3} = k_{\text{bulk}}.$$

For the surface-parallel orientation, $k_{2z} = 0$ is put in this equation to have $k_{2x} = 3k_{\text{bulk}}/2$. In a similar manner, the surface-perpendicular orientation is expressed by $k_{2z} = 3k_{\text{bulk}}$ after putting $k_{2z} = k_{2y} = 0$. Therefore, for an orientation of ϕ, the following relationships are obtained.

$$k_{2x}\left(= k_{2y}\right) = \frac{3}{2} k_{\text{bulk}} \sin^2\phi \tag{3.92}$$

$$k_{2z} = 3k_{\text{bulk}} \cos^2\phi \tag{3.93}$$

An example simulation curves using the equations are presented in Fig. 3.24 [13]. This figure has the same trends as the coefficients of the TO and LO functions in Fig. 3.13. These curves are for the $\nu_s(CH_2)$ band at 2850 cm^{-1} of a thin film with a thickness of 22.5 nm (corresponding to a 9 monolayer LB film of stearic acid) having the optical parameters of $n_{2x} = 1.48$, $n_{2x} = 1.56$, and $k_{\text{bulk}} = 0.3$. In this manner, the curves are easily calculated by using Hansen's equations, if the optical parameters are available.

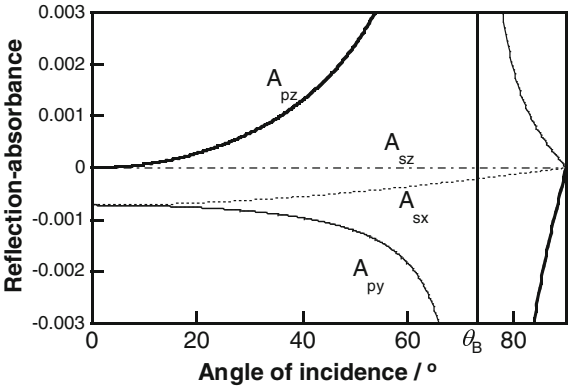

Fig. 3.24 Calculated absorbance of the p- and s-polarizations for a surface-parallel (x) and -normal (z) oriented mode on a silicon surface

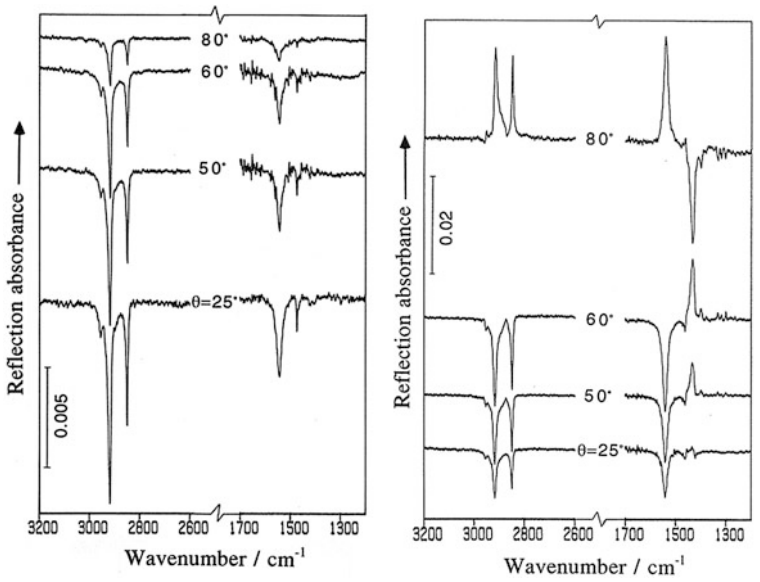

Fig. 3.25 IR s- (*left panel*) and p-polarized (*right panel*) ER spectra of a 9-monolayer LB film of cadmium stearate deposited on a single-side polished GaAs wafer as a function of the angle of incidence

When a surface-parallel transition moment is measured by the s-polarization, all the bands (A_{sx}) are found to be negative irrespective of the angle of incidence, which is apparently expressed by Eqs. (3.88) and (3.90). The negative bands develop with an increase of the angle of incidence as found in Fig. 3.25 [13]. Therefore, a low angle of incidence should be selected for high-quality measurements.

On the other hand, the p-polarized reflection absorbance changes the sign at Brewster's angle that is defined by Eq. (3.85), which is apparently observed as presented in Fig. 3.25. For example, the $\nu_s(COO^-)$ band at 1433 cm^{-1} having the surface-perpendicular transition moment appears as a positive band and it develops with increasing the angle of incidence. When the angle goes across Brewster's angle (ca. 73°), the band suddenly changes its sign, and a negative band appears. The complicated variation is perfectly theorized by both Eqs. (3.84) and (3.91).

Since the band intensity drastically increases when the angle of incidence is close to Brewster's angle, an angle near 73° looks good for high-sensitive measurements. As a matter of fact, however, this idea should be reconsidered, since it is an extremely dark measurement.

Figure 3.26 presents calculated 'reflectance' for both polarizations at the air/silicon interface. Since the reflectance of the p-polarization near Brewster's angle is close to zero, which makes the optical throughput terribly poor resulting in dark measurements with a poor signal-to-noise ratio. Therefore, for the

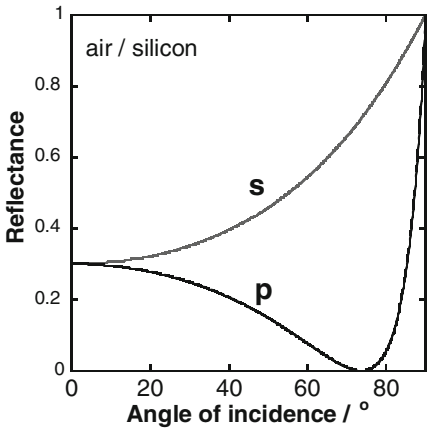

Fig. 3.26 Polarization-dependent reflectance with an angle of incidence at the air/silicon interface

p-polarization measurements, the angle of incidence should be chosen at an angle a little bit far from Brewster's angle [18], i.e., 60° or 80° is a good choice for the p-polarized ER measurements on a silicon surface ($n = 3.42$).

(D) **Attenuated total reflection (ATR) spectrometry**

The ATR technique is becoming a standard IR measurement technique for a bulk sample, which is squeezing out the KBr pellet technique, since the operation of ATR spectrometry is much easier than the KBr technique. Nevertheless, *this situation can make the scientific discussion on the ATR spectra go to a wrong direction*. Since ATR spectroscopy is based on a reflection measurement at an optical interface, *no α-spectrum cannot be obtained*, to which we have to pay special attention.

ATR is one of the internal reflection($n_1 > n_2$ in Fig. 3.27) spectrometries, and the angle of incidence, θ_1, is set at an angle greater than the *critical angle*, θ_c, which satisfies $(n_1/n_2')sin\theta_c = 1$ On this condition, the incident IR light is *totally reflected* at the ATR prism surface and going to the detector.

When the electric field of the incidental light is expressed as:

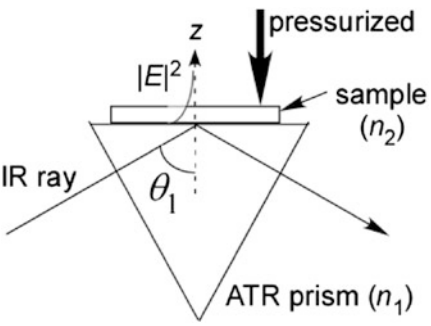

Fig. 3.27 Optical configuration of ATR spectrometry. An image of the electric field decay of the evanescent wave is overlaid

$$\boldsymbol{E} = \boldsymbol{E}_0 exp\{\mathrm{i}[k \cdot r - \omega t]\},$$

the z-component of the penetrated electric field into the sample phase (2nd phase) with an isotropic refractive index of n_2 is (see Eq. 1.36):

$$\boldsymbol{E}_z \propto \boldsymbol{E}_0 \exp\{\mathrm{i}[n_2 k \cos\theta_2 z - \omega t]\} \tag{3.94}$$

because of the continuity of the wavenumber vector across an interface (Eq. 3.41). When Snell's law is employed thanks to the isotropic system, the time-averaged (Eq. 3.19) electric field intensity decay is calculated by considering that both n_2 and $\cos\theta_2$ are complex (Eq. 3.42).

$$\begin{aligned}
\frac{1}{2}|\boldsymbol{E}_z|^2 &= \frac{1}{2}\boldsymbol{E}_z\boldsymbol{E}_z^* \\
&= \frac{1}{2}\boldsymbol{E}_0^2 \exp\{-2kz\,\mathrm{Im}(n_2\cos\theta_2)\} \\
&= \frac{1}{2}\boldsymbol{E}_0^2 \exp\left\{-2kz\,\mathrm{Im}\left(n_2\sqrt{1-\left(n_1^2/n_2'^2\right)\sin^2\theta_1}\right)\right\} \\
&= \frac{1}{2}\boldsymbol{E}_0^2 \exp\left\{-2kzn_2'\sqrt{\left(n_1^2/n_2'^2\right)\sin^2\theta_1 - 1}\right\}
\end{aligned} \tag{3.95}$$

The last deformation was done by considering that the angle is greater than θ_c with a condition of $n_1 > n_2$. In this manner, on the total reflection, the electric field of the evanescent wave decays exponentially with z.

If the *real penetration depth*, $d_\mathrm{p}^\mathrm{intensity}$, is determined as the depth where the *intensity* is decreased by a factor of e^{-1}, $d_\mathrm{p}^\mathrm{intensity}$ is obtained as:

$$\begin{aligned}
&-2kd_\mathrm{p}^\mathrm{intensity} n_2'\sqrt{\left(n_1^2/n_2'^2\right)\sin^2\theta_1 - 1} = -1 \\
&\Leftrightarrow d_\mathrm{p}^\mathrm{intensity} = \frac{\lambda}{4\pi\sqrt{n_1^2\sin^2\theta_1 - n_2'^2}}
\end{aligned}$$

If the sample thickness is smaller than $d_\mathrm{p}^\mathrm{intensity}$, n_2' is replaced by unity (air phase). In fact, as found in Eq. (3.87), the 3rd (air) and 1st (prism) phases are directly interrelated with each other for a thin sample. When the thickness is large enough, on the other hand, n_2' is set to the refractive index of the sample. In general, an organic compound has $n_2' = 1.5$.

If d_p is defined in terms of *amplitude of electric field* (not 'intensity' [18]) by using Eq. (3.94), the factor of 2 is removed to have another more popular definition [11]:

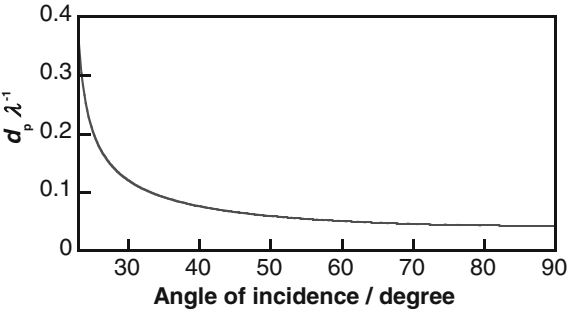

Fig. 3.28 d_p/λ is plotted against the angle of incidence calculated for $n_1 = 4.0$ (Ge) and $n_2 = 1.5$

$$\boxed{d_p = \frac{\lambda}{2\sqrt{n_1^2 \sin^2\theta_1 - n_2'^2}}}.$$

Of course, the purposes of the two definitions are common, but we have to pay attention when we use it for a quantitative purpose.

Figure 3.28 presents a plot d_p/λ against the angle of incidence for a general organic compound having $n_2' = 1.5$ contacted on an ATR prism of germanium ($n_1 = 4.0$). In general, the angle of incidence is taken a little bit far from the critical angle, for example 30° or larger. We find that the penetration depth reaches *about one-tenth as large as the wavelength*. Therefore, in the C–H stretching vibration region (ca. 3000 cm^{-1}, i.e., 3.3 μm), the IR light is expected to penetrate into the sample with a depth of ca. 300 nm.

Of interest is that this curve has a shape of convex downward, which is different from that of absorbance change (Fig. 3.17). This implies that *the ATR intensity is not driven by the penetration depth*.

Some researchers involving Harrick and Hansen reported in a similar time [19–21], the *actual* penetration depth, d_{act}, is represented by a more complicated equation. For example, for the s-polarization, d_{act}, is expressed by using Hansen's notation as:

$$d_{act} = \frac{(\lambda/n_2)n_{21}^2 \cos\theta}{\pi\left(n_{21}^2 - 1\right)\left(n_{21}^2 - \sin^2\theta\right)^{1/2}}, \tag{3.96}$$

which is presented in Fig. 3.29. Here, n_1 and n_2 corresponds to the refractive indices of the ATR prism and a bulky sample, respectively. n_{21} is a ratio of n_2 to n_1. The calculated curve is found quite similar to the C_s curve in Fig. 3.17b, which indicates that Eq. (3.96) works well.

Hirschfeld [21] tried to correlate d_{act} with d_p by considering Goos-Hänschen's shift. This shift is quite intuitively understandable as presented in Fig. 3.30: the reflected light is shifted by D, and the length of the virtually penetrated 'light' represented by the red curve with a length of d_s is correlated with the light absorption.

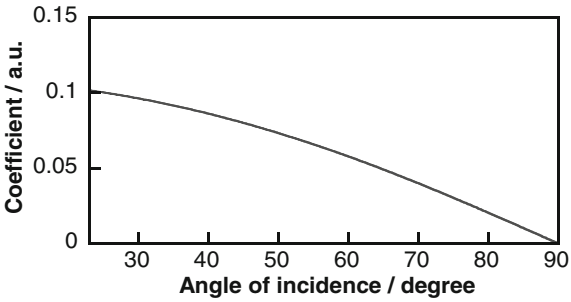

Fig. 3.29 The actual penetration depth curve for the s-polarization calculated with $n_1 = 4.0$ (Ge) and $n_2 = 1.5$

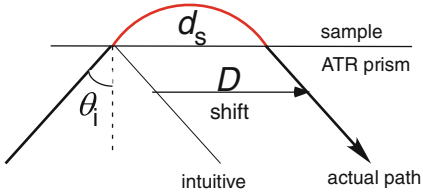

Fig. 3.30 Schematic of the Goos-Hänschen shift

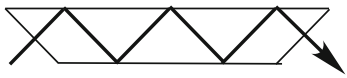

Fig. 3.31 An ATR prism having five times reflections

Unfortunately, however, the intuitive correlation does not work at all except the angle at the critical angle [22]. In this manner, the illustrative understanding of ATR spectrometry is quite difficult.

The ATR technique can be used for two purposes. The first one is for *reducing* the absorbance to measure an IR spectrum of *strongly absorbing thick* sample, such as a rubber. Since a rubber or water absorbs IR light too strongly, the transmission technique cannot be employed. ATR works powerfully for this case, since only the evanescent wave contributes to the IR absorption.

The second purpose is, on the contrary, for *enhancing the sensitivity*. Figure 3.31 presents a schematic of a side view of a trapezoidal-shaped ATR prism for multiple reflections. Because of the total reflections, only the absorption by the sample via the evanescent wave on both sides of the prism contributes to the IR spectrum, which is five times greater than the single reflection type in Fig. 3.27. The multiple-reflection type ATR is sometimes used for measurements of a monolayer-level thin film particularly in an aqueous solution as schematically shown in Fig. 3.32 [23]. In other words, in this case, the ATR prism is used, as if it were an optical fiber.

The SSR of ATR is available for only the s-polarization. As found in Eq. (3.88), an s-polarized ATR spectrum retrieves only the TO energy loss function of ε_x. Therefore, only the surface-parallel component (along x) of normal modes is observed in the spectrum. If a stretched polymer film is measured by this technique, in-plane orientation can be discussed.

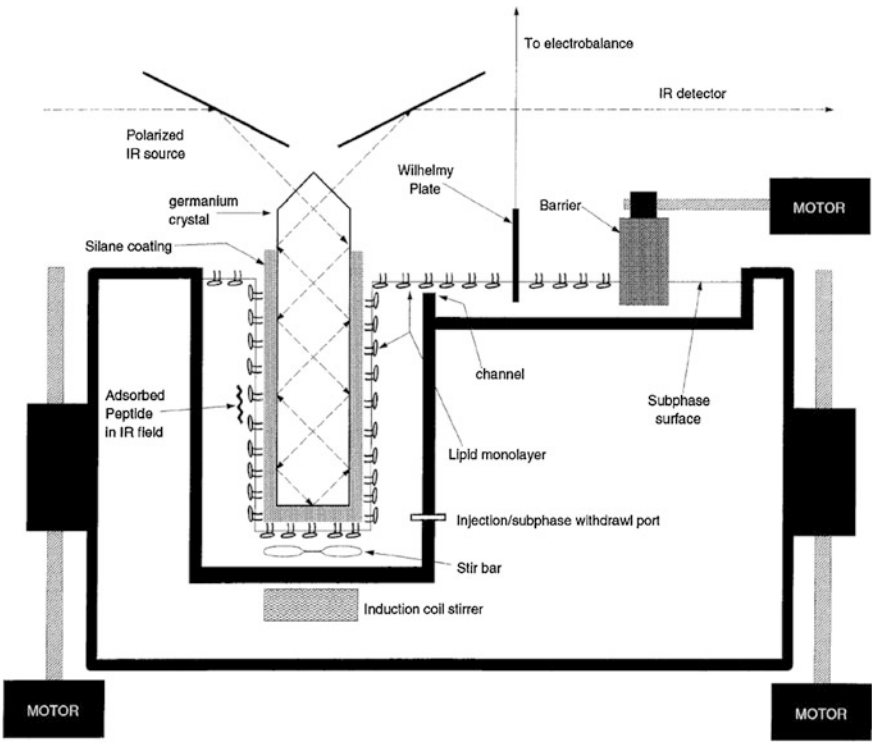

Fig. 3.32 An ATR prism made of germanium is used as an IR optical fiber to monitor molecular adsorbates from an aqueous solution [22]

If the p-polarization is employed, both TO and LO functions appear in an overlaid manner. Since the surface-perpendicular component of a transition moment is observed by the p-polarization only, however, the difference from the s-polarization spectrum is useful for discussing the orientation in a thinly adsorbed layer.

Tripp et al. [24] employed a similar optical configuration for studying the molecular orientation of cetyltrimethylammonium bromide (CTAB) adsorbed at the silica/solution interface over the pH range from 2 through 10 using both s- and p-polarizations. The dichroic ratio of the two polarizations is defined by using the surface electric fields as:

$$\frac{A_{\mathrm{s}}}{A_{\mathrm{p}}} = \frac{E_y^2}{E_x^2 + E_z^2}.$$

They employ the electric field intensities derived by Harrick [19], which correspond to the coefficients appeared in Eqs. (3.87) and (3.88), to propose an order parameter: 1.22 and 0.65 for perpendicular and random orientations, respectively.

3.16 Sampling Techniques

Practically useful sampling techniques for FT-IR are described. To analyze the molecular structure and orientation, *comparison of an isotropic sample with an oriented sample is necessary*, since the isotropic sample provides a spectrum of the intrinsic relative band intensities.

Isotropic sample

(A) **KBr pellet technique (solid samples)**

When an IR spectrum of a solid sample is measured by FT-IR, the KBr pellet technique is the most fundamental one. Note that IR *spectra database is mostly constructed on the KBr pellet spectra*. This technique is usually employed for a solid sample. To make a pellet with a diameter of 1 cm, for example, ca. 100 mg of dried KBr powder is taken, which is subjected to grind in an agate mortar (Fig. 3.33) to obtain a very fine powder. The ground KBr powder is pressed to have a visually transparent disk, which is called 'pellet.' Recently, a simple press without vacuuming is conveniently used, and 7 mm- or 5 mm disk is also used. The KBr disk involving no sample is used for the background measurement.

On the other hand, another KBr powder containing a sample disk is prepared. The sample is diluted by the KBr powder during the grinding with a concentration of ca. 1 wt% or lower. *A high concertation disk results in too strong absorbance peaks more than 0.5, which would inaccurate relative band intensities* because of the apodization function (Sect. 2.4). If the most intense band is more than 0.5, the sample disc should be remade by adding KBr powder for dilution.

Grinding usually keeps the crystallinity of the sample, i.e., the crystallite is crushed by the grinding into *many micro crystallites with random orientations*. Figure 1.5 presents an IR KBr pellet spectrum of stearic acid. The νCH_2 bands at 2918 and 2849 cm^{-1} apparently indicate that the hydrocarbon chains have the

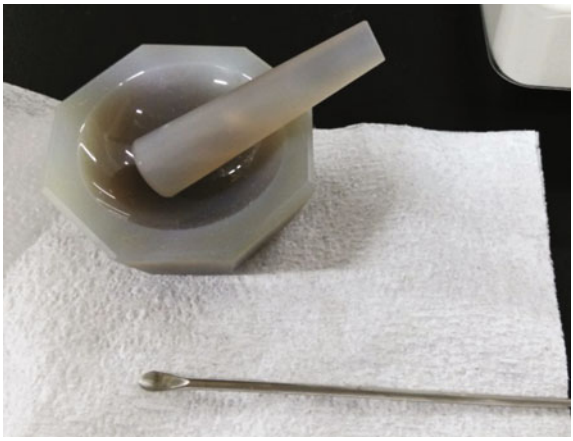

Fig. 3.33 Agate mortar and a micro spatula on a Kimwipes paper

all-trans conformation (Table 1.2), which strongly implies that the molecules are involved in a crystallite. In fact, the δCH_2 band is split into two peaks at 1473 and 1462 cm^{-1} accompanying the band progression, which confirms that the molecules with the planer-zigzag molecular skeleton are packed with the orthorhombic subcell packing, i.e., crystallite. In this manner, the crystallinity is kept even after the find grinding. Therefore, the key points of the KBr pellet technique are summarized briefly.

1. Crystallite of the sample compound is crushed into minute parts, but crystallinity is not lost in many cases.
2. The molecular orientation is disordered as a result of the *random orientation* of the micro crystallites, which yields an "α *spectrum* (Eq. 6.4)."
3. Water vapor in ambient air is absorbed in the KBr powder because of the hygroscopicity.

(B) **Nujol mull method (mostly solid samples)**

Another sampling technique for a solid sample is the *Nujol mull method*. Nujol is liquid paraffin, which consists of only the methylene chain terminated with the methyl group. If the sample is reacted with potassium or bromide ions, the KBr pellet technique cannot be employed, and instead the Nujol method is employed.

Since Nujol is a paraffin, most of organic compounds having an alkyl chain is dissolved to be a liquid, which is subjected to an IR transmission spectrometry using IR-transparent windows such as NaCl, CaF_2 and KBr.

Note that the solubility is quite high, and the crystallinity of the sample would be lost during the mixing process. Another notable point is that useful IR window region is limited *except* some regions related to the C–H stretching, and deformation bands, i.e., 2950–2800, 1475–1450 and 1380–1370 cm^{-1}.

(C) **Solvent soluble samples**

If the sample is soluble in chloroform or carbon tetrachloride, an IR spectrum of the sample can be measured by using a liquid film jacket that consists of two IR-transparent windows sandwiching a spacer ring.

To suppress IR absorption, a low concentration sample should be used, and path length should also be small such as 10 μm. Unfortunately, however, this liquid thickness sometimes generates optical fringes in the spectrum. Therefore, the thickness must be changed by replacing a spacer ring. Another note is that too small thickness would not yield an α-spectrum.

As a solvent, carbontetrachloride (CCl_4) and chloroform are conveniently used, since they are good solvent for many organic compounds, and many band regions are useful as *IR window regions*. As presented in Fig. 3.34a, in particular, carbontetrachloride has a very wide window region having no absorption band.

Oriented sample

When an oriented sample is measured by FT-IR, the angle of incidence must be fixed at an accurate position. In addition, the reflected light must be led to the

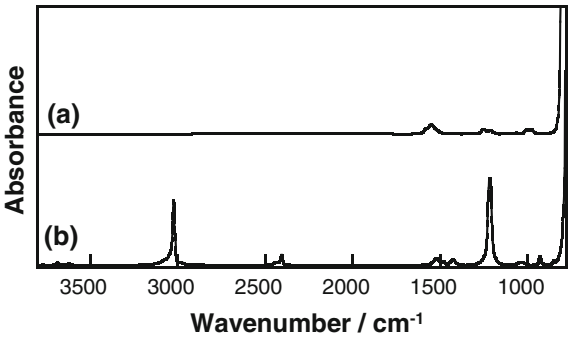

Fig. 3.34 IR spectra of **a** carbontetrachloride and **b** chloroform

detector, as if no reflector were present in the sample room. To do that, a specially designed reflector should be used as presented in Fig. 3.35.

The modulated IR light coming from the right window passes through the polarizer, and the polarized IR light is reflected three times to attain the sample surface. The sample is held on the angle adjusting stage, which determines the angle of incidence accurately. The reflected light on the sample goes to the detector via three bounces on mirrors, which are necessary to adjust the light path and the focusing on the detector, as if a transmission measurement were performed.

When the angle of incidence is changed by rotating the angle adjusting stage, the irradiating point on the sample often changes. If the sample thin film is not homogeneous on the substrate, we should keep the irradiating point by adjusting the concave mirror. For the light alignment, the leaked He–Ne laser light should be used as a convenient marker, since the IR light is invisible. As mentioned in Sect. 2.3, the laser light had already been measured by a small detector near the interferometer, the red laser light can be intercepted by the sample or polarizer.

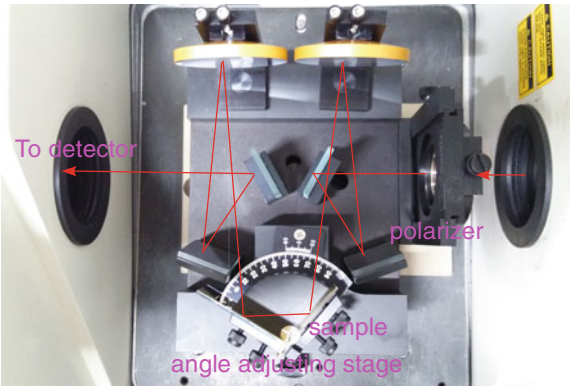

Fig. 3.35 A sample stage for reflection measurements, which can commonly be used for RA, ER and specular reflection measurements. The *red line* is the path of invisible IR light

References

1. J.D. Jackson, *Classical Electrodynamics,* 3rd edn. (Wiley, New York, 1998)
2. Y. Itoh, T. Hasegawa, J. Phys. Chem. A **116**, 5560–5570 (2012)
3. D.W. Berreman, Phys. Rev. **130**, 2193–2198 (1963)
4. P. Yeh, *Optical Waves in Layered Media*, 2nd edn. (Wiley, Hoboken, 2005)
5. V.P. Tolstoy, I.V. Chernyshova, V.A. Skryshevsky, *Handbook of Infrared Spectroscopy of Ultrathin Films* (Wiley, Hoboken, 2003)
6. H. Ibach, H. Lueth, *Solid-State Physics: An Introduction to Principles of Materials Science,* 4th edn. (Springer, Berlin, 2009)
7. M. Born, E. Wolf, *Principles of Optics: Electromagnetic Theory of Propagation, Interference and Diffraction of Light*, 7th edn. (Cambridge University Press, Cambridge, 1999)
8. Y. Itoh, A. Kasuya, T. Hasegawa, J. Phys. Chem. A **113**, 7810–7817 (2009)
9. K. Yamamoto, H. Ishida, Appl. Spectrosc. **48**, 775–787 (1994)
10. J. Umemura, T. Kamata, T. Kawai, T. Takenaka, J. Phys. Chem. **94**, 62–67 (1990)
11. T. Hasegawa, J. Nishijo, J. Umemura, W. Theiß, J. Phys. Chem. B **105**, 11178–11185 (2001)
12. S. Babar, J.H. Weaver, Appl. Opt. **54**, 477–481 (2015)
13. T. Hasegawa, S. Takeda, A. Kawaguchi, J. Umemura Langmuir **11**, 1236–1243 (1995)
14. H. Hoffmann, U. Mayer, A. Krischanitz, Langmuir **11**, 1304–1312 (1995)
15. M. Tasumi, A. Sakamoto, *Introduction to Experimental Infrared Spectroscopy* (Wiley, Chichester, 2015)
16. P.R. Griffiths, J.A. de Haseth, *Fourier Transform Infrared Spectroscopy,* 2nd edn. (Wiley, Hoboken, 2007)
17. R.G. Greenler, J. Chem. Phys. **44**, 310–315 (1966)
18. D. Blaudez, T. Buffeteau, B. Desbat, P. Fournier, A.-M. Ritcey, M. Pézolet, J. Phys. Chem. B **102**, 99–105 (1998)
19. N.J. Harrick, *Internal Reflection Spectroscopy* (Interscience, New York, 1967)
20. W.N. Hansen, Spectrochim. Acta **21**, 815 (1965)
21. T. Hirschfeld, Appl. Spectrosc. **20**, 336 (1966)
22. T. Hirschfeld, Appl. Spectrosc. **31**, 243–244 (1977)
23. P.H. Axelsen, W.D. Braddock, H.L. Brockman, C.M. Jones, R.A. Dluhy, B.K. Kaufman, F.J. Puga II, Appl. Spectrosc. **49**, 526–531 (1995)
24. D.J. Neivandt, M.L. Gee, M.L. Hair, C.P. Tripp, J. Phys. Chem. B **102**, 5107–5114 (1998)

Chapter 4
IR Absorption of a Dielectric Matter: Phase Retardation of the Polarization Density

4.1 Dielectric Matter and Electric Permittivity

We have already found through Sect. 1.6 and Chap. 3 that IR light is absorbed by a dielectric matter, which is theorized by using complex optical parameters within a framework of electrodynamics. One of the great benefits of using electrodynamics is that a dielectric matter that is a collection of dipoles is easily characterized by using the polarization density, $\boldsymbol{P}$.

If the molecular induced-dipoles, $\boldsymbol{p}$, are fully organized with a common orientation, $\boldsymbol{P}$ can simply be correlated with N dipoles such as $\boldsymbol{P} = \sum \boldsymbol{p} = N\boldsymbol{p}$. In practice, however, the distribution of the molecular dipoles is not simple in a matter other than crystals, and thus we have to find a way to construct a physical framework to discuss the light absorption of a dielectric matter using a concept of polarization density, not a dipole.

When the intensity of IR light is not strong, the generated polarization density can linearly be written in a good approximation as [1]:

$$\boldsymbol{P} = \chi_e \varepsilon_0 \boldsymbol{E}. \tag{4.1}$$

Here, χ_e is the electric susceptibility, and spectroscopy on this equation is called *linear spectroscopy*. Fundamental spectroscopies represented by IR and UV–vis spectroscopies are mostly categorized into the linear spectroscopy. Details are discussed in Sec 4.3.

As described in Sect. 7.1 in Appendix, the induced polarization generates apparent new charge on the surface of the dielectric matter. To keep the genuine charge in the matter unchanged, a new parameter, $\boldsymbol{D}$, is defined (Eq. 7.3) and introduced.

$$\boldsymbol{D} \equiv \varepsilon_0 \boldsymbol{E} + \boldsymbol{P} \tag{4.2}$$

T. Hasegawa, *Quantitative Infrared Spectroscopy for Understanding of a Condensed Matter*, DOI 10.1007/978-4-431-56493-5_4

$\boldsymbol{D}$ is called "electric flux density" or "electric displacement." Note that this is a definition. If Eqs. (4.1) and (4.2) are merged, the next equation is obtained.

$$\boldsymbol{D} = \varepsilon_0 \boldsymbol{E} + \chi_e \varepsilon_0 \boldsymbol{E} = \varepsilon_0 (1 + \chi_e) \boldsymbol{E} \tag{4.3}$$

$\boldsymbol{D}$ is thus also linearly related to the electric field. When Eq. (7.5) or a constituent equation (Eq. 1.34) is referred, the following simple relationship is deduced:

$$\varepsilon_r = 1 + \chi_e, \tag{4.4}$$

where ε_r is the relative electric permittivity. The generation of the polarization in the dielectric matter theorized by Eq. (4.1) is the intrinsic physical phenomenon induced by the IR absorption. Note that, however, the equation holds only for a "static" electric field. In other words, we *cannot* write:

$$\boldsymbol{P}(t) = \chi_e(t) \varepsilon_0 \boldsymbol{E}(t) \tag{4.5}$$

as described in Sect. 4.3, to which we have to pay attention.

4.2 Electric Susceptibility and Linear Convolution

The generation of the "polarization oscillation" in a matter by an externally applied electric field oscillation via irradiating IR light is easily understood by considering a simple physical model that a polarization is induced by applying an electric field "pulse," which occurs one after another. In other words, a pulse is "input" to a "system" of a dielectric matter, which works as a black box to "output" a signal as a polarization, and the continuous phenomena are overlaid to have the time-dependent result.

To theorize the continuous black-box phenomena, the following three conditions should be satisfied; otherwise the system would highly be complicated to consider.

(1) Causality,
(2) Linearity and
(3) Time-invariance

Causality is very easy to understand: "a result never occurs before the reason," which gives the origin of the time scale for considering the phenomenon. Of course, causality always holds for every physical phenomenon, and we don't have to take care about it too much at the moment. Causality plays an important role in deduction of the Kramers–Kronig relation (Sect. 4.4). The other conditions may need some explanations below.

Linearity: A pulse signal, $x(t)$, is input to a "system," and the output signal, $y(t)$, is recorded. If two different pulses of $x_1(t)$ and $x_2(t)$ are input to the system

simultaneously with intensities of a and b, respectively, the output signal is generated as:

$$a \cdot x_1(t) + b \cdot x_2(t) \rightarrow \text{system} \rightarrow a \cdot y_1(t) + b \cdot y_2(t).$$

Since the output responds to the input as a linear combination, the system is called "a linear system."

Fortunately, the generation of polarization by an electric field pulse is a linear system, as long as the IR light intensity is moderate.

Time-invariance: This condition guarantees a constant time-shift. If an input signal is given to the system with a time delay of u, the output signal is generated with the same delay.

$$x(t-u) \rightarrow \text{system} \rightarrow y(t-u)$$

This system is called a "time-invariant" system. In our case of IR absorption by a condensed matter to generate the polarization density, both linear and time-invariant conditions are satisfied.

To predict the output signal without knowing details of the system, the response of the system to an external input should be theorized by using a many cosine waves having various frequencies. When the many cosine waves are overlaid, a wave packet is generated as found in Eq. (2.8), which is denoted by a sinc function. If infinite number of cosine waves are overlaid, the sinc function would be converged, which is represented by Dirac's delta function, $\delta(t)$. In other words, when a pulse of the delta function is input to the system, this experiment corresponds to inputting various cosine waves in a very short period of time. Therefore, the response to the delta function is critical to predict the output signal to any input signal to the system.

According to Dirac, the definition of $\delta(t)$ is given by the couple of the two equations as follows [2]:

$$\int_{-\infty}^{\infty} \delta(t)\,\mathrm{d}t = 1 \tag{4.6}$$

$$\delta(t) = 0 \quad (t \neq 0) \tag{4.7}$$

This definition is generally rewritten as an intuitive form:

$$\delta(t) = \begin{cases} 0 & (t \neq 0) \\ \infty & (t = 0). \end{cases}$$

This type of discontinuous "function" is recognized as "distribution." As mentioned above, the delta "function" can also be considered to be a wave packet that is a result of summation of infinite number of cosine waves having different

frequencies. This is another representation of the delta function, which can be understood as the inverse Fourier transform of $f(\omega) = 1$ (i.e., broadband spectrum).

$$\delta(t) = \frac{1}{2\pi} \int_{-\infty}^{\infty} \mathrm{e}^{\mathrm{i}\omega t} \mathrm{d}\omega \tag{4.8}$$

The proportional constant, $1/2\pi$, is necessary to satisfy the definition of Eq. (4.6), which exactly matches the definition of the inverse Fourier transform.

By using the inverse Fourier representation, another important property of the delta function is introduced. Any time-domain function, $f(t)$, can be written via the Fourier transform as follows.

$$\begin{aligned} f(t) &= \frac{1}{2\pi} \int_{-\infty}^{\infty} \left(\int_{-\infty}^{\infty} f(\tau) \mathrm{e}^{-\mathrm{i}\omega\tau} \mathrm{d}\tau \right) \mathrm{e}^{\mathrm{i}\omega t} \mathrm{d}\omega \\ &= \int_{-\infty}^{\infty} f(\tau) \left(\frac{1}{2\pi} \int_{-\infty}^{\infty} \mathrm{e}^{\mathrm{i}\omega(t-\tau)} \mathrm{d}\omega \right) \mathrm{d}\tau \\ &\Leftrightarrow \boxed{f(t) = \int_{-\infty}^{\infty} f(\tau)\delta(t-\tau)\mathrm{d}\tau} \end{aligned} \tag{4.9}$$

In the equation deformation, an exchange of the integral order and Eq. (4.8) are used considering the time invariance. Equation (4.9) with the wave line is an important representation of the delta function.

Now, let us consider that the delta function is used for probing the *impulse response function*, $h(t)$, of the black-box system, which is schematically presented as:

$$\delta(t) \rightarrow \text{system} \rightarrow h(t).$$

As mentioned above, the use of the delta function means that a light comprised of various angular frequencies (broadband) is input the system, and the response is collected. If the role of the system is denoted by a linear and time-invariant operator, $\hat{S}$, the scheme is simply represented by the next equation:

$$\hat{S}[\delta(t)] = h(t). \tag{4.10}$$

If a function, $x(t)$, is input to the system, the output signal, $y(t)$, is obtained by considering Eq. (4.9) as:

$$y(t) = \hat{S}[x(t)] = \hat{S}\left[\int_{-\infty}^{\infty} x(\tau)\delta(t-\tau)\mathrm{d}\tau\right]$$
$$= \int_{-\infty}^{\infty} x(\tau)\hat{S}[\delta(t-\tau)]\mathrm{d}\tau$$
$$\Leftrightarrow \boxed{y(t) = \int_{-\infty}^{\infty} x(\tau)h(t-\tau)\mathrm{d}\tau \equiv (x*h)(t)}.$$

In this deformation, Eq. (4.10) is taken into account. The integral on the wave line is called "*convolution*," and the asterisk is the symbol of the convolution operation. In this manner, once the impulse response function of the black-box system to the delta function is obtained, the output signal responding any input function through the system can be predicted, as long as the linear and time-invariant conditions are both satisfied.

Since the delta function corresponds to *broadband light* (cf. Eq. 4.8), let us next consider a light with a *single* angular frequency like laser as the input. If a cosine wave with a single frequency, ω, is input to the system, the frequency would be kept unchanged; whereas the amplitude and phase can be changed, which can be expressed as:

$$\hat{S}\left[\mathrm{e}^{\mathrm{i}\omega t}\right] = H(\omega)\mathrm{e}^{\mathrm{i}\omega t}. \tag{4.11}$$

Note that $H(\omega)$ is a complex function, so that any phase retardation can be considered.

Equation (4.11) can be integrated in terms of the angular frequency:

$$\int_{-\infty}^{\infty} \hat{S}\left[\mathrm{e}^{\mathrm{i}\omega t}\right]\mathrm{d}\omega = \int_{-\infty}^{\infty} H(\omega)\mathrm{e}^{\mathrm{i}\omega t}\,\mathrm{d}\omega. \tag{4.12}$$

The left-hand side can be deformed by considering the linearity of $\hat{S}$ and Eq. (4.10):

$$(\text{Lefthand}) = \hat{S}\int_{-\infty}^{\infty} \mathrm{e}^{\mathrm{i}\omega t}\,\mathrm{d}\omega = 2\pi\hat{S}[\delta(t)] = 2\pi h(t).$$

The right hand side of Eq. (4.12) is $2\pi\mathscr{F}^{-1}[H(\omega)]$ where $\mathscr{F}^{-1}$ indicates the inverse Fourier transform. Therefore, the following equation can be obtained.

$$\mathscr{F}[h(t)] = H(\omega) \tag{4.13}$$

Here, $\mathscr{F}$ denotes the Fourier transform. Equation (4.13) reveals the general relationship between the "impulse response function ($h(t)$)" and the "*frequency response function* ($H(\omega)$)."

4.3 Electric Susceptibility and Green's Function

Now, let us consider an apparatus of "dielectric matter," and an external electric field oscillation, $E(t)$, is applied to the matter to generate a polarization density, $P(t)$. If the operator of the apparatus is denoted as $\hat{A}$, then the response can schematically be written as:

$$\hat{A}[E(t)] = P(t). \tag{4.14}$$

Of course, $\hat{A}$ is a linear and time-invariant operator. By using Eq. (4.9), the electric field oscillation is expressed via the delta function as:

$$E(t) = \int_{-\infty}^{\infty} E(\tau)\delta(t-\tau)\mathrm{d}\tau. \tag{4.15}$$

Equations (4.14) and (4.15) are merged to have the next equation.

$$\hat{A}\left[\int_{-\infty}^{\infty} E(\tau)\delta(t-\tau)\mathrm{d}\tau\right] = \int_{-\infty}^{\infty} E(\tau)\hat{A}[\delta(t-\tau)]\mathrm{d}\tau = P(t) \tag{4.16}$$

This implies that the conversion mechanism from the electric field to the polarization density would fully be revealed, if we have $\hat{A}[\delta(t-\tau)]$ in detail. As described in the previous section, this term is the impulse response function of the apparatus to the delta function. Since this term can be solved later as a solution of an inverse problem, it is recognized as Green's function. Due to the time-invariant character of $\hat{A}$, the Green function can be expressed as:

$$\hat{A}[\delta(t-\tau)] = G(t-\tau).$$

Green's function is conveniently used as if it had already been "solved," and the polarization density is expressed by referring Eq. (4.16) as follows:

$$\begin{aligned} P(t) &= \int_{-\infty}^{\infty} E(\tau)G(t-\tau)\mathrm{d}\tau \\ &= (E * G)(t). \end{aligned} \tag{4.17}$$

When Eq. (4.17) is compared to Eq. (4.1) on considering Eq. (4.13), *the electric susceptibility corresponds to the Green function* or the impulse response function.

$$\chi_{\mathrm{e}}(t) = G(t) \tag{4.18}$$

Therefore, Eq. (4.17) straightforwardly implies that the *1st-order electric susceptibility works as the impulse response function* of a dielectric matter. In this manner, χ_{e} *is revealed to play a central role to absorb the IR light to yield the induced polarization in a dielectric matter*. This is the nature of IR absorption by a condensed matter. In this sense, the linear spectroscopy driven by χ_{e} is most important and fundamental to understand the light absorption.

When a mathematical formula of

$$\mathscr{F}[f * g] = \mathscr{F}[f] \cdot \mathscr{F}[g] \tag{4.19}$$

is referred, Fourier transform of Eq. (4.17) can easily be calculated to have:

$$\boxed{P(\omega) = E(\omega) \cdot G(\omega)}. \tag{4.20}$$

This relationship holds *only for the angular frequency domain*. As already noted at Eq. (4.5) for a 'static field,' this relationship *cannot* be expanded to a time-domain equation because 'phase retardation' occurs in the response.

In this manner, the theory for a static electric field has readily been developed to that of interaction with IR light by using the Green function. The detail of the Green function is, however, not available at the moment. Before revealing the details of the Green function, Eq. (4.17) is calculated by using the electric field oscillation at a single angular frequency:

$$E(t) = E_0 \exp(\mathrm{i}\omega_0 t).$$

Since this time-domain equation can be Fourier transformed to have the frequency-domain equation:

$$E(\omega) = E_0 \delta(\omega - \omega_0),$$

Equation (4.17) can be rewritten as:

$$P(t) = \int_{-\infty}^{\infty} G(\omega)E_0\delta(\omega - \omega_0)\mathrm{e}^{\mathrm{i}\omega t}\mathrm{d}\omega$$
$$= G(\omega_0)E_0\mathrm{e}^{\mathrm{i}\omega_0 t}$$

This equation apparently implies that the frequency of the polarization-density oscillation is the same as that of the incidental IR light, as noted at Eq. (4.11).

If this fact that the polarization density is oscillated at the same frequency as the light is simply taken into account, is the light absorbed by the matter at any frequency? Of course, the answer is no. To answer this question in more detail, we have to know the property of the Green function.

4.4 Complex Electric Permittivity

In the former sections, the causality does not seem to play an important role. If a fact that a physical phenomenon occurs after a trigger is taken into account, a very important physical law is built by using the convolution.

The causality is simply expressed by the step function as Eq. (4.21).

$$s(t) = \begin{cases} 1 & (t \geq 0) \\ 0 & (t < 0) \end{cases} \tag{4.21}$$

Then, $G(t)$ having the causality is readily expressed as:

$$G(t) = G(t)s(t). \tag{4.22}$$

When the next mathematical formula is referred,

$$\mathscr{F}(fg) = \frac{1}{2\pi}\mathscr{F}[f] * \mathscr{F}[g]$$

Equation (4.22) can be Fourier transformed as:

$$G(\omega) = \frac{1}{2\pi}G(\omega) * \mathscr{F}[s(t)]. \tag{4.23}$$

Since $\mathscr{F}[s(t)]$ is mathematically known to be:

$$\mathscr{F}[s(t)] = \pi\delta(\omega) + \frac{\mathrm{i}}{\omega},$$

Equation (4.23) is rewritten as:

$$\begin{aligned} G(\omega) &= \int_{-\infty}^{\infty} G(\varpi)\left[\frac{1}{2}\delta(\omega-\varpi)+\frac{\mathrm{i}}{2\pi(\omega-\varpi)}\right]\mathrm{d}\varpi \\ &= \frac{1}{2}G(\omega)+\frac{\mathrm{i}}{2\pi}\int_{-\infty}^{\infty}\frac{G(\varpi)}{\omega-\varpi}\mathrm{d}\varpi \\ \Leftrightarrow G(\omega) &= \frac{\mathrm{i}}{\pi}\int_{-\infty}^{\infty}\frac{G(\varpi)}{\omega-\varpi}\mathrm{d}\varpi. \end{aligned} \tag{4.24}$$

If $G(\varpi)$ is a complex, $G(\varpi) \equiv G'(\varpi) + \mathrm{i}G''(\varpi)$ is put in Eq. (4.24) to have

$$G'(\varpi)+\mathrm{i}G''(\varpi) = -\frac{1}{\pi}\int_{-\infty}^{\infty}\frac{G''(\varpi)}{\omega-\varpi}\mathrm{d}\varpi+\mathrm{i}\frac{1}{\pi}\int_{-\infty}^{\infty}\frac{G'(\varpi)}{\omega-\varpi}\mathrm{d}\varpi.$$

As a result, the two equation set is obtained as follows.

$$\begin{aligned} \mathrm{Re}(G(\omega)) &= -\frac{1}{\pi}\int_{-\infty}^{\infty}\frac{\mathrm{Im}(G(\varpi))}{\omega-\varpi}\mathrm{d}\varpi \\ \mathrm{Im}(G(\omega)) &= \frac{1}{\pi}\int_{-\infty}^{\infty}\frac{\mathrm{Re}(G(\varpi))}{\omega-\varpi}\mathrm{d}\varpi \end{aligned} \tag{4.25}$$

Here, the integral indicates Cauchy's principal value. Of course, $G(\omega)$ can be replaced by $\chi_\mathrm{e}(\omega)$ because of Eq. (4.18). Equation (4.25) explicitly indicates that the frequency-domain electric susceptibility, $G(\omega)$, is a complex in fact. In addition, *the real and imaginary parts of* $G(\omega)$ *are dependent on each other*.

When $G(\omega)$ is divided into the real and imaginary parts as:

$$\begin{aligned} G(\omega) &= \int_{-\infty}^{\infty} G(t)\mathrm{e}^{-\mathrm{i}\omega t}\mathrm{d}t \\ &= \int_{-\infty}^{\infty} G(t)\,\cos\,\omega t\,\mathrm{d}t - \mathrm{i}\int_{-\infty}^{\infty} G(t)\,\sin\,\omega t\,\mathrm{d}t\,, \end{aligned}$$

then the next relationships hold for the inversion of angular frequency.

$$G(-\omega) = \int_{-\infty}^{\infty} G(t)\,\cos\,\omega t\,\mathrm{d}t + \mathrm{i}\int_{-\infty}^{\infty} G(t)\,\sin\,\omega t\,\mathrm{d}t$$

This implies that $\mathrm{Re}[G(\omega)]$ and $\mathrm{Im}[G(\omega)]$ are even and odd functions in terms of ω, respectively. With these characteristics, Eq. (4.25) can further be deformed as follows ($-\varpi = \sigma$).

$$\begin{aligned}
-\int_{-\infty}^{\infty} \frac{\mathrm{Im}(G(\varpi))}{\omega - \varpi}\mathrm{d}\varpi &= \int_{-\infty}^{0} \frac{\mathrm{Im}(G(\varpi))}{\varpi - \omega}\mathrm{d}\varpi + \int_{0}^{\infty} \frac{\mathrm{Im}(G(\varpi))}{\varpi - \omega}\mathrm{d}\varpi \\
&= \int_{0}^{\infty} \frac{\mathrm{Im}(G(\sigma))}{\varpi + \omega}\mathrm{d}\sigma + \int_{0}^{\infty} \frac{\mathrm{Im}(G(\varpi))}{\varpi - \omega}\mathrm{d}\varpi \\
&= \int_{0}^{\infty} \frac{2\varpi\mathrm{Im}(G(\varpi))}{\varpi^2 - \omega^2}\mathrm{d}\varpi
\end{aligned}$$

Therefore, the integration range ($-\infty$to$+\infty$) can readily be changed to be the positive range only. Therefore, the following relations are obtained after replacing G by χ_e.

$$\boxed{\begin{aligned}
\mathrm{Re}(\chi_\mathrm{e}(\omega)) &= \frac{2}{\pi}\int_{0}^{\infty} \frac{\varpi\mathrm{Im}(\chi_\mathrm{e}(\varpi))}{\varpi^2 - \omega^2}\mathrm{d}\varpi \\
\mathrm{Im}(\chi_\mathrm{e}(\omega)) &= -\frac{2\omega}{\pi}\int_{0}^{\infty} \frac{\mathrm{Re}(\chi_\mathrm{e}(\varpi))}{\varpi^2 - \omega^2}\mathrm{d}\varpi
\end{aligned}} \tag{4.26}$$

This equation set is known as the *Kramers–Kronig (KK) relation*. Here, remember $\varepsilon_\mathrm{r}(t) = 1 + \chi_\mathrm{e}(t)$ (Eq. 4.4). Since $\chi_\mathrm{e}(\omega)$ is obtained by Fourier transform of $\chi_\mathrm{e}(t)$, then $\varepsilon_\mathrm{r}(\omega) - 1 = \chi_\mathrm{e}(\omega)$ holds, which makes the KK relation to have another form (cf. Eq. 1.45) [3].

$$\boxed{\begin{aligned}
\mathrm{Re}(\varepsilon(\omega)) - \varepsilon_\infty &= \frac{2}{\pi}\int_{0}^{\infty} \frac{\varpi\mathrm{Im}(\varepsilon(\varpi))}{\varpi^2 - \omega^2}\mathrm{d}\varpi \\
\mathrm{Im}(\varepsilon(\omega)) &= -\frac{2\omega}{\pi}\int_{0}^{\infty} \frac{\mathrm{Re}(\varepsilon(\varpi)) - \varepsilon_\infty}{\varpi^2 - \omega^2}\mathrm{d}\varpi
\end{aligned}} \tag{4.27}$$

This is one of the variations of the KK relation [1–4]. Since the electric permittivity is directly appeared, this KK relation is more conveniently used. In this manner, the electric permittivity also proves to be complex, and the real and the imaginary parts are dependent on each other. Of course, the relation can further be rewritten for the complex refractive index.

The deduction process of the KK relation is mathematically written by using the complex integration, which requires the regular condition satisfying the Cauchy–Riemann equations. Equation (4.27), for example, when $\omega = \omega_1 + \mathrm{i}\omega_2$ is defined, the real and imaginary parts are rewritten as:

$$\mathrm{Re}(\varepsilon(\omega_1, \omega_2)) = \varepsilon_\infty + \int_0^\infty G(\varpi)\cos\omega_1\varpi\, \mathrm{e}^{-\omega_2\varpi}\mathrm{d}\varpi$$

$$\mathrm{Im}(\varepsilon(\omega_1, \omega_2)) = \int_0^\infty G(\varpi)\sin\omega_1\varpi\, \mathrm{e}^{-\omega_2\varpi}\mathrm{d}\varpi\,,$$

which satisfy the Cauchy–Riemann equations (Eq. 4.28).

$$\frac{\partial \mathrm{Re}(\varepsilon)}{\partial\omega_1} = \frac{\partial \mathrm{Im}(\varepsilon)}{\partial\omega_2} \text{ and } \frac{\partial \mathrm{Re}(\varepsilon)}{\partial\omega_2} = -\frac{\partial \mathrm{Im}(\varepsilon)}{\partial\omega_1}. \tag{4.28}$$

In this manner, ε proves to satisfy the KK relation.

When referring Eq. (4.20), the following relationship is obtained.

$$\begin{aligned} \boldsymbol{P}(\omega) &= \varepsilon_0[\varepsilon_\mathrm{r}(\omega) - 1]\boldsymbol{E}(\omega) \\ &= \varepsilon_0[(\mathrm{Re}(\varepsilon(\omega)) - 1) + \mathrm{iIm}(\varepsilon(\omega))]\boldsymbol{E}(\omega) \end{aligned} \tag{4.29}$$

Equation (4.29) apparently implies that *the imaginary part of the electric permittivity is the reason to cause the phase retardation*.

Equation (1.43) in Chap. 1 shows that the spectral shape is governed by the imaginary part of the refractive index, n''. At the baseline of an absorbance spectrum where no absorption occurs, $n'' = 0$ holds. Therefore, $\mathrm{Im}(\varepsilon(\omega)) = 2n'n''$ also becomes nil at the baseline. In this manner, the light absorption by a condensed matter depends on whether the imaginary part of the permittivity is nil or not. This further means that *no absorption of the IR light induces "no phase retardation"* of the polarization, even if the polarization oscillates at the same frequency. This is the intrinsic nature of light absorption by a condensed matter.

In short, if the oscillation of the polarization perfectly pursues the IR light, no absorption occurs in the matter; whereas the light is absorbed when the phase retardation occurs. When the retardation reaches $\pi/2$, the absorption reaches the maximum.

Application studies using the KK relations are available in Chap. 6.

References

1. J.D. Jackson, *Classical Electrodynamics*, 3rd edn. (Wiley, New York, 1998)
2. P.A.M. Dirac, *The Principles of Quantum Mechanics*, 4th edn. (Oxford University Press, London, UK, 1962)
3. V.P. Tolstoy, I.V. Chernyshova, V.A. Skryshevsky, *Handbook of Infrared Spectroscopy of Ultrathin Films* (Wiley, Hoboken, 2003)
4. J.S. Plaskett, P.N. Schatz, J. Chem. Phys. **38**, 612–617 (1963)

Chapter 5
Chemometrics for FTIR

5.1 Beer's Law and a Single-Constituent System

In Chap. 3, we have learned that absorbance spectrum of a 'thin film' deposited on a substrate can accurately be reproduced by considering the optical configuration and optical parameters of each phase. Regardless, this accurate electrodynamic approach is inconvenient for calibrating a 'bulky matter.' One of the reasons is that the molecular density (or concentration) is not explicitly involved in the optical parameters. For the purpose of concentration calibration of a bulky matter, an analytical technique based on Beer's law (Eq. (5.1)) works conveniently:

$$A(\tilde{\nu}) = \varepsilon(\tilde{\nu})c. \tag{5.1}$$

Here, the path length, d, is fixed at $d = 1$ cm, so that d is removed from the equation. This equation apparently indicates that the shape of an absorbance spectrum, $A(\tilde{\nu})$, is determined by $\varepsilon(\tilde{\nu})$. If the wavenumber is fixed at a position, $\varepsilon(\tilde{\nu})$ becomes a scalar, ε, which is called *molar extinction coefficient*.

Equation (5.1) is apparently used for the *calibration curve method*, which is a classical and most fundamental method for quantitatively analyzing absorbance spectra. In Fig. 5.1a, schematic UV–vis absorbance spectra depending on concentration are presented. Since the *spectral shape is kept unchanged* within the concentration range, the spectral variation is recognized to be derived from a *single chemical constituent* system. If the solution involves two different chemical species, the shape-invariant results imply that the two species increase simultaneously as if they were coupled to be a single species. In this manner, anyway, the shape-invariant intensity change is spectroscopically recognized as a single-constituent system.

When we have spectra of a calibration sample set (concentrations are known a priori) as found in Fig. 5.1a, the peak intensity is measured at the most intensive band as presented by the red-dashed line, and the intensities are plotted against the

T. Hasegawa, *Quantitative Infrared Spectroscopy for Understanding of a Condensed Matter*, DOI 10.1007/978-4-431-56493-5_5

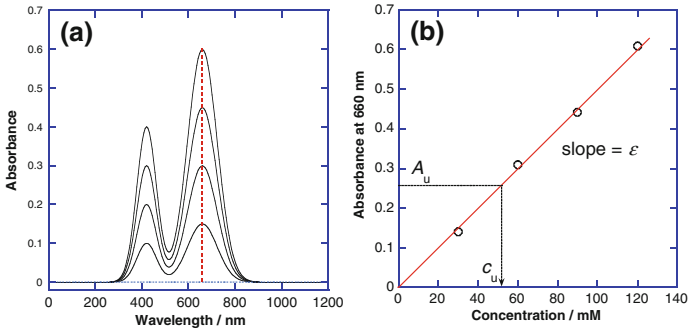

Fig. 5.1 **a** Schematic concentration-dependent absorbance spectra of a single-constituent system, and **b** the calibration curve measured at 660 nm

concentration to have the *calibration curve* (straight line though) as shown in Fig. 5.1b. Reflecting instability and noise, the plots represented by the open circles are generally not on a line perfectly. Since the absorbance is theoretically governed by Beer's law (Eq. (5.1)), a calibration curve (red straight line) can be drawn on the data as the least squares solution (see Sect. 5.3). Since the ordinate and abscissa of the figure are absorbance and concentration, respectively, Fig. 5.1b is a representation of Eq. (5.1), and therefore the slope of the calibration curve corresponds to the molar extinction coefficient, ε.

Once ε is obtained, the concentration of an unknown sample, c_u, is easily analyzed using the calibration curve as presented by the black arrow in the figure. Here, A_u is the band intensity of the unknown sample at the same band position as used for building the calibration curve. Note that, however, the concentration prediction can be performed without using the figure, but by a simple calculation as:

$$c_u = A_u/\varepsilon. \tag{5.2}$$

This conventional technique implies a very important fundamental: *once ε or a conceptually same parameter is obtained, concertation prediction can be performed, even if we cannot draw the calibration figure*. This idea can be used for extending Beer's law to chemometrics.

The conventional quantitative calibration on Beer's law has an intrinsic limitation as follows. The peak intensity only at a single wavelength is used, and the rest spectral information is discarded. Therefore, only a single-constituent system can be calibrated, and a mixture cannot be analyzed, which is a big barrier for most analytical purposes. In addition, the peak intensity is directly influenced by noise. Therefore, for multi-constituent and multi-wavelength analysis, a more sophisticated analytical technique is needed. To make the best use of all the spectral data, $\varepsilon(\tilde{\nu})$ should be reconsidered.

$\varepsilon(\tilde{\nu})$ is obtained by normalizing spectra in terms of concentration.

$$\frac{A(\tilde{\nu})}{c} = \varepsilon(\tilde{\nu}).$$

$\varepsilon(\tilde{\nu})$ is thus found to be a "spectrum at the concentration of 1 mol dm^{-3}." In practice, the measurements at such a high concentration are impossible, since the solution would absorb the IR light too much, and the IR light would also be scattered in such a dense medium. Therefore, $\varepsilon(\tilde{\nu})$ is a concentration-normalized spectrum.

When we measure a spectrum on a modern spectrometer, the spectrum is recorded as digital data, and it can be output as text data as presented in Fig. 5.2. Although the absorbance spectrum appears as a continuous curve as the thick curve in Fig. 5.3a, it is a collection of discrete data points. In this meaning, the spectrum is not a 'function' of wavelength, and it should be written as a 'vector.' If the absorbance column has N numeric values, the spectrum can be stored in a vector, $\boldsymbol{a}$:

$$\boldsymbol{a} \equiv (a_1\, a_2\, a_3 \ldots a_{N-1}\, a_N).$$

For this example, the spectrum, **a**, is synthesized to have two bands at 420 and 660 nm as found in the figure.

No matter how the spectral shape is complicated, the spectrum can be written as "a vector" in N-dimensional space as schematically illustrated in Fig. 5.3b. The N-dimensional space is schematically illustrated using a three-dimensional image. In the multivariate (or multidimensional) space, the vector can be recognized as "a point" as shown by the open circle in Fig. 5.3b. In this manner, *any spectrum can be converted to be a point in multivariate space*. This is the most important fundamental of chemometrics.

When the spectrum develops with increasing the concentration without changing its shape as found in Fig. 5.3a, what would happen in the multivariate space? Invariance of the shape means that the vector, $\boldsymbol{a}$, is simply multiplied by a scalar factor, k, such as

Fig. 5.2 An example of text data of a UV–vis spectrum. The *left* and *right columns* store the wavelength and absorbance data, respectively, and the two columns are separated by comma

```
3.500000e+002,4.350000e-002
3.520000e+002,4.460000e-002
3.540000e+002,4.634000e-002
3.560000e+002,4.861000e-002
3.580000e+002,5.037000e-002
3.600000e+002,5.159000e-002
3.620000e+002,5.409000e-002
3.640000e+002,5.606000e-002
3.660000e+002,5.760000e-002
⋮
```

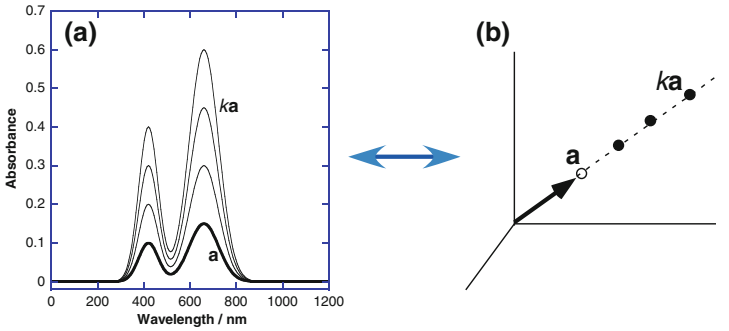

Fig. 5.3 **a** Normal spectral representation of a single-constituent system and **b** schematic *N*-dimensional space representation of the spectra in (**a**)

$$\boldsymbol{a} \rightarrow k\boldsymbol{a}.$$

This means that $k\boldsymbol{a}$ must appear on an extended line of the original vector, $\boldsymbol{a}$, as drawn by the solid circles in Fig. 5.3b.

As a result, a very important concept of the multivariate space representation of spectra is found as follows [1]:

1. The *direction* of a vector in multivariate space represents the spectral *shape* in the normal representation, and
2. The *norm* (magnitude) of the vector represents the spectral *intensity*.

5.2 Extended Beer's Law for a Multi-Constituent System: CLS Regression

What would happen, if another chemical constituent is added to the system to have a 'two-constituent' system? Since a chemically different species yields a different-shape spectrum, the added species must yield another vector with a 'different direction' in the multivariate space representation judging from the conclusion in the previous section. In other words, the points in the multivariate space cannot be on a line passing through the origin.

In Fig. 5.4a, schematic spectra of a 'two-constituent' system are presented. The spectral shape is changed by using two components: $\boldsymbol{a}$ having the peak position at 490 nm and $\boldsymbol{b}$ having the peak position at 600 nm:

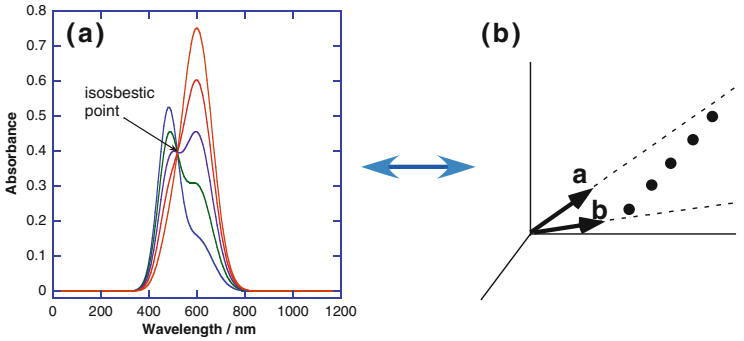

Fig. 5.4 **a** Normal spectral representation of a two-constituent system and **b** schematic *N*-dimensional space representation of the spectra in (**a**)

$$\boldsymbol{a} \equiv (a_1\, a_2\, a_3 \ldots a_{N-1}\, a_N)$$
$$\boldsymbol{b} \equiv (b_1\, b_2\, b_3 \ldots b_{N-1}\, b_N).$$

In this example, the concentration of $\boldsymbol{b}$ increases while that of $\boldsymbol{a}$ decreases synchronously. When two species change the quantities in the opposite directions synchronously, an *isosbestic point* appears, at which all the spectra go across.

Then, what is going on in the *N*-dimensional space? Since the spectrum of $\boldsymbol{b}$ has a different shape from that of $\boldsymbol{a}$, the vector $\boldsymbol{b}$ must have a different direction from the vector $\boldsymbol{a}$ as schematically presented in Fig. 5.4b. The mixture spectra vector, $\boldsymbol{m}$, should be expressed as a linear combination of the two vectors as long as no chemical interaction occurs between the two species:

$$\boldsymbol{m} = c_a\boldsymbol{a} + c_b\boldsymbol{b}. \tag{5.3}$$

Therefore, the points, $\boldsymbol{m}$, in the *N*-dimensional space must be *involved in the plane spanned by the two vectors* (see Fig. 5.4b). In other words, the *point variance needs two-dimensional space*.

This suggests another very important conclusion that *the dimension needed for involving the points equals to the number of chemical constituents* in the system. In other words, the dimension analysis of the point variance is the analysis of the number of constituents in the system. This is a basis for analysis of the number of independent chemical species involved in the system via spectroscopy.

As an example study, let us consider the isosbestic point using Eq. (5.3). As mentioned above, the spectra in Fig. 5.4a are synthesized by changing the concentrations of the spectra of $\boldsymbol{a}$ and $\boldsymbol{b}$ synchronously, but the directions are opposite to each other. This situation is expressed using a parameter of t as:

$$\boldsymbol{m} = t\boldsymbol{a} + (1-t)\boldsymbol{b} \quad (0 \le t \le 1).$$

In fact, the points in Fig. 5.4b are on this line. This equation is organized in terms of t to have:

$$\boldsymbol{m} = t(\boldsymbol{a} - \boldsymbol{b}) + \boldsymbol{b}.$$

The isosbestic point is an unmoved position irrespective of t, which is achieved when $\boldsymbol{a} - \boldsymbol{b} = 0$ holds. Since the spectra of $\boldsymbol{a}$ and $\boldsymbol{b}$ are different from each other, however, $\mathbf{a} \neq \mathbf{b}$ holds *except the isosbestic point*. In other words, only at the crossing points of the two spectra, $\boldsymbol{m}$ becomes invariant to any t. In this manner, the reason for the isosbestic point is easily understood using the vector representation.

If we prepare two or more mixture samples with various concentrations for $\boldsymbol{a}$ and $\boldsymbol{b}$, Eq. (5.3) is inconvenient to denote the concentration systematically; instead, two indices (i and j) should be introduced for labeling the concentration:

$$\begin{aligned} \boldsymbol{m}_1 &= c_{11}\boldsymbol{k}_1 + c_{12}\boldsymbol{k}_2 \\ \boldsymbol{m}_2 &= c_{21}\boldsymbol{k}_1 + c_{22}\boldsymbol{k}_2 \\ &\vdots \\ \boldsymbol{m}_M &= c_{M1}\boldsymbol{k}_1 + c_{M2}\boldsymbol{k}_2. \end{aligned} \tag{5.4}$$

By introducing c_{ij}, M samples comprising any components can thus be written systematically. Equation (5.4) can further be summarized using matrix.

$$\begin{pmatrix} \boldsymbol{m}_1 \\ \boldsymbol{m}_2 \\ \vdots \\ \boldsymbol{m}_M \end{pmatrix} = \begin{pmatrix} c_{11} & c_{12} \\ c_{21} & c_{22} \\ \vdots & \vdots \\ c_{M1} & c_{M2} \end{pmatrix} \begin{pmatrix} \boldsymbol{k}_1 \\ \boldsymbol{k}_2 \end{pmatrix} \Leftrightarrow \boldsymbol{A} = \boldsymbol{C}\boldsymbol{K}. \tag{5.5}$$

Here, $\boldsymbol{A}$ is a matrix comprising M vectors of $\boldsymbol{m}_j$. $\boldsymbol{C}$ is, of course, the concentration matrix. In the row-wise vector, the concentration of each constituent of a mixture sample is stored; whereas the column-wise vector indicates the concentration 'profile' on changing the sample. $\boldsymbol{K}$ involves the '*pure-component spectra*' of the independent chemical species. The generalized form of $\boldsymbol{A} = \boldsymbol{C}\boldsymbol{K}$ is recognized to be *an expanded form of Beer's law* in terms of both row- (wavelength) and column-wise (constituents) directions [2]. A benefit of using the general form is that it holds for any numbers of constituents and wavelengths.

By comparing Eq. (5.5) to Eq. (5.1), the matrix of $\boldsymbol{K}$ is found to correspond to ε. When referring to the previous section, once $\boldsymbol{K}$ is obtained, the calibration should be carried out using the concentration-dependent spectra.

Equation (5.5) has a form that the mixture spectra matrix, $\boldsymbol{A}$, is calculated by multiplying the concentration and the pure-component matrices. In practice,

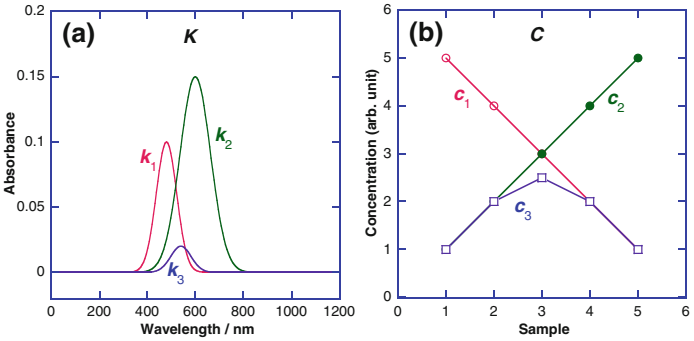

Fig. 5.5 **a** Three seed spectra forming a matrix, $\boldsymbol{K}$, and **b** concentration profiles, $\boldsymbol{C}$

however, the mixture spectra are obtained by measurements using a spectrometer. What we want do is, therefore, decomposing the observed spectra into the concentration and pure-constituent matrices.

In chemometrics, the decomposing is called "modeling," i.e., the spectra matrix, $\boldsymbol{A}$, is "modeled" (not theorized) by linear combination of the two matrices of $\boldsymbol{C}$ and $\boldsymbol{K}$. Here, we have to note that the modeling accompanies some inaccuracy, since $\boldsymbol{A}$ involves some noise and experimental error. Therefore, such an inaccuracy is to be discarded in a residual term, $\boldsymbol{R}$:

$$\boxed{\boldsymbol{A} = \boldsymbol{CK} + \boldsymbol{R}}. \tag{5.6}$$

This equation accompanying the residual term is called the *classical least squares* (*CLS*) *regression*. The term of "regression" is used for meaning "prediction" due to a historical reason in the field of genomics.

Here, for a better understanding, the seed spectra and concentration are disclosed in Fig. 5.5, which are used to construct the mixture spectra in Fig. 5.4.

The red, green, and blue spectra in Fig. 5.5a are the first-, second-, and third-row spectra, which are collected to yield a matrix of $\boldsymbol{K}$, and the corresponding concentration column vectors stored in $\boldsymbol{C}$ are presented in Fig. 5.5b. For the construction of the spectra of the two-component system, only the first two spectra and concentration vectors are used. With the use of these two matrices, model spectra, $\boldsymbol{A}$, are synthesized using $\boldsymbol{A} = \boldsymbol{CK}$, which are presented in Fig. 5.4a.

5.3 Least Squares Solution of a Regression Equation

As already mentioned, 'obtaining $\boldsymbol{K}$' using a calibration sample set corresponds to 'making a calibration curve.' If we have a calibration sample set, i.e., the concentrations in $\boldsymbol{C}$ are all known for the measured spectra of the mixture sample, $\boldsymbol{A}$, how do we calculate $\boldsymbol{K}$? If the parameters are all scalars, a simple division as found

in Eq. (5.2) can be employed. What if all the parameters are matrices? Here we have to note that all the three matrices need not be square matrices in practical cases. This means that the inverse matrix cannot be calculated for the CLS regression, either.

To overcome this dilemma, in an intuitive understanding, a transpose matrix is multiplied to make a square matrix. For example, to solve $\boldsymbol{K}$ in Eq. (5.6), the transpose matrix of $\boldsymbol{C}$ ($\boldsymbol{C}^{\mathrm{T}}$) is multiplied to $\boldsymbol{C}$ from the left side:

$$\boldsymbol{C}^{\mathrm{T}}A = \boldsymbol{C}^{\mathrm{T}}\boldsymbol{C}\boldsymbol{K}.$$

$\boldsymbol{R}$ is ignored because of the reason mentioned later. Since $\boldsymbol{C}^{\mathrm{T}}$ and $\boldsymbol{C}$ have matrix sizes of $(c \times M)$ and $(M \times c)$, respectively, $\boldsymbol{C}^{\mathrm{T}}\boldsymbol{C}$ has a size of $(c \times c)$, which is smaller than the original size where 'c' is the number of chemical constituents. Note that the 'rank' of $\boldsymbol{C}$ is the same as that of $\boldsymbol{C}^{\mathrm{T}}\boldsymbol{C}$, that is c. This situation guarantees that the inverse matrix of $\boldsymbol{C}^{\mathrm{T}}\boldsymbol{C}$ can be calculated with no problem. Therefore, $\boldsymbol{K}$ can readily be calculated as:

$$\boldsymbol{K} = (\boldsymbol{C}^{\mathrm{T}}\boldsymbol{C})^{-1}\boldsymbol{C}^{\mathrm{T}}\boldsymbol{A}. \tag{5.7}$$

This solution is called the *least squares solution*. To understand why this is the 'least squares' solution, we should consider the normal least squares solution of several points in a graph.

Figure 5.6 presents a schematic image of a calibration curve to an experimental plot of four points. The linear calibration curve is obtained as the least squares (LS) solution of $y = ax + b$. The slope and the intercept are calculated as follows.

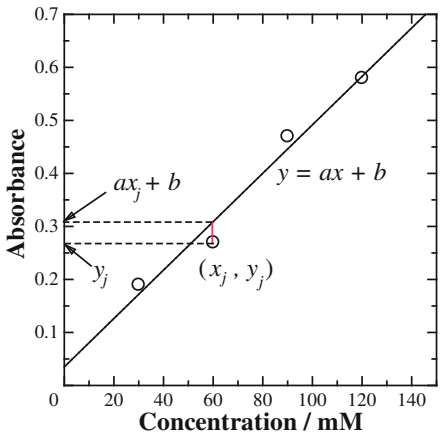

Fig. 5.6 A schematic of linear calibration curve obtained by the least squares method. The experimental points are presented by the *open circles*

In the LS analysis, the difference between the line and the *j*th experimental point measured along the *y*-axis (indicated by the red line) is squared, and all the squared differences are summed up to have *s*:

$$s = \sum_{j=1}^{n} (y_j - ax_j - b)^2.$$

The LS analysis finds the optimal set of a and b to make s minimum. To do that, s is partial-differentiated in terms of a and b, which must be equal to zero:

$$\frac{\partial s}{\partial a} = -2\sum_{j=1}^{n} (y_j - ax_j - b)x_j = 0$$
$$\frac{\partial s}{\partial b} = -2\sum_{j=1}^{n} (y_j - ax_j - b) = 0.$$

These equations are readily organized to have the following equation set:

$$\begin{aligned} \left(\sum_{j=1}^{n} x_j^2\right)a + \left(\sum_{j=1}^{n} x_j\right)b &= \sum_{j=1}^{n} x_j y_j \\ \left(\sum_{j=1}^{n} x_j\right)a + nb &= \sum_{j=1}^{n} 1 \cdot y_j. \end{aligned} \tag{5.8}$$

Since the summations of x_j, x_j^2, and $x_j y_j$ are easily carried out using computer, these simultaneous linear equations are easily solved to have the optimized a and b. This is the normal LS method. Here, however, we note coefficients in Eq. (5.8). For example, right-hand side can be decomposed as

$$\begin{pmatrix} \sum_{j=1}^{n} x_j y_j \\ \sum_{j=1}^{n} 1 \cdot y_j \end{pmatrix} = \begin{pmatrix} x_1 & x_2 & \cdots & x_n \\ 1 & 1 & \cdots & 1 \end{pmatrix} \begin{pmatrix} y_1 \\ y_2 \\ \vdots \\ y_n \end{pmatrix} = \boldsymbol{\xi}^{\mathrm{T}} \boldsymbol{Y}.$$

Here, two parameters are newly introduced as:

$$\boldsymbol{\xi} = \begin{pmatrix} x_1 & 1 \\ x_2 & 1 \\ \vdots & \vdots \\ x_n & 1 \end{pmatrix} \quad \text{and} \quad \boldsymbol{Y} \equiv \begin{pmatrix} y_1 \\ y_2 \\ \vdots \\ y_n \end{pmatrix}.$$

The new parameters represent a line, which runs through all the experimental points:

$$\mathbf{Y} = \boldsymbol{\xi}\begin{pmatrix} a \\ b \end{pmatrix} \Leftrightarrow \begin{pmatrix} y_1 \\ y_2 \\ \vdots \\ y_n \end{pmatrix} = \begin{pmatrix} x_1 & 1 \\ x_2 & 1 \\ \vdots & \vdots \\ x_n & 1 \end{pmatrix}\begin{pmatrix} a \\ b \end{pmatrix} \Leftrightarrow \begin{array}{l} y_1 = ax_1 + b \\ y_2 = ax_2 + b \\ y_3 = ax_3 + b \end{array}.$$

In this manner, $\boldsymbol{\xi}$ and $\boldsymbol{Y}$ readily express the straight line in Fig. 5.6. With the use of $\boldsymbol{\xi}$, the coefficients in the right-hand side of Eq. (5.8) can readily be expressed in a very simple manner:

$$\boldsymbol{\xi}^{\mathrm{T}}\boldsymbol{\xi} = \begin{pmatrix} x_1 & x_2 & \cdots & x_n \\ 1 & 1 & \cdots & 1 \end{pmatrix}\begin{pmatrix} x_1 & 1 \\ x_2 & 1 \\ \vdots & \vdots \\ x_n & 1 \end{pmatrix} = \begin{pmatrix} \sum_{j=1}^{n} x_j^2 & \sum_{j=1}^{n} x_j \\ \sum_{j=1}^{n} x_j & n \end{pmatrix}.$$

Therefore, the two equations in Eq. (5.8) can simply be rewritten as:

$$\begin{aligned} & \boldsymbol{\xi}^{\mathrm{T}}\boldsymbol{\xi}\begin{pmatrix} a \\ b \end{pmatrix} = \boldsymbol{\xi}^{\mathrm{T}}\boldsymbol{Y} \\ \Leftrightarrow \quad & \boxed{\begin{pmatrix} a \\ b \end{pmatrix} = \left(\boldsymbol{\xi}^{\mathrm{T}}\boldsymbol{\xi}\right)^{-1}\boldsymbol{\xi}^{\mathrm{T}}\boldsymbol{Y}}. \end{aligned} \tag{5.9}$$

Thus, a and b are found to be solved in the same way as Eq. (5.7), which is exactly the same as the solving process of the LS solution. This is the reason why the solution via Eq. (5.9) is called *the LS solution*.

5.4 Intrinsic Limitation of CLS Regression

To understand the concept of CLS regression in a more familiar manner, some simulated spectra are prepared.

Let us consider that the spectra, $\boldsymbol{A}$, in Fig. 5.7a are obtained for a calibration sample set. The concentrations of the calibration sample set (see $\boldsymbol{c}_1$ and $\boldsymbol{c}_2$ in Fig. 5.5b) are:

$$\boldsymbol{C} = \begin{pmatrix} \boldsymbol{c}_1 & \boldsymbol{c}_2 \end{pmatrix} = \begin{pmatrix} 5 & 1 \\ 4 & 2 \\ 3 & 3 \\ 2 & 4 \\ 1 & 5 \end{pmatrix}.$$

With the use of $\boldsymbol{A}$ and $\boldsymbol{C}$, the rest matrix of the CLS regression, $\boldsymbol{K}$, is calculated as presented in Fig. 5.8a. As mentioned above, $\boldsymbol{K}$ has a meaning of

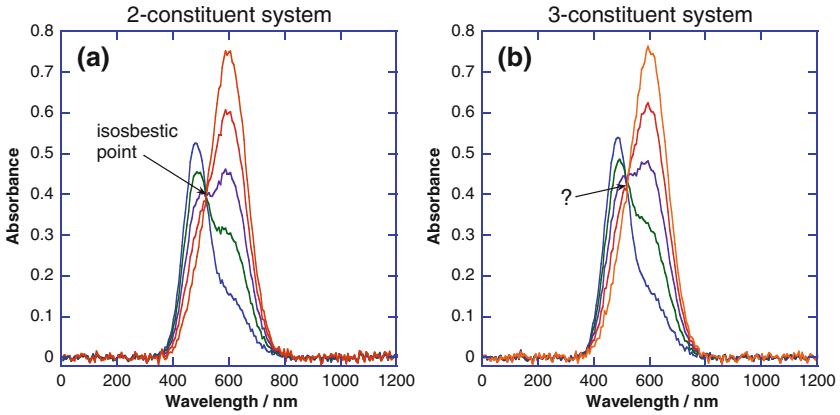

Fig. 5.7 Comparison between **a** a two-constituent system (the same as Fig. 5.4a except noise) and **b** a three-constituent one

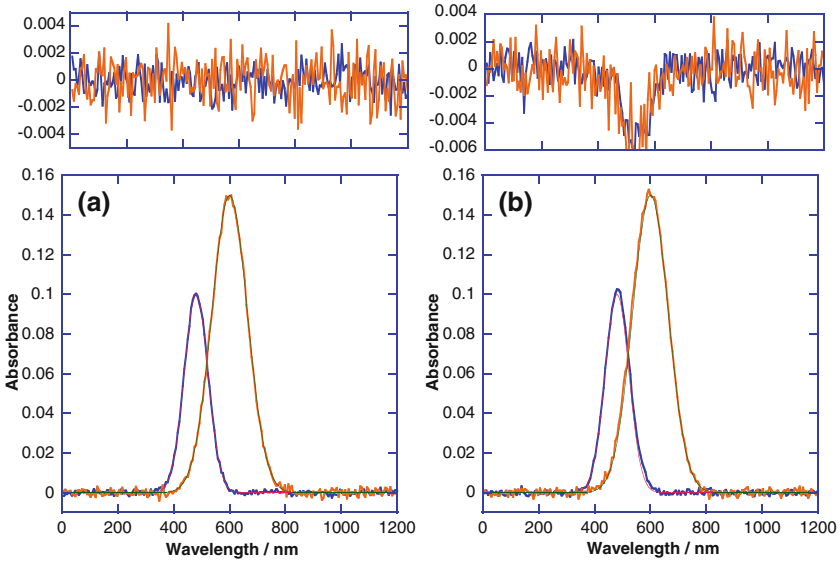

Fig. 5.8 The "*K*" spectra calculated from **a** a genuine two-constituent system, and from **b** a three-constituent system using the common "*C*." The two seed spectra (k_1 and k_2) in Fig. 5.5a are overlaid on the calculated spectra. The *upper panels* present the differences between the predicted and seed spectra

"pure-constituent spectra." Therefore, calculation of $\boldsymbol{K}$ has an important meaning of *spectral decomposition* from the mixture spectra, $\boldsymbol{A}$, as well as another meaning of the calibration curve. The decomposed spectra accompany less noise than that involved in the original spectra (Fig. 5.7a), since some of the noise has been discarded into $\boldsymbol{R}$ (Eq. (5.6)) as a result of the LS calculation.

In this manner, if we have full information of the concentration of the calibration samples (i.e., *the number of the constituents is exactly the same as expectation*) a very accurate spectral decomposition is achieved, which means that the 'calibration curve' is accurately obtained.

Once $\boldsymbol{K}$ is obtained as the LS solution from the spectra of the calibration samples, prediction of the concentration of an unknown sample can be performed, since $\boldsymbol{K}$ works as the calibration curve. If the 'spectra of the unknown samples' are stored in a matrix of $\boldsymbol{a}_{\mathrm{u}}$, the concentration of each chemical constituent in every sample is simultaneously predicted as another LS solution as:

$$\boldsymbol{c}_{\mathrm{u}} = \boldsymbol{a}_{\mathrm{u}}\boldsymbol{K}^{\mathrm{T}}\left(\boldsymbol{K}\boldsymbol{K}^{\mathrm{T}}\right)^{-1} \equiv \boldsymbol{a}_{\mathrm{u}}\boldsymbol{K}_{\mathrm{cal}}. \tag{5.10}$$

The *calibration matrix* of $\boldsymbol{K}_{\mathrm{cal}} \equiv \boldsymbol{K}^{\mathrm{T}}\left(\boldsymbol{K}\boldsymbol{K}^{\mathrm{T}}\right)^{-1}$ is thus conveniently used for the simultaneous determinations of concentrations of a multi-constituent system.

For a better understanding, an "unknown" spectrum, $\boldsymbol{a}_{\mathrm{u}}$, is synthesized using the two seed of spectra, $\boldsymbol{k}_1$ and $\boldsymbol{k}_2$, with concentrations of $(2.5 \;\; 1.5)$, which is presented in Fig. 5.9.

By putting the vector, $\boldsymbol{a}_{\mathrm{u}}$, into Eq. (5.10), the concentrations are calculated to be 2.50 and 1.50 with an analytical error below 1×10^{-12}%, which is extremely great when we remember that the artificial noise is about 1% of the signal. This is achieved because the majority of noises are attributed to the nonlinear response to the concentration change, which are discarded into $\boldsymbol{R}$ of Eq. (5.6). This is, indeed, a great benefit of using CLS regression, and the conventional 'calibration curve' method cannot attain such a super result.

We have to note again, however, that this beautiful spectral calibration can be performed only when the number of constituents is exactly the same as the real constituents involved in the system.

What would happen, if the expected number of constituents is incorrect? Even if only two constituents are dissolved in the solvent, a new product would be generated after some reaction and association, which results in three-constituent

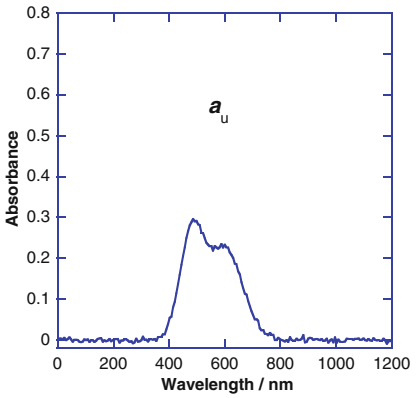

Fig. 5.9 A sample spectrum synthesized using a concentration vector of (2.5 1.5). Artificially generated noise is added

system. This situation is presented in Fig. 5.7b. The spectra are synthesized using all the seed spectra in Fig. 5.5a with the three concentration profiles in Fig. 5.5b. By adding the third component, the 'isosbestic point' in Fig. 5.7b becomes ambiguous. If we have the spectra as experimental data at hand, however, what do we make a decision about the number of constituents? One may consider that the ambiguous isosbestic point is due to an experimental error, and the system can be recognized to have two constituents. On the other hand, one cannot ignore the ambiguous crossing, and consider an additional constituent. In any case, making an appropriate decision is quite difficult, but calculation of Eq. (5.7) is readily carried out.

Let us put the three-constituent spectra in $\boldsymbol{A}$, and $\boldsymbol{K}$ is calculated by using the two-constituent concentration matrix, $\boldsymbol{C}$, since we have only the two-constituent data for the calibration sample set. Although the three-constituent information is involved in $\boldsymbol{A}$, the matrix size of $\boldsymbol{A}$ is kept unchanged. Therefore, calculation of Eq. (5.7) has no problem. The results are presented in Fig. 5.8b. When we take a look at the difference spectra between the predicted spectra and the seed one (upper panel), the calculated spectra, $\boldsymbol{K}$, are found to be a little bit different from the seed spectra, which is not found in Fig. 5.8a. This suggests that the 'calibration curve' is inaccurate. In fact, using the matrix of $\boldsymbol{K}$, the concentrations of the unknown spectrum, $\boldsymbol{a}_{\mathrm{u}}$, in Fig. 5.9 are calculated using Eq. (5.10). The predicted concentrations are 2.40 and 1.43 having analytical errors of 3.97 and 4.64%, respectively (depending on the random noise). The error level is apparently degraded when comparing to the exactly two-constituent case.

In this manner, the analytical accuracy becomes largely degraded when the number of constituents is different from the actual one. In practice, having knowledge of the exact number of constituents a priori is impossible, which should be an analytical purpose (Sect. 5.6). Therefore, CLS intrinsically has a big problem of an inaccurate calibration on a wrong number of constituents, although it has another great function of 'spectral decomposition' as well as the highly accurate calibration in principle, which is a dilemma of CLS.

5.5 Inverse Beer's Law: ILS Regression (or MLR)

The reason why the calibration accuracy is largely degraded on a wrong number of constituents should be attributed to a fact that "rich information of $\boldsymbol{A}$ having the full constituents is modeled by using a less number of constituents in $\boldsymbol{C}$." As found in Fig. 5.8b, an error is found as a result of modeling the three-constituent spectra using only two pure-component spectra. This is schematically presented as:

$$\boldsymbol{A} \rightarrow \boldsymbol{ck},$$

where the capital letter is used for involving rich information, whereas small letters involve inadequate information. Once an inadequate matrix of $\boldsymbol{k}$ is calculated, a

portion of the spectral information is lost, and as a result, reconstruction of $\boldsymbol{A}$ is impossible as schematically expressed as below.

$$\boldsymbol{ck} \not\rightarrow \boldsymbol{A} \tag{5.11}$$

This implies that CLS requires a very strict constraint that *all the information of every factor influencing the spectral variation must explicitly be quantified in* $\boldsymbol{C}$, which indicates a limit of CLS. The influencing factor involves the experimental error of the spectrometer, baseline drift, and unexpectedly generated chemical species such as associated molecular species. Since the quantitative prediction of the chemical information is nearly impossible, CLS is not practically used for calibration purposes. Only the exception is found in MAIRS technique (Sect. 6.2), which makes the best use of CLS in terms of spectral decomposition.

To overcome the intrinsic limit of CLS, the direction of modeling (Eq. (5.11)) is focused, i.e., the concentration matrix having inadequate information should be modeled using the spectral matrix having full information. In short, $\boldsymbol{A}$ and $\boldsymbol{C}$ are exchanged [2] as schematically presented by:

$$\boldsymbol{c} \rightarrow \boldsymbol{Ap}.$$

Here, another correlation matrix, $\boldsymbol{p}$, is used instead of using $\boldsymbol{k}$ to discriminate the new concept from CLS. The new regression equation is, therefore, represented by

$$\boxed{\boldsymbol{C} = \boldsymbol{AP}_{\mathrm{ILS}} + \boldsymbol{R}}. \tag{5.12}$$

Since $\boldsymbol{P}$ is used for PCA later, $\boldsymbol{P}_{\mathrm{ILS}}$ is used for ILS. This regression equation is based on a concept of the *inverse Beer's law*, and the equation is thus officially named *inverse least squares* (*ILS*) *regression*. Due to a historical reason, the same technique is often called as *multiple linear regression* (*MLR*). In this technique, $\boldsymbol{P}_{\mathrm{ILS}}$ has no apparent physical meaning, and it works as only a correlation matrix. Therefore, ILS (or MLR) is sometimes called "P-matrix method." In the same fashion, CLS is rarely called "K-matrix method."

For the same calibration sample set used for CLS, $\boldsymbol{P}_{\mathrm{ILS}}$ can be calculated as follows:

$$\boldsymbol{P}_{\mathrm{ILS}} = (\boldsymbol{A}^{\mathrm{T}}\boldsymbol{A})^{-1}\boldsymbol{A}^{\mathrm{T}}\boldsymbol{C}. \tag{5.13}$$

Once $\boldsymbol{P}_{\mathrm{ILS}}$ is calculated, which corresponds to the calibration curve of ILS, the concentrations of unknown samples, $\boldsymbol{c}_{\mathrm{u}}$, are very easily calculated as:

$$\boldsymbol{c}_{\mathrm{u}} = \boldsymbol{A}_{\mathrm{u}}\boldsymbol{P}_{\mathrm{ILS}}. \tag{5.14}$$

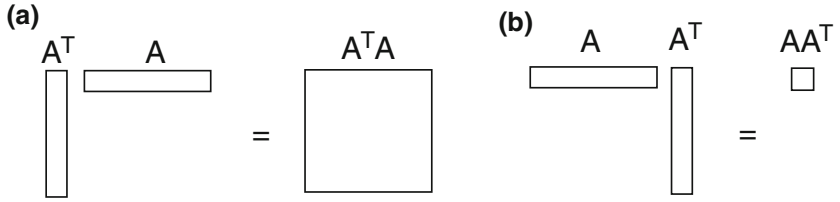

Fig. 5.10 Matrix size depends on the order of $\boldsymbol{A}$ and $\boldsymbol{A}^{\mathrm{T}}$

Nevertheless, if we perform the calculation of $\boldsymbol{P}_{\mathrm{ILS}}$ using Eq. (5.13), the calculation stops with an error saying "Matrix is close to singular or badly scaled." This means that the calculation of $\left(\boldsymbol{A}^{\mathrm{T}}\boldsymbol{A}\right)^{-1}$ cannot be performed.

In general, the matrix of $\boldsymbol{A}$ very often has a landscape shape $(M \times N)$, since the number of wavelength positions (N) is larger than the number of samples (M). As shown in Fig. 5.10a, the product of $\boldsymbol{A}^{\mathrm{T}}\boldsymbol{A}$ has a size of $(N \times N)$, which is a large square matrix.

Here, we have to note that the large square matrix still has a 'rank' of M, since the original spectra matrix, $\boldsymbol{A}$, has a rank of M. When the matrix size is larger than the rank of the matrix, according to linear algebra, the determinant of the matrix becomes nil $(\det(\boldsymbol{A}^{\mathrm{T}}\boldsymbol{A}) = 0)$. Since the inverse of a matrix is a product of the reciprocal determinant and the cofactor matrix:

$$(\boldsymbol{A}^{\mathrm{T}}\boldsymbol{A})^{-1} = \frac{1}{\det(\boldsymbol{A}^{\mathrm{T}}\boldsymbol{A})}(\text{cofactor matrix}),$$

The large matrix makes the calculation of the inverse matrix impossible. In this manner, the LS calculation of ILS is difficult to perform, although the idea is great to overcome the analytical inaccuracy of CLS caused by the inaccurate estimation of the number of constituents.

To get over the problem, the spectral matrix, $\boldsymbol{A}$, must be square or portrait (vertically long). This is achieved by two strategies:

1. The number of samples is increased.
2. The number of wavelength points is decreased.

The first strategy may be impractical to prepare hundreds of samples with various concentrations. Therefore, in general, the second strategy is taken for the ILS analysis. In short, only limited data on several wavelength points are taken out from the spectra, and the rest data are discarded. This spoils a great benefit of the multivariate analysis, and the analytical results depend on the selection of the data

points. This intrinsic problem involved in ILS will be improved by introducing PCA (Sect. 5.6). Before moving to PCA, the benefit of ILS is confirmed as below by using the spectra in Fig. 5.7b.

1. **Only one point at 600 nm is used**:

One 'column' of $\boldsymbol{A}$ (5×1) is input into Eq. (5.12) with $\boldsymbol{C}$ (5×2), and $\boldsymbol{P}$ (1×2) is calculated using Eq. (5.13). With the calculated $\boldsymbol{P}$ and only one column of $\boldsymbol{a}_u$ (Fig. 5.9) at 600 nm, the unknown concentrations are calculated to be 0.9751 and 1.4921. Since the correct concentrations are 2.5 and 1.5, the analytical error becomes 60.9948 and 0.5250%, respectively (depending on the random noise). In this manner, the ILS analysis on only one point yields a very poor result.

2. **Two points at 420 and 600 nm are used**:

Another point at 420 nm is added for the ILS analysis. Two columns of $\boldsymbol{A}$ (5×2) are used for the same procedure. As a result, the unknown concentrations are calculated to be 2.4358 and 1.4483 with analytical errors of 2.5681 and 3.4466%, respectively. In this manner, the analytical errors have significantly been reduced by adding only one point.

3. **Three points at 420, 540, and 600 nm are used**:

Another point at 540 nm is added, and three columns of $\boldsymbol{A}$ (5×3) are used for the same procedure. The unknown concentrations are calculated to be 2.5000 and 1.5000, which exactly match the correct concentrations. In this case, therefore, three-point analysis reaches the ideal results. In principle, the number of points can be increased up to five, in this case, but no improvement is found even if two additional points are added.

In this fashion, ILS exhibits a surprisingly powerful performance on spectral calibration with a very few points extracted from the spectra as theoretically expected. In other words, ILS is quite robust in comparison to CLS. One problem remains, however, that the ILS results depend on the selection of the points; whereas CLS can take full spectra without artificial selection of wavelength points. To solve the dilemma, PCA is necessary.

5.6 Principal Component Analysis (PCA)

The regression equation of CLS can be 'expanded' by the use of 'vectors' taken from the $\boldsymbol{C}$ and $\boldsymbol{K}$ matrices as presented by the third row of the next equation.

$$
\begin{aligned}
\boldsymbol{A} &= \boldsymbol{CK} + \boldsymbol{R} \\
&= \begin{pmatrix} c_{11} & c_{21} & \cdots & c_{r1} \\ \vdots & \vdots & \ddots & \vdots \\ c_{1M} & c_{2M} & \cdots & c_{rM} \end{pmatrix} \begin{pmatrix} k_{11} & \cdots & k_{1N} \\ k_{21} & \cdots & k_{2N} \\ \vdots & \ddots & \vdots \\ k_{r1} & \cdots & k_{rN} \end{pmatrix} + \boldsymbol{R} \\
&= \begin{pmatrix} c_{11} \\ \vdots \\ c_{1M} \end{pmatrix} \begin{pmatrix} k_{11} & \cdots & k_{1N} \end{pmatrix} + \begin{pmatrix} c_{21} \\ \vdots \\ c_{2M} \end{pmatrix} \begin{pmatrix} k_{21} & \cdots & k_{2N} \end{pmatrix} \\
&\quad + \cdots + \begin{pmatrix} c_{r1} \\ \vdots \\ c_{rM} \end{pmatrix} \begin{pmatrix} k_{r1} & \cdots & k_{rN} \end{pmatrix} + \boldsymbol{R} \\
&= \sum_{j=1}^{r} \boldsymbol{c}_j \boldsymbol{k}_j + \boldsymbol{R}
\end{aligned}
$$

This expanded form implies that the number of expansion terms, r, is limited by the number of pure-component spectra that are known a priori. Therefore, if the spectra are influenced by unexpectedly generated chemical species such as molecular associates, the new constituent and its quantity are missed in the CLS analysis.

To fully cover all the constituents involving the unexpected species, the number of the expanded terms should *not* be limited. In place of using the pure-component spectra known a priori, therefore, *mutually orthogonal vectors* should be used to expand the spectra matrix as follows:

$$\boldsymbol{A} = \boldsymbol{t}_1\boldsymbol{p}_1 + \boldsymbol{t}_2\boldsymbol{p}_2 + \cdots + \boldsymbol{t}_c\boldsymbol{p}_c = \sum_{j=1}^{c} \boldsymbol{t}_j\boldsymbol{p}_j \equiv \boldsymbol{TP}. \tag{5.15}$$

Here, c is the lesser one of M or N, and $\boldsymbol{p}_j$ represents the mutually orthogonal vectors satisfying Eq. (5.16), which is called "*loading*" vector:

$$\boldsymbol{p}_i \cdot \boldsymbol{p}_j = \boldsymbol{p}_i \boldsymbol{p}_j^{\mathrm{T}} = \delta_{ij}. \tag{5.16}$$

The dot represents the inner product, and δ_{ij} denotes Kronecker's delta. Since $\boldsymbol{p}_i$ is a row-wise vector, $\boldsymbol{p}_j$ is transposed for the calculation.

If a vector, $\boldsymbol{a}$, is involved in two-dimensional space (plane) spanned by mutually orthogonal two unit vectors, $\boldsymbol{p}_1$ and $\boldsymbol{p}_2$, as illustrated in Fig. 5.11, the vector, $\boldsymbol{a}$, can be expressed as:

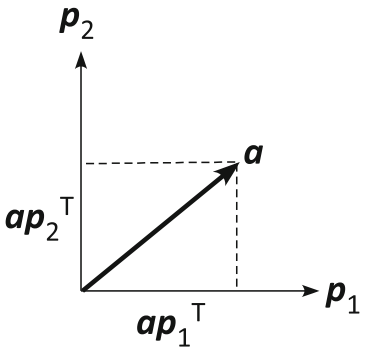

Fig. 5.11 A schematic concept of vector projection onto mutually orthogonal vectors. The projection is calculated by the inner product between $\boldsymbol{a}$ and $\boldsymbol{p}_j$

$$\boldsymbol{a} = (\boldsymbol{a}\boldsymbol{p}_1{}^{\mathrm{T}})\boldsymbol{p}_1 + (\boldsymbol{a}\boldsymbol{p}_2{}^{\mathrm{T}})\boldsymbol{p}_2. \tag{5.17}$$

When Eq. (5.17) is compared to Eq. (5.15), $\boldsymbol{t}_j$ is found to be

$$\boldsymbol{t}_j = \boldsymbol{a}\boldsymbol{p}_j{}^{\mathrm{T}} \Leftrightarrow \boldsymbol{T} = \boldsymbol{A}\boldsymbol{P}^{\mathrm{T}} \tag{5.18}$$

The coefficient vector, $\mathbf{t}_j$, is often called '*score*' vector. When all the score and loading vectors are put together to have $\boldsymbol{T}$ and $\boldsymbol{P}$, they are called score and loading matrices.

The loading vectors are calculated, so that the variance of the points in multivariate space should be maximized along a loading vector, which is schematically illustrated in Fig. 5.12.

If each spectrum has N absorbance data as a function of wavelength, the spectra need N-dimensional space. To visualize the space intuitively understandable, a cross-sectional image spanned by two orthogonal axes of $\boldsymbol{x}_j$ and $\boldsymbol{x}_k$ is presented in the figure. If the plot has an ellipsoidal variation as found in Fig. 5.12, *the 1st loading vector, $\boldsymbol{p}_1$, is determined, so that the loading vector should span the largest variance of the plot*. This loading vector works as the new axis for positioning the points.

At the moment, only the $\boldsymbol{p}_1$-parallel component is revealed for the plot, and the perpendicular component is left un-positioned, which requires the second loading vector, $\boldsymbol{p}_2$. The second loading vector is also determined to make the rest variance largest. If the points are within a plane, as in this example case, $\boldsymbol{p}_2$ is determined as illustrated in the figure.

To explain the calculation procedure of the loading vectors, some statistical variables must be introduced to discuss the variance of points. Let us use two-dimensional space for convenience. First of all, *average* is defined in terms of the two axes of x_1 and x_2:

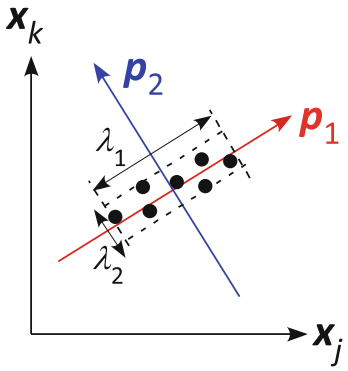

Fig. 5.12 Relationship between the points and the loading vector, $\boldsymbol{p}_1$, which maximizes the variance of the plot, λ_1. The loading vectors are calculated for the mean-centered data

$$\bar{x}_1 \equiv \frac{1}{n}\sum_j x_{1j} \quad \text{and} \quad \bar{x}_2 \equiv \frac{1}{n}\sum_j x_{2j}.$$

Here, (x_{1j}, x_{2j}) denotes the position of the jth point on the x_1–x_2 coordinate. With the use of the averages, *variance* is defined as follows:

$$V_1 \equiv \frac{1}{n}\sum_j (x_{1j} - \bar{x}_1)^2, \quad V_2 \equiv \frac{1}{n}\sum_j (x_{2j} - \bar{x}_2)^2.$$

In this discussion, the variance is not used for evaluating the population, and therefore $1/(n-1)$ is not necessary to be taken into account for the constant of proportion. Next, covariance, V_c, is also defined in a similar manner:

$$V_c \equiv \frac{1}{n}\sum_j (x_{1j} - \bar{x}_1)(x_{2j} - \bar{x}_2).$$

We are finding a new coordinate, which more appropriately spans the variance of the plot. To do that, a new coordinate, ξ_1–ξ_2, is considered with related to the original x_1–x_2 coordinate by rotating the relative angle, θ, i.e., unitary transformation:

$$\begin{pmatrix} \cos\theta & -\sin\theta \\ \sin\theta & \cos\theta \end{pmatrix} \begin{pmatrix} x_{1j} \\ x_{2j} \end{pmatrix} = \begin{pmatrix} \cos\theta \cdot x_{1j} - \sin\theta \cdot x_{2j} \\ \sin\theta \cdot x_{1j} + \cos\theta \cdot x_{2j} \end{pmatrix} \equiv \begin{pmatrix} \xi_{1j} \\ \xi_{2j} \end{pmatrix}.$$

Therefore, the new coordinate is expressed using θ:

$$\xi_{1j} = \cos\theta \cdot x_{1j} + \sin\theta \cdot x_{2j} \equiv a_1 x_{1j} + a_2 x_{2j}. \tag{5.19}$$

Here, $\cos\theta$ and $\sin\theta$ are replaced by a_1 and a_2, respectively, for making the following equations visually simpler. Now, we have to mind the constraint:

$$a_1^2 + a_2^2 = 1. \tag{5.20}$$

On the newly defined coordinate, the variance of the plot along the ξ_1 axis, $V(\xi_1)$, is expressed as:

$$V(\xi_1) = \frac{1}{n}\sum_j \left(\xi_{1j} - \bar{\xi}_1\right)^2.$$

The coordinate transformation (Eq. (5.19)) is put in this equation to have the next equation:

$$\begin{aligned} V(\xi_1) &= \frac{1}{n}\sum_j \left[\left(a_1 x_{1j} + a_2 x_{2j}\right) - \left(a_1\bar{x}_1 + a_2\bar{x}_2\right)\right]^2 \\ &= \frac{1}{n}\sum_j \left[a_1\left(x_{1j} - \bar{x}_1\right) - a_2\left(x_{2j} - \bar{x}_2\right)\right]^2 = a_1^2\left(\frac{1}{n}\sum_j \left(x_{1j} - \bar{x}_1\right)^2\right) \\ &\quad + 2a_1a_2\frac{1}{n}\sum_j \left(x_{1j} - \bar{x}_1\right)\left(x_{2j} - \bar{x}_2\right) + a_2^2\left(\frac{1}{n}\sum_j \left(x_{2j} - \bar{x}_2\right)^2\right) \\ &= a_1^2 V_1 + 2a_1a_2V_c + a_2^2V_2. \end{aligned} \tag{5.21}$$

In this manner, the 'new variance' on the new axis (loading vector) is simply expressed by using the variance and covariance on the original coordinate.

Now, we have a problem "how to make the new variance largest" by changing the slope (θ) of the new axis. In other words, this is the maximum-value problem with a constraint of Eq. (5.20). To solve a stationary-value problem involving the maximum-value problem under a constraint, *Lagrange's method of undetermined multipliers* works powerfully.

This method requires a modification of the constraint as:

$$a_1^2 + a_2^2 - 1 = 0,$$

and this is subtracted from the analytical target, $V(\xi_1)$, with a undetermined multiplier, λ, to have F:

$$F \equiv a_1^2V_1 + 2a_1a_2V_c + a_2^2V_2 - \lambda\left(a_1^2 + a_2^2 - 1\right).$$

To search for the best couple of a_1 and a_2 for maximizing F, the partial derivatives in terms of a_1, a_2 and λ must be nil as follows:

$$\frac{\partial F}{\partial a_1} = 2a_1V_1 + 2a_2V_c - 2a_1\lambda = 0$$
$$\frac{\partial F}{\partial a_2} = 2a_1V_c + 2a_2V_2 - 2a_2\lambda = 0$$
$$\frac{\partial F}{\partial \lambda} = -\left(a_1^2 + a_2^2 - 1\right) = 0.$$

The third equation definitely holds because of the constraint. Therefore, we are considering the first two equations only. The two equations can be organized to be:

$$\begin{aligned} a_1V_1 + a_2V_c &= a_1\lambda \\ a_1V_c + a_2V_2 &= a_2\lambda. \end{aligned} \tag{5.22}$$

These equations can be organized to be a more generalized form:

$$\begin{pmatrix} V_1 & V_c \\ V_c & V_2 \end{pmatrix}\begin{pmatrix} a_1 \\ a_2 \end{pmatrix} = \lambda\begin{pmatrix} a_1 \\ a_2 \end{pmatrix}. \tag{5.23}$$

This has a typical form of an eigenvalue problem. Of interest is that the undetermined multiplier, λ, has been changed to be the eigenvalue of a matrix consisting of variances and covariance. Equation (5.23) can be deformed as:

$$\begin{pmatrix} V_1 & V_c \\ V_c & V_2 \end{pmatrix}\begin{pmatrix} a_1 \\ a_2 \end{pmatrix} = \begin{pmatrix} \lambda & 0 \\ 0 & \lambda \end{pmatrix}\begin{pmatrix} a_1 \\ a_2 \end{pmatrix},$$

which can further be simplified as:

$$\begin{pmatrix} V_1 - \lambda & V_c \\ V_c & V_2 - \lambda \end{pmatrix}\begin{pmatrix} a_1 \\ a_2 \end{pmatrix} = 0.$$

This equation has nontrivial solutions for a_1 and a_2, if the next condition is satisfied (Cramer's solution):

$$\det\begin{pmatrix} V_1 - \lambda & V_c \\ V_c & V_2 - \lambda \end{pmatrix} = 0$$
$$\Leftrightarrow (V_1 - \lambda)(V_2 - \lambda) - V_c^2 = 0.$$

This equation yields two eigenvalues, λ_1 and λ_2. When one of the eigenvalues is put into the original simultaneous equations (Eq. (5.22)), the following equations hold:

$$\begin{aligned} a_1V_1 + a_2V_c &= a_1\lambda_1 \\ a_1V_c + a_2V_2 &= a_2\lambda_1. \end{aligned} \tag{5.24}$$

After multiplying a_1 and a_2 respectively to the two equations, the summation of the equations yields:

$$a_1^2 V_1 + 2a_1 a_2 V_c + a_2^2 V_2 = \left(a_1^2 + a_2^2\right)\lambda_1.$$

Since the left-hand side equals to $V(\xi_1)$ (Eq. (5.21)), the next very simple conclusion is obtained:

$$\boxed{V(\xi_1) = \lambda_1}.$$

This conclusion implies a very important fact that *the eigenvalue is a measure of variance along the newly generated axis* (*loading vector*) as illustrated in Fig. 5.12. This is one of the most fundamental natures of linear algebra about matrix.

Once the eigenvalue is calculated, the corresponding eigenvector can easily be obtained by referring to Eq. (5.24) as follows:

$$a_2 = \frac{\lambda - V_1}{V_c} a_1.$$

Due to the constraint of Eq. (5.20), a_1 and a_2 are readily calculated as (double-sign correspond)

$$\begin{aligned} a_1 &= \pm \frac{V_c}{\sqrt{V_c^2 + (\lambda_1 - V_1)^2}} \\ a_2 &= \pm \frac{\lambda_1 - V_1}{\sqrt{V_c^2 + (\lambda_1 - V_1)^2}}. \end{aligned} \tag{5.25}$$

In this manner, the coefficients of ξ_{1j} (Eq. (5.19)) are determined, which means that the loading vectors are calculated from the matrix of variances and covariance.

Note that the double sign of Eq. (5.25) means the loading vector can have two opposite directions. Our analytical purpose is, however, calculating an 'axis' and the direction of the axis is for nothing. In other words, both directions can be accepted. Regardless, the score vector, $\boldsymbol{t}_j$, depends on the direction (sign) of the loading vector, $\boldsymbol{p}_j$, via Eq. (5.18). If the score vectors are discussed quantitatively, therefore, we have to take care of the sign of the loading vector.

In this manner, once the *variance–covariance matrix* is obtained, both loading vectors, eigenvalues and score vectors are soon calculated. In practice, some useful algorithms to calculate the values have already been established involving the QR decomposition, Jordan decomposition, Gram–Schmidt process, NIPALS, and *singular-value decomposition* (*SVD*) [4]. SVD is particularly famous, since it is applicable to non-square matrix, and it is thus quite often found in computer software represented by MATLAB, Scilab, and Igor.

The variance–covariance matrix is easily generated using the spectra matrix, $\boldsymbol{A}$. To do that, the mean-centered matrix, $\boldsymbol{A}_c$, is calculated such as:

$$\boldsymbol{A}_c = \begin{pmatrix} x_{11} - \bar{x}_1 & x_{12} - \bar{x}_2 & x_{13} - \bar{x}_3 & \cdots & x_{1N} - \bar{x}_N \\ x_{21} - \bar{x}_1 & x_{22} - \bar{x}_2 & x_{23} - \bar{x}_3 & \cdots & x_{2N} - \bar{x}_N \\ \vdots & \vdots & \vdots & \ddots & \vdots \\ x_{M1} - \bar{x}_1 & x_{M2} - \bar{x}_2 & x_{M3} - \bar{x}_3 & \cdots & x_{MN} - \bar{x}_N \end{pmatrix}.$$

This corresponds to displacement of the origin to that of the loading coordinate. Then, the transposed matrix is multiplied from the left-hand side, which generates the variance–covariance matrix on one step for any case:

$$\begin{aligned} \boldsymbol{A}_c{}^{\mathrm{T}}\boldsymbol{A}_c = & \begin{pmatrix} x_{11} - \bar{x}_1 & x_{21} - \bar{x}_1 & \cdots & x_{M1} - \bar{x}_1 \\ x_{12} - \bar{x}_2 & x_{22} - \bar{x}_2 & \cdots & x_{M2} - \bar{x}_2 \\ x_{13} - \bar{x}_3 & x_{23} - \bar{x}_3 & \cdots & x_{M3} - \bar{x}_3 \\ \vdots & \vdots & \ddots & \vdots \\ x_{1N} - \bar{x}_N & x_{2N} - \bar{x}_N & \cdots & x_{MN} - \bar{x}_N \end{pmatrix} \\ & \times \begin{pmatrix} x_{11} - \bar{x}_1 & x_{12} - \bar{x}_2 & x_{13} - \bar{x}_3 & \cdots & x_{1N} - \bar{x}_N \\ x_{21} - \bar{x}_1 & x_{22} - \bar{x}_2 & x_{23} - \bar{x}_3 & \cdots & x_{2N} - \bar{x}_N \\ \vdots & \vdots & \vdots & \ddots & \vdots \\ x_{M1} - \bar{x}_1 & x_{M2} - \bar{x}_2 & x_{M3} - \bar{x}_3 & \cdots & x_{MN} - \bar{x}_N \end{pmatrix} \\ = n \cdot & \begin{pmatrix} V_{11} & \mathrm{cov}(1,2) & \cdots & \mathrm{cov}(1,N) \\ \mathrm{cov}(2,1) & V_{22} & \cdots & \mathrm{cov}(2,N) \\ \vdots & \vdots & \ddots & \vdots \\ \mathrm{cov}(N,1) & \mathrm{cov}(N,2) & \cdots & V_{NN} \end{pmatrix}. \end{aligned}$$

The calculation procedure is summarized as:

$$\boldsymbol{A}_c{}^{\mathrm{T}}\boldsymbol{A}_c\boldsymbol{P} = \boldsymbol{\Lambda}\boldsymbol{P},$$

where $\boldsymbol{\Lambda}$ is a matrix involving the eigenvalues on the diagonal elements.

Note that *the mean-centering is not necessary for the purpose of PCA expansion*. If the mean-centering is omitted, the origin of the loading vectors stays at the origin of the original coordinate. In other words, *the origin of the original coordinate is added to the plot* as represented by the dotted ellipsoid in Fig. 5.13.

In general, the points of the measured spectra are relatively far from the origin, and the ellipsoid often has a long shape. In this case, the first loading vector, $\boldsymbol{p}_1$, passes near the center of gravity of the points. Since the center of gravity is the average of the spectra, $\boldsymbol{p}_1$ *intrinsically shows a spectrum similar to the average*

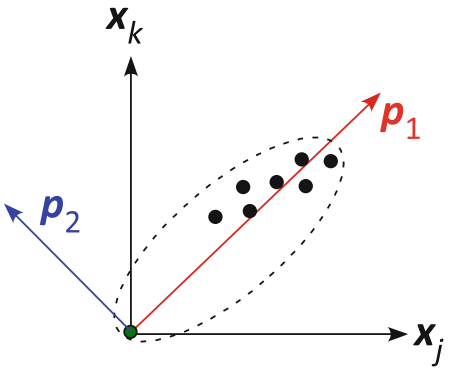

Fig. 5.13 Loading vectors calculated for 'non-mean centered' data. The origin of the new axes (*green solid circle*) stays at the original position

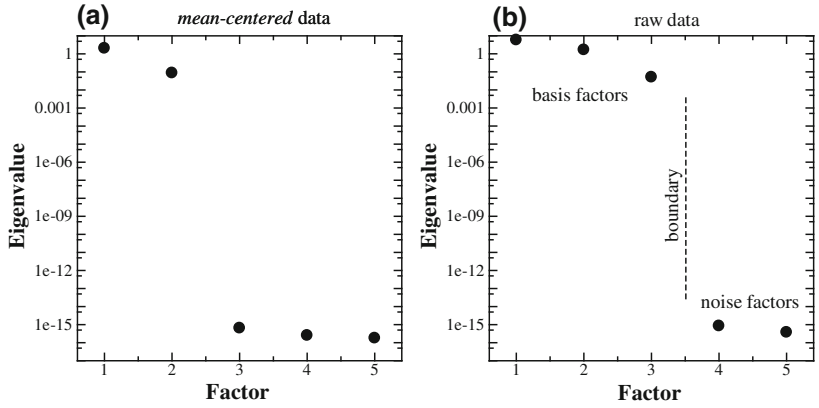

Fig. 5.14 Eigenvalues against factor (j) calculated from the spectra in Fig. 5.7b in semi-log scale calculated on **a** mean-centered data, and **b** raw data

spectrum. In other words, it is no surprise to have an average-like spectrum as the first loading vector.

Since the loading vectors are generated to make the variance maximized along each loading, *the eigenvalues are definitely generated in the decreasing order*. For example, the three-component spectra in Fig. 5.7b are put in the spectra matrix of $\boldsymbol{A}$, and the eigenvalues are calculated as plotted in Fig. 5.14.

Since the number of spectra (or rank) is five, five eigenvalues are calculated as presented by the solid circles. As theoretically expected, they are in a decreasing order. When the mean-centering is applied to the data as a pretreatment, as found in Fig. 5.14a, only the first two eigenvalues are significant, which is inconsistent with the synthesized three-component spectra. This is because the pretreatment of mean-centering decreases the degree of freedom of the data. This is confirmed by

take a look at the loading vectors in Fig. 5.15: the first loading vector of mean-centered data corresponds to the second loading of the raw data. In other words, the average-like spectrum (should be the 1st loading) is missed by the pretreatment.

On the other hand, on the raw data without mean-centering, the three constituents are correctly figured out by the significant eigenvalues in Fig. 5.14b. To analyze the number of constituents, in this manner, the raw data must be applied to the PCA expansion. The significant three eigenvalues imply that *the points of spectra are mostly involved in three-dimensional space*. Therefore, in the present case, the PCA expansion is expressed as:

$$\boldsymbol{A} = \boldsymbol{t}_1\boldsymbol{p}_1 + \boldsymbol{t}_2\boldsymbol{p}_2 + \boldsymbol{t}_3\boldsymbol{p}_3 + \boldsymbol{t}_4\boldsymbol{p}_4 + \boldsymbol{t}_5\boldsymbol{p}_5 \,. \tag{5.26}$$

The first three factors are called "*basis factor*s" whereas the rest ones are called "*noise factors*." Analysis of criteria between the basis and noise factors can be difficult, since the boundary often becomes ambiguous. Many analytical techniques such as Malinowski's IND function and '*cross validation*,' which is most useful technique. For the details of the criteria analysis, the reader is referred to literature [4].

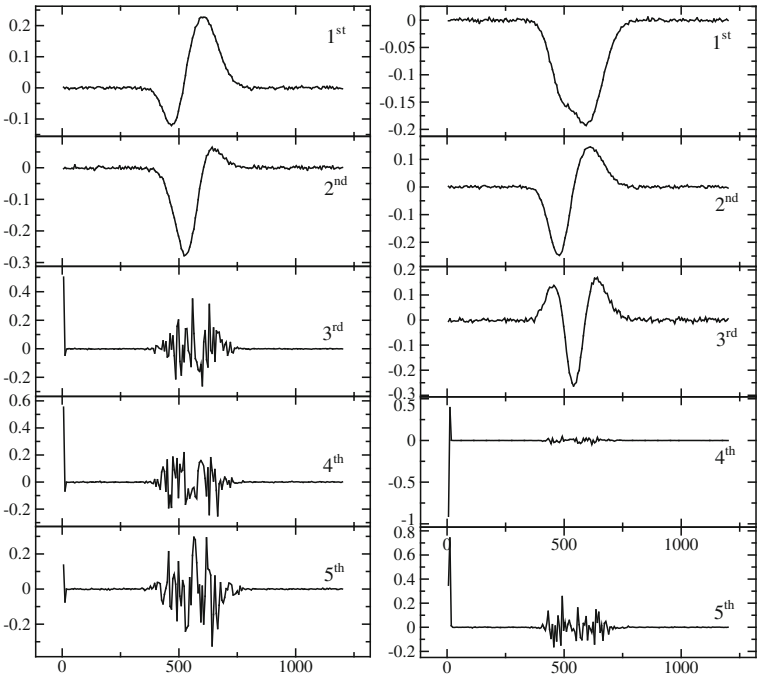

Fig. 5.15 Loading spectra calculated on the mean-centered data (*left column*) and those on the raw data (*right column*)

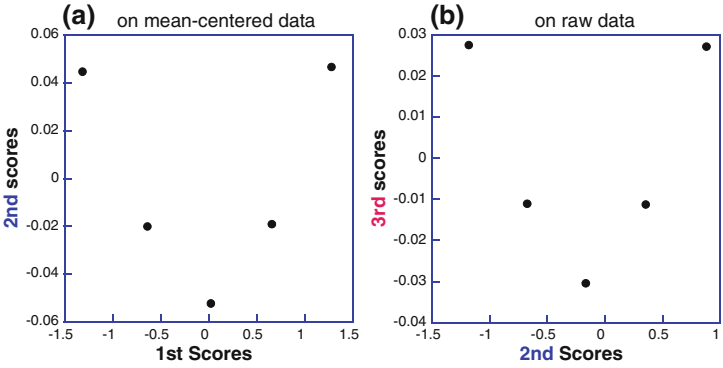

Fig. 5.16 Score–score plots of **a** the mean-centered spectra and **b** the raw spectra corresponding to the loadings in Fig. 5.15

As stated at Eq. (5.25), the sign of the loading vector can be changed. The first loading 'spectrum' of the raw data in right column of Fig. 5.15 exhibits an overturned shape, which is because the sign of the loading vector is opposite to our expectation. If you want to discuss the spectrum, therefore, the spectrum can be multiplied by −1 to overturn it. In this case, note that the corresponding score vector must also be multiplied by −1.

The influence by the mean-centering can be visualized by magnifying the point variation in the multidimensional space (for example, see Fig. 5.12). To efficiently visualize a cross-sectional (two-dimensional) image of the point variation, of course, a mutually orthogonal axis set should be chosen, which should also capture the maximum variance of the plot. If loading vectors are used, therefore, this magnification can effectively be achieved, which is called "*score–score plot*." In other words, *point projections onto a two-dimensional plane spanned by two loading vectors are used to discuss the spectral variation in shape*.

Figure 5.16 presents score–score plots calculated (Eq. (5.18)) for the raw and mean-centered spectra. The spectral *variation in shape* is represented by the *curved plot* in the figures. Of interest is that a similar curve appears in different factor sets: (a) is for the first to second set while (b) is for the second to third set. This apparently implies that (1) the factor level goes down by one because of the mean-centering, and (2) the variation of the spectral shape is kept even after a different loading set (Fig. 5.15) is chosen.

In this manner, score–score plot is found to be useful to discuss a minute change of the spectral shape. This powerful character is conveniently employed to discriminate agricultural products via the measurements of IR spectra especially when the spectral quality is not good enough.

The left panel of Fig. 5.17 presents IR ATR spectra of strawberry, raspberry, and apple purees [3]. Since the major chemical constituents are common to the three fruits, the IR spectra are very similar to each other, which is highly difficult to

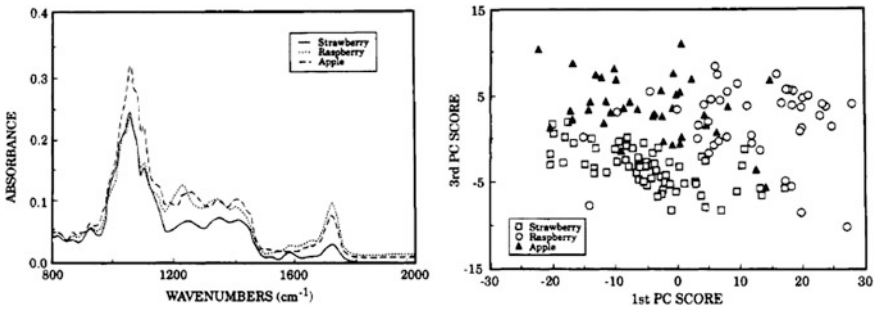

Fig. 5.17 IR spectra of strawberry, raspberry, and apple (*left*), and the score–score plot between the first and second loadings (*right*) [3]

discriminate visually. Regardless, the very minute differences in spectral shape are reflected by the positions of the points in multidimensional space.

The right panel of Fig. 5.17 presents the score–score plot between the first and third loading vectors. The three symbols (□, ○, and ▲) are separated from each other, although the boundary is not sharp. In this manner, the score–score plot technique based on PCA works powerfully when the spectral change in shape is very minor and high spectral quality measurement cannot be expected.

5.7 Merge of ILS and PCA: PCR

The intrinsic problem of CLS that the analytical accuracy is largely degraded on a wrong number of constituents is overcome by introducing ILS (or MLR). Nevertheless, the number of absorbance data must largely be reduced to have an LS solution as found in a previous section. This is a big dilemma to perform ILS, since the reduction of the absorbance data spoils the great benefit of multivariate analysis that the spectral data are fully used for calibration. To get over this dilemma, PCA works powerfully.

As found in Eq. (5.12), ILS correlates the concentration, $\boldsymbol{C}$, with the spectra, $\boldsymbol{A}$, via the correlation matrix of $\boldsymbol{P}_{\mathrm{ILS}}$. This can be understood in another way that the points of spectra in the original coordinate (x_j and x_k) in Fig. 5.13 are correlated to the concertation matrix. Even if the coordinate is unitary transformed to have $\boldsymbol{p}_1$ and $\boldsymbol{p}_2$ (PCA loadings), the points of spectra are kept unchanged. Therefore, "the scores on the PCA loadings" fully possesses the quantity information of the spectral variation, and they can thus be used in place of the absorbance spectra [1, 2].

Since the matrices $\boldsymbol{A}$ and $\boldsymbol{P}$ have a size of $(M \times N)$ and $(M \times N)$, the size of $\boldsymbol{T}$ is revealed to be $(M \times M)$ via the next matrix-size analysis:

$$\boldsymbol{A} = \boldsymbol{TP} \leftrightarrow (M \times N) = (M \times M)(M \times N).$$

In this manner, the score matrix of $\boldsymbol{T}$ is a 'square' matrix. As mentioned in Sect. 5.5, if the spectra matrix of ILS is square, the LS solution would be calculated with no problem. Therefore, *the PCA scores, $\boldsymbol{T}$, should be used in place of the raw spectra, $\boldsymbol{A}$, in the ILS regression*, which is represented as:

$$\boxed{\boldsymbol{C} = \boldsymbol{TP}_{\mathrm{ILS}} + \boldsymbol{R}}.$$

This merged technique of PCA and ILS is called *principal component regression* (*PCR*), which is quite often used for calibration purposes as well as the PLS technique in the next section. PCR has both benefits of CLS and ILS that the spectral data are fully used for calibration even if the proper number of constituents is not known.

The procedure of PCR is as follows:

1. The PCA score matrix, $\boldsymbol{T}$, is calculated using Eq. (5.18).
2. $\boldsymbol{P}_{\mathrm{ILS}}$ is calculated using $\boldsymbol{T}$ via Eq. (5.13)
3. A concentration-unknown sample is calibrated by using the measured spectra, $\boldsymbol{A}_{\mathrm{u}}$, as

$$\boldsymbol{c}_{\mathrm{u}} = \left(\boldsymbol{A}_{\mathrm{u}}\boldsymbol{P}_{\mathrm{PCA}}{}^{\mathrm{T}}\right)\boldsymbol{P}_{\mathrm{ILS}}.$$

   As emphasized by the parenthesis, do not forget to convert the unknown spectra to PCA scores using $\boldsymbol{P}_{\mathrm{PCA}}$, which is the 'PCA loading' matrix.

In practice, the same spectra (Figs. 5.7b and 5.9) as those used for CLS and ILS, and the two-component concentration matrix are employed for checking PCR. As a result, the concentrations are predicted as 2.5000 and 1.5000, which perfectly agree with the correct concentrations.

If the spectra are very noisy, the noise can selectively be reduced by discarding the noise factors in the PCA process (Eq. (5.26)). This PCA noise reduction is quite powerful when the number of spectra is large as found in Sect. 5.9.

5.8 Independent Residual Terms: PLS

All the regression models mentioned previously are based on an assumption that the analytical and experimental errors are all attributed to the residual term, $\boldsymbol{R}$. This means that the errors are involved only in the objective variable, i.e., $\boldsymbol{A}$ in CLS and $\boldsymbol{C}$ in ILS. Theoretically, however, experimental errors independently occur in both $\boldsymbol{A}$ and $\boldsymbol{C}$, although they are correlated with each other via the spectra measurements.

To keep the independency of the two errors [2], the equations having the residual terms of $\boldsymbol{R}_A$ and $\boldsymbol{R}_C$ should be separated from each other as found in the equations below:

$$\boldsymbol{A} = \sum_h \boldsymbol{t}_h \boldsymbol{p}_h + \boldsymbol{R}_A = \boldsymbol{TP} + \boldsymbol{R}_A \tag{5.27}$$

$$\boldsymbol{C} = \sum_h \boldsymbol{u}_h \boldsymbol{q}_h + \boldsymbol{R}_C = \boldsymbol{UQ} + \boldsymbol{R}_C. \tag{5.28}$$

The regression technique based on the separated equations is called *partial least squares* (*PLS*) regression [5]. The equations are intrinsically the same as the formulation of PCA: both $\boldsymbol{A}$ and $\boldsymbol{C}$ are expanded by the use of mutually orthogonal loading vectors, $\boldsymbol{p}_h$ and $\boldsymbol{q}_h$, respectively.

Since $\boldsymbol{A}$ and $\boldsymbol{C}$ have individual experimental errors, there is no common loading vector that simultaneously explains the points in $\boldsymbol{A}$ and $\boldsymbol{C}$ spaces. One of the characteristics of PLS is, therefore, that a latent variable of *weight loading*, $\boldsymbol{w}_h$, is implicitly used as an optimal common loading. Once a weight loading is obtained, it is used to calculate score vectors step by step by changing h. For $h = 1$, Eqs. (5.27) and (5.28) are roughly approximated by only one factor:

$$\begin{aligned} \boldsymbol{A} &\approx \boldsymbol{t}_1 \boldsymbol{w}_1 \\ \boldsymbol{C} &\approx \boldsymbol{u}_1 \boldsymbol{q}_1 \end{aligned}. \tag{5.29}$$

As found in Eq. (5.29), the spectral loading vector, $\boldsymbol{p}_1$ is replaced by the 'temporary' weight loading, $\boldsymbol{w}_1$. In PLS, unlike PCA, the weight-loading vector is calculated by maximizing the variances of *both scores* of $\boldsymbol{A}$ and $\boldsymbol{C}$. Since the scores are calculated as a projection on the loading vector, they are approximately calculated using the weight loading:

$$\boldsymbol{t}_1 \approx \boldsymbol{A}{\boldsymbol{w}_1}^{\mathrm{T}} \tag{5.30}$$

$$\boldsymbol{u}_1 \approx \boldsymbol{C}{\boldsymbol{q}_1}^{\mathrm{T}}. \tag{5.31}$$

To maximize the correlation of the two score vectors, the covariant matrix

$${\boldsymbol{t}_1}^{\mathrm{T}} \boldsymbol{u}_1 = \left(\boldsymbol{A}{\boldsymbol{w}_1}^{\mathrm{T}}\right)^{\mathrm{T}} \boldsymbol{C}{\boldsymbol{q}_1}^{\mathrm{T}} = {\boldsymbol{w}_1}^{\mathrm{T}} \left(\boldsymbol{A}^{\mathrm{T}} \boldsymbol{C}\right) \boldsymbol{q}_1$$

should be maximized [6]. According to Manne [7], this calculation can be carried out by performing the SVD calculation of the 'covariant' matrix, $\boldsymbol{S} \equiv \boldsymbol{A}^{\mathrm{T}} \boldsymbol{C}$. By choosing this order of multiplying, the size of $\boldsymbol{S}$ becomes very small having the same size as the rank, which makes the calculation speed very fast. In this case, the first weight-loading vector is obtained by:

$$\boldsymbol{w}_1 = \boldsymbol{S}\boldsymbol{q}_1{}^{\mathrm{T}}/\sqrt{\lambda_1}.$$

Here, $\boldsymbol{q}_1$ and λ_1 are eigenvector and eigenvalue, which are both directly obtained by SVD. With the use of the weight loading, the score, $\boldsymbol{t}_1$, is calculated by Eq. (5.30). $\boldsymbol{u}_1$ is also calculated by Eq. (5.31). Then, the spectral loading, $\boldsymbol{p}_1$, is calculated as

$$\boldsymbol{p}_1 = \boldsymbol{t}_1{}^{\mathrm{T}}\boldsymbol{A}/\|\boldsymbol{t}_1\|^2.$$

Once the first set of the parameters are obtained, the rest data being modeled by $\boldsymbol{t}_2\boldsymbol{w}_2$ are calculated as $(h \geq 2)$:

$$\boldsymbol{t}_h\boldsymbol{w}_h = \boldsymbol{A} - \sum_{j=1}^{h-1} \boldsymbol{t}_j\boldsymbol{p}_j.$$

The proportionality matrix, $\boldsymbol{b}$, between $\boldsymbol{t}$ and $\boldsymbol{u}$ is defined as:

$$\boldsymbol{b}_j = \boldsymbol{u}_j{}^{\mathrm{T}}\boldsymbol{t}_j.$$

With the use of this parameter, in a similar manner to the spectral matrix, the rest concentration matrix is represented as:

$$\boldsymbol{u}_h\boldsymbol{q}_h = \boldsymbol{C} - \sum_{j=1}^{h-1} \boldsymbol{b}_j\boldsymbol{t}_j\boldsymbol{q}_j. \tag{5.32}$$

This procedure is repeated between Eqs. (5.30) and (5.32) by adding one to h, which yields the PLS modeling at Eqs. (5.27) and (5.28).

To predict the concentrations of unknown samples, $\boldsymbol{C}_{\mathrm{u}}$, the spectra of the samples stored in $\boldsymbol{A}_{\mathrm{u}}$ and the weight loadings are used to calculate $\boldsymbol{t}_{\mathrm{u},j}$. Using $\boldsymbol{b}_j$, $\boldsymbol{u}_{\mathrm{u},j}$ is soon obtained. By employing $\boldsymbol{q}_j$ obtained in the PLS calibration, the concentrations are summed up to have:

$$\boldsymbol{C}_{\mathrm{u}} = \sum_j \boldsymbol{u}_j\boldsymbol{q}_j.$$

This basic concept of PLS is sometimes called *PLS2*, where multiple constituents are simultaneously calibrated. If a single component is calibrated, on the other hand, such a PLS is called *PLS1*. Intrinsically, PLS1 and PLS2 are the same as each other, and no discrimination is needed. In former days, PLS1 was preferred because a computer program of PLS1 is simply coded, which was suitable for a low-power computer. A single component requires a single-column concentration "vector," $\boldsymbol{c}$, instead of using a matrix of $\boldsymbol{C}$, which further results in making the score vector of $\boldsymbol{u}_h$ changed to a *scalar*, u_h.

$$\boldsymbol{c} = \sum_h u_h \boldsymbol{q}_h + \boldsymbol{R}_C = \boldsymbol{UQ} + \boldsymbol{R}_C.$$

This characteristic was favored when an iteration algorithm such as NIPALS and Gram–Schmidt ones [4] was employed for the calculation instead of using SVD, since a scalar score do not need an iteration algorithm. In a modern PLS analysis, the discrimination is not needed, since a high-power computer is available to run SVD at a low cost.

5.9 Efficient Removal of Spectral Noise Using PCA

In Sect. 5.6, PCA is introduced to bridge ILS and PCR. PCA is intrinsically a matrix expansion technique using mutually orthogonal vectors, which is represented by Eq. (5.15). As found in Fig. 5.14, major constituents that contribute apparent spectral changes are reflected by some limited factors having significant eigenvalues, which are called the "*basis factors*." Since the rest factors belong to the "*noise factors*" (Sect. 5.6), Eq. (5.26) would be quite useful to make the spectral quality better, if the noise factors are discarded.

This noise-discarding technique works powerfully especially when the number of the noise factors is much larger than that of the basis factors. Imaging analysis after mapping measurements satisfies this condition [8], and another good case is the time-resolved measurements.

Figure 5.18a presents selected IR ATR spectra in a time course of mixing of ethylene glycol (EG) and water [9]. Since the mixing occurs very quickly, the

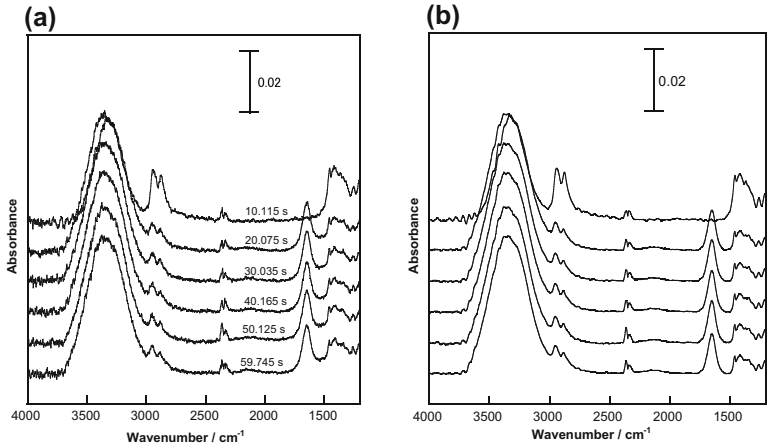

Fig. 5.18 **a** IR ATR spectra of an aqueous solution of EG in the mixing process measured by the rapid-scan technique, and **b** the noise reduced spectra by PCA

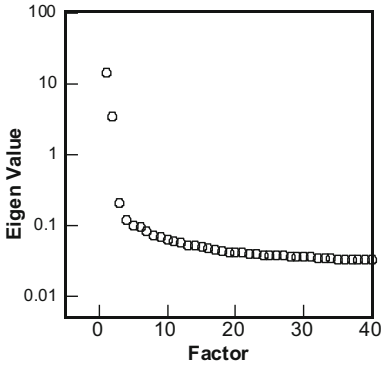

Fig. 5.19 An eigenvalue plot for the first 40 factors calculated for the time-resolved 360 IR ATR spectra

interval of the measurements was set to 0.18 s, which can be performed by choosing the "rapid scan" mode of FT-IR. As a result, 360 IR spectra are recorded in about only 64 s.

Of course, each spectrum is obtained without accumulation, which results in a poor signal-to-noise ratio as found in the figure. Regardless, this is a good situation that the number of the constituents would be only a few, whereas the total number of the spectra is 360 that is very many.

In fact, the eigenvalue plot of the 360 spectra shows that only three factors are important to explain the series of spectra (Fig. 5.19) [9].

This situation can be summarized using the next PCA equation:

$$\boldsymbol{A} = \boldsymbol{t}_1\boldsymbol{p}_1 + \boldsymbol{t}_2\boldsymbol{p}_2 + \cdots + \boldsymbol{t}_b\boldsymbol{p}_b + \boldsymbol{t}_{b+1}\boldsymbol{p}_{b+1} + \cdots + \boldsymbol{t}_M\boldsymbol{p}_M. \tag{5.33}$$

The subscript, b, in Eq. (5.33) is the number of the basis factors, i.e., 3, and M is 360. If only the basis factors are kept remained by discarding the rest 357 noise factors, the reconstructed spectra, $\boldsymbol{A}^{\mathrm{rec}}$, would become much better in quality:

$$\boldsymbol{A}^{\mathrm{rec}} = \boldsymbol{t}_1\boldsymbol{p}_1 + \boldsymbol{t}_2\boldsymbol{p}_2 + \cdots + \boldsymbol{t}_b\boldsymbol{p}_b.$$

The reconstructed spectra are shown in Fig. 5.18b. The noise on spectra is readily removed significantly.

An appropriate PCA noise reduction is quite powerful, since the chemically important signal is kept unchanged for both qualitative and quantitative characters. As shown in the next section, this can be used as a useful 'pretreatment' for a further spectral decomposition, which needs quantitative reliability and accuracy.

5.10 Alternative Least Squares (ALS) for Spectral Decomposition

As found in Sect. 5.4, the CLS regression technique has an intrinsic powerful function that a collection of spectra of multiple constituents can be decomposed to yield individual pure-constituent spectra, if a correct concentration matrix with an appropriate number of constituents is known in advance. This is in fact a uniquely powerful characteristic of CLS, which should be used for physicochemical discussion. We have already learned, fortunately, that the number of chemically independent components can be analyzed by using PCA.

With the accurate number of constituents, the principle of CLS can be employed in an expanded manner to decompose the spectra matrix, $\boldsymbol{A}$, into $\boldsymbol{C}$ and $\boldsymbol{K}$ *without using* a priori *knowledge at all*, which seems a magic. This technique is called alternative least squares (ALS) regression, which is one of the multivariate curve resolution (MCR) techniques.

In principle, two matrices of CLS must be known to have a least squares (LS) solution. To calculate $\boldsymbol{K}$, for example, $\boldsymbol{A}$ and $\boldsymbol{C}$ must be available at hand. In ALS, however, only $\boldsymbol{A}$ is needed, and the LS solution is calculated using a tentative matrix *consisting of random numbers*. If $\boldsymbol{C}$ made of random numbers is used, then a tentative matrix of $\boldsymbol{K}'$ is calculated as:

$$\boldsymbol{K}' = \left(\boldsymbol{C}^{\mathrm{T}}\boldsymbol{C}\right)^{-1}\boldsymbol{C}^{\mathrm{T}}\boldsymbol{A}.$$

Since random numbers are used, $\boldsymbol{K}'$ involves negative numbers for some elements. Considering that a normal absorbance spectrum has no negative band, the negative numbers are replaced by nil (or very small negative values for a quick convergence). This is called "non-negative constraint." The renewed $\boldsymbol{K}$ is used for calculating a tentative $\boldsymbol{C}'$:

$$\boldsymbol{C}' = \boldsymbol{A}\boldsymbol{K}^{\mathrm{T}}\left(\boldsymbol{K}\boldsymbol{K}^{\mathrm{T}}\right)^{-1}.$$

In a similar manner to $\boldsymbol{K}'$, the negative values in $\boldsymbol{C}'$ are replaced by nil (or very small negative values). These calculations are repeated until no negative value appears in both $\boldsymbol{C}$ and $\boldsymbol{K}$, which is the final convergence.

In this manner, ALS is an application of CLS, and $\boldsymbol{C}$ and $\boldsymbol{K}$ are dependent on each other quantitatively. In other words, ALS is not used for quantitative analysis. Regardless, ALS is still powerful, since *it reveals the shape of vectors* in both $\boldsymbol{C}$ and $\boldsymbol{K}$.

Here, an example study using ALS is presented. ALS is employed for decomposing the concentration-dependent IR ATR spectra of ethyleneglycol (EG)/water solutions. Figure 5.20 presents selected IR spectra of the series [9]. Since two constituents of EG and water are mixed, isosbestic points appears at several points. On a closer inspection, however, some band shifts are found especially in the νC–H region, which cannot be explained by only the two constituents. In fact, the

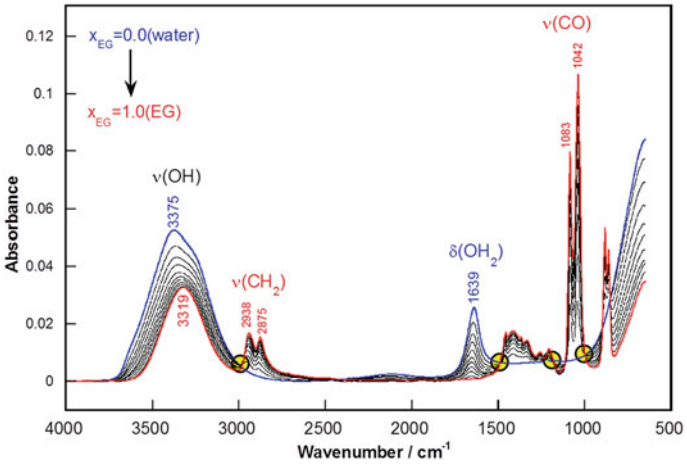

Fig. 5.20 Concentration-dependent IR ATR spectra of EG/water solutions [9]

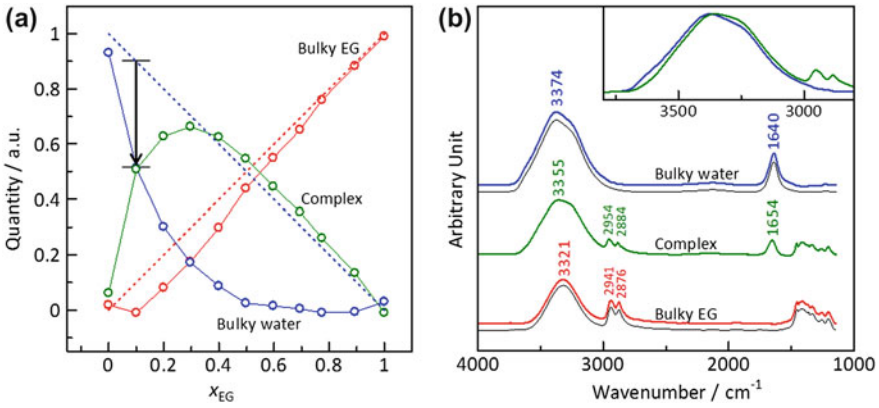

Fig. 5.21 Converged **a** *C* and **b** *K* obtained by ALS calculation [9]

eigenvalue plot of the spectra after PCA revealed that 'three' constituents were necessary to fully account for the spectral changes [9].

Next what we have to do is that $\boldsymbol{C}$ and $\boldsymbol{K}$ matrices having 'three' columns and rows, respectively, are prepared for running ALS. The converged results are presented in Fig. 5.21.

The decomposed spectra of the blue and red curves in Fig. 5.21b perfectly reproduce the IR spectra of neat water and EG, respectively, which straightforwardly implies the powerful character of ALS. Of more interest is, however, found at the green spectrum. The third spectrum looks to have both characters of water and EG, but the band positions of the νC–H at about 2900 cm^{-1} and δOH_2 modes

at about 1640 cm^{-1} are both different from the neat ones. As a matter of fact, this spectrum is assigned to the complex of water and EG [9]. In this manner, *the accuracy of the shape* of the analytical results is a powerful character of ALS to discuss the decomposed IR spectra.

In fact, the concentration variation in Fig. 5.21a is of interest. When EG is added to water, at the initial stage, no bulky EG is found, and instead the complex increases rapidly. The maximum of the complex is found at $x_{EG} = 0.3$, which corresponds to 60 wt%. Conventionally, the EG/water solution has long been known to exhibit the best anti-freezing effect at 60 wt%, which agrees with the maximum of the complex. In this manner, spectral decomposition by ALS is quite useful for quantitative physicochemical discussion.

5.11 Factor Analytical Resolution of Minute Signals (FARMS)

In principle, the PCA loading vectors have no explicit chemical meaning, since they are calculated, so that they would only be orthogonal to each other. In a limited case, however, a PCA loading can be a meaningful spectrum.

The limited case is that a constituent exits with an extremely minute quantity to the rest constituents. In other words, if the mixture comprises with a significantly large concentration ratio, the individual spectrum of the minute constituent would readily be revealed as a PCA loading. This unique character of PCA is named factor analytical resolution of minute signals (FARMS) [10].

If you find a loading spectrum like a pure-component spectrum, you are encouraged to consider whether the quantity would be very minor or not. If the quantity can be very minor, the PCA loading spectrum should be attributed to the minor species, and the spectrum can be discussed chemically, as if the component is readily separated from the mixture.

As an example study using FARMS, molecular structure of "the interfacial water" at the solid/bulk water interface is analyzed via IR ATR measurements at various angles of incidence [11]. At an interface, the structure of water is different from that of bulk water, but the interfacial water is very minute buried in bulky water.

As shown in Sect. 3.15D, the penetration depth of the electric-field amplitude into the water phase is decreased by making the angle of incidence larger as schematically presented in Fig. 5.22. The observed IR ATR spectra are presented in Fig. 5.23.

The intensity changes mostly reflect Harrick–Hansen's actual penetration depth of Eq. (3.96), which implies that the intensity ratio of the minute interfacial water to the bulky water changes on the angle of incidence. Since the thickness of the interfacial water is much lesser than that of the bulky water, this situation is good for the analysis using FARMS.

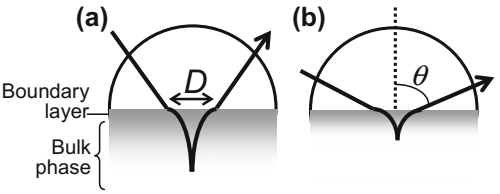

Fig. 5.22 Schematic of IR ATR measurements of water at **a** a small angle of incidence and **b** a large angle. The Goos–Hänschen shift (*D*; Fig. 3.30) is emphasized to illustrate the electric-field decay

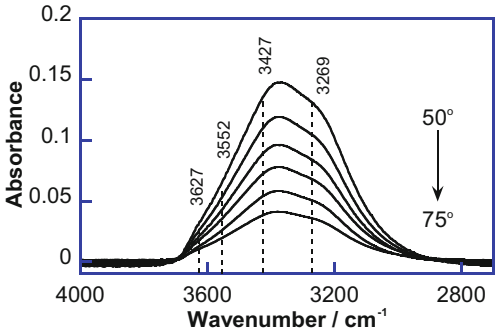

Fig. 5.23 IR ATR spectra of water measured across the silicon/water interface as a function of the angle of incidence

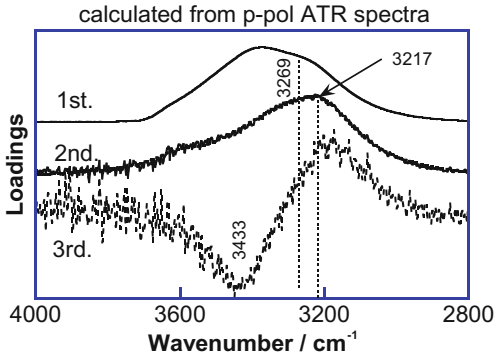

Fig. 5.24 The first three PCA loading spectra of the nine ATR spectra

The first three PCA loadings of the nine ATR spectra are presented in Fig. 5.24. As mentioned near Fig. 5.13, the first loading vector is close to the average spectrum in principle. In fact, the first loading corresponds to the spectrum of bulky water.

The next second loading spectrum of interest: no negative peak appears in it, which is the FARMS case. Since the first and second eigenvalues are 8.4074×10^{0} and 2.6068×10^{-3}, respectively, the second loading vector should have a sufficiently weak intensity, which satisfies the FARMS condition in fact. The peak position of 3217 cm^{-1} agrees with a predicted position by quantum chemical

calculation for the interfacial water. In this manner, by employing PCA, only FT-IR spectra provide sufficiently useful molecular information without an unnecessarily high technique such as nonlinear optic-based spectroscopy.

References

1. T. Hasegawa, Principal component regression and partial least squares modeling, in Handbook of Vibrational Spectroscopy, vol. 3, eds. by J.M. Chalmers, P.R. Griffiths (Wiley, Hoboken, 2002), pp. 2293–2312
2. R. Kramer, *Chemometric Techniques for Quantitative Analysis* (Dekker, New York, 1998), pp. 132–142
3. M. Defernez, E.K. Kemsley, R.H. Wilson, J. Agric. Food Chem. **43**, 109–113 (1995)
4. E.R. Malinowski, Factor Analysis in Chemistry, 3rd edn. (Wiley, Hoboken, 2002)
5. M. Sjöström, H. Wold, W. Lindberg, J.-A. Persson, H. Martens, Anal. Chim. Acta **150**, 61–70 (1983)
6. S. de Jong, Chemom. Intell. Lab. Syst. **18**, 251–263 (1993)
7. R. Manne, Chemom. Intell. Lab. Syst. **2**, 187–197 (1987)
8. T. Sakabe, S. Yamazaki, T. Hasegawa, J. Phys. Chem. B **114**, 6878–6885 (2010)
9. T. Shimoaka, T. Hasegawa, J. Mol. Liq. **223**, 621–627 (2016)
10. T. Hasegawa, Anal. Chem. **71**, 3085–3091 (1999)
11. T. Hasegawa, J. Nishijo, T. Imae, Q. Huo, R.M. Leblanc, J. Phys. Chem. B **105**, 12056–12060 (2001)

Chapter 6
Applications: Various Techniques to Make the Best Use of IR Spectroscopy

6.1 Specular Reflection and KK Analysis

As found in Eq. (3.22), Fresnel's amplitude reflection coefficient, r, for the normal incidence from the air phase is represented as:

$$r = \frac{n' + \mathrm{i}n'' - 1}{n' + \mathrm{i}n'' + 1} = \sqrt{R}\mathrm{e}^{\mathrm{i}\phi}, \tag{6.1}$$

since $R = |r|^2$ holds (Eq. (3.20)). Here, the observable using FT-IR is the reflectance, R, and note that r cannot directly be measured, since FT-IR observes light intensity only and the phase, ϕ, is discarded. If $n \equiv n' + \mathrm{i}n''$ and $\hat{\mathrm{e}} \equiv \mathrm{e}^{\mathrm{i}\phi}$ are introduced, Eq. (6.1) can be deformed as follows:

$$r = \frac{n-1}{n+1} = \sqrt{R}\hat{\mathrm{e}} \Leftrightarrow n - 1 = (n+1)\sqrt{R}\hat{\mathrm{e}} \Leftrightarrow n = \frac{\sqrt{R}\hat{\mathrm{e}} + 1}{1 - \sqrt{R}\hat{\mathrm{e}}}$$

When $\hat{\mathrm{e}} = \cos\phi + \mathrm{i}\,\sin\phi$ is put back in this equation, the following deformation can be done.

$$\begin{aligned} n &= \frac{\sqrt{R}(\cos\phi + \mathrm{i}\,\sin\phi) + 1}{1 - \sqrt{R}(\cos\phi + \mathrm{i}\,\sin\phi)} \\ &= \frac{\left(\sqrt{R}\,\cos\phi + 1\right) + \mathrm{i}\sqrt{R}\,\sin\phi}{\left(1 - \sqrt{R}\,\cos\phi\right) - \mathrm{i}\sqrt{R}\,\sin\phi} \cdot \frac{\left(1 - \sqrt{R}\,\cos\phi\right) + \mathrm{i}\sqrt{R}\,\sin\phi}{\left(1 - \sqrt{R}\,\cos\phi\right) + \mathrm{i}\sqrt{R}\,\sin\phi} \\ &= \frac{1 - R\,\cos^2\phi - R\,\sin^2\phi + \mathrm{i}2\sqrt{R}\,\sin\phi}{\left(1 - \sqrt{R}\,\cos\phi\right)^2 + R\,\sin^2\phi} \\ &= \frac{1-R}{1 + R - 2\sqrt{R}\,\cos\phi} + \mathrm{i}\frac{2\sqrt{R}\,\sin\phi}{1 + R - 2\sqrt{R}\,\cos\phi} \end{aligned}$$

T. Hasegawa, *Quantitative Infrared Spectroscopy for Understanding of a Condensed Matter*, DOI 10.1007/978-4-431-56493-5_6

As a result, the following representations are obtained.

$$\boxed{n' = \frac{1-R}{1-2\sqrt{R}\cos\phi + R}} \quad \text{and} \quad \boxed{n'' = \frac{2\sqrt{R}\sin\phi}{1-2\sqrt{R}\cos\phi + R}} \tag{6.2}$$

These equations imply that both real and imaginary parts of the complex refractive index can be obtained, if R and ϕ are both available. As mentioned above, the direct measurements of ϕ by FT-IR is impossible in principle. Fortunately, however, the Kramers–Kronig (KK) relation solves this analytical matter as follows.

In Chap. 4, we have learned that a complex physical parameter, which is driven by the causality, has a useful characteristic that the real and imaginary parts are interrelated with each other by the KK relation. Since the causality corresponds to the complex integration in the upper half of the Gauss plane, $r(\omega)$ can also be treated in a similar manner. If logarithm is taken to Eq. (6.1), the next equation is obtained.

$$\ln r(\omega) = \frac{1}{2}\ln R(\omega) + \mathrm{i}\phi(\omega)$$

When Eq. (4.26) is referred, another KK relation is readily obtained [1, 2].

$$\phi(\omega) = -\frac{\omega}{\pi}\int_0^\infty \frac{\ln R(\varpi)}{\varpi^2 - \omega^2}\mathrm{d}\varpi \tag{6.3}$$

This straightforwardly implies that the observable reflectance, $R(\omega)$, yields the latent phase, $\phi(\omega)$.

An IR reflectance measurements, $R(\omega)$, are conveniently used for obtaining an IR spectrum of a matt bulk matter. For a matt material, the ATR technique is also employed, but the ATR prism must directly be pressed onto the sample. If we need to measure the matt sample "without any physical contact." the measurement of $R(\omega)$ is much more useful, which is called "*specular reflection*" measurements (cf. Sect. 3.14).

Once an $R(\omega)$ spectrum is obtained, it can be converted to be the n' and n'' spectra via Eqs. (6.2) and (6.3). Since the KBr pellet transmission spectrum is driven by "α spectrum" (Eq. (1.43)):

$$\alpha = \frac{4\pi n''}{\lambda}z, \tag{6.4}$$

the $R(\omega)$ spectrum can finally be converted to be a KBr method-like spectrum.

This is a big benefit of using the KK relation, since the $R(\omega)$ is driven by the real part of the refractive index, n' (Sect. 3.14) , whose shape is far from the absorption spectrum we need. As an example, a raw IR specular reflection spectrum of LDPE

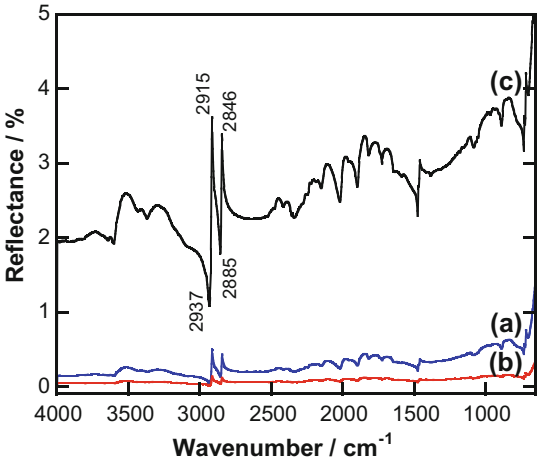

Fig. 6.1 IR specular reflection spectra of LDPE: **a** Raw spectrum, **b** Corrected spectrum considering the mesh filter function, and **c** the $R(\omega)$ function corrected by considering the number of reflections on the sample

without modification is presented in Fig. 6.1a by the blue curve. Details of the measurement procedure are described below.

Specular reflection measurements require a high skill for obtaining an accurate $R(\omega)$ spectrum. Since the reflectance spectrum is obtained as:

$$R(\omega) = \frac{s_{\text{sample}}(\omega)}{s_{\text{BG}}(\omega)},$$

two single-beam spectra of sample and background have to be collected (Fig. 6.2). An issue comes up here that the sample of a bulk matter *has no concept of the background*, which is largely different from the ordinary measurements of a thin film or a solution. At last, a mirror surface (Fig. 6.2a) is placed to bring back the IR light in the same light path as that on the sample surface, which is used as the background.

To keep the path length accurately the same, some reflection equipment is commercialized. An example is presented in Fig. 6.3, which has a double-reflection optical path on the sample surface. On the background measurement, the mirror position is changed by rotating it about the rotational axis indicated by the dot mark in Fig. 6.3a. As a result, the path length is common for both Fig. 6.3a and b. The reflectance spectrum in Fig. 6.1a is measured on this equipment.

In general, a dielectric (nonmetallic) matter has a much smaller refractive index than a metallic one, and the reflectance is thus very small (Eq. (3.21)). In the case of LDPE having the refractive index of ca. 1.5, the reflectance is calculated to be 4 and 0.16% for a single- and double-reflections, respectively, under an approximation that the angle of incidence of 12° can roughly be recognized to be normal incidence. The spectrum of the double-reflection measurement is presented in Fig. 6.1a (blue), which is located at about 0.2% as predicted by calculation. Note that such a "dark" measurements needs an MCT detector to have a good signal-to-noise ratio.

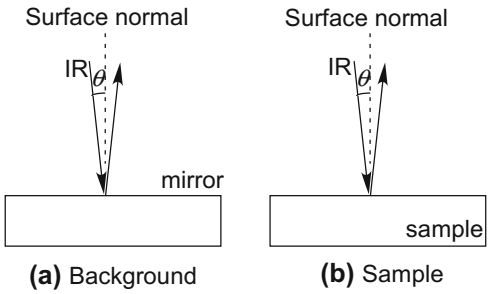

Fig. 6.2 Schematic of "specular reflection" measurements. The angle of incidence, θ, is chosen to be as small as 12°

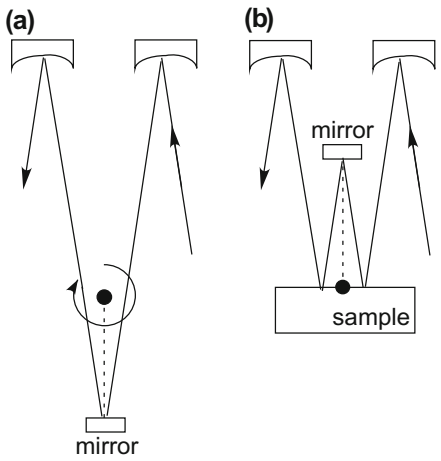

Fig. 6.3 Optical paths of the **a** background and **b** sample measurements on a Harrick's reflector. The mirror position is changed by rotation about the point (●)

Here, we have to pay attention to the significant difference between the reflectance on the sample and mirror surfaces. On the background measurements, a very bright light with a reflectance of nearly 100% on the mirror reaches the detector, which definitely makes the MCT detector saturated. Therefore, a mesh filter must be placed in the light path to reduce the light intensity. If the filter has an apparatus function of $T_{\text{filter}}(\omega)$, the measurements are represented by Eq. (6.5).

$$[R(\omega)]^n = \frac{s_{\text{sample}}(\omega)}{s_{\text{BG}}(\omega)} = \frac{s_{\text{sample}}(\omega)}{s_{\text{BG}}^{\text{filter}}(\omega)} \cdot T_{\text{filter}}(\omega) \tag{6.5}$$

The second term corresponds to the observed "raw" spectrum. Here, n is the number of reflections on the sample surface, and $s_{\text{BG}}^{\text{filter}}(\omega)$ is the "corrected" single-beam spectrum of the background measurement by using the filter function. In the case of Fig. 6.3b, $n = 2$ is used.

$T_{\text{filter}}(\omega)$ is the transmittance spectrum of the mesh filter using the background of air, which should be measured by using a TGS detector, since the "air" measurement should be too bright for MCT (Fig. 6.4).

The corrected spectrum (red), $s_{\mathrm{BG}}^{\mathrm{filter}}(\omega)$, by the use of $T_{\mathrm{filter}}(\omega)$ is presented by the red curve in Fig. 6.1b. The finally obtained spectrum of $R(\omega)$ considering $n = 2$ is also presented by the black curve in Fig. 6.1c, which exhibits ca. 3% as roughly predicted above by the calculation considering the refractive index.

As theoretically predicted in Sect. 3.14, the corrected spectrum, $R(\omega)$, has a n'-driven shape, which is characterized by the derivative-shaped peaks. As a result, the band positions appear very inaccurately. For example, the $\nu_s CH_2$ mode exhibits two positive and negative "peaks" at 2846 and 2855 cm^{-1}, which are both inaccurate for LDPE having the all-trans zigzag conformation when compared to the spectrum in Fig. 1.1.

Then, $R(\omega)$ is converted by the KK relation at Eq. (6.3) to have $\phi(\omega)$. Via Eq. (6.2), the complex refractive index spectra are finally obtained as presented in Fig. 6.5: the real and imaginary parts are presented by the black and blue spectra, respectively.

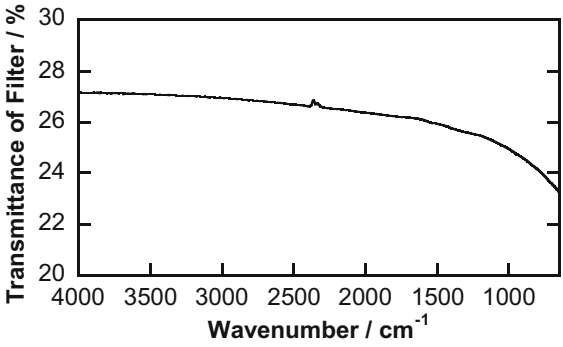

Fig. 6.4 Transmittance spectrum, $T_{\mathrm{filter}}(\omega)$, of a mesh filter measured by using a TGS detector

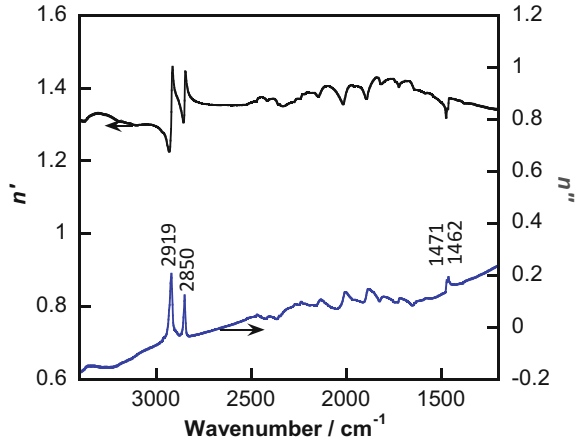

Fig. 6.5 The complex refractive index of LDPE calculated from the specular reflection spectrum in Fig. 6.1

The real part spectrum has a similar shape to that of the reflectance spectrum. Since the baseline of this spectrum should be ca. 1.5, the accuracy along the ordinate axis is found poor. This is because the absolute value along the ordinate axis is not determined as found at Eq. (4.27).

On the other hand, the imaginary part spectrum has an accurate "shape" of normal absorption spectrum as expected. In fact, the band position is accurately obtained: the $\nu_s CH_2$ and $\nu_s CH_2$ bands appear at 2850 and 2919 cm^{-1}, which is acceptable for the nearly all-trans zigzag conformation of the hydrocarbon chains in LDPE (Table 1.2). The δCH_2 band is split into two peaks at 1471 and 1462 cm^{-1}, which apparently indicates that the molecular packing is in the orthorhombic subcell structure (mentioned near Table 1.1).

The imaginary part spectrum is, however, not satisfying for understanding the spectrum, as if it was measured by a transmission technique. To do that, "*α spectrum*" represented by Eq. (6.4) has to be taken into account. Figure 6.6 is the α spectrum calculated from the n'' spectrum in Fig. 6.5. The band positions are not changed from the n'' spectrum, but the relative band intensity ratio changes. For example, the $\nu_a CH_2$ band develops relative to the $\nu_s CH_2$ band, which is close to the transmission spectrum of LDPE in Fig. 1.1. In fact, α spectrum can directly be compared to "an IR spectral database", which is traditionally collected by the use of KBr and Nujol techniques (see Sect. 3.16).

6.2 IR pMAIRS Technique: Quantitative Molecular Orientation Analysis in a Thin Film

In Chap. 3, various kinds of measurement techniques of a thin film supported by a substrate are discussed based on electrodynamics, which are represented by the transmission (Tr), reflection-absorption (RA), and ATR techniques. One of the important points of these techniques is that they are all driven by only two functions, i.e., the TO and LO energy-loss functions. In particular, we have to note that the normal incidence Tr $\left(A^{\mathrm{Tr}}_{\theta_1=0}\right)$ and the p-polarized grazing angle incidence

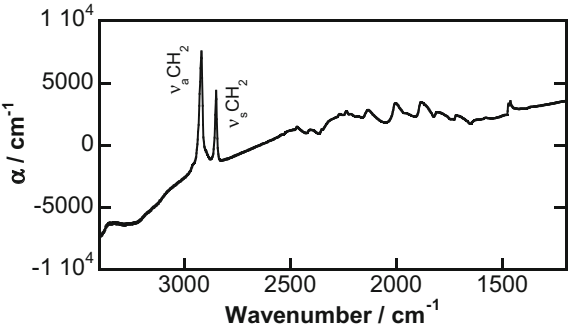

Fig. 6.6 α spectrum of LDPE

RA (A^{RA}) spectra are driven by the pure TO $\left(\mathrm{Im}\left(\varepsilon_{x,2}\right)\right)$ and LO $\left(\mathrm{Im}\left(-1/\varepsilon_{z,2}\right)\right)$ functions, respectively (see Sects. 3.9 and 3.11).

$$A^{\mathrm{Tr}}_{\theta_1=0} = \frac{8\pi d_2}{\ln 10 \cdot \lambda} \cdot \frac{1}{n_1 + n_3} \mathrm{Im}\left(\varepsilon_{x,2}\right) \tag{6.6}$$

$$A^{\mathrm{RA}} = \frac{8\pi d_2}{\ln 10 \cdot \lambda} n_1^3 \frac{\sin^2 \theta_1}{\cos \theta_1} \mathrm{Im}\left(-\frac{1}{\varepsilon_{z,2}}\right) \tag{6.7}$$

To calculate the molecular orientation angle of a transition moment, the intensity ratio of a band in the Tr and RA spectra would be useful, since the angle is defined in the x–z plane. If a weak absorption approximation ($n_2'^2 \gg n_2''^2$) and isotropic real part approximation ($n'_{2,x} = n'_{2,z}$) are employed [3], the ratio for is calculated to be

$$\frac{A^{\mathrm{Tr}}_{\theta_1=0}}{A^{\mathrm{RA}}} = \frac{\cos \theta_1}{n_1^3 \sin^2 \theta_1} \frac{1}{n_1 + n_3} \frac{n_2'^4 n''_{2,x}}{n''_{2,z}}.$$

If we have the angle of incidence, θ_1, of the RA measurement, and the refractive indices of the phases 1 and 3, then we have $n_2'^4 n''_{2,x} \Big/ n''_{2,z}$ from the observed spectra set. Since the orientation angle, ϕ, is roughly obtained as [4]:

$$\phi = \tan^{-1} \sqrt{\frac{2n''_{2x}}{n''_{2z}}},$$

the angle can be obtained, if accurate n_2' is available at hand in theory. In practice, however, determination of n_2' for every band is a difficult task, which makes the accurate orientation analysis close to impossible. To get over the limitation, a big change of the analytical concept should be necessary, which is presented in the next section.

- Basic concept of MAIRS

To totally change the analytical concept, a chemometric technique is introduced. As mentioned in Sect. 5.4, CLS has a powerful character that chemically (or physically) independent spectra are individually drawn from a collection of spectra, if the appropriate number of the independent constituents is known a priori. The constraint of "appropriate number" is generally too tough for a chemical analysis. If the concept of "chemical constituent" is expanded to "polarization," however, the situation largely improves. The polarization is characterized by the direction of oscillating electric field, and thus the direction has only two degrees of freedom: parallel and perpendicular to the film surface. In other words, the number of constituents is always exactly two without any exceptions. Therefore, if polarizations are taken as the constituents, the CLS would work powerfully to decompose the collected spectra into the x (surface parallel) and z (surface normal) spectra.

To measure the x and z components of transition moments in a thin film on this concept, a unique polarization schematic is considered as illustrated in Fig. 6.7. One of the important key points of this technique is that both x and z components are measured by "transmission" optical geometry with "normal incidence" to measure the transmitted light intensities of $\boldsymbol{s}_{\mathrm{IP}}$ and $\boldsymbol{s}_{\mathrm{OP}}$. The light having the z-component electric field oscillation is a virtual light, which is a schematic light. If we have the virtual light, no metallic substrate is needed even for the z component measurements. Of course, the z measurements using the virtual light cannot be performed actually.

In practice, as illustrated in Fig. 6.8, unpolarized IR ray is incident on the substrate (or film-covered substrate) with an angle of incidence of θ, and the transmitted light, $\boldsymbol{s}_{\mathrm{obs}}$, is measured by the detector. Since the jth single-beam spectrum, $\boldsymbol{s}_{\mathrm{obs},j}$, is composed of $\boldsymbol{s}_{\mathrm{IP}}$ and $\boldsymbol{s}_{\mathrm{OP}}$ at the jth angle of incidence of θ_j, the following regression equation holds.

$$\boldsymbol{S} \equiv \begin{pmatrix} \boldsymbol{s}_{\mathrm{obs},1} \\ \boldsymbol{s}_{\mathrm{obs},2} \\ \vdots \end{pmatrix} = \begin{pmatrix} r_{\mathrm{IP},1} & r_{\mathrm{OP},1} \\ r_{\mathrm{IP},2} & r_{\mathrm{OP},2} \\ \vdots & \vdots \end{pmatrix} \begin{pmatrix} \boldsymbol{s}_{\mathrm{IP}} \\ \boldsymbol{s}_{\mathrm{OP}} \end{pmatrix} + \boldsymbol{U} \equiv \boldsymbol{R} \begin{pmatrix} \boldsymbol{s}_{\mathrm{IP}} \\ \boldsymbol{s}_{\mathrm{OP}} \end{pmatrix} + \boldsymbol{U}$$

Here, $\boldsymbol{U}$ receives un-modeled factors rejected by the CLS modeling, and $\boldsymbol{R}$ is a matrix of weighting coefficients of $\boldsymbol{s}_{\mathrm{IP}}$ and $\boldsymbol{s}_{\mathrm{OP}}$, which is represented by [1, 5].

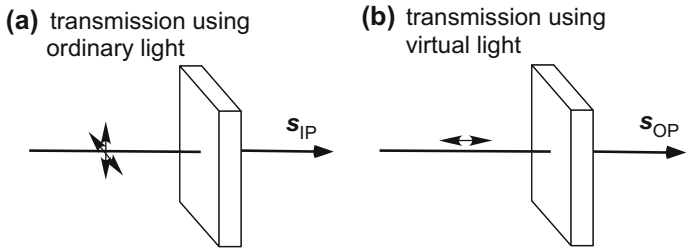

Fig. 6.7 Schematic concept of MAIRS measurements of **a** the in-plane (IP) and **b** out-of-plane (OP) components of transition moments of surface adsorbates

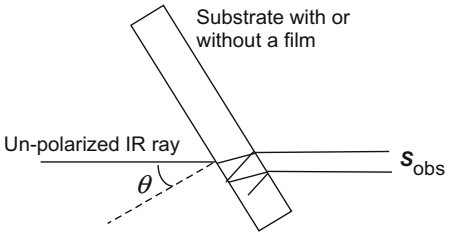

Fig. 6.8 Measurement schematic of the IR MAIRS technique

$$\boldsymbol{R} = \begin{pmatrix} 1 + \cos^2\theta_j + \sin^2\theta_j \tan^2\theta_j & \tan^2\theta_j \\ \vdots & \vdots \end{pmatrix}.$$

Therefore, if several single-beam spectra at various angles of incidence are measured, both $\boldsymbol{S}$ and $\boldsymbol{R}$ are experimentally available at hand. Then, $\boldsymbol{s}_{\mathrm{IP}}$ and $\boldsymbol{s}_{\mathrm{OP}}$ are calculated as the least-squares solution of the CLS regression.

$$\begin{pmatrix} \boldsymbol{s}_{\mathrm{IP}} \\ \boldsymbol{s}_{\mathrm{OP}} \end{pmatrix} = \left(\boldsymbol{R}^{\mathrm{T}}\boldsymbol{R}\right)^{-1}\boldsymbol{R}^{\mathrm{T}}\boldsymbol{S}$$

In this manner, even the virtual measurement, $\boldsymbol{s}_{\mathrm{OP}}$, can be carried out by using the measurement theory within the chemometric framework. This measurement technique of a thin film on an IR transparent substrate is called "*Multiple-Angle Incidence Resolution Spectrometry*" or *MAIRS*.

After the MAIRS analysis for the sample- and background-measurement set, the explicit absorbance spectra are calculated as:

$$\boldsymbol{A}_{\mathrm{IP}} = -\log\left(\boldsymbol{s}^{\mathrm{S}}_{\mathrm{IP}}/\boldsymbol{s}^{\mathrm{B}}_{\mathrm{IP}}\right) \quad \text{and} \quad \boldsymbol{A}_{\mathrm{OP}} = -\log\left(\boldsymbol{s}^{\mathrm{S}}_{\mathrm{OP}}/\boldsymbol{s}^{\mathrm{S}}_{\mathrm{OP}}\right).$$

An example spectrum of a 5-monolayer Langmuir–Blodgett (LB) film of cadmium stearate deposited on a germanium (Ge; IR transparent) substrate is presented in Fig. 6.9, which reproduces the Tr and RA spectra in Fig. 3.21.

In fact, both IP and OP spectra perfectly correspond to the Tr and RA spectra, respectively, in shape and band positions. Discussion of the ordinate scale will be made later in the section of "pMAIRS."

Of interest is that the symmetric COO^- stretching vibration mode appears at 1423 and 1433 cm^{-1} in the IP and OP spectra, respectively, which has already been found in the Tr and RA spectra (Fig. 3.21). On the conventional results, the band shift was sometimes attributed to the difference of the substrates. The MAIRS

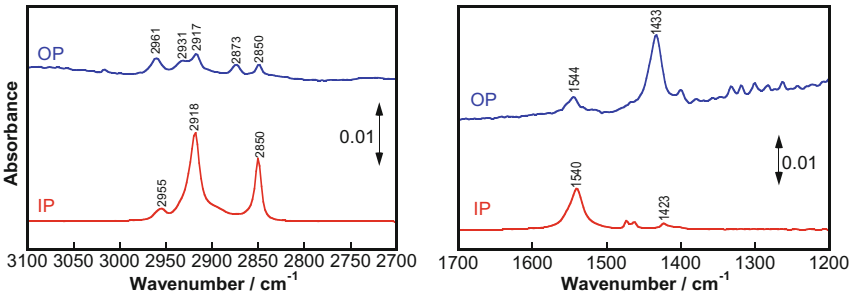

Fig. 6.9 IR MAIRS spectra of 5-monolayer Langmuir–Blodgett film of cadmium stearate on Ge (n = 4.0)

results, however, apparently denies the substrate dependency, since both IP and OP spectra are from an identical sample. MAIRS has, in this manner, unique characteristics, which cannot be realized on the conventional electrodynamics only.

MAIRS has already been analyzed theoretically on accurate electrodynamics by Itoh et al. [6], and the physical expression is obtained as follows.

$$\begin{aligned} A_{\mathrm{IP}} &= \frac{8\pi d_2}{\lambda} h_x^{\mathrm{IP}} \operatorname{Im}\left(\varepsilon_x\right) + \frac{8\pi d_2}{\lambda} h_z^{\mathrm{IP}} \operatorname{Im}\left(-\frac{1}{\varepsilon_z}\right) \\ A_{\mathrm{OP}} &= \frac{8\pi d_2}{\lambda} h_x^{\mathrm{OP}} \operatorname{Im}\left(\varepsilon_x\right) + \frac{8\pi d_2}{\lambda} h_z^{\mathrm{OP}} \operatorname{Im}\left(-\frac{1}{\varepsilon_z}\right) \end{aligned} \tag{6.8}$$

For details of the parameters in the coefficients, refer to a reference [6]. These equations apparently imply that A_{IP} would be driven by the IP function only, if the coefficient of h_z^{IP} is adequately smaller than h_x^{IP}. In a similar manner, A_{OP} would be driven by the OP function only, if h_x^{OP} is adequately smaller than h_z^{OP}. In fact, these relations hold well for an IR transparent substrate having a high refractive index such as Ge (n = 4.0), Si (n = 3.4), and ZnSe (n = 2.4). When a refractive index, n, of the substrate is small, on the other hand, these relations no longer hold [7]. For example, a substrate of CaF_2 having n = 1.4 cannot be used for the MAIRS measurements, which requires pMAIRS.

- Moving to pMAIRS

To overcome the problem, the s-polarization should be removed [7]. The p-polarized MAIRS technique is called "*pMAIRS*". For pMAIRS, the $\boldsymbol{R}$ matrix must be changed to be $\boldsymbol{R}_{\mathrm{p}}$ by removing the s-polarization component.

$$\boldsymbol{R}_{\mathrm{p}} = \begin{pmatrix} \cos^2\theta_j + \sin^2\theta_j \tan^2\theta_j & \tan^2\theta_j \\ \vdots & \vdots \end{pmatrix}$$

IR pMAIRS has a great benefit that the quantitative analysis of molecular orientation can be done more accurately, since the polarization dependency of FT-IR can be ignored.

In addition, pMAIRS overcomes a big limitation of the original MAIRS. As shown in Fig. 6.10a, the single-beam spectra for the original MAIRS are very impervious to the angle of incidence in a low wavenumber region especially below ca. 1100 cm^{-1}. In fact, in the low wavenumber region, MAIRS spectra have a lot of artifacts, and the 1100 cm^{-1} is thus the analytical lower limit. On the other hand, the single-beam spectra of "pMAIRS" have no problem until 700 cm^{-1} as presented in Fig. 6.10b, which almost covers the full MCT range [8]. Thanks to the great improvement, the C–H out-of-plane bending (γC–H) mode of an aromatic ring, which appears in the range of 700–850 cm^{-1} can readily be used for the orientation analysis.

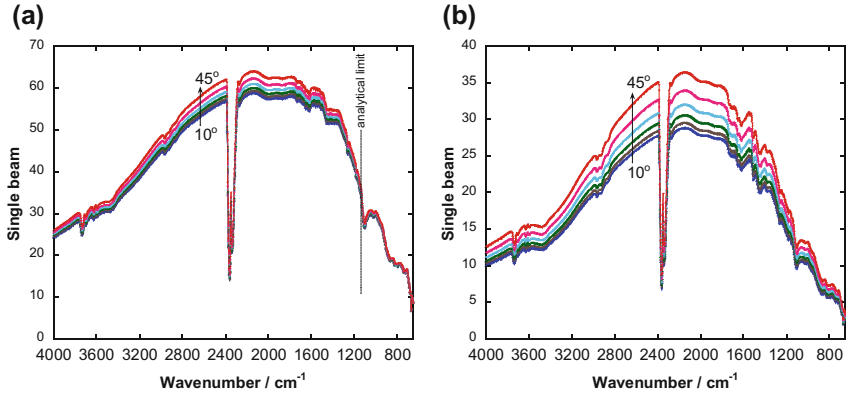

Fig. 6.10 Single-beam spectra at various angles of incidence by 7° steps measured on a Si substrate using **a** an unpolarized and **b** a p-polarized IR light

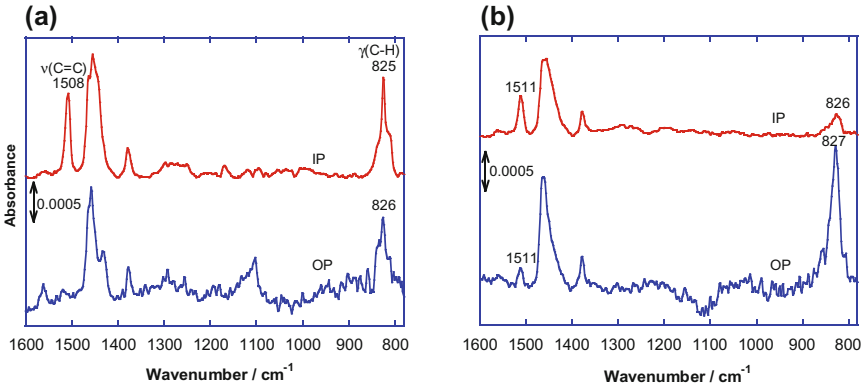

Fig. 6.11 IR pMAIRS spectra of a thin film of **a** P3BT and **b** P3HT spin-coated on a Si substrate

As an application study using pMAIRS, a spin-coated thin film of a polythiophene having an alkyl tail with a different length is presented in Fig. 6.11 [8].

Polythiophene having a benzyl chain is named P3BT, while that having a hexyl chain is named P3HT (see a chart in Fig. 6.13). Most impressive band is found at ca. 825 cm^{-1}, which is the γC–H mode at a thiophene ring. This band of P3BT appears stronger in the IP spectrum than that in the OP one; whereas P3HT yields the overturned result only for the γC–H band. This clearly shows that the thiophene ring has an "edge-on" and "face-on" orientations for P3BT and P3HT films, respectively (Table 6.1). In this manner, only by changing the tail length by C2, the orientation of the thiophene rings is totally changed. The clear visibility of the molecular orientation is an outstanding benefit of using pMAIRS.

Table 6.1 Molecular orientation in a spin-coated thin film analyzed by IR pMAIRS. B, H, O and DD stand for buthyl, hexyl, octhyl, and dodecyl, respectively

P3AT	ϕ_{C-H} / °	$\phi_{C=C}$ / °	$\phi_{C-H} + \phi_{C=C}$ / °	Orientation
P3BT	59	76	135	Edge-on
P3HT	28	63	91	Face-on
P3OT	30	53	83	Face-on
P3DDT	38	52	90	Face-on

Since no significant difference is found for the νC=C band at ca. 1510 cm^{-1} between the two samples, the main chain (long axis) of the polythiophene is suggested to lie randomly to the substrate for both samples. In fact, the orientation angle of the long axis ($\phi_{C=C}$) is nearly random as found in Table 6.1.

Of another interest is that the face-on oriented samples has a nearly 90° for the summation of ϕ_{C-H} and $\phi_{C=C}$; whereas only BT exhibits a largely different value. This implies a very important fact on the molecular orientation of the long chain. If the short axis of the chain is fixed parallel to the surface, the rest mutually orthogonal transition moments have a simple relationship of $\phi_{C-H} + \phi_{C=C} = 90°$ [8] as illustrated in Fig. 6.12.

In this manner, the face-on orientation of P3AT in a thin film has quantitatively been revealed to have a random orientation for the long axis, while a highly parallel orientation for the short axis as illustrated in Fig. 6.13 [8].

This example study indicates that the quantitative orientation analysis can easily be performed by using IR pMAIRS *even for a film having a surface roughness* prepared by the spin-coating technique. Of another note is that the films used in the study has very poor crystallinity, i.e., amorphous. pMAIRS on IR spectroscopy is thus found to be quite powerful for polymer thin film analysis.

Another significant result using pMAIRS is shown for a thin film of a porphyrin-derivative. Zinc tetraphenylporphyrin (ZnTPP) presented in Fig. 6.14 is a promising chemical compound satisfying both a good semiconductor characteristic and the good processability using a wet process due to a good solubility in an organic solvent [9]. Since porphyrin alone exhibits no solubility, the solubility is attributed to the four phenyl rings hanging on the porphyrin ring.

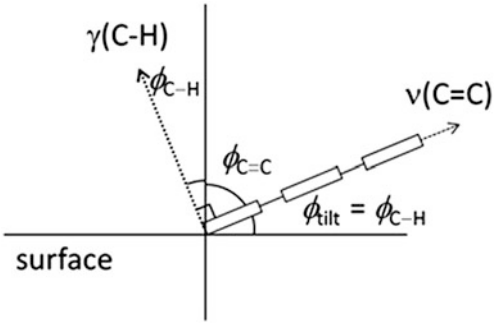

Fig. 6.12 Schematic side view of a polythiophene chain having a parallel orientation of the short axis to the substrate

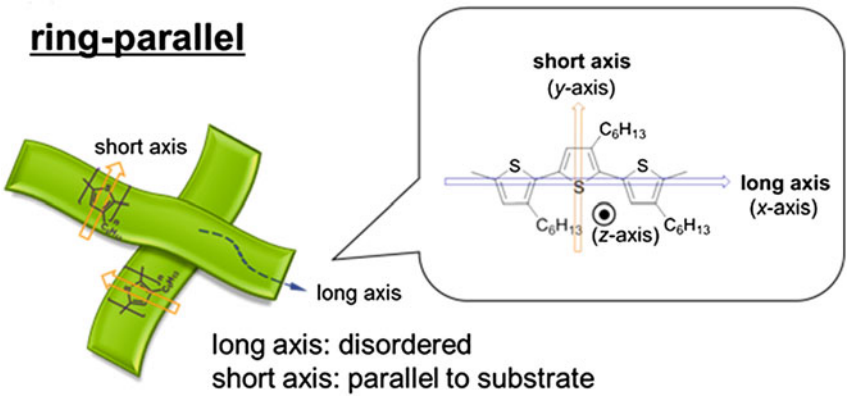

Fig. 6.13 Schematic molecular orientation image of P3HT in a spin-coated film on a silicon surface [8]

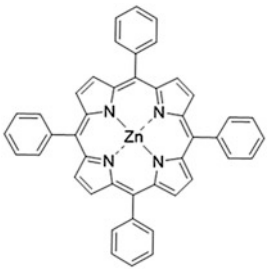

Fig. 6.14 Chemical structure of ZnTPP

Molecular arrangement in a thin film of ZnTPP on a silicon surface depends on a combination of two film preparation parameters: solvent and a preparation technique. As listed in Table 6.2, chloroform (Chl) and 1,2,4-trichlorobenzene (TCB) are selected as a fast and slowly evaporating solvents, respectively, and two representative wet-process techniques, spin-coating (SC), and drop-casting (DC) techniques, are chosen. As a result, the four combinations controls the "evaporation time" of the solvent, which is directly correlated with the molecular arrangement [9].

Figure 6.15 presents IR pMAIRS spectra of a thin film of ZnTPP on silicon as a function of the combination of the film preparation parameters [9]. The IP and OP spectra are presented by the red blue curves, respectively.

When Chl-SC is employed without annealing, the film exhibits an isotropic result: the IP and OP spectra are identical to each other in terms of shape and intensity. In other words, this preparation condition yields randomly oriented

Table 6.2 Combinations of film preparation parameters correlated with the evaporation time of the solvent

solvent	preparation technique	evaporation time
Chl	SC	short
Chl	DC	↓
TCB	SC	↓
TCB	DC	long

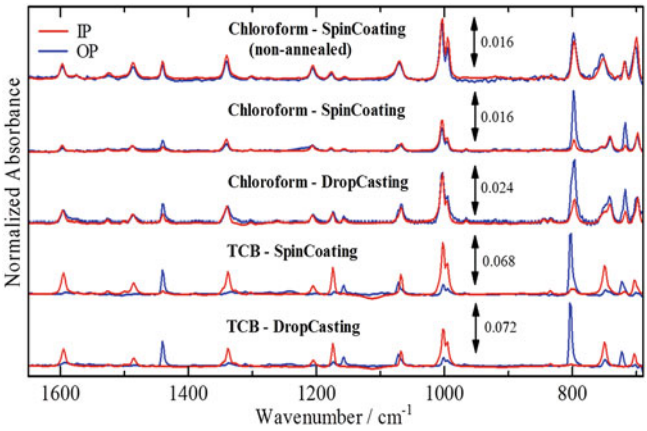

Fig. 6.15 IR pMAIRS spectra of a ZnTPP film prepared by different combinations of solvents and film preparation techniques. Only the top spectrum is a result for a sample without thermal annealing

molecules in the film. On the other hand, when the film is prepared most slowly by employing TCB-DC followed by annealing, a surprisingly highly oriented molecular arrangement is obtained as shown at the bottom in Fig. 6.15. For example, the bands at 798 and 718 cm^{-1}, both of which are assigned to the γ(C–H) modes of "porphyrin" ring ($\gamma(C–H)_{por}$; see Fig. 6.16a), are strong for OP, while it is nearly zero for IP. This straightforwardly implies that the porphyrin ring is aligned parallel to the surface.

On the other hand, γ(C–H) bands of the "phenyl" ring ($\gamma(C–H)_{ph}$; Fig. 6.16b) at about 700 cm^{-1} between the IP and OP spectra exhibits an opposite ratio. Therefore, all the phenyl rings are found to have the nearly perpendicular orientation to the surface as illustrated in Fig. 6.16.

In this manner, IR pMAIRS is quite powerful for discussing the orientation of each chemical group *even for a drop-coated film having a large surface roughness*.

- Optimization of pMAIRS for high accuracy

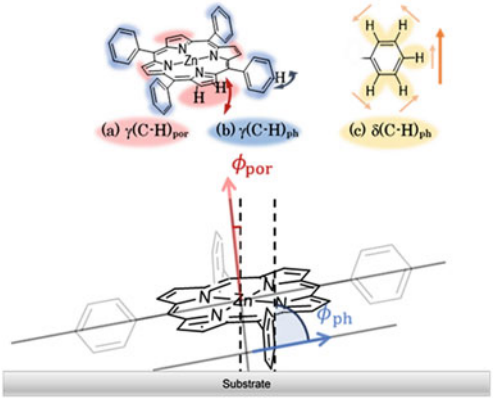

Fig. 6.16 Schematics of vibrational modes and the angle between the substrate surface normal and the direction of a transition moment. The angles of ϕ_{por} and ϕ_{ph} correspond to the ϕ(C–H)$_{por}$ **a** and ϕ(C–H)$_{ph}$ **b** modes, respectively

Table 6.3 Optimal angle sets for accurate IR pMAIRS

Substrate	Refractive index	Angle set	Angle step
Ge	4.0	9°–44°	5°
Si	3.4	9°–44°	5°
ZnSe	2.4	9°–44°	5°
CaF_2	1.4	8°–38°	6°

For the quantitative analysis, the "*optimal angle set*" must be employed for the pMAIRS measurements [10]. The optimal angle set consists of the starting and ending angles of incidence as well as the angle steps, which depend on the refractive index of the substrate. In other words, *the optical parameter of the substrate is readily considered for obtaining the optimal angle sets*. For example, for a Ge substrate, the angle of incidence should be from 9° to 44° by 5° steps (Table 6.3), which needs 8 (= (44–9)/5 +1) single-beam spectra [10].

The optimization has already been done for representative IR transparent substrates [10] as listed in Table 6.3. Fortunately, the angle set of 9°–44° with the step of 5° is common for a substrate with a refractive index of 2.4 or higher. For only a low-refractive index substrate such as CaF_2, we have to pay attention to switch the experimental condition by referring to the table. Once the optimal condition is employed, the optical parameter of the substrate is readily taken into account, and quantitatively useful results are obtained without considering optical parameters.

Since pMAIRS yields the x/z ratio of a transition moment via the IP/OP spectra, the orientation angle, $\boldsymbol{\phi}$, is defined as a uniaxial orientation angle of the transition moment, p, from the surface normal as found in Fig. 6.17.

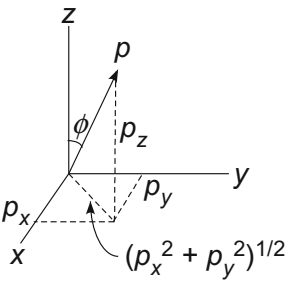

Fig. 6.17 A schematic of a transition moment in Cartesian coordinate

Under the *uniaxial distribution* where the orientation angle is determined by only one parameter, ϕ, the distribution in the x–y plane is averaged to have $p_x = p_y$. Therefore, $\tan\phi$ is simply obtained as

$$\tan\phi = \frac{\sqrt{p_x^2 + p_y^2}}{p_z} = \frac{\sqrt{2}p_x}{p_z} = \sqrt{\frac{2A_{\mathrm{IP}}}{A_{\mathrm{OP}}}}, \tag{6.9}$$

since "absorbance" is proportional to the "squared transition moment" on Fermi's golden rule.

To check the accuracy of the orientation angle, a pentacene film having a thickness of 100 nm was analyzed by IR pMAIRS. Pentacene is a fused-ring compound of five benzene rings (Fig. 6.18), which is relatively stiff.

This compound yields three vibrational modes along x, y, and z directions, which are highly maintained due to the stiff skeleton. In other words, the three directions are always mutually orthogonal to each other. The three bands are found in Fig. 6.19 at separated positions.

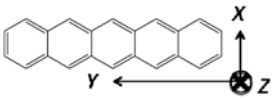

Fig. 6.18 Pentacene and Cartesian coordinate

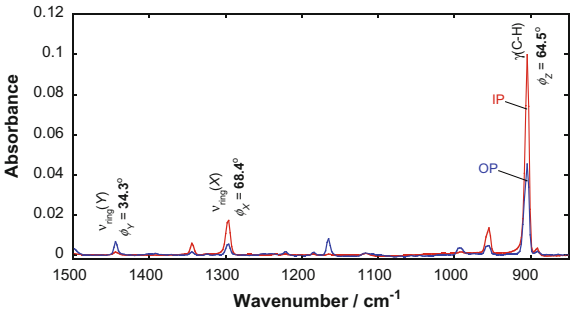

Fig. 6.19 IR pMAIRS spectra of an evaporated pentacene film with a thickness of 100 nm on a silicon substrate

By using Eq. (6.9), the orientation angles are easily obtained as found in Fig. 6.19. Since the three directions are kept to have the mutually orthogonal relations, the three angles should satisfy the "direction cosine" relationship theoretically [4].

$$\cos^2 \phi_x + \cos^2 \phi_y + \cos^2 \phi_z = 1$$

When the calculated three angles are put in this equation, the summation is obtained to be 1.00, which straightforwardly proves that the analyzed angles are quantitatively acceptable.

- For more accurate analysis using a refractive index of the sample

As presented above, IR pMAIRS is quite powerful for analyzing the molecular orientation in a thin film even with a surface roughness such as a spin-coated film irrespective of the crystallinity. Regardless, it still has an unresolved matter, that is, the ordinate scale of the OP spectrum.

Since the OP spectrum is measured by using the conceptual longitudinal-wave light with the normal incidence to the surface (Fig. 6.8), it is unclear whether the absorbance scale is common to the IP one or not. In addition, if the refractive index of the sample thin film is largely apart from 1.5, which is for a normal organic compound, the electric field near the film/substrate interface should largely be influenced by the index. Therefore, the refractive index of the film layer would become another factor to change the ordinate scales of the IP and OP spectra.

According to Fermi's golden rule, the absorbance ratio of the IP and OP spectra is expressed as:

$$\frac{A_{\mathrm{IP}}}{A_{\mathrm{OP}}} = \left(\frac{\mu_x E_x}{\mu_z E_z}\right)^2.$$

The matter of the ordinate scale is thus directly related to E_x/E_z, which is difficult to calculate, since E_z is of the conceptual longitudinal-wave light. Thus far, *this electric field ratio has been approximated to be unity*. If an ideally isotropic sample is employed for making $\mu_x/\mu_z = 1$ hold, which reveals E_x/E_z experimentally via the pMAIRS measurement of $A_{\mathrm{IP}}/A_{\mathrm{OP}}$.

For that purpose, poly(2-perfluorobutyletyl acrylate) (C4FA; Fig. 6.20) is employed [11]. Since the side chain of the polymer has a short perfluoroalkyl group, molecular interaction between the side chains is weak [12], and as a result, the material is liquid at ambient temperature having an ideally random orientation.

Here, two approximations are introduced [11]:

(1) the real part of the refractive index of the sample, $n'_{2\rho}$ ($\rho = x, y$ and z), is *isotropic* to have n having *no dispersion*, and

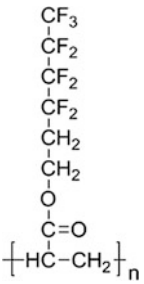

Fig. 6.20 Primary chemical structure of C4FA

(2) the film is a weak IR absorber: $n_2'^2 \gg n_2''^2$.

The second condition holds for many organic compounds, with which Eq. (6.8) can be simplified to have:

$$A_{\mathrm{IP}} = \frac{8\pi d_2}{\lambda} h_x^{\mathrm{IP}} \left[2n'_{2x} n''_{2x}\right] \approx \frac{8\pi d_2}{\lambda} h_x^{\mathrm{IP}} \left[2nn''_{2x}\right]$$
$$A_{\mathrm{OP}} = \frac{8\pi d_2}{\lambda} h_z^{\mathrm{OP}} \frac{n'_{2z} n''_{2z}}{\left(n_{2z}'^2 + n_{2z}''^2\right)^2} \approx \frac{8\pi d_2}{\lambda} h_z^{\mathrm{OP}} \frac{1}{n^4} \left[2nn''_{2z}\right].$$

With the two equations, the dichroic ratio of pMAIRS is simplified as:

$$\frac{A_{\mathrm{IP}}}{A_{\mathrm{OP}}} = \frac{h_x^{\mathrm{IP}} n''_{2x}}{h_z^{\mathrm{OP}} \frac{1}{n^4} n''_{2z}} \equiv n^4 H \frac{n''_{2x}}{n''_{2z}} \quad \left(H \equiv \frac{h_x^{\mathrm{IP}}}{h_z^{\mathrm{OP}}}\right). \tag{6.10}$$

Since $n'_{2\rho}$ is approximated to have no dispersion, absorbance can simply be regarded as being proportional to $n''_{2\rho}$. As a result, Eq. (6.10) implies that the pMAIRS dichroic ratio can be corrected by introducing n^4H, which corresponds to E_x/E_z. Note that H is a substrate specific constant by pulling out n. As mentioned above, this constant can be obtained by measuring a thin film of C4FA considering its refractive index, 1.35.

In Table 6.4, the obtained constants are listed. For a substrate having a high refractive index, H is found at about 0.14; whereas only the low-refractive index substrate has an outstandingly high value.

By using H, correction factors of n^4H are calculated for some representative compounds having various refractive indices (Table 6.5).

Normal compounds having ca. $n = 1.55$, e.g., P3HT and polyethylene (PE), on a germanium substrate are found to have n^4H near unity as marked by bold. This is the reason why pMAIRS with no correction works well for the quantitative orientation analysis of a normal organic compound.

On the other hand, the compounds having an *abnormal refractive index* such as fullerene and polytetrafluoroethylene (PTFE) exhibit a value *far from unity* even on

Table 6.4 A correction factor, H, depending on the substrate

Substrate	Refractive index of substrate	H
Ge	4.0	0.15
Si	3.4	0.14
ZnSe	2.4	0.11
CaF_2	1.4	0.21

Table 6.5 n^4H calculated for some organic compounds having various refractive indices measured on Ge and CaF_2

Sample	Refractive index of "sample"	n^4H_{Ge}	$n^4H_{CaF_2}$
C_{60}	1.83	1.68	2.52
P3HT	1.60	**0.98**	1.47
PE	1.52	**0.82**	1.23
PTFE	1.35	0.50	0.75

the same germanium substrate. In addition, when the substrate is changed to be a *low-refractive index substrate*, e.g., CaF_2, this *correction becomes necessary for all the film materials*.

Since the current commercial pMAIRS equipment takes this correction factor into account, we do not have to take care about this matter too much. If we choose a substrate tab, both optimal angle set and correction factors are automatically set. For the refractive index of the sample film, $n = 1.55$ is set as a default value, but we can change it as needed for the material.

Figure 6.21 presents a corrected pMAIRS spectrum of a thin film of fullerene deposited on silicon prepared by vacuum evaporation. Since C_{60} has a spherical shape, the molecular orientation can be regarded as perfectly random. After the correction of the intensity ratio using n^4H, both IP and OP spectra exhibit the same shape and intensity as expected.

The same intensity spectra straightforwardly yield the orientation angle of 54.7° using Eq. (6.9). In other words, pMAIRS is quite useful for *determining the perfectly random orientation quantitatively, which can apparently be discriminated from an oriented sample having the orientation angle of* 54.7°.

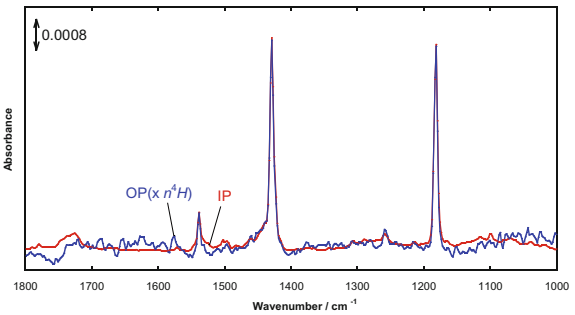

Fig. 6.21 Corrected IR pMAIRS spectra by n^4H of a thin film of C_{60} evaporated on silicon

6.3 Fluorocarbon-Specific IR Spectroscopy

As a vibrational spectroscopy, IR spectroscopy is on the concept of a normal mode that is roughly regarded as a localized vibration on a chemical group (Sect. 1.2). As presented in Table 1.1, this "local vibration" approximation, i.e., a normal mode is regarded as the corresponding "group vibration", is conveniently used for analyzing IR spectra (Fig. 1.1 and 1.4–1.9) with no problem. However, *this approximation breaks down for perfluoroalkyl compounds*.

Figure 6.22 presents schematic molecular structures of normal alkyl (R) and perfluoroalkyl (Rf) groups. They may seem to have similar structures, but they have largely different characteristics from each other in terms of the following three points:

(1) The mass of H is smaller than that of C; whereas the mass of F is larger than that of C.
(2) An R group has a planer skeleton, in which the conformation is the all-trans zigzag, if the molecules are in crystal. This structure exhibits the even–odd effect on the melting point against the chain length (○ in Fig. 6.23) [13, 14]. On the other hand, *an Rf group has a helical (twisted) structure* about the

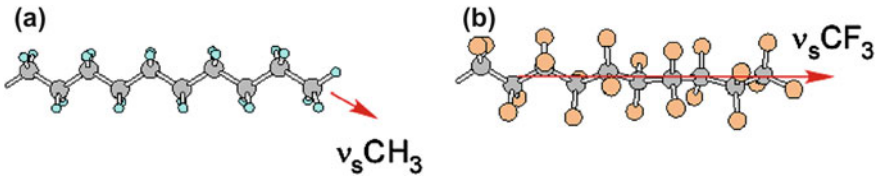

Fig. 6.22 Schematics of **a** normal alkyl group and **b** perfluoroalkyl group. The *gray*, *light blue*, and orange denote carbon, hydrogen, and fluorine atoms, respectively

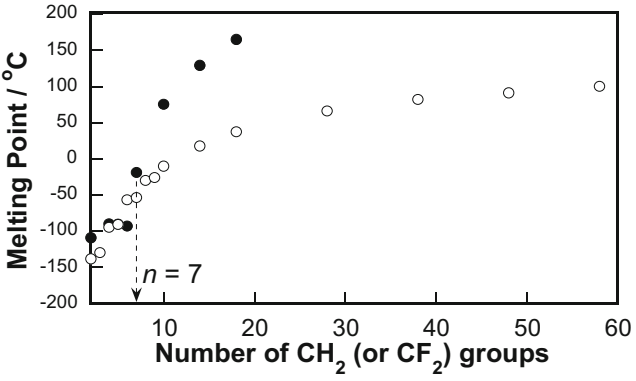

Fig. 6.23 Melting point of normal (○) and perfluoro (●) alkanes as a function of the number of CH_2 or CF_2 groups [17]

molecular axis [15, 16], which exhibits continuous melting point with the Rf length (● in Fig. 6.23) of $n = 7$ or longer.

(3) Spectrum distortion induced by a strong absorption must be taken into account. Since the C–F bond has a fairly large dipole moment due to the large electronegativity of F, the IR absorption of an Rf group is very strong due to Eq. (1.22), which induces changes of the band position and the relative band intensities [12].

These Rf-specific characters are discussed in detail as below.

- The mass of F is larger than that of C:

The characteristic of (1) influences the normal mode significantly. For example, let us consider the ν_sCH_3 mode of an R group (Fig. 6.22a). This mode is mainly due to the symmetric CH_3 stretching vibration, which can be regarded to be *localized at the terminal methyl group*, although the rest part is also vibrated to some extent. Therefore, the concept of "group vibration" of the methyl group can conveniently be used, and the transition moment is expressed by the red arrow in Fig. 6.22a.

On the other hand, in the case of an Rf group, the situation totally changes. Because of the larger mass of F than that of C, *the F atoms relatively stay unmoved; whereas the C atoms are apparently vibrated*. Since the C atoms are directly connected, *the vibration cannot be localized at a chemical group, but it spreads over the Rf group* (Fig. 6.22b) [18].

Figure 6.24 presents IR "α-spectra (cf. Eq. (1.43) or [12])" of some Rf-containing myristic acids (bulk) after a conversion from ATR spectra (Sect. 3.13 and 3.15D). This wavenumber region is for the C–F stretching vibration region. As mentioned in Sect. 3.16(A), an α-spectrum can be a substitute of a KBr pellet spectrum. A portion of the molecule is replaced by an Rf group with a different length, n (the number of the CF_2 groups). The molecule presented in Fig. 6.24 is an example of $n = 9$.

Since a normal mode is spread over the Rf group, the band position of the ν_sCF_3 mode is totally different from an image of a normal hydrocarbon. In fact, the band is located at an extraordinarily higher position than that found for the ν_sCH_3 band. Remember that the ν_sCH_3 band is always found between the ν_aCH_2 and ν_sCH_2 bands. The significantly higher position is thus due to the helical structure of the Rf group [15]. In addition, this band position is largely dependent on the Rf length because the band is influenced by the coupled oscillation of the carbon chain. As a result, the ν_sCF_3 band exhibits a significantly large shift by more than 50 cm^{-1} when the Rf length is changed from 3 to 9.

Because of the unique normal mode spread over the Rf group, the direction of the transition dipole moment of the ν_sCF_3 mode is along the Rf group, which is indicated by an arrow in Fig. 6.22b. This characteristic enables us to easily discuss the molecular orientation of an Rf group in a thin film on a surface [12, 18].

Figure 6.25 presents IR RA spectra (Sect. 3.11 and 3.15B) of single-monolayer Langmuir–Blodgett films on gold transferred at the surface pressure of 15 mN m^{-1}

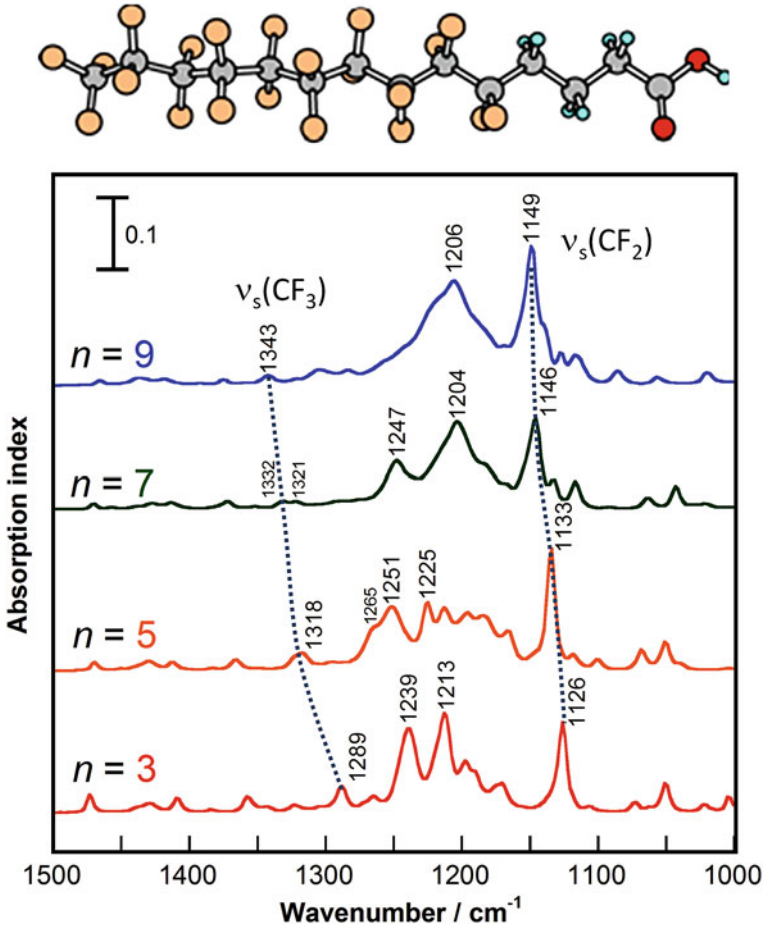

Fig. 6.24 IR "α spectra" obtained via ATR measurements of myristic acids involving an Rf group with different length. *n* represents the number of CF_2 groups

[12], which consists of the same compounds as those for Fig. 6.24. This surface pressure is a specific pressure where the molecules are *spontaneously aggregated* for $n = 7$ and 9. Note that RA spectrometry has the RA-specific surface selection rule (Sect. 3.15B), i.e., only the surface-perpendicular component of a transition moment appears in the RA spectrum. Therefore, the strongly appeared ν_sCF_3 band for $n = 9$ means that the Rf group (*not* the ν_sCF_3 group) has a nearly surface-perpendicular orientation; whereas the almost disappeared band for $n = 3$ straightforwardly implies that the short Rf group is entirely lying parallel to the surface.

In a similar manner, the ν_sCF_2 mode also exhibits a large band shift depending on the Rf length. Since the Rf chains are spontaneously aggregated when the Rf

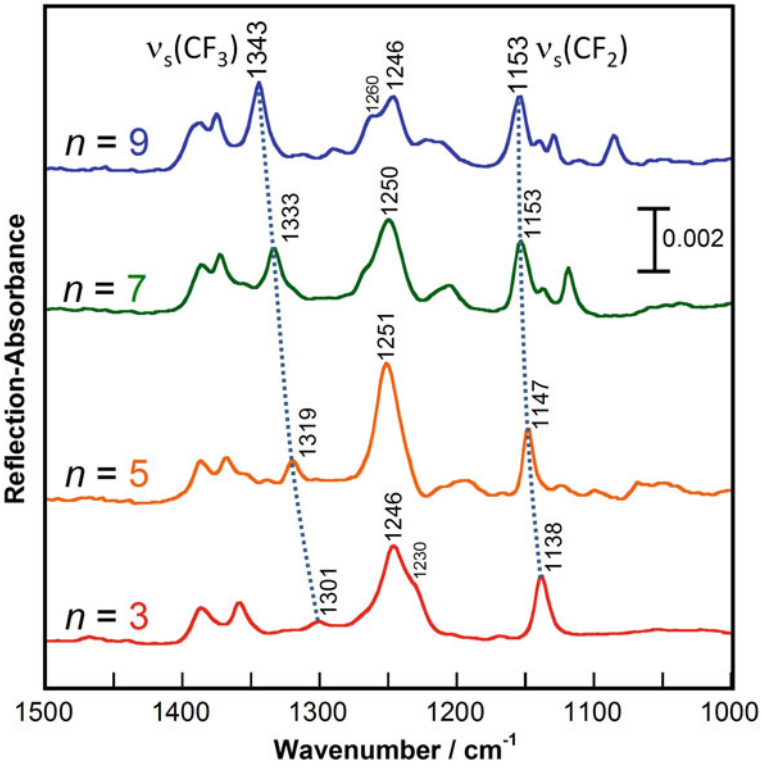

Fig. 6.25 IR RA spectra of single-monolayer Langmuir–Blodgett films on a gold surface. The compounds are the same as those for Fig. 6.12

length is $n = 7$ or longer [12], the aggregation-sensitive $\nu_s CF_2$ band is particularly shifted between $n = 5$ and 7.

- An Rf group has a helical (twisted) structure about the molecular axis:

The most important characteristic of an Rf group in terms of chemical structure is that the skeleton has a helical structure about the molecular axis. This is often called molecular "conformation" for convenience. Although the conformation of a normal hydrocarbon chain is the planer zigzag, the conformation of an Rf group has 15_7 or 13_6 helix depending on temperature. A representative Rf polymer is poly (tetrafluoroethylene) (PTFE) that is known as Teflon®, a product name of DuPont. PTFE has a transition temperature at 19 °C under an ambient pressure, and the 13_6 and 15_7 helices appear below and above 19 °C, respectively [15, 16], which are in the phase II and IV, respectively [19].

Details of the helical structure of 15_7 are schematically illustrated in Fig. 6.26 [15]. As found in the figure, "15_7" means that the helix has 7 turns over 15 chemical units of $(CF_2)_{15}$. Since an Rf chain consists of a repeat unit, the vibrational analysis should be done by using the factor group analysis (Sect. 1.5) [20]. The factor group

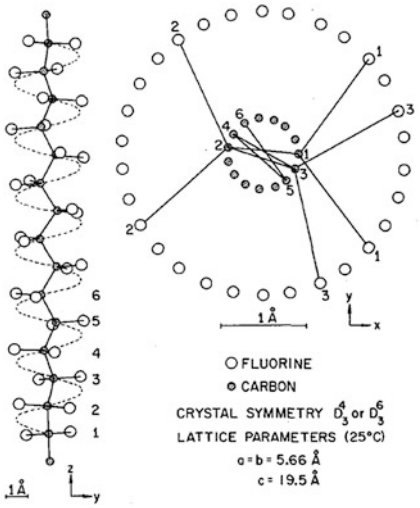

Fig. 6.26 Schematics of the 15_7-helix conformation of PTFE

of the line group has the C_{30} skeleton, which belongs to the point group of D_{15} (Table 6.6).

To count the unmoved atoms on a symmetry operation, the schematic presented in Fig. 6.27 is referred. Note that $\theta = \pm n\psi$ as defined by Higgs [21], in which the integer, n, varies from 1 to $n - 1$. ψ is a phase shift between the adjacent two units, which is simply defined by

$$\psi = 2\pi\frac{m}{n},$$

for representing the n_m helix, which is m helical rotations along n units. Therefore, $\theta = \pm n\psi$ is proportional to $2m\pi$, which is equivalent to the $k = 0$ condition for the units (see about Fig. 1.14). In this manner, an Rf group yields a limited number of νCF_2 bands.

Table 6.6 Character table of D_{15} (g = 30)

D_{15}	E	$2C_{15}^1$	$2C_{15}^2$	$\cdots$	$2C_{15}^7$	$15C_2$	
A_1	1	1	1	$\cdots$	1	1	$x^2 + y^2, z^2$
A_2	1	1	1	$\cdots$	1	−1	z
E_1	2	$2\cos\theta$	$2\cos 2\theta$	$\cdots$	$2\cos 7\theta$	0	(x, y) (xz, yz)
E_2	2	$2\cos 2\theta$	$2\cos 4\theta$	$\cdots$	$2\cos 14\theta$	0	$(x^2 - y^2, xy)$
⋮	⋮	⋮	⋮	⋯	⋮	⋮	
E_7	2	$2\cos 7\theta$	$2\cos 14\theta$	$\cdots$	$2\cos 49\theta$	0	
N_R	45	0	0	$\cdots$	0	1	
χ_R	3	$1 + 2\cos\psi$	$1 + 2\cos 2\psi$	$\cdots$	$1 + 2\cos 3\psi$	−1	
χ	135	0	0	$\cdots$	0	−1	

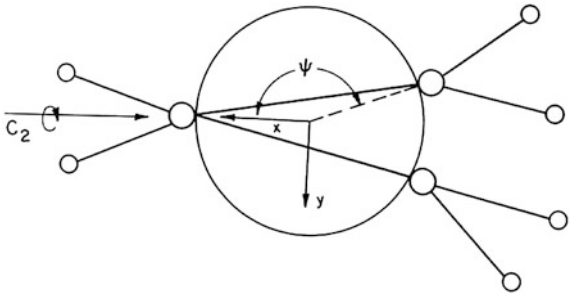

Fig. 6.27 The schematic top view of the n_m helix of PTFE [20]

Thanks to a fact that the C_{15}^m operation makes all the atoms moved, the reducible representation, χ, is very easily calculated as found in Table 6.6. Note that, in addition, the C_2 operation influences only one carbon atom irrespective of the conformation numbers, m and n.

In this manner, the irreducible representation is easily calculated as:

$$\Gamma = 4A_1 + 5A_2 + 9E_1 + 9E_2 + 9(E_3 + E_4 + E_5 + E_6 + E_7).$$

By removing the translational and rotational modes, we finally have the representation of the vibrational modes as:

$$\Gamma^{\text{vib}} = 4A_1 + 3A_2 + 8E_1 + 9E_2 + 9(E_3 + E_4 + E_5 + E_6 + E_7).$$

If this representation is separated in terms of spectroscopic activity, the following easy-to-use representations are soon obtained by referring Table 6.6.

$$\Gamma^{\text{IR}} = 3A_2 + 8E_1$$
$$\Gamma^{\text{Raman}} = 4A_1 + 8E_1 + 9E_2$$
$$\Gamma^{\text{Inactive}} = 9(E_3 + E_4 + E_5 + E_6 + E_7)$$

The analytical procedure for the 13_6 helix conformation is available in Appendix (Sect. 7.3), which shows that both 15_7 and 13_6 conformations yield the same irreducible representation. As a result, IR spectroscopy should commonly have 11 bands on PTFE for both phases II and IV.

In the νCF region, three bands appear at ca. 1251, 1226, and 1141 cm^{-1}, which are roughly assigned [22] to the ν_aCF_2 mode, the chain stretching vibration mode and the ν_sCF_2 mode, respectively. Note that these modes are not solely assigned to a specific pure group vibration, but a mixture of some group vibrations. In fact, the chain stretching vibration should not be IR active in general, but it is observable because this mode is largely influenced by C–F stretching vibration [22]. In a similar manner, the ν_aCF_2 mode is also impure "group vibration," which is largely

influenced by the wagging vibration. On the other hand, the $\nu_s CF_2$ band is, fortunately, useful, since it is relatively largely by the C–F stretching vibration as expected intuitively.

- Spectrum distortion induced by strong absorption must be taken into account:

The $\nu_s CF_2$ band cannot be used for the molecular orientation analysis in a thin film on a surface [12]. Since the CF_2 groups are located on a twisted line because of the helical structure, the $\nu_s CF_2$ groups have various tilt angles to the surface normal when the Rf group is tilted.

This band is, on the other hand, quite useful to discuss the molecular packing. For $n = 7$ or higher, the molecules are two-dimensionally aggregated spontaneously because of the dipole–dipole interaction [12], which is much stronger than the dispersion force [23]. The two-dimensional strong dipole–dipole interaction makes the $\nu_s CF_2$ band move to a lower wavenumber position.

To discuss the molecular packing in the monolayer on gold, the corresponding IR spectra of un-oriented samples must be referred. The ATR spectra in Fig. 6.24 can be used for this purpose, but we have to take great care that *IR spectra of a thin film at an interface measured by different techniques cannot directly be compared with each other*. In short, the RA and ATR spectra cannot be compared in terms of the band position and relative band intensity. To understand this point, we have to go back to Fig. 1.19 in Chap. 1.

When an absorption band has a large absorbance, which corresponds to a large peak of n'' (Fig. 1.19b), the corresponding n' exhibits a large anomalous dispersion (Fig. 1.19a). As a result, a strong absorber results in an apparent band shift between the TO ($\mathrm{Im}(\varepsilon)$) and LO ($\mathrm{Im}(-1/\varepsilon)$) energy-loss function spectra as presented in Fig. 6.28.

This means that no concerns are necessary for a weak absorber such as normal hydrocarbon chain even when spectra measured by different techniques are compared. On the other hand, *a strong absorber represented by an Rf compound needs*

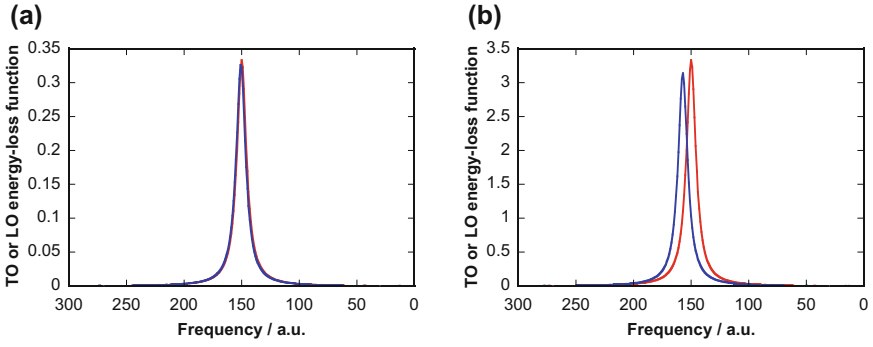

Fig. 6.28 Simulated TO (*red*) and LO (*blue*) energy-loss function spectra calculated by using the electric permittivity in Fig. 1.19 for **a** a weak and **b** strong IR absorber. The ordinate scale is normalized, so that the TO and LO functions are readily compared in (**a**)

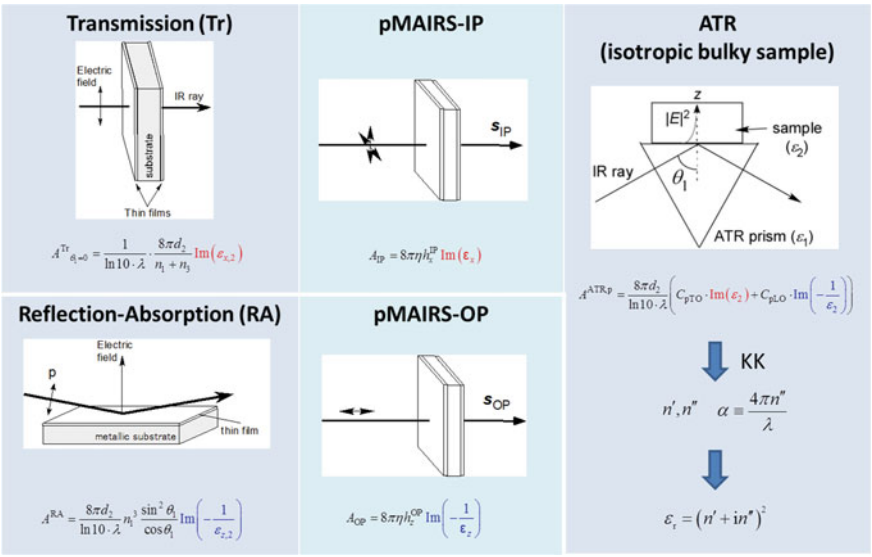

Fig. 6.29 Correlation of representative spectrometries via the mathematical representations

an appropriate spectral conversion. To understand the conversion, representative IR spectrometries are summarized in Fig. 6.29.

For details of the mathematical representations, refer to Chap. 3. This figure clearly indicates that all the "surface spectrometries" are driven by only the TO and LO energy-loss functions. As shown in Chap. 3, reflection measurements except the RA technique, i.e., p-polarized ER and ATR spectrometries, are represented by a linear combination of the TO and LO spectra. On the other hand, Tr and RA spectrometries yield pure TO and LO spectra, respectively, which correspond to pMAIRS-IP and -OP spectra individually. This is the reason why a raw ATR spectrum cannot be compared to a spectrum measured by another spectrometry especially for a strong IR absorption band.

Fortunately, the Kramers–Kronig (KK) relationship (Sect. 4.4) considering the angle of incidence [2, 24, 25] can be employed to convert the raw ATR spectrum to the complex refractive index via Eq. (6.2). In recent years, some FT-IR spectrometers accompany a conversion program to yield an α-spectrum considering the refractive indices of the sample and the prism as well as the angle of incidence. In this case, only the n''-spectrum of the sample is obtained as well as n'. The entire shape of the complex refractive index spectra are thus obtained, with which we readily have the complex electric permittivity, ε_r (Fig. 6.29). As a result, *a thin-film spectrum of an isotropic sample can be predicted from the bulk spectrum measured by ATR* [12, 18].

Once the ATR spectra in Fig. 6.24 are converted to be the LO energy-loss function spectra (Fig. 6.30), they are ready to be compared to the RA spectra in Fig. 6.25 [12].

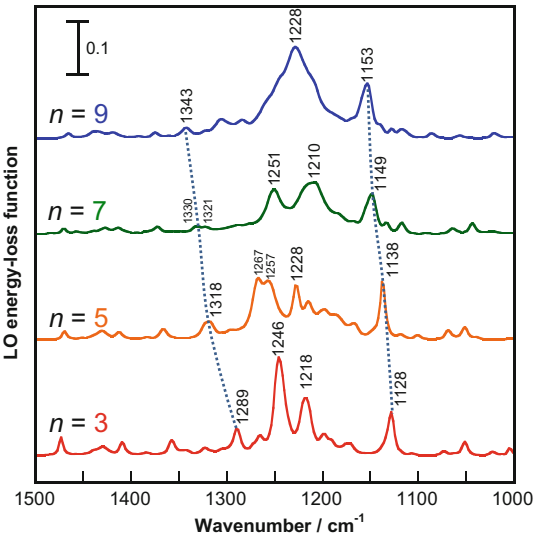

Fig. 6.30 LO energy-loss function spectra converted from the ATR spectra in Fig. 6.24

When the LO spectra are compared with the original ATR spectra, we find that both relative band intensity and band position are largely changed. For example, the compound of $n = 9$ has the $\nu_s CF_2$ band at 1149 cm^{-1} in the ATR spectrum; whereas the same mode appears at 1153 cm^{-1} in the LO spectrum. Of interest is that the LO band position is the same as that of the RA spectrum (see also Table 6.7). This implies that the spontaneously aggregated molecules are in the same molecular packing as in a bulk solid used for the ATR measurements. Table 6.7 summarizes the comparison between the converted LO band position and the RA band position [12]. For a short n, the difference between the LO and RA positions becomes significantly large, which implies that a compound involving a short Rf group exhibits a weak molecular aggregation property.

In this manner, the spectrum conversion considering the TO and LO energy-loss functions works quite powerfully to discuss the Rf-related IR spectra quantitatively.

Table 6.7 Band positions of the LO function calculated from the infrared ATR spectra, and those of the RA spectra of the monolayer LB films

n	$\nu_s(CF_2)/cm^{-1}$			
	Bulk (raw ATR)	Bulk (ATR-**LO**)	Monolayer (**RA**)	Δ/cm^{-1}
3	1126	1128	1138	10
5	1133	1138	1147	9
7	1146	1149	1153	4
9	1149	1153	1153	0

References

1. J.S. Plaskett, P.N. Schatz, J. Chem. Phys. **38**, 612–617 (1963)
2. J.A. Bardwell, M.J. Dignam, J. Chem. Phys. **83**, 5468–5478 (1985)
3. N. Shioya, T. Shimoaka, Richard Murdey, T. Hasegawa, Appl. Spectrosc. **70** (2016), in press. doi:10.1177/0003702816658673
4. T. Hasegawa, S. Takeda, A. Kawaguchi, J. Umemura, Langmuir **11**, 1236–1243 (1995)
5. T. Hasegawa, The coefficient of the ***R*** matrix is removed, since it is not necessary and confusing. J. Phys. Chem. B **106**, 4112–4115 (2002)
6. Y. Itoh, A. Kasuya, T. Hasegawa, J. Phys. Chem. A **113**, 7810–7817 (2009)
7. T. Hasegawa, Anal. Chem. **79**, 4385–4389 (2007)
8. N. Shioya, T. Shimoaka, K. Eda, T. Hasegawa, Phys. Chem. Chem. Phys. **17**, 13472–13479 (2015)
9. M. Hada, N. Shioya, T. Shimoaka, K. Eda, M. Hada, T. Hasegawa, Chem. Eur. J. **70** (2016), in press. doi:10.1002/chem.201603291
10. N. Shioya, S. Norimoto, N. Izumi, M. Hada, T. Shimoaka, T. Hasegawa, Appl. Spectrosc. **70** (2016), in press. doi:10.1177/0003702816658673
11. N. Shioya, T. Shimoaka, R. Murdey, T. Hasegawa, Appl. Spectrosc. **70** (2016). doi:10.1177/0003702816676492
12. T. Hasegawa, T. Shimoaka, N. Shioya, K. Morita, M. Sonoyama, T. Takagi, T. Kanamori, ChemPlusChem **79**, 1421–1425 (2014)
13. C.M. Scrimgeour, J.L. Harwood, in *The Lipid Handbook*, ed. by F.D. Gunstone, J.L. Harwood, A.J. Dijkstra, 3rd edn. (CRC Press, Boca Raton, 2007), pp. 1–36
14. K. Larsson, J. Am. Oil Chem. Soc. **43**, 559–562 (1966)
15. L. Piseri, B.M. Powell, G. Dolling, J. Chem. Phys. **58**, 158–171 (1973)
16. C.W. Bunn, E.R. Howells, Nature **174**, 549–551 (1954)
17. H.W. Starkweather, Macromol. **19**, 1131–1134 (1986)
18. T. Hasegawa, T. Shimoaka, Y. Tanaka, N. Shioya, K. Morita, M. Sonoyama, H. Amii, T. Takagi, T. Kanamori, Kanamori. Chem. Lett. **44**, 834–836 (2015)
19. E.S. Clark, Polymer **40**, 4659–4665 (1999)
20. P.C. Painter, M.M. Coleman, J.L. Koenig, *The Theory of Vibrational Spectroscopy and Its Application to Polymeric Materials* (Wiley, New York, 1982), pp. 227–252
21. P. Higgs, Proc. Roy. Soc. (London) **A220**, 472–485 (1953)
22. M.J. Hannon, F.J. Boerio, J.L. Koenig, J. Chem. Phys. **50**, 2829–2836 (1969)
23. T. Hasegawa, Chem. Phys. Lett. **627**, 64–66 (2015)
24. A.E. Tshmel, V.I. Vettegren, Spectrochim. Acta **29A**, 1681–1686 (1973)
25. A. Ikehata, N. Higashi, Y. Ozaki, J. Chem. Phys. **129**, 234510 (2008)

Chapter 7
Appendix

7.1 Fundamental Parameters in Electrodynamics

To understand the light absorption by a condensed matter, the most important physical parameter is *polarization density*, which is the charge polarization in the matter induced by the externally applied electric field of the light.

The most fundamental principle of *electric field*, $\boldsymbol{E}$, is defined by the measured force, $\boldsymbol{F}_{\mathrm{E}}$, of a probe charge, q, put in the field [1].

$$\boldsymbol{F}_{\mathrm{E}} = q\boldsymbol{E}$$

Now, let us take a situation that the electric field is yielded by a point charge in vacuum. Since the field is emitted radially from the point, the field 'intensity' is defined as the density of electric lines of force per a unit area, through which the lines go perpendicularly.

The schematic picture of a point charge emitting the electric lines of force is represented by *Gauss*' *rule*:

$$\oiint_A \varepsilon_0 \boldsymbol{E} \cdot \mathrm{d}\boldsymbol{S} = \iiint_V \rho \mathrm{d}\boldsymbol{V} = q_0. \tag{7.1}$$

A closed sphere about the charge, q_0, is imagined, and the number of the electric lines of force is counted by summation of the perpendicular component to the minute area, $\mathrm{d}\boldsymbol{S}$. In this manner, the electric-line density corresponds to $\boldsymbol{E}$. ε_0 is necessary for adjusting unit. The schematic of a point charge can be expanded to be charged space with a charge density of ρ. In any case, this model is for *un*-polarized space.

Next, let us consider a dielectric matter that is composed of many dipoles. The dipole is categorized into the permanent dipole and the induced dipole by external electric field. Since the induced dipole has an electric field with the opposite

T. Hasegawa, *Quantitative Infrared Spectroscopy for Understanding of a Condensed Matter*, DOI 10.1007/978-4-431-56493-5_7

direction to the external one, this can be regarded as if another charge, δq, is generated in the matter such as

$$\oiint_A \varepsilon_0 \boldsymbol{E} \cdot \mathrm{d}\boldsymbol{S} = q_0 + \delta q. \tag{7.2}$$

If the *additional electric field density by the induced dipoles only* is denoted as: $\boldsymbol{P}$, Gauss' rule can be written as:

$$\delta q = -\oiint_A \boldsymbol{P} \cdot \mathrm{d}\boldsymbol{S},$$

by considering the direction of the induced field to the external field. $\boldsymbol{P}$ is called polarization density. With this parameter, Eq. (7.2) can be rewritten as:

$$\oiint_A \varepsilon_0 E \cdot \mathrm{d}\boldsymbol{S} = \boldsymbol{q}_0 - \oiint_A \boldsymbol{P} \cdot \mathrm{d}\boldsymbol{S}.$$

To make the net charge, q_0, remained in the equation, therefore the next deformation would be convenient:

$$\oiint_A (\varepsilon_0 E + \boldsymbol{P}) \cdot \mathrm{d}\boldsymbol{S} = q_0$$

Here, the integrand is newly defined as:

$$\boldsymbol{D} \equiv \varepsilon_0 \boldsymbol{E} + \boldsymbol{P}, \tag{7.3}$$

which is called "*electric flux density*" or "*electric displacement*." Note that, in this manner, Eq. (7.3) is not an equation, but a definition.

At this moment, $\boldsymbol{P}$ is not physically clear, but it is apparently induced by the external field, $\boldsymbol{E}$. Therefore, if $\boldsymbol{E}$ is not strong, $\varepsilon_0 \boldsymbol{E}$ and $\boldsymbol{P}$ would *approximately* be correlated with each other by a *linear* equation as:

$$\boldsymbol{P} = \varepsilon_0 \chi_e \boldsymbol{E}. \tag{7.4}$$

The proportional coefficient, χ_e, is called *electric susceptibility*. As found in Chap. 4, this equation becomes a very important fundamental for the linear spectroscopy. Equations (7.3) and (7.4) can be merged to be:

$$\boldsymbol{D} = \varepsilon_0 (1 + \chi_e) \boldsymbol{E} \equiv \varepsilon_0 \varepsilon_r \boldsymbol{E} \equiv \varepsilon \boldsymbol{E}. \tag{7.5}$$

$\boldsymbol{D}$ is thus linearly correlated with $\boldsymbol{E}$ using a newly defined parameter:

$$\varepsilon_{\mathrm{r}} \equiv 1 + \chi_{\mathrm{e}},$$

which is called *electric relative permittivity*. Once the unit adjustment constant, ε_0, is multiplied, the product, $\varepsilon \equiv \varepsilon_0 \varepsilon_{\mathrm{r}}$, is called *electric permittivity* or *dielectric constant*.

7.2 Continuity of Electric and Magnetic Fields at an Interface

One of the most significant benefits of using electrodynamics for spectroscopy is that an optical interface, which is a junction of two phases with different electric permittivities, can readily be taken into account [1]. In electrodynamics, an interface is treated as continuity of the electric and magnetic fields at the interface, which is deduced from Maxwell equations. Here, the deduction process of the continuity is presented below.

Equations (7.1) and (7.3) are merged to have the derivative representation of Gauss' rule as Eq. (7.8). Since no magnetic monopole (corresponds to "charge") is available for magnetic field, Eq. (7.9) is obtained. Equation (7.6) is known as Maxwell–Ampere's rule: motion of electric charge involving electric current generates magnetic field. Equation (7.7) is for Faraday's electromagnetic induction rule:

$$\nabla \times \boldsymbol{H} - \dot{\boldsymbol{D}} = j \tag{7.6}$$

$$\nabla \times \boldsymbol{E} + \dot{\boldsymbol{B}} = 0 \tag{7.7}$$

$$\nabla \cdot \boldsymbol{D} = \boldsymbol{\rho} \tag{7.8}$$

$$\nabla \cdot \boldsymbol{B} = 0 \tag{7.9}$$

In these equations, $\boldsymbol{E}$ and $\boldsymbol{H}$ are not directly correlated with each other, but via $\boldsymbol{D}$ and $\boldsymbol{B}$, which are defined as the constituent (or material) equations:

$$\boldsymbol{j} = \sigma \boldsymbol{E},$$

$$\boldsymbol{D} = \varepsilon \boldsymbol{E} \text{ and}$$

$$\boldsymbol{B} = \boldsymbol{\mu} \boldsymbol{H}.$$

As mentioned at Eq. (7.5), the linear relation between $\boldsymbol{D}$ and $\boldsymbol{E}$ is an approximation, and therefore the correlations are put aside the main four equations.

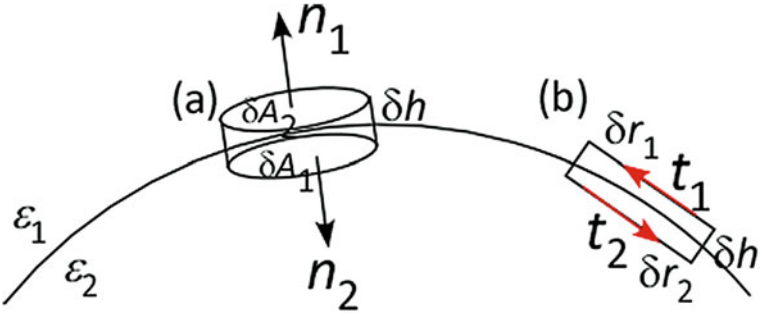

Fig. 7.1 Schematic image of a boundary between two phases. **a** A thin cylinder and **b** the thin square are used to consider the Gauss and Stokes theorems about the boundary

Now, let us imagine a very thin cylinder involving a part of the interface with a thickness of $\boldsymbol{\delta h}$ (Fig. 7.1a). The top and bottom surfaces have areas of $\boldsymbol{\delta A}_1 = \boldsymbol{\delta A}_2 (\equiv \boldsymbol{\delta A})$, respectively. Here, a mathematical formula of Gauss' theorem is employed on considering Eq. (7.9):

$$\int \nabla \cdot \boldsymbol{B} \, \mathrm{d}V = \int \boldsymbol{B} \cdot \boldsymbol{n} \, \mathrm{d}S = 0, \tag{7.10}$$

which conveniently correlates a surface integral to a volume integral. The surface normal vectors to the cylinder top and bottom surface are represented by $\boldsymbol{n}_1$ and $\boldsymbol{n}_2$, respectively. If the thickness of the cylinder has no contribution at the limit of $\delta h \to 0$, the right-hand side of Eq. (7.10) is written as:

$$\begin{aligned} 0 &= \boldsymbol{B}_1 \cdot \boldsymbol{n}_1 \, \delta A_1 + \boldsymbol{B}_2 \cdot \boldsymbol{n}_2 \, \delta A_2 + \text{wall} \\ &\approx (\boldsymbol{B}_1 - \boldsymbol{B}_2) \cdot \boldsymbol{n}_{12} \delta A \\ &\Leftrightarrow \boxed{\boldsymbol{n}_{12} \cdot \boldsymbol{B}_1 = \boldsymbol{n}_{12} \cdot \boldsymbol{B}_2,} \end{aligned} \tag{7.11}$$

since $\boldsymbol{n}_1 = -\boldsymbol{n}_2 \equiv \boldsymbol{n}_{12}$ and $\delta A_1 = \delta A_2 \equiv \delta A$ can hold within a good approximation.

Equation (7.11) is a very important conclusion that *the normal component of the magnetic flux density is continuous* at an optical interface. A very similar discussion can be made for the electric field to have:

$$\boldsymbol{n}_{12} \cdot (\boldsymbol{D}_2 - \boldsymbol{D}_1) = \rho$$

If no charge is available in the vicinity of the interface, i.e., the interface region is electrically neutral, the following relation is available.

$$\boldsymbol{n}_{12} \cdot (\boldsymbol{D}_2 - \boldsymbol{D}_1) = 0 \Leftrightarrow \boxed{\boldsymbol{n}_{12} \cdot \boldsymbol{D}_1 = \boldsymbol{n}_{12} \cdot \boldsymbol{D}_2} \tag{7.12}$$

The normal component of the electric flux density is continuous at an optical interface. Note that the continuity holds for flux density, *not* for electric/magnetic *field*.

On the other hand, the continuity *along the interface* is discussed by considering a thin square involving a part of the interface in a cross-sectional image (Fig. 7.1b). A mathematical formula of Stokes' theorem is employed to consider Eq. (7.7). Stokes' theorem correlates a surface integral to a line integral [Eq. (7.13)].

$$\int \nabla \times \boldsymbol{E} \cdot \boldsymbol{b} \, \mathrm{d}S = -\int \dot{\boldsymbol{B}} \cdot \boldsymbol{b} \, \mathrm{d}S = \int \boldsymbol{E} \cdot \mathrm{d}\boldsymbol{r} \tag{7.13}$$

The vector, $\boldsymbol{b}$ is defined as:

$$\boldsymbol{n}_{12} \times \boldsymbol{t} = \boldsymbol{b}$$

where $\boldsymbol{n}_{12}$ is a vector perpendicular to the interface and $\boldsymbol{t}$ is a vector along the rim.

Then, the second and third terms of Eq. (7.13) are written for the thin square:

$$-\dot{\boldsymbol{B}} \cdot \boldsymbol{b} \delta r \delta h = \boldsymbol{E}_1 \cdot \boldsymbol{t}_1 \, \delta r_1 + \boldsymbol{E}_2 \cdot \boldsymbol{t}_2 \, \delta r_2 + \text{wall.}$$

At the limit of $\delta h \to 0$, the left-hand side goes to zero, and as a result,

$$(\boldsymbol{E}_1 \cdot \boldsymbol{t}_1 + \boldsymbol{E}_2 \cdot \boldsymbol{t}_2)\delta r = 0 \quad \Leftrightarrow \quad \boldsymbol{E}_1 \cdot \boldsymbol{t}_1 + \boldsymbol{E}_2 \cdot \boldsymbol{t}_2 = 0$$

is obtained by considering the approximation of $\delta r_1 = \delta r_2 \equiv \delta r$.

If $\boldsymbol{t}_1 = -\boldsymbol{b} \times \boldsymbol{n}_{12}$ and $\boldsymbol{t}_2 = \boldsymbol{b} \times \boldsymbol{n}_{12}$ are taken into account, the next equation is obtained:

$$\boldsymbol{b} \cdot (\boldsymbol{n}_{12} \times (\boldsymbol{E}_2 - \boldsymbol{E}_1)) = 0$$

Since the vector, $\boldsymbol{b}$, can have any direction on the selection of the thin square, the following relation is the necessary and sufficient condition:

$$\boxed{\boldsymbol{n}_{12} \times (\boldsymbol{E}_2 - \boldsymbol{E}_1) = 0}. \tag{7.14}$$

In this manner, we have reached another important conclusion that the *tangential component of the electric 'field' is continuous* at an optical interface.

7.3 Factor Group Analysis of PTFE Having the 13_6 Helix Conformation

When the temperature is below 19 °C, PTFE is in the phase II, in which the helix conformation takes 13_6 [2]. This conformation belongs to the point group of D_{13} for the factor group analysis [3]. Details are found in Table 7.1.

As a result, the irreducible representation is the same as that for the 15_7 helix.

Table 7.1 Character table of D_{13} ($g = 26$)

D_{13}	E	$2C_{13}^1$	$2C_{13}^2$	$\cdots$	$2C_{13}^6$	$13C_2$	
A_1	1	1	1	$\cdots$	1	1	$x^2 + y^2$, z^2
A_2	1	1	1	$\cdots$	1	−1	z
E_1	2	$2\cos\theta$	$2\cos 2\theta$	$\cdots$	$2\cos 6\theta$	0	(x,y) (xz,yz)
E_2	2	$2\cos 2\theta$	$2\cos 4\theta$	$\cdots$	$2\cos 12\theta$	0	$(x^2 - y^2, xy)$
$\vdots$	$\vdots$	$\vdots$	$\vdots$	$\cdots$	$\vdots$	$\vdots$	
E_6	2	$2\cos 6\theta$	$2\cos 12\theta$	$\cdots$	$2\cos 36\theta$	0	
N_R	39	0	0	$\cdots$	0	1	
χ_R	3	$1 + 2\cos\psi$	$1 + 2\cos 2\psi$	$\cdots$	$1 + 2\cos 6\psi$	−1	
χ	117	0	0	$\cdots$	0	−1	

References

1. J.D. Jackson, *Classical Electrodynamics*, 3rd edn. (Wiley, New York, 1998)
2. L. Piseri, B.M. Powell, G. Dolling, Lattice dynamics of polytetrafluoroethylene. J. Chem. Phys. **58**, 158–171 (1973)
3. P.C. Painter, M.M. Coleman, J.L. Koenig, *The Theory of Vibrational Spectroscopy and Its Application to Polymeric Materials* (Wiley, New York, 1982), pp. 196–226